C.A. Bignozzi   *Editor*

Photocatalysis

303

Topics in Current Chemistry

Topics in Current Chemistry
Recently Published and Forthcoming Volumes

Photocatalysis

Volume Editor: Carlo Alberto Bignozzi

With Contributions by

B.D. Alexander · R. Argazzi · J. Augustyński · C.A. Bignozzi ·
M. Bonchio · S. Campagna · S. Caramori · M. Carraro · V. Cristino ·
K. Domen · O. Ishitani · K. Maeda · A. Maldotti · L. Meda ·
A. Molinari · M. Prato · F. Puntoriero · A. Sartorel · F. Scandola ·
K. Sekizawa · R. Solarska · Y. Tamaki · F.M. Toma · T. Yui

Editor
Prof. Dr. Carlo Alberto Bignozzi
Dipartimento di Chimica dell'Università di Ferrara
Università di Ferrara
Via Luigi Borsari 46
44121 Ferrara
Italy
g4s@unife.it

Topics in Current Chemistry
Also Available Electronically

Topics in Current Chemistry is included in Springer's eBook package *Chemistry and Materials Science*. If a library does not opt for the whole package the book series may be bought on a subscription basis. Also, all back volumes are available electronically.

For all customers with a print standing order we offer free access to the electronic volumes of the series published in the current year.

If you do not have access, you can still view the table of contents of each volume and the abstract of each article by going to the SpringerLink homepage, clicking on "Chemistry and Materials Science," under Subject Collection, then "Book Series," under Content Type and finally by selecting *Topics in Current Chemistry*.

You will find information about the

– Editorial Board
– Aims and Scope
– Instructions for Authors
– Sample Contribution

at springer.com using the search function by typing in *Topics in Current Chemistry*.

Color figures are published in full color in the electronic version on SpringerLink.

Aims and Scope

The series *Topics in Current Chemistry* presents critical reviews of the present and future trends in modern chemical research. The scope includes all areas of chemical science, including the interfaces with related disciplines such as biology, medicine, and materials science.

The objective of each thematic volume is to give the non-specialist reader, whether at the university or in industry, a comprehensive overview of an area where new insights of interest to a larger scientific audience are emerging.

Thus each review within the volume critically surveys one aspect of that topic and places it within the context of the volume as a whole. The most significant developments of the last 5–10 years are presented, using selected examples to illustrate the principles discussed. A description of the laboratory procedures involved is often useful to the reader. The coverage is not exhaustive in data, but rather conceptual, concentrating on the methodological thinking that will allow the non-specialist reader to understand the information presented.

Discussion of possible future research directions in the area is welcome.

Review articles for the individual volumes are invited by the volume editors.

In references *Topics in Current Chemistry* is abbreviated *Top Curr Chem* and is cited as a journal.

Impact Factor 2010: 2.067; Section "Chemistry, Multidisciplinary": Rank 44 of 144

Preface

Solar energy is the only renewable and carbon neutral energy source of sufficient scale to replace fossil fuels. Direct conversion of this energy into clean fuels is one of the most important scientific challenges of the 21st century. In this context, both hydrogen production from solar water splitting and carbon dioxide conversion to organics are obviously attractive, being potentially convenient and clean methods to store solar energy in energy rich molecules which can be employed as virtually inexhaustible fuel sources.

Although the realization of a molecular level system mimicking natural photosynthesis for the production of solar fuels is certainly fascinating from a fundamental viewpoint, the achievement of efficient water splitting has so far been limited by a small driving force and kinetic complications arising from the need to realize a multiple proton coupled charge transfer, which is necessary to simultaneously overcome the demanding kinetics of water oxidation and reduction. For these reasons either sacrificial hole or electron scavengers have been coupled to most molecular level charge separators.

Since the experiment of Fujishima and Honda in 1972, the direct use of semiconductor photoelectrodes or nanoparticles, have appeared to be an alternative way for achieving photoinduced water splitting, thanks to the possibility of obtaining, with a practically unitary quantum yield, highly energetic charge carriers that can induce the required electrochemical reactions at the solid/electrolyte interface.

Photoanodes based on n-type metal oxides like TiO_2, WO_3 and Fe_2O_3 have been intensely studied, since, at appropriate pH, they couple ease of fabrication, high chemical stability in aqueous solution under evolving oxygen conditions, and reasonably high incident light to current generation when operated in a photoelectrochemical cell.

On the other hand, the development of molecular systems and interfaces for the conversion of carbon dioxide into energy rich molecules represents an important technological and environmental challenge due to the abundance of CO_2 in the biosphere that contributes significantly to the greenhouse effect. In this context important research activities are directed towards the preparation of photocatalysts containing a photosensitizer unit, which initiates photochemical one-electron

transfer events, and a catalyst which stores reducing equivalents to achieve multi-electron reduction of CO_2.

Finally, Photocatalysis is particularly relevant in order to realize chemical transformations of synthetic interest with a minimal environmental impact. In fact, photochemical reactions require milder conditions than thermal processes and may allow for the conception of short and efficient reaction sequences, minimizing side processes.

The research discussed within the framework of this volume aims to identify and provide solutions to these problems through the application of solar energy conversion schemes which involve the use of regenerative photoelectrochemical, photoelectrolytic or photoelectrosynthetic cells in which solar energy can be stored into chemical fuels and in the development of photocatalytic processes for selective photooxidation of organic compounds.

<div align="right">
Carlo Alberto Bignozzi
Stefano Caramori
</div>

Contents

Metal Oxide Photoanodes for Water Splitting

J. Augustyński, B.D. Alexander, and R. Solarska

Abstract Solar hydrogen production through photocatalytically assisted water splitting has attracted a great deal of attention since its first discovery almost 30 years ago. The publication of investigations into the use of TiO_2 photoanodes has continued apace since and a critical review of current trends is reported herein. Recent advances in the understanding of the behaviour of nanoparticulate TiO_2 films is summarized along with a balanced report into the utility and nature of titania films doped with non-metallic elements and ordered, nanostructured films such as those consisting of nanotubes. Both of these are areas that have generated a not insignificant degree of activity. One goal of doping TiO_2 has been to extend the photoresponse of the material to visible light. A similar goal has seen a resurgence in interest in Fe_2O_3 photoanodes. Herein, the influence of dopants on the photocurrent density observed at Fe_2O_3 photoanodes and, in this regard, the role of silicon has attracted much attention, and a little debate. Finally, we look beyond the binary oxides. Photoanodes made from new materials such as mixed metal oxides, perovskite structured semiconductors, metal (oxy)nitrides or composite electrodes offer the potential to either tailor the optical band gap or tune the conduction or valence band energetics. Recent work in this area is detailed here.

Keywords Hydrogen · Iron oxide · Mixed metal oxides · Titanium dioxide · Visible-light activation

J. Augustyński (✉) and R. Solarska
Department of Chemistry, Warsaw University, Pasteura 1, 02-093 Warsaw, Poland
e-mail: jaugustynski@chem.uw.edu.pl

B.D. Alexander
School of Science, University of Greenwich, Central Avenue, Chatham Martitime, Kent ME4 4TB, UK

Contents

1   Introduction

The term photoanode refers to an n-type semiconductor electrode in contact with an electrolyte, exposed to light, where the absorbed photons serve to decrease the potential and enhance the rate of an electrochemical oxidation process. The photoanode may be combined in an electrochemical cell either with a p-type semiconductor photocathode or with a metallic cathode. The latter configuration was used in the photoelectrolysis cell which first demonstrated the feasibility of photoelectrochemical water splitting, where an oxygen-evolving titanium dioxide, TiO$_2$, photoanode was associated with a hydrogen-evolving platinum cathode [1]. Since the band-gap energies of TiO$_2$, both in the rutile ($E_g = 3$ eV) and the anatase ($E_g = 3.2$ eV) form, preclude any significant solar light absorption, a large number of further studies were directed towards the search of photoelectrode materials that are able to capture a substantial part of the visible spectrum [2]. Those early investigations, including a variety of inorganic semiconductors, showed that the only materials able to photo-oxidize water whilst avoiding photocorrosion (in most cases for kinetic reasons) were metal oxides [2]. This chapter is restricted to the discussion of recent work regarding two binary oxides, TiO$_2$ and hematite, α-Fe$_2$O$_3$, and a series of ternary oxides used as photoanodes to split water. Properties of another important photoanode material, tungsten trioxide, WO$_3$, are discussed in [3] of the present issue and were also very recently reviewed by the present authors [4].

The choice of a suitable photoanode material for water splitting necessitates a trade off between its band-gap energy, which determines its sensitivity to the visible part of the solar spectrum, and its band energetics, which should allow water splitting to proceed with a minimum applied voltage bias. In fact, none of the known metal oxide semiconductors fulfil the criteria represented schematically in Fig. 1.

In another recent review [5], the principal properties of over 130 inorganic semiconductors are summarized. In most cases these materials are metal oxides but also some nitrides, oxynitrides and sulphides, used as photocatalysts (i.e. in the form of particle suspensions) to photosplit water.

Fig. 1 Band energetics
of an ideal semiconductor
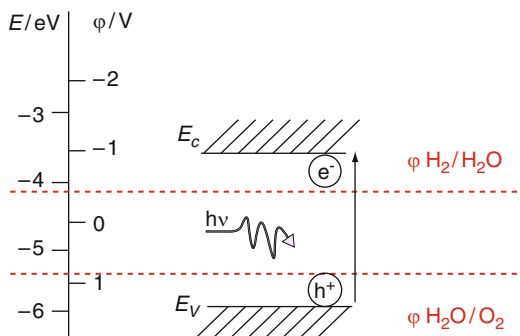
2 Titanium Dioxide

The continuing interest in titanium dioxide stems principally from its application
as photocatalyst for environmental remediation [6], which is greatly facilitated by
the position of its conduction-band edge, negative enough to allow easy oxygen
reduction. Note that the reduction potential of the O_2/O_2^- couple at pH 7 is -0.16 V
vs NHE [7] compared with the flat-band potential of anatase which is of the order
of -0.50 V. Although not specifically related to the field of photocatalysis, a number
of recent studies addressed how structuring TiO_2 film surfaces might improve light
capture as well as TiO_2 doping with non-metallic elements. In several cases, the
latter materials have been characterized as photoanodes for water splitting. These
various aspects are discussed in the present section.

2.1 Nanocrystalline TiO_2 Films

Early interest in nanocrystalline TiO_2 electrodes originated from their use as a
conductive matrix in dye-sensitized solar cells (DSSCs) [8]. Such highly porous
films consisted of a large number of interconnected anatase TiO_2 nanoparticles
(NPs) with diameters in the range of 10–15 nm, stacked onto conductive glass
substrates. Despite the low doping level and poor inherent conductivity of anatase
NPs, DSSCs featuring 10–15 µm thick TiO_2 films exhibited excellent photocurrent–
voltage characteristics and large fill factors [8]. Further studies, intended to charac-
terize photoelectrochemically the nanocrystalline TiO_2 electrodes under band gap
near-UV illumination (i.e. at wavelengths shorter than ca. 400 nm corresponding
to $E_g = 3.2$ eV of anatase), revealed their complex behaviour towards photo-
oxidation of various species in solution [9–12]. In a recent paper Hartmann et al.
[13] compared the photoelectrochemical activity towards water splitting of two
kinds of mesoporous anatase films formed either from pre-synthesized crystalline
TiO_2 NPs or obtained by the sol–gel method followed by high temperature anneal-
ing (up to 550 °C). They found that the sol–gel derived TiO_2 films delivered ca. ten

times larger water splitting photocurrents than their counterparts obtained from crystalline NPs, and tentatively assigned the poor photoelectrochemical performance of the latter films to insufficient electronic connectivity of the NP matrix. Although the above result regarding the ratio of the water splitting photocurrents is consistent with earlier observations [10], the explanation advanced by the authors is at odds with abundant experimental evidence pointing to surprisingly large electronic conductivity of illuminated NP anatase TiO_2 films [9]. A noteworthy feature of anatase NP film electrodes lies, in fact, in their exceptional sensitivity to the nature of the reducing species, present in the solution, acting as hole scavengers. This is illustrated by photocurrent–voltage (I_{ph}–V) plots depicted in Fig. 2a recorded for an NP TiO_2 electrode in a 0.1 M NaOH electrolyte, where water splitting takes place, and after addition to the latter solution of 0.1 M of methanol. The NP TiO_2 films employed in those experiments were formed from commercial P25 particles, 25–30 nm in diameter, composed of ca. 75% of anatase and 25% rutile, which are known to exhibit in photocatalytic reactions behaviour quite similar to that of pure anatase NPs [6]. As shown in Fig. 2a, the photo-oxidation of methanol results in about a 15-fold increase in photocurrent with respect to those corresponding to water splitting. Contrasting with characteristics of the NP TiO_2 electrode for water splitting is also the steep rise of the I_{ph}–V curve, which rapidly reaches the saturation value, and a substantial negative shift of the photocurrent onset potential. For comparison purposes, Fig. 2b shows the I_{ph}–V plots recorded in the same solutions for a compact anatase TiO_2 electrode formed by the sol–gel method. Although, also in the latter case, the occurrence of electron–hole, e^-–h^+, recombination accompanying water splitting is evidenced in a positive

Fig. 2 Photocurrent–voltage plots for (**a**) a nanoparticulate P25 TiO_2 film and (**b**) a compact, sol–gel derived anatase TiO_2 electrode recorded in a 0.1 M NaOH aq. solution and after addition of 0.1 M methanol. The electrodes were irradiated with the full output of a 150 W Xe lamp. The applied potentials are expressed vs reversible hydrogen electrode (RHE) in the same solution. (Reproduced with permission of the Royal Society of Chemistry from [10])
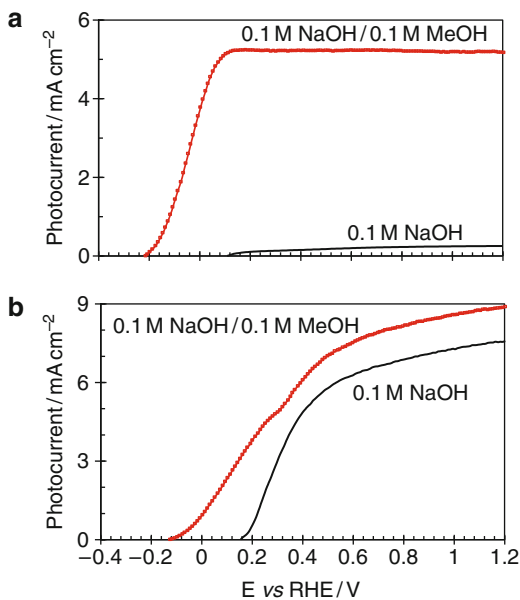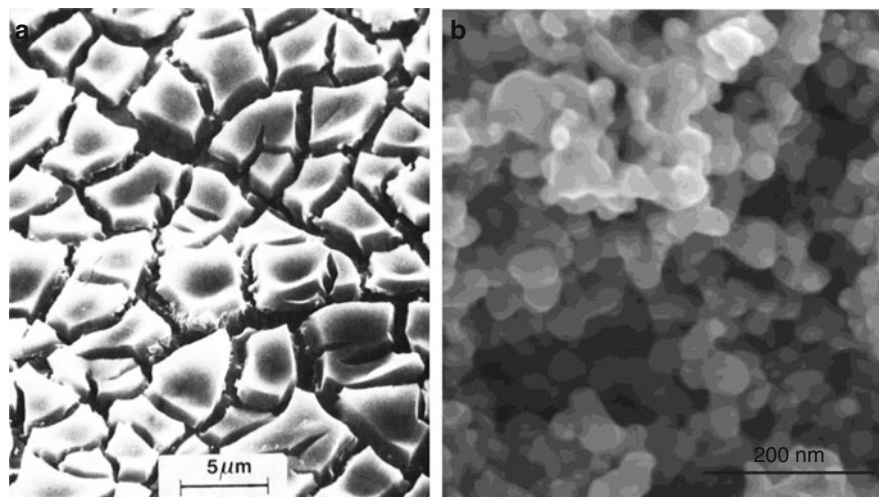
Fig. 3 SEM image showing (**a**) microcracked surface of a sol–gel derived TiO$_2$ film (reproduced with permission from [14]) and (**b**) a nanostructured TiO$_2$ film consisting of P25 particles

displacement of the photocurrent onset potential, both curves reach large saturation currents. A ca. 15% increase of the photocurrent observed for the sol–gel derived electrode, following addition of methanol to the NaOH solution, is attributable to the partial occurrence of the photocurrent doubling [10]. Scanning electron microscopic, SEM, images, given in Fig. 3, show that both kinds of TiO$_2$ films exhibit relatively large surface areas. However, the major difference lies in the fact that, in contrast to the sol–gel derived film [15], the NP film is wholly penetrated by the electrolyte due to its large 50–60% porosity. While the activity of both TiO$_2$ films represented in Fig. 2 towards photo-oxidation of methanol is similar, the NP electrode exhibits a drastic decrease in the water splitting photocurrents. Both the slow rise of the I_{ph}–V curve in Fig. 2a and the particularly low saturation currents characterizing water splitting at the NP TiO$_2$ film are indicative of the occurrence of intense e$^-$–h$^+$ recombination persisting at large anodic potentials – a behaviour attributable to the absence of a conventional space charge layer in such films [9].

To account for the results of early measurements involving NP semiconductor films, it was argued that, due to their small size, the individual nanoparticles do not support an in-built electrical field [16] and that the charge separation in such films occurs at the level of individual particles due to the differing rates of electron and hole transfer to the species present in the solution [17]. As will be shown below, charge separation may be affected by not only the solution species but also the reaction intermediates adsorbed at the semiconductor surface. According to an earlier proposed mechanism [11, 14, 18], the photo-oxidation of water at anatase TiO$_2$ is initiated by the formation of Ti$_S$–O$^\bullet$ radical species occurring, in the case of hole capture by a Ti$_S$–OH terminal group or, in alkaline solution, by the Ti$_S$–O$^-$, according to

$$TiO_2 + h\nu \rightarrow h^+ + e^- \tag{1}$$

$$Ti_S\text{–}OH + h^+ \rightarrow Ti_S\text{–}O^\bullet + H_{aq}^+ \tag{2a}$$

$$Ti_S\text{–}O^- + h^+ \rightarrow Ti_S\text{–}O^\bullet \tag{2b}$$
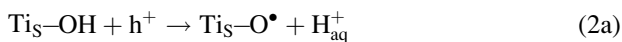
leading subsequently to the formation of bridged $Ti_S\text{–}O\text{–}O\text{–}Ti_S$ surface peroxo species [14, 18]. It is the presence of both $Ti_S\text{–}O^\bullet$ and $Ti_S\text{–}O\text{–}O\text{–}Ti_S$ surface species, which may be considered as trapped positive holes, acting as recombination centres for the photogenerated conduction-band electrons:

$$Ti_S\text{–}O^\bullet + e^- + H_{aq}^+ \rightarrow Ti_S\text{–}OH \tag{3}$$
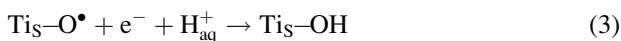
which appears as the most probable cause of the observed poor efficiency of water splitting at NP anatase films. Depending on the incident light intensity, the latter processes may occur in addition to the direct recombination of photogenerated e^-–h^+ pairs.

The formation of surface peroxo intermediates, inferred by earlier electrochemical measurements [11, 14, 18], was later confirmed by Nakamura and Nakato [19] on the basis of in situ IR absorption spectra taken at the NP rutile film/alkaline solution interface irradiated with UV light. Using multiple internal-reflection IR spectroscopy, the latter authors in fact observed a prominent absorption band at 812 cm^{-1} assigned to the bridged Ti–O–O–Ti surface peroxo species. It is also worth mentioning here a recent study by Cowan et al. [20] who investigated dynamics of the processes involved in water photosplitting at nanocrystalline TiO_2 films composed of anatase NPs ca. 15 nm in diameter. Using transient absorption spectroscopy at moderate laser excitation intensities they identified the presence of long-lived holes, characterized by an absorption band centred at 460 nm, which appear as key intermediates in the oxidation of water. The concentration of these long-lived holes, with a lifetime of ca. 30 ms, was found to follow the increase of the photocurrent with applied anodic potential until the photocurrent reached the plateau. Using pulsed illumination at 355 nm, the authors [20] determined the quantum yield of oxygen formation from alkaline solution to be ca. 8%. In fact, the latter value is quite similar to incident photon-to-current conversion efficiencies, IPCEs, for water splitting measured earlier (under steady-state conditions) in acidic solutions [9]. Clearly, regardless of the pH of the solution, the electron–hole recombination appears to be the dominant loss pathway in water splitting at NP TiO_2 film photoanodes.

The situation is completely different in the case of sol–gel derived compact anatase TiO_2 films where the extent of charge recombination is largely reduced due to the effect of anodic potential, E, applied through the space charge layer. The anodic bias causes the surface electron density, N_S, to decrease with the applied potential as [21]

$$N_S = N_B \exp[-e(E - V_{FB})/kT] \tag{4}$$

where N_B is the bulk electron density in the semiconductor, V_{FB} is its flat-band potential, e is the elementary charge, k is Boltzmann's constant and T is the absolute temperature. This explains the large water splitting photocurrents at the sol–gel formed anatase TiO_2 electrode shown in Fig. 2b, which are consistent with IPCE values for such films reaching 80% [15].

In contrast with their poor photoactivity for the water splitting, the NP anatase TiO_2 films exhibit both very large photocurrents under intense UV illumination and high IPCEs (recorded under low intensity monochromatic illumination) for the photo-oxidation of a number of organic molecules that act as hole scavengers, such as alcohols, aldehydes or carboxylic acids [9, 11]. All these compounds undergo rapid charge transfer at the anatase surface leading to CO_2 as the final product. Moreover, in most cases, the reaction intermediates are oxidized even more easily than the starting reactants. This is, for example, the case in the photo-oxidation of methanol [cf. (5) and (6)] where the $^\bullet CH_2OH$ intermediates are able to inject electrons into the conduction band of TiO_2 leading to photocurrent doubling:

$$CH_3OH_{ads} + h^+ \rightarrow {}^\bullet CH_2OH_{ads} + H^+_{aq} \tag{5}$$

$$^\bullet CH_2OH_{ads} \rightarrow {}^\bullet CH_2O + H^+_{aq} + e^-_{cb} \tag{6}$$
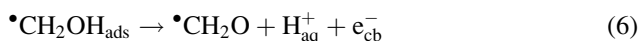
Due to the markedly negative redox potential of the $^\bullet CH_2OH$ radical, E° $(^\bullet CH_2OH/CH_2O) = -0.97$ V [11], which is located ca. 0.8 V above the conduction-band edge of anatase, resulting in strongly downhill nature of the reaction (6), the possibility of the back electron transfer (i.e. the reduction of the $^\bullet CH_2OH$ radical species by the photogenerated electrons) appears negligible. The situation is similar for the photo-oxidation of many other small organic molecules. Moreover, as the reduction of CO_2 at the TiO_2 surface is a notoriously slow process, in most cases, the above-mentioned reactions exhibit large IPCEs. This is illustrated in Fig. 4, showing spectral photoresponses for a ca. 10 μm thick NP TiO_2 film, composed of P25 particles, recorded in a solution of 0.1 M perchloric acid, where water splitting occurs, and after addition to the solution of formic acid or methanol. The IPCEs exceeding 140%, corresponding to the photo-oxidation of the two organic molecules, were observed for short wavelengths, decreased to ca. 10% in the case of water splitting. It is to be noted, however, that while very high IPCEs were already reached in the presence of 0.1 M formic acid, they increased strongly with increasing methanol concentration from 0.1 M to 3 M (cf. Fig. 4). Such behaviour may be explained by assuming that direct hole transfer followed by electron injection into the conduction band, resulting in photocurrent doubling (5) and (6), requires the presence of methanol adsorbed on the TiO_2 surface [11]. According to the results of an in situ study of the competitive adsorption of methanol and water on anatase TiO_2 nanoparticles, conducted using sum frequency generation, SFG, spectroscopy [22], the SFG signal corresponding to chemisorbed methoxy, $Ti_S–OCH_3$, species dropped below the detection limit for a ca. 0.15 M methanol concentration in water. This may imply an increasing contribution from the indirect photo-oxidation pathway with a decrease in the concentration of methanol in solution:
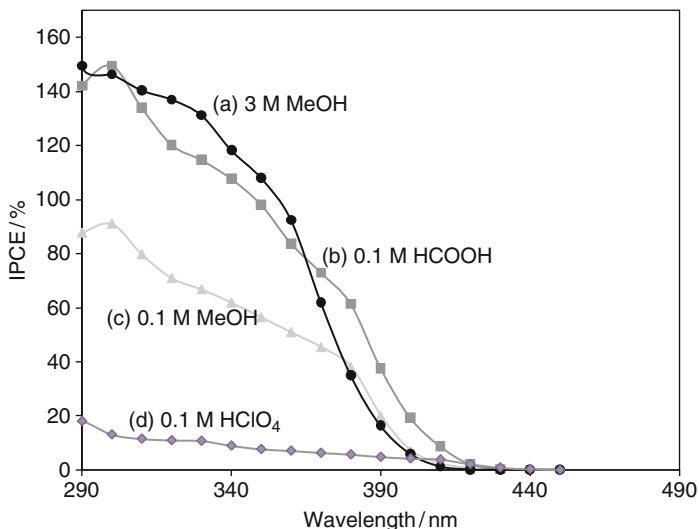
Fig. 4 Photocurrent action spectra for a ca. 10 μm thick NP TiO$_2$ electrode recorded in a 0.1 M HClO$_4$ solution (**d**) and after addition of (**a**) 3 M MeOH, (**b**) 0.1 M HCOOH and (**c**) 0.1 M CH$_3$OH. (Adapted from [9, 11])

$$CH_3OH + Ti_S-O^{\bullet} \rightarrow {}^{\bullet}CH_2OH + Ti_S-OH \tag{7}$$
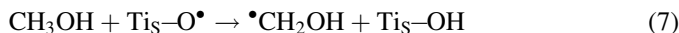
However, given the large IPCEs still observed in 0.1 M methanol solution, reaction (7) remains much faster than the conversion of Ti$_S$–O$^{\bullet}$ species into oxygen. The shape of the IPCE vs incident wavelength plots in Fig. 4, measured under irradiation through solution–electrode interface, confirms that, as expected, charge recombination occurs principally inside the illuminated portion of the NP anatase film. In fact, the larger the illuminated region of the film where the holes are photo-generated, traversed by the electrons, the smaller the observed photocurrent yield. However, the small ohmic losses that accompany collection of charge carriers at the back contact were unexpected. This is particularly well illustrated by the photo-current–voltage plot shown in Fig. 5, recorded for a ca. 45 μm thick NP TiO$_2$ film, irradiated through the solution–electrode interface in 0.1 M formic acid [12]. The penetration depth of the 300-nm light employed in this experiment is of the order of 30 nm [9], corresponding to less than 0.1% of the film thickness. Despite the light absorption occurring at a very large distance from the back contact, the photo-current rises steeply to reach, under an anodic potential bias of only 0.3 V, a maxi-mum corresponding to an IPCE of about 140%. The latter observation indicates, in addition to a small extent of electron–hole recombination, quite low resistive losses occurring across the large unilluminated part of the film. This, obviously, rules out photoconductivity as a possible mechanism of the effective electron transport through such inherently poorly conductive NP TiO$_2$ films.

The preparation of the NP TiO$_2$ films used for the experiments represented in Figs. 2a, 4, and 5 involved high temperature (450 °C) annealing which produced
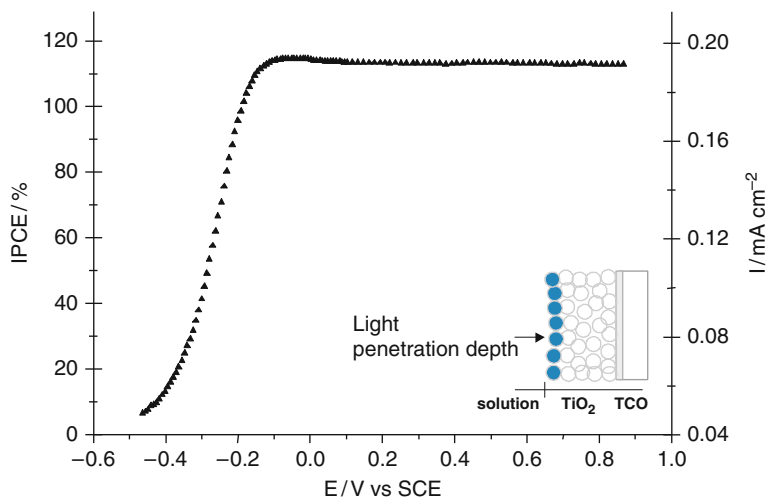
Fig. 5 Photocurrent vs potential plot recorded for a ca. 45 μm thick nanoparticulate TiO_2 film, immersed in a 0.1 M $HClO_4$/0.1 M HCOOH solution and irradiated with a 300-nm monochromatic light (700 μW cm^{-2}) from the side of the film/solution boundary. On the *left axis* is represented the corresponding incident photon-to-current conversion efficiency (IPCE). In the *insert* is represented schematically (marked in *grey*) the illuminated part of the TiO_2 film where the electron injection takes place. (Reproduced with permission from [12])

partial sintering of the particles (cf. the micrograph in Fig. 3b), allowing electrical contact between them to be established [9, 10]. In this context, it was surprising that electrophoretically deposited (from a suspension in water) NP P25 TiO_2 films, simply dried at room temperature, still exhibited large IPCEs and the shapes of the spectral photoresponses were similar to those represented in Fig. 4 for the annealed films [9]. Actually, in the absence of annealing, the network of the TiO_2 NPs, kept together only by the van der Waals–London interactions, might be expected to exhibit much higher resistance due to the presence of more numerous trap sites in the contact regions able to deplete the NPs of free carriers. All these results are in striking contrast to the hypothesis assigning the poor photoactivity of nanocrystalline TiO_2 films towards water splitting to insufficient electronic connectivity of the NP matrix [13].

To explain how an initially poorly conducting network of anatase TiO_2 nanoparticles allows excellent photocurrent–voltage characteristics, either in a dye sensitized liquid-junction solar cell [16] or under direct band-gap illumination in the presence of a suitable hole scavenger, it has been suggested that the film undergoes self-doping occurring in the initial stages of the photocurrent flow before the steady-state is attained [9]. Such photocharging, extending over the whole film thickness, leads to a substantial increase in the electron population within the donor band of anatase and a concomitant increase in conductivity. Importantly, this self-doping is made possible by the very nature of the NP films, which form an interpenetrating network of TiO_2 particles and the electrolyte-containing pores, whose phase boundaries produce a junction of large contact

area. This opens the possibility for the excess charge carrier concentration within the anatase NPs to be compensated simply by the adjustment in the coverage of cations from the electrolyte in the Helmholtz layer [9]. Note that the latter situation is totally different from that of a compact TiO_2 film where the compensation of an excess negative charge occurs through simultaneous injection into the solid phase of protons or alkali cations.

To be effective, the mechanism described above involving the excess charge compensation through the equivalent adsorption of cations in the Helmholtz layer requires the porous TiO_2 films to be composed of relatively small NPs, with diameters in the range of tens of nanometres, offering high internal surface-to-volume ratio. However, a greater surface area also increases the probability of electron–hole recombination in the surface and junction regions. This explains why the photocurrent efficiency of anatase TiO_2 NP films is so strongly affected by the nature of hole scavengers present in the solution. The fast and "irreversible" photoanodic reactions, which do not form intermediates or products able to act as scavengers for photogenerated electrons, usually yield large photon-to-current conversion efficiencies. This is the case for the photo-oxidation of a number of small organic molecules, especially when their concentration in solution is sufficiently large to favour direct hole transfer [11]. In contrast, the photoanodic reactions where an initial hole transfer leads to the formation of an easily reducible species, such as photo-oxidation of water, hydroquinone or iodide ions [9] are all characterized by low IPCEs.

2.2 *Ordered Arrays of TiO_2 Nanotubes and Nanorods*

In an attempt to improve light harvesting and charge separation in TiO_2 photoelectrodes, considerable effort was devoted to the preparation of complex surface structures such as nanotubes, nanorods or nanowires. Early work regarding fabrication and applications of ordered arrays of TiO_2 nanotubes was reviewed by Grimes [23] and more recently by Misra et al. [24] and Schmuki and co-workers [25]. Initially, the TiO_2 nanotube arrays were formed by anodization of titanium metal in fluoride (HF, KF, NaF) aqueous electrolytes [26, 27]. Subsequently, the use of polar organic solvent based electrolytes containing fluoride ions allowed a considerable increase in the length of the nanotubes up to several tens of microns. The geometrical features of the nanotube arrays including, in particular, wall thickness and pore diameter depend on a variety of anodization parameters, making precise control of the whole process quite complex. As-anodized TiO_2 nanotubes are amorphous and they are converted into the anatase phase by annealing in oxygen above 350 °C [23, 24]. The co-appearance of rutile occurs with increasing annealing temperature, especially within the barrier layer separating the nanotube array from the underlying titanium substrate. It is also to be noted that annealing in neutral (N_2) or reducing (H_2) atmosphere delays crystallization of amorphous TiO_2 [24]. Besides their use as hydrogen gas sensors [23], the TiO_2 nanotubes were

considered for application in DSSCs [28] and also as photoanodes for water splitting [29, 30]. The major obstacle for their use in DSSCs lies in the difficulty to fabricate onto the conductive glass substrate an optically transparent anatase nanotube array film required for cell illumination through the anode.

Several authors reported an occasional large water splitting photocurrent obtained with nanotube TiO_2 array electrodes, which appears to be a complex function of the aforementioned geometrical features and should be critically affected by the crystallinity of the walls. This last point, in fact, plays an essential role in the separation of photogenerated charges and in the vectorial electron transport to the back contact.

The assessment of the actual efficiency of the nanotube TiO_2 arrays for the photocleavage of water is made difficult by the lack of systematic data, in particular those showing how the nanotube length affects the IPCEs over the photoaction spectrum. The photocurrent densities exceeding 25 mA cm^{-2} reported by Paulose et al. [30] for a 45 μm long nanotube array raise questions about the way the incident light propagates within such structures and a possible role of multiple light reflections.

In another recent attempt at increasing active surface area and improving light absorption of the TiO_2 photoanode, Wolcott et al. [31] formed arrays of anatase nanorods ca. 1 μm in length, with widths ranging from tens to hundreds nanometres, onto conductive glass substrates. One particularly interesting aspect of this approach is the tilting geometry of the TiO_2 film obtained by oblique-angle electron-beam vapour deposition. The oriented growth induced by the latter method resulted in the formation of a dense array of nanorods, tilted at an angle of approximately 60 ° from substrate normal (cf. Fig. 6), exhibiting strong absorption in the near UV region. Following high temperature (550 °C) annealing, which allowed phase transition from initially amorphous TiO_2 to the anatase crystal structure, the nanorod array photoanode demonstrated particularly large IPCEs for water splitting under band-gap illumination reaching 80% at 350 nm [31].
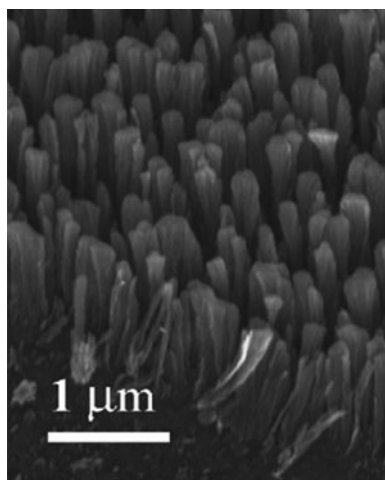
Fig. 6 SEM image of a TiO_2 nanorod array taken at a sample tilt of 35 °. The image reveals widening of the nanorods from the ITO substrate to the tip. (Reproduced with permission from [31])

This result is attributable to the combination of strong optical absorption and effective charge separation through the space charge layer. The authors calculated from Mott–Schottky plots of capacitance data the width of the space charge layer, W, of the order of 100 nm for an applied potential bias less than 1 V. Although smaller than the length of the TiO_2 nanorods present in the film, this width (W) appears sufficient to allow radial charge separation across the nanorods in contact with the electrolyte filling the pores.

The latter example, as also apparently that of TiO_2 nanotube array photoanodes, emphasizes the role played by the space charge layer in determining sizeable IPCEs for slow photo-oxidation reactions, in which intermediates or products able to act as scavengers for photogenerated electrons are formed.

2.3 TiO_2 Doping with Non-Metallic Elements

Earlier efforts to extend the photoresponse of TiO_2 from the UV into the visible spectral region involved mainly metal doping (with the exception of the sensitization with dyes). This work was recently extensively reviewed by Rajeshwar [2]. Although incorporation of a number of transition metal cations, such as Cr(III), into the TiO_2 lattice leads to some sub-band gap photoresponse, it induces, at the same time, enhanced electron–hole recombination over the whole absorption spectrum. This precludes the application of these materials for visible-light driven photosplitting of water. The deception caused by those rather fruitless attempts explains the vivid interest raised by a series of more recent reports on the "TiO_2 band-gap narrowing" by doping with non-metallic elements, in particular with nitrogen, carbon and sulphur. Asahi et al. [32] evaluated, on the basis of density of states, DOS, calculations, the consequences of substitutional doping of anatase crystals with N, C, S, P and F atoms. They concluded that nitrogen doping leads to the band-gap narrowing of TiO_2 through mixing N $2p$ states with O $2p$ states. The reported optical absorption spectra for films prepared by TiO_2 sputtering and high temperature annealing in N_2 atmosphere, extending above 500 nm [32], are indeed consistent with the formation of nitrogen-induced states lying above the valence band of TiO_2. This was confirmed by the results of photocatalytic experiments performed under visible (below 500 nm) light irradiation [32], in agreement with similar earlier observation by Sato [33] who used NO_x-doped TiO_2 samples obtained by calcinations with ammonia. Like the majority of other studies on TiO_2 doped with non-metallic elements, the latter authors [32, 33] used the photodegradation of organic pollutants in the presence of oxygen to test the visible-light photoactivity of their materials. Among notable exceptions to this is the work of Torres et al. [34] who investigated water splitting at the nitrogen-doped TiO_2 films. Those ca. 1 μm thick films prepared by reactive DC magnetron sputtering contained, based on the X-ray photoelectron spectroscopic, XPS, analyses, a slightly larger amount of nitrogen in the surface region, corresponding to a composition of $TiO_{1.987}N_{0.013}$, than the material described by Asahi et al. [32], $TiO_{1.9925}N_{0.0075}$, and exhibited

essentially the rutile structure. Despite the photoresponse extending above 500 nm, the water splitting current measured at ca. 1.5 V vs RHE (reversible hydrogen electrode in the same solution) under 100 mW cm^{-2} visible-light illumination from a sulphur lamp was only about 0.2 mA cm^{-2}. A relatively poor photoelectrochemical performance of the nitrogen-doped TiO$_2$ films was assigned to an enhanced electron–hole recombination consistent with a large positive shift of the photocurrent onset potential occurring specifically under visible-light irradiation. In addition to the observed high density of electron trap states distributed below the conduction band in the nitrogen-doped film, the low mobility of holes generated in localized N 2p electronic states located above the O 2p VB level of TiO$_2$ was evoked by the authors [34] to explain the observed large e$^-$–h$^+$ recombination. This interpretation, which questions the concept of band-gap narrowing in nitrogen-doped titania, involving mixing of N 2p and O 2p states [32], is also supported by the results of photocatalytic measurements of Irie et al. [35], conducted with TiO$_{2-x}$N$_x$ powders. In particular, the latter authors considered that the band structure calculations of Asahi et al. [32], made for the TiO$_{2-x}$N$_x$ with x as large as 0.25 and 0.12, might be irrelevant for the materials with much lower nitrogen doping levels used in photocatalytic experiments. Another attempt to obtain visible-light sensitive titania involved nitrogen ion implantation of TiO$_2$ nanotube arrays [36]. Those anodically formed nanotubes had a length of approximately 0.8 μm. The nitrogen ion bombardment resulted initially in a partial amorphization of the nanotube films and required an additional annealing step to restore the anatase structure. The annealed material exhibited the principal N $1s$ XPS peak at ca. 396 eV, similar to that observed by Asahi [32] and assigned to atomic β-N state. The absence of reported photocurrent–voltage characteristics determined under simulated solar irradiation makes any assessment of the practical water splitting efficiency of those electrodes difficult. However, the IPCEs, based on the photocurrent action spectrum measured for the N-doped TiO$_2$ nanotubes in neutral sodium sulphate solution, culminating at about 20% in the UV region and decreasing from ca. 5% at 400 nm to 2% at 450 nm [36], indicate the persistence of a relatively strong electron–hole recombination.

The band-gap narrowing of TiO$_2$ was also evoked in the case of sulphur doping [37]. Oxidation of a TiS$_2$ powder at 600 °C in air was found to result in the formation of anatase TiO$_2$ including some incorporated sulphur as revealed by a relatively weak XPS signal assigned to a Ti–S bond. Both a relatively small shift of the optical absorption spectrum towards visible wavelengths (to ca. 430 nm) and the white colour of the sulphur-doped sample hardly support a significant band narrowing as deduced from ab initio band structure calculations [37]. The sulphur-doped TiO$_2$ photocatalyst exhibited visible-light activity for the decolorization of methylene blue [38] although the rigour of using this compound, which absorbs visible light by itself, as a test might be questioned.

Among all the attempts aimed at modifying visible-light photoactivity of TiO$_2$ by incorporation of non-metallic elements, it is carbon doping which inspired the largest number of investigations [29, 39–45] and discussions [46–49], especially with regard to the application of such materials for water splitting. Sakthivel and Kisch [40] characterized photocatalysts prepared by hydrolysis of TiCl$_4$ with

tetrabutylammonium hydroxide followed by calcination at 400 °C in air. The samples had an anatase structure and contained ca. 0.4 and 3 mol% of carbon with XPS and IR spectroscopic signatures corresponding to carbonate species (note that longer annealing resulted in smaller carbon content). Both carbon-modified TiO_2 powders exhibited optical absorption extending to red wavelengths, above 700 nm, which the authors [40] assigned to the presence of localized surface states within the band gap lying above the O $2p$ VB edge. A relatively small band-gap narrowing of 0.14 eV (to 3.02 eV) deduced from the analysis of the Kubelka-Munk function for the anatase sample with 3% of carbon was consistent with the observed positive shift of the flat-band potential and the concomitant down shift of the conduction-band edge. The carbon-modified TiO_2 powders described above showed large visible-light activity towards photodegradation of organic pollutants, such as 4-chlorophenol and remazol red azo dye [40].

Interestingly, the materials described in [40] were subsequently used to fabricate thin films, tested as photoelectrodes for water splitting and oxidation of formic acid [44]. The oxygen and carbon dioxide formation were monitored using differential electrochemical mass spectroscopy. No perceptible oxygen signal arising from the carbon-doped electrodes was observed, neither under visible-light nor UV irradiation in sulphuric acid electrolyte. In comparison with undoped TiO_2 films, made from P25 (anatase–rutile) NPs, the carbon-doped electrodes also exhibited much lower photocurrents under UV light after addition to the solution of formic acid, indicating occurrence of an enhanced electron–hole recombination [44]. The latter was assigned to the relaxation of holes photogenerated in the O $2p$ valence band of TiO_2 into localized midgap states, induced by the carbon doping. However, relatively poor crystallinity combined with the small size of NPs (ca. 10 nm in diameter) that form the carbon-doped films appears to be yet another reason for large density of defect states that act as recombination centres. The fact that the same carbon-modified TiO_2 material, when employed in the form of powder suspension, shows excellent photocatalytic activity towards oxidative degradation of organic pollutants points at the essential role played by oxygen in these reactions which, acting as scavenger of photogenerated CB electrons, to a large extent prevents charge recombination. As already discussed in the introduction, this is made possible by the position of the conduction-band edge of TiO_2 negative enough to allow the oxygen reduction and formation of superoxide ion.

The structure and properties of carbon-doped TiO_2 materials vary significantly depending on the preparation method which may involve either an oxidizing or a reducing environment. While in the anatase powders that were obtained by calcination in air at 400 °C described above, the carbon was present as carbonate species [40], i.e. in the positive oxidation state, the situation may be quite different in the case of films prepared by combustion of titanium metal in the flame of a gas burner [42, 43]. In the latter case, the final $TiO_{2-x}C_x$ films included carbon, apparently, in substitutional or interstitial sites and exhibited the rutile structure. Khan et al. [42] obtained carbon-modified TiO_2 films through pyrolysis of Ti metal samples in a natural gas flame at about 850 °C. The films consisted of the rutile polymorph and,

based on XPS measurements, contained ca. 15% of carbon corresponding formally to a composition of $TiO_{2-0.15}C_{0.15}$, suggesting the presence of C atoms in the substitutional form, i.e. replacing O atoms. The optical absorption spectra of those carbon-doped films [42] indicated the presence of two thresholds, one close to the UV region (at 2.8 eV) and another situated in the visible region (at 2.3 eV). As discussed by others [46–49], in the absence of the related IPCE data, it is unclear to what extent the optical absorption figures reported in [42] translate into visible-light water splitting photocurrents.

The properties of titania films formed by combustion of the Ti metal in the flame of a burner fed with various gas mixtures, i.e. under more or less reductive conditions, were examined by Noworyta and Augustynski [43]. Two major changes observed in the bulk composition of flame-formed TiO_2 films included the concomitant presence of disordered carbon, revealed by Raman spectra, and that of lower non-stoichiometric titanium oxides, identified by X-ray diffraction. As expected, the intensity of the Raman bands attributable to carbon was larger for the samples obtained in a carbon-rich flame fed with a propane–butane mixture. However, there was no indication of the formation of oxycarbides, which, normally, should produce additional Raman signals. The only sizeable shift of the photoresponse beyond the fundamental absorption edge of rutile was observed for the carbon-doped TiO_2 film formed in the reductive zone of the propane/butane–oxygen flame. Due to relatively large IPCEs of ca. 20% at 400 nm and 10% at 410 nm, the latter sample exhibited non-negligible, stable water splitting photocurrent of 0.55 mA cm^{-2} determined at 1.23 V vs RHE under simulated solar AM1.5 illumination. Given the presence of lower titanium oxides in those carbon-containing rutile samples, obtained by the combustion of Ti metal in a comparatively reducing environment, their (moderate) visible-light water-splitting activity is to be associated with the formation of oxygen vacancies. Such a conclusion is consistent with the calculations of Di Valentin et al. [50] indicating that carbon doping under oxygen-deficient conditions may favour the formation of oxygen vacancies in bulk TiO_2. As the optical penetration depth in doped TiO_2 at the wavelengths close to the band edge is certainly larger than 1 μm, the measured IPCEs should, in fact, be affected by the bulk composition of such samples. High temperature treatment (up to 1,000 °C) of nanostructured TiO_2 films in ambient air (containing CO_2 and traces of CO and hydrocarbons) has been shown to result in the incorporation of a very large amount of carbon and in the decrease of the optical band gap to 2.06 eV [51]. Based on XPS analyses, the film annealed at 1,000 °C contained an amount of carbon almost equivalent to that of titanium. No significant signal related to carbide was observed and the chemical nature of the incorporated carbon was not indicated.

Park et al. [29] incorporated carbon into anodically formed TiO_2 nanotubes (ca. 3 μm in length) by annealing in a carbon monoxide atmosphere up to 700 °C. It is to be recalled in this connection that, following high temperature annealing, the as-formed amorphous nanotube walls are converted essentially into anatase with the simultaneous appearance of rutile, especially within the barrier layer that separates the nanotube array from the underlying titanium substrate. It is probably the

increase in thickness (and resistance) of this barrier layer, which explains the decrease of the photocurrents observed for heating temperatures exceeding 600 °C [29]. Based on the XPS spectra, the authors found within the $TiO_{2-x}C_x$ nanotube arrays the carbon concentrations ranging from 8 to 42%, depending on the annealing temperature, but the nature of the observed C $1s$ peak was not indicated. A Tauc plot, that is $(j_{ph} \, hv)^{1/2}$ vs hv (where j_{ph} is the photocurrent and hv is the energy of the incident light), was found to be linear and from this it was deduced that the carbon-doped TiO_2 sample had a band-gap energy of 2.2 eV consistent with the observed significant visible-light ($\geq$420 nm at 100 mW cm^{-2}) photocurrents reaching 0.8 mA cm^{-2} [29]. Raja et al. [45] heated the TiO_2 nanotube arrays in an acetylene–hydrogen gas mixture at 650 °C. The incorporation of the carbon species into TiO_2 occurred, at least partially, by diffusion from the thin layer of carbon formed during the treatment on the surface of the samples. The carbon-doped nanotube arrays exhibited an important red shift of the absorption spectrum and a photocurrent of 0.45 mA cm^{-2} when illuminated with visible light ($\geq$400 nm). The particularly large photocurrent reported under AM1.5 light of 2.75 mA cm^{-2} was, apparently, measured under light intensity substantially higher than 100 mW cm^{-2} [45]. To explain the visible-light photoactivity of those samples, the combined effect of oxygen vacancies and, possibly, of intercalated carbon species was evoked. It is to be noted that, despite the highly reductive atmosphere of the heat treatment, Raja et al. [45] report the presence in the annealed samples of carbonate species, identified through the C $1s$ XPS signal at 288.4 eV, similar to those observed earlier in the carbon-doped anatase powders obtained by calcinations in air [40].

In view of the results reported to date, the TiO_2 films doped with non-metallic elements offer rather poor prospects for application as effective sunlight-driven photoanodes for water splitting. As discussed earlier, the situation is quite different in the case of nitrogen- and especially carbon-doped titania powders which have been demonstrated to act as efficient visible-light active photocatalysts for the degradation of various organic pollutants.

3 Iron Oxide

Much as TiO_2 has attracted the vast majority of attention as a photocatalyst, both for the photolytic splitting of water and for photo-oxidation of organic species, its long-term potential as a useful photoanode for solar hydrogen production is hindered by its comparatively large band gap of 3.2 eV in the case of anatase. In essence, this means that only photons with wavelengths shorter than 395 nm can be successfully used to generate electron–hole pairs. This corresponds to approximately 4% of photons that reach the surface of the Earth [52], as shown in Fig. 7. It is therefore unsurprising that the development of so-called "visible-light activated" photocatalysts has attracted much attention. There are many reports of visible-light activated photocatalysts in the literature [53, 5], although such claims have been made for any material with an optical band gap that corresponds to wavelengths longer than
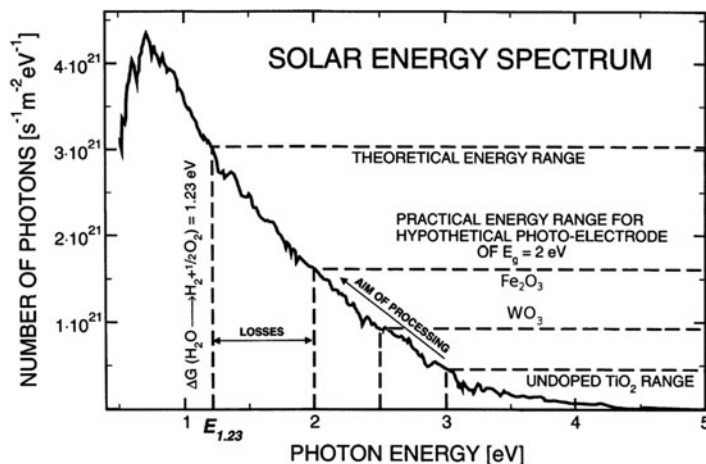
Fig. 7 Spectrum of AM1.5 solar irradiation. The optical band gaps of common metal oxide photocatalysts are indicated for comparison. (Reproduced with permission from [52])

420 nm. The utility of nanostructured tungsten trioxide films, with a band gap of 2.5 eV has recently been reviewed elsewhere [54, 4]. This would substantially enhance the portion of the solar spectrum towards which the photoanode is active. It is possible to develop materials that have even smaller optical band gaps. Although the thermodynamic limit implies that no material with a band gap smaller than 1.2 eV can be used for the photosplitting of water, the practical limit, taking into consideration ohmic losses and overpotentials associated with hole-transfer reactions, is thought to be around 2.0 eV [5, 54]. To this end, iron oxide, in particular α-Fe_2O_3 (hematite) which is an n-type semiconductor with a band gap in the region of 2.0–2.2 eV, would appear to be a suitable candidate for solar hydrogen production as it allows access to the conversion of approximately 40% of photons from ambient sunlight (photons with wavelengths shorter than 550–600 nm). Indeed, iron oxide has been studied as a photoanode since the 1970s [55], and these studies have in part been inspired by the facts that iron oxide is a low-cost, readily available material and environmentally benign. Much of the early literature concerns iron oxide electrodes prepared from either thermal oxidation of the metal, single crystals or polycrystalline powders which were pressed to form disks and then used as electrodes. These have tended to yield poor photocurrents and poor reproducibility, most likely associated with the mechanical [56] and chemical stability of such pressed-disk electrodes which are unstable in acidic solutions or, in the case of films prepared via thermal oxidation, the iron oxide layer was considered to be too thin, although this is unlikely given the short hole diffusion length (see below).

There are, however, problems associated with the use of iron oxide as a photoanode that are intrinsic to the material itself, e.g. α-Fe_2O_3 is a Mott insulator. The conduction band edge lies at too positive a potential with respect to the hydrogen evolution potential. Although this may be mitigated by the fabrication of iron oxide

photoanodes polarized by a suitable bias, substantial electron–hole recombination rates are observed. This can be evidenced by the fact that the photocurrent onset potential can often occur at substantially positive potentials, which are often little more than 0.5 V more negative than the thermodynamic electrochemical oxidation of water [57]. Indeed, early reports of α-Fe_2O_3 photoanodes yielded poor photocurrent densities. Such rapid electron–hole recombination was accounted for by the low diffusion of charge carriers, and in particular the low hole mobility, $10^{-2}\,cm^2\,V\,s^{-1}$ [58]. As a result of this and the poor electrical conductivity of α-Fe_2O_3, the hole diffusion length is typically of the order of 4 nm. Nevertheless, progress has been made. The synthesis of thin film electrodes from the spray pyrolysis of an iron-containing precursor solution onto heated substrates yielded well-crystallized films that were comparatively dense [59, 60], although the choice of precursor species can induce some nanoporosity into the films [61]. A common theme in many of these reports has been the ease with which the film composition and properties can be tailored by carefully choosing the precursor composition, in particular with respect to the addition of foreign elements, e.g. doping.

3.1 Doping

Doping iron oxide is not a new phenomenon. Morin first reported an increase in conductivity of iron oxide upon the addition of small amounts (0.05 at.%) of Ti^{4+} [62, 63] although the exact amount of titanium required to effect an increase in conductivity was open to question [64]. Similarly, the mechanism for conduction, and how titanium might improve this has been debated. Morin proposed conduction to be mediated by electron hopping involving Fe d orbitals or through sp orbitals of oxygen atoms; the role of oxygen vacancies has also been invoked [65]. Morin's original observation was that an increase in conductivity is commensurate with the addition of one electron into the conduction process per titanium atom. Thus the increase in conductivity is not through the dopant acting as a donor or acceptor, but as an agent which compensates the charge of iron ions present in the film, e.g. conduction through small polaron hopping, $Fe^{3+} + Ti^{3+} \rightarrow Fe^{2+} + Ti^{4+}$ [66]. As such, it is perhaps not surprising that doping with Ti^{4+} remains a common route to improving photocatalytic efficiency. Jorand Sartoretti et al. observed an increase in photocurrents from 0.78 to 4.05 mA cm^{-2} upon doping with a significant amount of Ti^{4+} (5 at.%) under illumination from a 150 W Xe lamp [59, 60]. This was attributed to both an increase in film conductivity and the stabilization of oxygen vacancies by Ti^{4+} ions. An increase in incident-photon-to-current efficiency also occurred upon doping, reaching up to 25% for films produced by spray pyrolysis. The addition of a comparatively large quantity of titanium into the films did not appear to cause a change in the optical band gap, either experimentally observed or in modelling by density functional theory [67]. These findings are in contrast to those of Satsangi and co-workers who observed a decrease in the band gap energy when precursor solutions with increasing concentrations of titanium ions were used

[61]. Interestingly, iron oxide films prepared by spray pyrolysis of iron nitrate solutions containing 0.05 M titanium tetrachloride were reported to have a band gap of 1.27 eV, which would presumably be too low for solar hydrogen production for the reasons stated above. Indeed, the films prepared with this level of titanium displayed the poorest photocurrents under illumination from 150 mW cm^{-2} of a Xe arc lamp. Kumari et al. [61] noticed that as the concentration of titanium present in the precursor solution increased, the flat band potential and the photocurrent onset moved to a more cathodic potential. This is in general agreement with Glasscock et al. [68].

Despite the clear success of Ti doping in bringing about an increase in efficiency, it is not wholly agreed that the main reason for this is the increase in conductivity. Indeed, only a minor decrease in resistivity, and decrease in voltage drop, is expected for photoanodes operating at a maximum possible photocurrent density, and a decrease in resistivity should not change the onset potential. This is contrary to experimental observation for titanium doping and therefore it is thought that the main mechanism contributing to the increase in photocurrent may not be associated with an increase in conductivity [68]. It has been suggested that titanium impurities might segregate between grains in polycrystalline iron oxide films, thereby leading to a passivation of recombination at grain boundaries. This would lead to an increase in the hole diffusion length, which is exceptionally short (ca. 4 nm) in undoped hematite films [69]. Should such a partitioning of titanium to grain boundaries exist, then one might expect to detect a change in the Raman spectra, which will sample less of the film than XRD, going from undoped to doped films. However this is generally not observed. Even so, what often is observed is a distinct change in the morphology of the surface of the films, as evidenced by the scanning electron microscopy images summarized in Fig. 8 where the differences in morphology upon doping can be quite pronounced.

Tetravalent ions such as Ti^{4+} and Si^{4+} and pentavalent ions such as Ta^{5+} and Nb^{5+}, when added, are considered to act as donors. Upon doping with either Ti^{4+} or Si^{4+}, Glasscock et al. [68] observed an increase in the number of charge carriers present in α-Fe_2O_3 films. Addition of Pt^{4+} to spray-pyrolysed thin films did not yield positive results: the observed photocurrents were almost totally suppressed compared to the undoped iron oxide electrodes [60]. In contrast to this, Hu et al. [70] successfully obtained photocurrents in excess of 1 mA cm^{-2} from electrodeposited iron oxide films, in itself an achievement, doped with up to 10 at.% Pt. Films were found to be predominantly hematite in composition although the increase in intensity of a band at 657 cm^{-1} in the Raman spectra with increasing Pt content was not ascribed to an increase in disorder, as is often thought [60, 71, 72], as neither FeO nor magnetite were observed in XPS data. Indeed, only Pt^{4+} was detected by XPS. Pt^{0} was absent, leading to the conclusion that these observations were indicative of a change in surface structure although the Pt concentration was found to be relatively stable throughout the depth of the films. In contrast to previous reports, Hu et al. [70] found that Pt doping can affect an increase in photocurrent density. Undoped electrodeposited films gave photocurrents in the region of 0.69 mA cm^{-2} whereas an optimal concentration of Pt^{4+} of 5 at.%
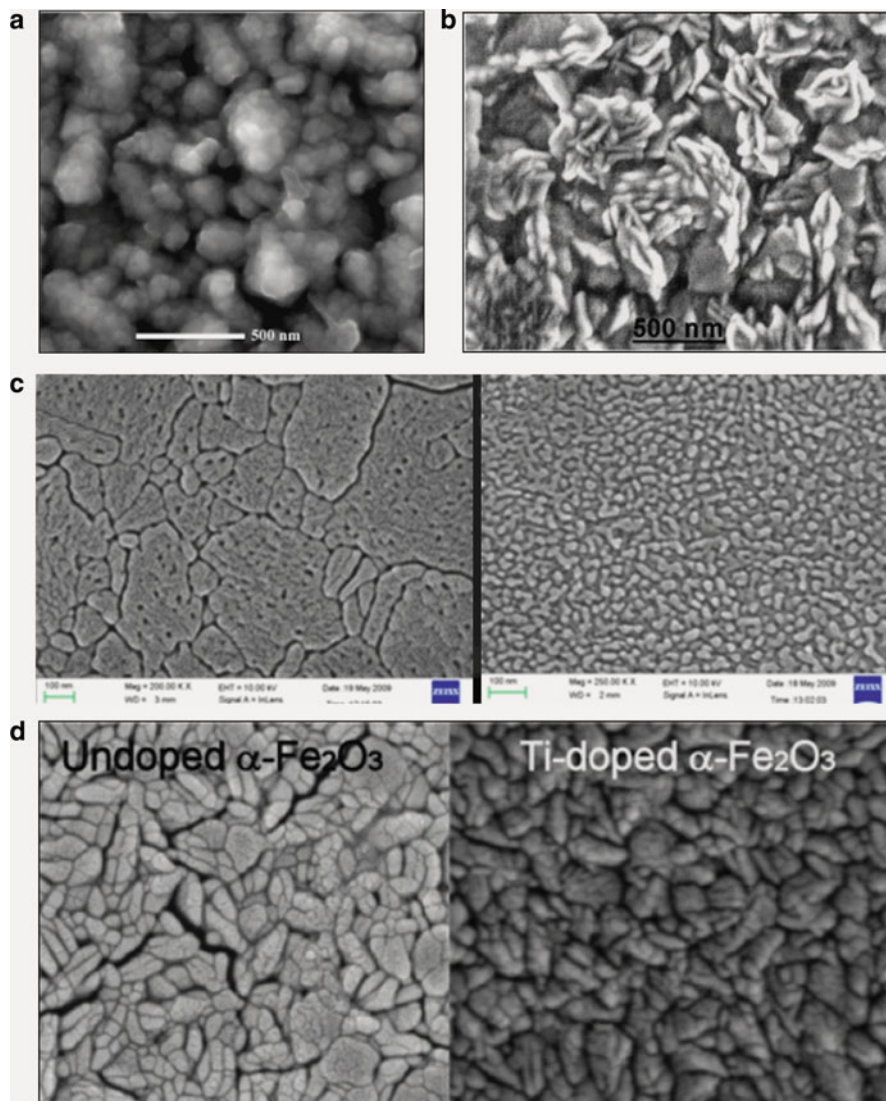
Fig. 8 Scanning electron micrographs of iron oxide films prepared from (**a**) spray pyrolysis of Fe (acetylacetonate)$_3$ solutions, undoped (reproduced with permission from [60]), (**b**) spray pyrolysis of iron(III) chloride solutions doped with 5 at.% Ti^{4+} (reproduced with permission from [59]), (**c**) spray pyrolysis of iron(III) nitrate solutions undoped (*left*) and doped with Ti^{4+} (*right*) at a magnification of 200,000 (reproduced with permission from [61], and (**d**) magnetron sputtering (reproduced with permission from [68])

afforded an increase in photocurrent density to 1.43 mA cm^{-2}. The linear dependence of photocurrent density on light intensity was cited as evidence of a substantially reduced recombination rate compared to that of the undoped films.

Aroutiounian and co-workers made electrodes with the addition of Nb^{5+} at dopant levels and higher [73]. The goal was not so much to add donor species, but to combine the favourable band gap of Fe_2O_3 with the rather negative flat band potential of Nb_2O_5 in order to overcome the thermodynamically unfavourable conduction band edge of Fe_2O_3. Small IPCEs and photocurrents were observed throughout (lower than 10 μA cm^{-2} under illumination from approximately five suns), perhaps as a function of the synthesis of electrodes from a ceramic method. Nevertheless, this serves as an example of how the addition of foreign metal ions can induce behaviour other than an increase in conductivity. Nb was added in amounts of up to 50 at.%, at which point solid solutions were reported to have formed. Indeed, the addition of 10 at.% Nb brought about a significant change in the flat band potential (−0.94 V) thus demonstrating the possibility, if not the practice, to alter favourably the properties of iron oxide.

The addition of large amounts of Nb^{5+} to form solid solutions or new materials, or indeed V^{5+} in the case of $FeVO_4$ [74], may represent an extreme case for the addition of foreign elements. However, it is essentially the ability to change structure or crystallinity that is the desired effect here. α-Fe_2O_3 appears to be the favoured phase of iron oxide for photocatalytic applications. Given that it has the corundum structure, it is isostructural with Al_2O_3 and Cr_2O_3. Therefore, additions of Al^{3+} or Cr^{3+} were expected to act as structure-directing agents, aiding the formation of α-Fe_2O_3 [60, 75]. Although doping with 5 at.% Cr did not produce a beneficial effect on iron oxide films deposited by spray pyrolysis, an increase in photocurrent densities from 0.69 mA cm^{-2} was observed for iron oxide films electrodeposited with 5 at.% Cr^{3+} (1.31 mA cm^{-2}) and as much as 15 at.% Mo^{6+} (1.86 mA cm^{-2}). Electrodeposited iron oxide films were found to have a maximum IPCE of ca. 4% around 400 nm, which is comparatively small compared to those prepared by spray pyrolysis although this increased to 6 and 12% in the case of electrodeposited films doped with 5 at.% Cr^{3+} and 15 at.% Mo^{6+}, respectively. In contrast to the case of Pt^{4+} [70], a substantial degree of surface enrichment was found for both Cr and Mo.

Unlike the cases of Pt^{4+} and Mo^{6+} doping, where reports as to their effects on photocurrents have varied depending on the thin film preparation method, doping iron oxide with small amounts of Al^{3+} has been shown to yield consistent improvements in photoelectrochemical performance. Jorand Sartoretti et al. observed an increase in IPCE from ca. 15% for undoped films to 25% for films doped with 5 at.% Ti and 1 at.% Al [59, 60]. These were accompanied by an increase in the measured photocurrent density which was also sensitive to a thermal treatment and the presence of other dopants. For example, doping with 1 at.% Al effected an increase in photocurrent density only when accompanied by co-doping with 5 at.% Ti. When the concentration of Ti decreased, so too did the photocurrent density and films doped solely with 1 at.% Al displayed a poor photoresponse. Al^{3+} was originally added to favour formation of α-Fe_2O_3 and films were indeed crystalline. However, the performance of the films was sensitive to the form in which Al^{3+} was added. Al_2O_3 particles gave electrodes with poor performance and the use of aluminium(III) chloride hexahydrate as a source was key to achieving high

photocurrent densities. Aluminium doping was also found to improve the performance of electrodeposited films. Kleiman-Shwarsctein et al. [75] reported an increase in photocurrent density and IPCE when $AlCl_3$ was added to the precursor solution. Here the increase in photoresponse was a function of the concentration of Al^{3+} in the film and an optimum concentration was found to be around 0.5 at.%. It was proposed that, although the addition of Al^{3+} did not yield a substantial change in the electronic structure or optical properties of the resulting films, replacing Fe^{3+} with the smaller Al^{3+} leads to shorter Fe–O–Al bonds. Therefore strain was placed on the crystal lattice to accommodate this substitutional doping. This shortening of the metal–oxygen bond was proposed to have an important effect on the small polaron migration, therefore bringing about an improvement in conductivity.

3.1.1 p-Type Dopants

Whereas doping with tetravalent and pentavalent metal ions is grossly considered to induce increased donor levels, doping with divalent or monovalent ions is thought to increase positive charge carriers. For example, the addition of Zn^{2+} or Mg^{2+} to ferric oxide films was initially reported to induce p-type behaviour in what, undoped, would be an n-type semiconductor [76, 77]. Ingler and co-workers reported clear cathodic photocurrents, if small photon conversion efficiencies, with the addition of large quantities of Mg^{2+} or Zn^{2+}. Such p-type behaviour was not reproduced by Satsangi et al. who reported n-type behaviour upon doping ferric oxide films produced by spray pyrolysis or sol–gel synthesis [78, 79]. Photocurrent densities varied substantially depending on the synthetic route but could reach up to 0.64 mA cm^{-2} for spray pyrolysed ferric oxide films doped with 5 at.% Zn. Similar to the case of Zn, Ingler and Khan observed p-type behaviour in ferric oxide films when doped with copper; cathodic photocurrents of ca. 0.95 mA cm^{-2} were observed for films spray pyrolysed from solutions containing 10 at.% Cu [80]. However, similar to the case of Zn, this p-type behaviour was not reported by Satsangi et al. [78] who observed the largest anodic photocurrent density to be ca. 0.07 mA cm^{-2} for films produced by spray pyrolysis from solutions containing 5 at. % Cu. Indeed, little corroboration of the p-type behaviour of Zn-doped ferric oxide electrodes has been reported in recent years. Jorand Sartoretti et al. managed to obtain an additional increase in photocurrent density from ca. 3.3 mA cm^{-2} for undoped electrodes to ca. 7.5 mA cm^{-2} for electrodes doped with 4 at.% Zn and 5 at.% Ti under illumination from the full output of a 150 W Xe lamp. In addition to this, a clear shift (ca. 0.2 V more negative) in the photocurrent onset potential was observed upon doping with Zn, although no p-type behaviour was observed. It is perhaps interesting that the co-doping with a tetravalent ion and a bi- or monovalent ion should give such an increase in performance and it is a strategy which may be worth further exploration although co-doping with 5 at.% Ti and 1 at.% Li appeared not to have a marked effect.

3.1.2 Silicon

Of all the choices of dopants to be used in recent years, the role of Si^{4+} has attracted the most attention. Its role was perhaps serendipitously discovered during studies comparing spray-pyrolysis prepared iron oxide films with those produced by ultrasonic spray pyrolysis [71], which revealed a novel surface nano-platelet morphology, shown in Fig. 9, although this type of morphology had previously been observed in spray pyrolysed films doped with Ti [59], shown in Fig. 8b. Nevertheless, during the course of their studies, Grätzel and co-workers noticed an effect of the tubing used to pump the precursor solutions during the ultrasonic spray pyrolysis. Films prepared using silicone tubing afforded higher photocurrent densities than those prepared using silicon-free tubing and so the deliberate doping of iron oxide films commenced [81]. Upon deliberate doping of hematite films through the use of tetraethyl orthosilicate, TEOS, in the precursor solution, a clear change in the morphology of the films associated with a reduction in the particle size was observed, as shown in Fig. 10. Atmospheric pressure chemical vapour deposition (APCVD) Si-doped ferric oxide thin films afforded a photocurrent density of 2.2 mA cm^{-2} at 1.23 V vs RHE under one sun illumination. In addition, silicon doping was observed to favour the preferential orientation along the 110 axis vertical to the substrate [71, 81, 82]. Upon further refinement it was suggested that the reason for the increased photocurrent density may lie in the possible formation of an insulating SiO_2 layer between the conducting glass substrate and iron oxide film [82]. Indeed, the morphology shown in Fig. 10 may contribute to the enhanced performance of the films. The dendritic structures may offer a shorter pathlength through which holes have to travel to reach the surface. This is of note given the short hole diffusion length that is generally thought to hinder the
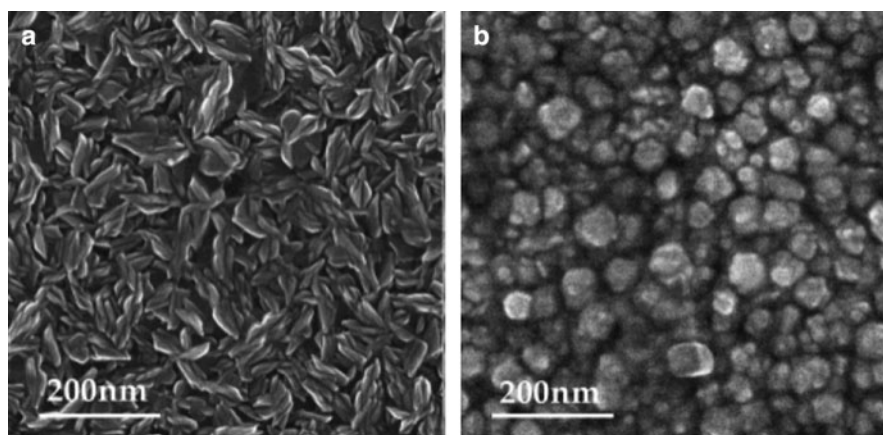
Fig. 9 Scanning electron micrograph of iron oxide thin films prepared from (**a**) ultrasonic spray pyrolysis and (**b**) conventional spray pyrolysis of Fe(acetylacetonate)$_3$ solutions. (Reproduced with permission from [71])
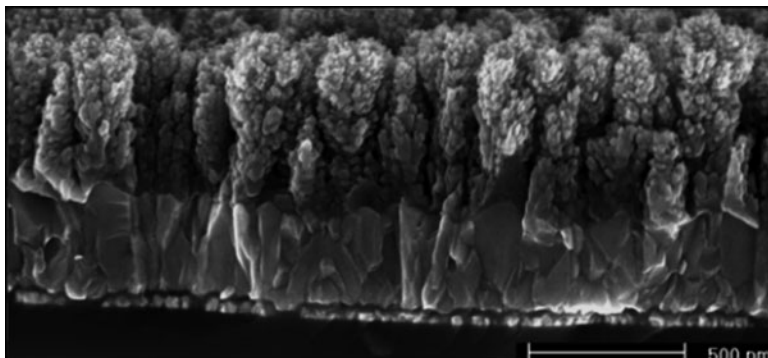
Fig. 10 Scanning electron micrograph of APCVD grown iron oxide films. (Reproduced with permission from [82])
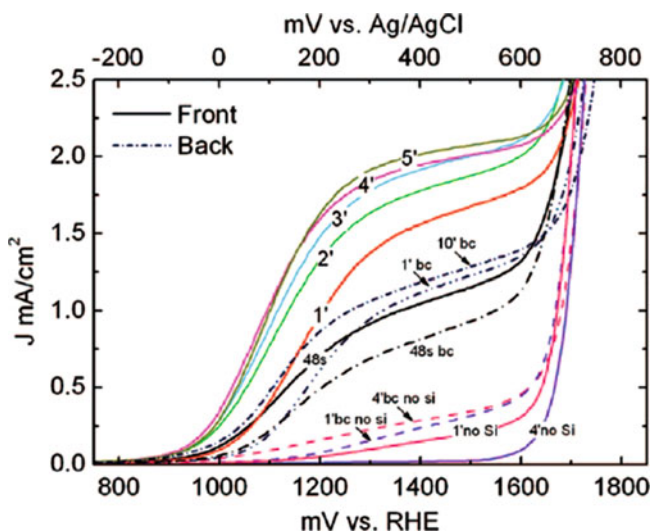
Fig. 11 Effect of deposition time (1′ corresponds to 1 min), and therefore film thickness on photocurrent density. Films were illuminated from the solution interface unless denoted "bc". These films were illuminated from the back contact. Undoped films are denoted "no Si". Photocurrent density recorded in 1 M NaOH under illumination from AM1.5 G light. (Reproduced with permission from [83])

performance. Cesar et al. [83] observed a steady increase in photocurrent density with film thickness for films that were up to 600 nm thick. The photocurrent density was found to plateau for thicker films, shown in Fig. 11. Fe_2O_3 films 60 nm thick were found to be photoactive, particularly when using a high surface area support (WO_3) for the iron oxide film [84].

However, although they could agree that silicon promoted the growth of smaller particles, Saremi-Yarahmadi et al. [85] could not conclusively observe

the formation of such a laminar structure. Following the use of a range of silicon sources for APCVD film growth, they concluded instead that the silicon was incorporated into the film as Si^{4+} in interstitial sites and that the exact role of silicon might result from a combination of factors. The exact nature of any perceived SiO_2 layer between the transparent conducting oxide and the iron oxide remains unknown. Liang et al. [86] have reported that an insulating layer, that need not be SiO_2 (in their case, a 5-nm layer of SnO_2) has beneficial effects on the photocurrent densities, as does the doping of their spray-pyrolysis produced films with 0.4 at.% Si. The utility of the ultrathin insulating layer was tentatively ascribed to either the passivation of surface states or band alignment between the transparent conducting oxide and the iron oxide film.

The beneficial effect of silicon inducing preferential orientation in iron oxide films was also reported by Souza et al. [87] who also observed preferential growth of the 110 planes. However, following deposition of films through magnetron sputtering, Glasscock et al. [68] observed higher photocurrents for films doped with Ti rather than Si, and concluded that this may be linked to a higher amorphous content in films prepared from tetramethyl silane precursors. Furthermore, based on their XRD data, the authors concluded that "it appears unlikely that crystallographic orientation is a dominant factor determining the photocatalytic performance of these films" although they agreed that silicon impurities promoted smaller grains. There remains cordial disagreement as to the exact role of silicon in hematite films.

It is perhaps prescient to summarize that the conflicting reports of the role of particular dopants may lead to confusion as to the "best choice" for future development. It would appear that, in the most part, this discord comes not from a confusion about the behaviour of the dopant per se, but seems to stem from the range of preparative routes to ferric oxide thin films. In particular, how one incorporates a particular dopant into a lattice will depend critically on the solution chemistry and speciation of the metal and it is perhaps right to expect differences on attempting to compare thin films prepared from sol–gel synthesis with those from electrodeposition, or even comparing films prepared from "standard" spray pyrolysis with ultrasonic spray pyrolysis or chemical vapour deposition. The "unknowns" are therefore the final location of the dopant, e.g. surface enrichment, substitutional or interstitial doping, the oxidation state of the dopant in the film and the concentration of the dopant in the film. One might very well start with a precursor solution that has 5 at.% of Ti^{4+}, but the concentration of Ti^{4+} in the final film remains to be ascertained. Indeed, there is no guarantee that the use of titanium ethoxide precursors, for example, would give the same concentration of titanium in a film as titanium butoxide precursors. A recent paper by Sivula et al. [88], serves as an excellent illustrative example where doping arising from migration of atoms from the substrates used was found to influence the film properties. The nature and quantification of the dopants were detected by XPS and magnetic measurements. In general, any evidence that helps uncover these "known unknowns" is lacking in a large part of the wider literature, particularly concerning detailed analysis of the final film composition, and it is therefore unsurprising that such confusion arises.

4   Beyond the Binary Oxide

As has been stated above, the vast majority of research into photocatalysts or photoanodes has focused on TiO_2. That which has not considered TiO_2 has tended to concern other binary oxides such as WO_3 or Fe_2O_3. As a consequence, there has been a drive either to shorten the band gap in comparatively wide band gap materials, e.g. through doping, or to overcome unfavourable conduction band energetics. The attainment of both of these goals has seen work in areas outwith these "standard" binary oxides gather pace. Notably strategies have involved the synthesis of photoanodes consisting of selected mixed metal oxides, perovskite-like semiconductors, composite electrodes or metal (oxy)nitrides.

4.1   Binary Metal Oxides

There is renewed interest in binary semiconducting oxides, other than TiO_2, Fe_2O_3 or WO_3. Both n-type (ZnO, CdO, Bi_2O_3, In_2O_3, SnO_2) and p-type (Cu_2O, NiO) semiconducting oxides have been considered both as powder photocatalysts or as photoelectrodes for water splitting. However, many of them possess either band-gap energies that are too large, such as SnO_2, ZnO, or suffer from substantial electron–hole recombination losses and, in some cases, from poor stability under irradiation [2, 5, 89, 90]. It is worth mentioning that some metal oxides, either conductive (RuO_2, IrO_2) or semiconducting (NiO, Cr_2O_3), are widely used as co-catalysts in photocatalytic and photoelectrochemical systems for water splitting [5, 53, 91].

Following earlier work regarding TiO_2 doping with nonmetallic elements, as discussed in Sect. 2, various efforts have been undertaken to extend the photo-activity of other large band gap semiconducting oxides towards visible wavelengths. This approach is well illustrated by a recent work of Yang et al. [92] describing nitrogen-doped ZnO nanowire array photoanodes. The choice of ZnO was motivated by the relatively negative potential of its conduction-band edge and the high electron mobility in this material. Relatively large amounts of nitrogen, up to 4 at.% vs Zn, were incorporated into the nanowire array through high temperature treatment in ammonia. The major component of the broad N *1s* peak observed in the XPS spectrum of the ZnO:N nanowires, centred at 389.3 eV, was assigned to the oxynitride O–Zn–N species, formed by substitutional (to oxygen) nitrogen doping. In comparison with the undoped ZnO nanowire arrays, the ZnO:N samples exhibited a moderate red shift of the photoresponse with an IPCE of about 15% at 400 nm and a water splitting photocurrent of 0.4 mA cm^{-2} measured at 1 V (vs Ag/AgCl) under AM 1.5 irradiation. An interesting aspect of this work, revealed by the photoaction spectrum, is that the nitrogen doping did not inhibit the photocurrent efficiencies recorded in the fundamental absorption range of ZnO with IPCEs exceeding 80% at 360–370 nm [92].

Rayes-Gil et al. [93] reported an extensive study of nitrogen doping of In_2O_3 powders and films synthesized by a sol–gel method. Large amounts of NH_4Cl or

urea, chosen as dopant sources, were added to the initial In_2O_3 sol–gel which was subsequently submitted to high-temperature calcinations in air. Consequently, the incorporation of nitrogen species into In_2O_3 occurred under essentially oxidizing conditions which is in contrast with the method described above used for the formation of the ZnO:N nanowires [92]. While doping In_2O_3 with urea produced only a minor increase in anodic photocurrents in comparison with the undoped samples, the addition of NH_4Cl led to a significant red shift of the absorption spectrum, extending up to 700 nm. However, this translated to relatively modest water splitting photocurrents, reaching 1 mA cm^{-2} under UV-visible light and approximately five times less under visible ($\lambda \geq 378$ nm) irradiation. Moreover, these photocurrents were measured at 0.7 V (vs Ag/AgCl in a 1 M KOH solution), a voltage substantially higher than the thermodynamic potential of oxygen evolution, which reflects apparently large ohmic and recombination losses occurring within 15 μm thick films. Based on the combined XPS and NMR spectroscopic studies, the authors [93] tentatively assigned the visible-light photoactivity of N-doped In_2O_3 samples to the presence of 1–2 at.% of interstitial NO_x^- species. These "nitrate like" NO_x^- species were suggested to lead to the formation of F-centres, identified by EPR measurements, through the electron transfer to oxygen vacancies existing within In_2O_3. Given the absence of any clear change in the photocurrent onset potentials, associated with N doping, in the reported photocurrent–voltage curves, the observed narrowing of the band gap of In_2O_3 is most likely due to formation of localized electronic states lying above the O $2p$ valence band [94].

Sun et al. [95] investigated the effect of carbon doping upon the photoresponse of In_2O_3 films prepared by spray pyrolysis. Two different carbon sources, glucose and octanoic acid, added to the precursor solution produced films with a similar carbon content, ca. 4 at.%, and the optical band gaps shifted to 2.6–2.7 eV. XPS and ^{13}C solid state NMR studies suggested that carbonate species were responsible for the observed visible-light photoactivity of the carbon-doped In_2O_3 samples [95]. The formation of the carbonate species might, indeed, be expected given the final high-temperature annealing in air of the films. This assignment is consistent with a number of reports regarding carbon-doped TiO_2 (especially anatase) samples [40, 44], where the presence of carbonate species has been suggested to lead to the formation of localized surface states within the band gap, lying above the O $2p$ valence band-edge [40]. The carbon-doped In_2O_3 films [95] afforded relatively low photocurrents, ca. 0.35 mA cm^{-2} under visible-light irradiation, essentially similar to those reported by the same group for the N-doped In_2O_3 samples [93] and again these photocurrents were only obtained under a very large anodic bias.

4.2 Mixed Metal Oxides

One possible approach to decrease the band gap energy of a metal oxide semiconductor may consist of modifying the O $2p$ valence band through hybridization with transition metal orbitals. Therefore, much of the interest is still directed towards

mixed metal oxides allowing the valence band level to be raised by mixing the O 2p orbital with orbitals of a corresponding transition metal, such as Bi(6s), Ag(4d), Ta(5d), V(3d), Tl (6s).

Bismuth vanadate, $BiVO_4$, is an example of a widely studied mixed metal oxide for photocatalytic and, subsequently, for photoelectrochemical water splitting purposes. The band structure of $BiVO_4$ differs from its component metal oxides. The top of the valence band consists of Bi 6s and O 2p orbitals, thus it is less positive, and according to DFT calculations it may even be up to −1.0 eV from the original position of the O 2p orbital [96]. XPS analysis of $BiVO_4$ suggested that the top of valence band of $BiVO_4$ is, in fact, negatively shifted with respect to that of V_2O_5, but without any positive shift of the conduction band level. Therefore, the band gap energy is reduced to 2.4 eV opening the possibility to effect visible-light driven water splitting [96–99].

In 2006 Sayama et al. [96] reported the IPCE efficiency of 44% at 420 nm for oxygen generation under 1.6 V external voltage at a $BiVO_4$ thin film prepared by a modified metal-organic decomposition. In fact, a pretreatment with Ag^+ was used and, due to these results, $BiVO_4$ was placed just after nanocrystalline WO_3 [100] in order of promising photoanodes for water splitting. There has been a substantial amount of effort undertaken to enhance its performance as a result.

To date, several synthesis methods have been used to obtain effective $BiVO_4$ photocatalysts and photoanodes. In this regard, it is worth noting that the photo-electrochemical performance of $BiVO_4$ is strongly affected by the crystallinity of the film rather than by a high surface area. This issue is highlighted by Su et al. [97] who investigated the properties of pyramidal-shaped $BiVO_4$ nanowire arrays for water splitting application. The nanowire arrays were grown vertically onto a $BiVO_4$ seed layer deposited on an $F-SnO_2$ support and the growing conditions were varied as a function of the deposition temperature and additional annealing treatments. It is only after additional annealing at 500 °C, reducing substantially the surface area of the film but, apparently, also the number of surface defects, that the transformed nanopyramid $BiVO_4$ film delivered a photocurrent of 0.4 mA cm^{-2} at 1 V (vs Ag/AgCl) under simulated one sun irradiation. A different approach was chosen by Iwase and Kudo [98] who recently investigated the photoelectrochemical activity of $BiVO_4$ films prepared by pasting a fine nanopowder onto conductive FTO glass plates. A photocurrent of 1 mA cm^{-2} at 1.5 V (vs Ag/AgCl) under visible-light irradiation was reported.

An improvement in the photoelectrochemical behaviour of thin $BiVO_4$ films prepared by ultrasonic spray deposition was obtained by doping with 1 at.% of tungsten atoms [99]. Surprisingly, the authors also mention the merits of the $BiVO_4$ film annealing in hydrogen atmosphere.

Other vanadates have attracted attention. A recent report describes the preparation of $InVO_4$ and thin films where indium atoms were substituted by thallium atoms [101]. This substitution resulted in a significant decrease of the band-gap energy allowing generation of the anodic photocurrent under visible-light illumination and also the appearance of a cathodic photocurrent. Despite the n-type nature of $TlVO_4$, the cathodic photocurrent might appear due to the presence for surface

states within the band gap. This claim is supported by a series of cyclic voltammetric measurements showing a shoulder on a voltammogram, indicative for redox processes involving vanadium oxyanions on the surface. The presence of thallium in the vanadate lattice caused delocalization of the density of states at valence band level and a negative shift of the conduction band edge.

Other mixed metal oxides have been reported besides vanadates; the ferrite based mixed oxides are also attracting more attention. An example of such an oxide is provided by $ZnFe_2O_4$, which showed good photocurrent performance, up to 1 mA cm^{-2} at 0.7 V vs Ag/AgCl (Table 1) under simulated solar illumination [102]. The relatively good efficiency for water splitting under external bias was achieved through a strict control of the deposition parameters during the entire synthesis process by aerosol-assisted chemical vapour deposition.

4.3 Oxynitrides

Nitrogen-doped metal oxides have attracted a lot of attention due to the observed modification of their optical band gaps through incorporation of small amounts of nitrogen. Oxynitrides are partially nitride-substituted semiconducting oxides, and some of them are able to drive the water splitting reaction in the presence of sacrificial reagents [103–109]. The substitution of nitride ions in oxygen sites results in hybridization of N *2p* with O *2p* orbitals leading to the upwards shift in the valence band edge. In consequence, the photoactivity may be extended into the visible range and for some oxynitrides the band positions become suitable for photocatalytic water splitting. This is the case for TaON in particular, which has indeed been extensively studied over the last decade [103, 107–109]. However, despite the use of sophisticated co-catalysts, the efficiencies of TaON based powder photocatalysts for hydrogen production remain rather low. Attempts to use TaON in the form of a photoanode brought about more convincing results. Misra and co-workers [103] prepared TaON nanotube arrays through anodization of the tantalum metal followed by nitridation of the initially formed oxide. These photoanodes delivered water splitting photocurrents of 2.6 mA cm^{-2} at a potential of 0.5 V (vs Ag/AgCl).

Very recently Domen et al. [104] demonstrated high IPCEs (76% at 400 nm) for the photo-oxidation of water at a TaON photoanode formed by electrophoretic deposition of the corresponding powder. The reported high photocurrents, 3.6 mA cm^{-2} (at 0.6 V vs Ag/AgCl), are in a large part attributable to the use of an IrO_2 co-catalyst. Stability of TaON is a critical issue. The authors also claim a significant improvement in this regard due to a partial suppression of the self-photo-oxidation of TaON.

Lanthanum titanium oxynitride is another oxynitride whose performance has recently been improved due to an increased crystallinity of the film and the use of IrO_2 co-catalyst [105]. Due to its band gap in the range of 2.05–2.35 eV, the perovskite derived $LaTiO_xN_y$ is a potentially attractive water-splitting

Table 1 Overview of recent advances in "non-standard" semiconductor materials that have been considered for the photoelectrochemical water splitting

Photo-anode	Synthesis	Morphology	Band gap energy (eV)	Measurement conditions	Photocurrent (mA cm^{-2}) at E (vs. Ag/AgCl)	IPCE (%)	Ref
N-ZnO	Hydrothermal method followed by annealing in NH$_3$	Nanowire array	Redshifted vs. ZnO	AM1.5; 0.5 M NaClO$_4$, pH 7	(0.4) at 1 V	14.6% at 400 nm	[92]
N-In$_2$O$_3$	Sol–gel with NH$_4$Cl used as N source	Coating consisting of uniform particles and islands	2.1	300 W Xe lamp set at 130 mW cm^{-2} (Uv–Vis); 1 M KOH	(0.3) at 0.7 V (3 μm thick film) (1.0) at 0.7 V (15 μm thick film)	–	[93]
C-In$_2$O$_3$	Spray pyrolysis	Cracked morphology due to the annealing-induced shrinkage	2.6–2.7	130 mW cm^{-2} (Uv–Vis); 1 M KOH	(1.0) at 0.7 V (90 μm thick film)	–	[95]
BiVO$_4$	Metal-organics decomposition	Porous BiVO$_4$ film with spherical nanoparticles 90–120 nm in size	2.4	175 mW cm^{-2} (350–500 nm); 0.5 M Na$_2$SO$_4$	(2.2) at 1 V (4.0) at 1 V when pretreated with Ag$^+$ ions	44% at 440 nm (pretreated with Ag$^+$ ions)	[96]
BiVO$_4$	Surfactant free seed mediated growth in aqueous solution	Pyramidal shaped nanowire array	–	100 mW cm^{-2}; 0.5 M Na$_2$SO$_4$	(0.4) at 1 V	–	[97]
BiVO$_4$	Liquid–solid state reaction followed by pasting the precursor on FTO	Film consisting of spherical nanoparticles 100–150 nm in size	2.4–2.5	300 W Xe lamp (λ ≥ 420 nm); 0.1 M K$_2$SO$_4$	(1.0) at 1.5 V	12% at 440	[98]
W-BiVO$_4$	Ultrasonic spray deposition	Densely packed nanoparticles 100 nm in size	2.65	Monochromatic light; 0.5 M Na$_2$SO$_4$	–	10% at 400–450 nm	[99]
TiVO$_4$	Aqueous solution method	Interconnected large particles 1–5 μm in diameter	2.98 eV	150 W Xe lamp (λ ≥ 400 nm); 0.1 M K$_2$SO$_4$, pH 4	(0.063) at 1 V	–	[101]

Material	Method	Morphology	Band gap (eV)	Conditions	Photocurrent at potential	IPCE	Ref.
$ZnFe_2O_4$	Aerosol-assisted chemical vapour deposition	Interconnected cactus-like $ZnFe_2O_4$ structures growing vertically	–	100 mW cm^{-2}; 1 M NaOH	(0.35) at 0.23 V (1.05) at 0.7 V	13.5% at 350 nm	[102]
NTs-TaON	Sonoelectro-chemical anodization of tantalum foil followed by nitridation	Nanotube arrays on a Ta foil	2.07	300 W Xe lamp equipped with AM1.5 G filter; 1 M KOH	(2.6) at 0.5 V	–	[103]
IrO_2-TaON	Electrophoretic deposition from TaON powder	IrO_2 loaded TaON film	2.5	300 W Xe lamp ($\lambda \geq 400$ nm); 0.1 M Na_2SO_4, pH 6	(3.5) at 0.6 V	76% at 400 nm	[104]
IrO_2-LaTiO$_x$N$_y$	Reactive radio-frequency sputtering on Nb-doped $SrTiO_3$	Epitaxially grown oxynitride film	2.35–2.05	300 W Xe lamp ($\lambda \geq 420$ nm); 0.5 M Na_2SO_4, pH 4.5	(0.07) at 1 V	–	[105]
$InVO_4$:$TiVO_4$	$TiVO_4$ grown onto $InVO_4$ seed layer	Film consisting of clusters of small nanoparticles	2.94	150 W Xe lamp ($\lambda \geq 400$ nm); 0.1 M K_2SO_4, pH 4	(0.012) at 1 V	–	[101]
Co-Pi/α-Fe_2O_3	Electrodeposition of Co-Pi onto the surface of APCDV-grown Si-doped α-Fe_2O_3	Continuous Co-Pi layer onto dendritic like structure of Si-α-Fe_2O_3	2.2	AM1.5 1 M NaOH	(1.2) at 0.2 V	–	[115]

photoanode. However, the LaTiO$_x$N$_y$ film photoanode with an optimized nitrogen content afforded a water photo-oxidation current of only 70 µA cm^{-2} (at 1 V vs Ag/AgCl) under visible-light illumination.

From the standpoint of their band-gap energies, allowing absorption of visible light, and also the possibility of tuning the position of their conduction-band edge through compositional changes, the semiconducting metal oxynitrides represent an attractive class of potential photoanode materials for water splitting. The further progress is, however, closely related to their long-term stability under the anodic potentials which are normally applied. This property remains to be demonstrated.

4.4 Perovskite-Type Semiconductors and Composite Electrodes

Perovskites with the general formula ABO$_3$ have been mainly investigated in the form of powder suspensions for photocatalytic light conversion [2, 5]. A few studies, intended to examine their photoelectrochemical activity for water splitting, made use of single crystals or deposits modified by addition of co-catalysts, but the obtained efficiencies were rather low. More complex perovskites having substituted both A and B positions have layered structure which, from the standpoint of the crystallographic orientation, preclude their use as visible-light-driven photoanode materials [5]. However, it is worth noting that a photoelectrochemical study of a series of lanthanide titanium oxides, with layered perovskite structure, revealed Sm$_2$Ti$_2$O$_7$ to have a band gap energy of 2.79 eV whilst also being photoactive under visible-light irradiation [110].

The structural and stoichiometric complexity of multinary perovskites, often requiring laborious synthetic procedures, makes the search for visible-light photoactive materials time-consuming. What is more, the charge compensation phenomena associated with the introduction of dopants render prediction of electronic and optical properties of such semiconductors rather difficult. Therefore, an automated synthesis method opens the possibility of accelerating and systemizing the screening of semiconducting materials with varying compositions. Such a high-throughput synthesis approach might rely on an automated liquid-handling platform followed by consecutive printing and annealing. This strategy has been used in the screening of p-type Bi oxide based semiconductors as well as of n-type, Fe based semiconductors [111, 112]. More recently, a similar screening method has been employed in search of new, ternary metal oxide semiconductors containing Fe, Ti and an additional metal cation [113]. This method is well suited to preparation of metal oxides having different compositions and dopant ratios. The employed precursor solutions are stabilized by organic additives before thermal decomposition. Following this procedure, a matrix of 25 different metal cations and 26 compositions for each added metal cation has been tested. As a result, an Fe–Ti–Sr oxide semiconductor has been found to afford, among the tested compositions, the highest photocurrent under visible-light irradiation, although it should be stated that this remains relatively small in the context of the wider literature.

Another approach offering prospects for improvement of photoelectrochemical efficiency of solar water splitting is a composite photoanode [114, 115]. In contrast to multinary metal oxides or alloys of different semiconductors, in composite materials there is no mixing of the components at the molecular level. Instead, in a composite photoanode the particles of different semiconductors are in electronic contact, thereby allowing the flow of charge carriers dependent on the respective band positions. This eventually improves the charge separation [2]. Such a situation is illustrated by the case of mixed $InVO_4/TlVO_4$ photoanode described in [101].

A different concept of a composite photoanode, involving combination of an n-type semiconductor with an effective oxygen evolution electrocatalyst, namely cobalt phosphate, called Co-Pi, has recently been proposed by Zhong and Gamelin [114, 115]. In contrast with the usual water photo-oxidation co-catalysts, such as RuO_2 or IrO_2 deposited on the semiconductor surfaces in the form of isolated nanocrystals, continuous thin layers of Co-Pi were electrodeposited onto silicon-doped α-Fe_2O_3 films. In spite of some additional light absorption losses, the Co-Pi/ α-Fe_2O_3 composite photoanode exhibited a pronounced cathodic shift (by 180 mV) in the onset potential with respect to the parent α-Fe_2O_3 film. This was accompanied by increased photocurrents reaching ca. 1.4 mA cm^{-2} at 1.2 V (vs RHE) under simulated AM1.5 sunlight [115]. These improvements were attributed to an efficient transfer of holes, photogenerated within the α-Fe_2O_3 film, to the Co-Pi water-oxidation electrocatalyst resulting in reduced charge recombination.

It will be interesting to see whether this concept of the "composite photoanode" will be extended to other semiconductors and electrocatalysts in the future.

References

1. Fujishima A, Honda K (1972) Electrochemical photolysis of water at a semiconductor electrode. Nature 238:37–38
2. Rajeshwar K (2007) Hydrogen generation at irradiated oxide semiconductor-solution interfaces. J Appl Electrochem 37:765–787
3. Caramori S, Cristino V, Meda L, Argazzi R, Bignozzi CA (2011) Hydrogen production with nanostructured and sensitized metal oxides. Top Curr Chem doi: 128_2011_137
4. Alexander BD, Augustynski J (2009) Nanostructured thin-film WO_3 photoanodes for solar water and sea-water splitting. In: Vayssieres L (ed) On solar hydrogen & nanotechnology. Wiley, Singapore
5. Osterloh FE (2008) Inorganic materials as catalyst for photochemical splitting of water. Chem Mater 20:35–54
6. Herrmann J-M (2005) Heterogeneous photocatalysis: state of the art and present applications. Top Catal 34:49–65
7. Sawyer DT, Valentine JS (1981) How super is superoxide? Acc Chem Res 14:393–400
8. O'Regan B, Grätzel M (1991) A low-cost, high-efficiency solar cell based on dye-sensitized colloidal TiO_2 films. Nature 353:737–740

9. Wahl A, Augustynski J (1998) Charge carrier transport in nanostructured anatase TiO$_2$ films assisted by the self-doping of nanoparticles. J Phys Chem B 102:7820–7828
10. Wahl A, Ulmann M, Carroy A, Augustynski J (1994) Highly selective photo-oxidation reactions at nanocrystalline TiO$_2$ film electrodes. J Chem Soc Chem Commun 19:2277–2278
11. Solarska R, Rutkowska I, Morand R, Augustynski J (2006) Photoanodic reactions occurring at nanostructured titanium dioxide films. Electrochim Acta 51:2230–2236
12. Solarska R, Augustynski J, Sayama K (2006) Viewing nanocrystalline TiO$_2$ photoelectrodes as three-dimensional electrodes: effect of the electrolyte upon the photocurrent efficiency. Electrochim Acta 52:694–703
13. Hartmann P, Lee D-K, Smarsly BM et al (2010) Mesoporous TiO$_2$: comparison of classical sol-gel and nanoparticle based photoelectrodes for the water splitting reaction. ACS Nano 4: 3147–3154
14. Ulmann M, Tacconi NR, Augustynski J (1986) Behavior of surface peroxo species in the photoreactions at TiO$_2$. J Phys Chem 90:6523–6530
15. Stalder C, Augustynski J (1979) Photoassisted oxidation of water at beryllium-doped polycrystalline TiO$_2$ electrodes. J Electrochem Soc 126:2007–2011
16. Hagfeldt A, Grätzel M (2000) Molecular photovoltaics. Acc Chem Res 33:269–277
17. Hodes G, Howell IDJ, Peter LM (1992) Nanocrystalline photoelectrochemical cells. J Electrochem Soc 139:3136–3140
18. Augustynski J (1988) Aspects of photo-electrochemical and surface behaviour of titanium (IV) oxide. Struct Bonding 69:1–61 and refs therein
19. Nakamura R, Nakato Y (2004) Primary intermediates of oxygen photo-evolution reaction on TiO$_2$ (rutile) particles, revealed by in situ FTIR absorption and photoluminescence measurements. J Am Chem Soc 126:1290–1298
20. Cowan AJ, Tang J, Leng W et al (2010) Water splitting by nanocrystalline TiO$_2$ in a complete photoelectrochemical cell exhibits efficiencies limited by charge recombination. J Phys Chem C 114:4208–4214
21. Wilson RH (1980) Observation and analysis of surface states on TiO$_2$ electrodes in aqueous electrolytes. J Electrochem Soc 127:228–234
22. Wang C, Groenzin H, Shultz MJ (2004) Direct observation of competitive adsorption between methanol and water on TiO$_2$: an in situ sum-frequency generation study. J Am Chem Soc 126:8094–8095
23. Grimes CA (2007) Synthesis and applications of highly ordered arrays of TiO$_2$ nanotubes. J Mater Chem 17:1451–1457
24. Misra M, Raja KS (2009) Ordered titanium dioxide nanotubular arrays as photoanodes for hydrogen generation. In: Vayssieres L (ed) On solar hydrogen & nanotechnology. Wiley, Singapore
25. Nah Y-C, Paramasivam I, Schmuki (2010) Doped TiO$_2$ and TiO$_2$ nanotubes: synthesis and applications. Chem Phys Chem 11:2698–2713
26. Gong D, Grimes CA, Varghese OK et al (2001) Titanium oxide nanotube arrays prepared by anodic oxidation. J Mater Res 16:3331–3334
27. Macak JM, Tsuchiya H, Schmuki P (2005) High-aspect-ratio TiO$_2$ nanotubes by anodization of titanium. Angew Chem Int Ed 44:2100–2102
28. Zhu K, Neale NR, Miedaner A et al (2007) Enhanced charge-collection efficiencies and light scattering in dye-sensitized solar cells using oriented TiO$_2$ nanotubes arrays. Nano Lett 7: 69–74
29. Park JH, Kim S, Bard AJ (2006) Novel carbon-doped TiO$_2$ nanotube arrays with high aspect ratios for efficient water splitting. Nano Lett 6:24–28
30. Paulose M, Shankar K, Yoriya S et al (2006) Anodic growth of highly ordered TiO$_2$ nanotube arrays to 134 μm in length. J Phys Chem B 110:16179–16184
31. Wolcott A, Smith WA, Kuykendal TR et al (2009) Photoelectrochemical water splitting using dense and aligned TiO$_2$ nanorod arrays. Small 5:104–111
32. Asahi R, Morikawa T, Ohwaki T et al (2001) Visible light photocatalysis in nitrogen doped titanium oxides. Science 293:269–271

33. Sato S (1986) Photocatalytic activity of NO_x-doped TiO_2 in the visible light region. Chem Phys Lett 123:126

34. Torres GR, Lindgren T, Lu J et al (2004) Photoelectrochemical study of nitrogen-doped titanium dioxide for water oxidation. J Phys Chem B 108:5995–6003

35. Irie H, Watanabe Y, Hashimoto K (2003) Nitrogen-concentration dependence on photocatalytic activity of TiO2-x Nx powders. J Phys Chem B 107:5483–5486

36. Ghicov A, Macak JM, Tsuchiya H et al (2006) Ion implantation and annealing for an efficient N-doping of TiO_2 nanotubes. Nano Lett 6:1080–1082

37. Umebayashi T, Yamaki T, Itoh H et al (2002) Bandgap narrowing of titanium dioxide by sulfur doping. Appl Phys Lett 81:454–456

38. Umebayashi T, Yamaki T, Tanaka S et al (2003) Visible light-induced degradation of methylene blue on S-doped TiO_2. Chem Lett 32:330–331

39. Lettman C, Hindenbrad K, Kisch H et al (2001) Visible ligtht photodegradation of 4-chlorophenol with a coke-containing titanium dioxide photocatalyst. Appl Catal B Environ 32:215–227

40. Sakthivel S, Kisch H (2003) Daylight photocatalysis by carbon-modified titanium dioxide. Angew Chem Int Ed 42:4908–4911

41. Irie H, Watanabe Y, Hashimoto K (2003) Carbon-doped anatase TiO_2 powders as a visible-light sensitive photocatalyst. Chem Lett 32:772–773

42. Khan SUM, Al-Shahry M, Ingler WB Jr (2002) Efficient photochemical water splitting by a chemically modified n-TiO_2. Science 297:2243–2245

43. Noworyta K, Augustynski J (2004) Spectral photoresponses of carbon-doped titanium dioxide electrodes. Electrochem Solid State Lett 7:E31–E33

44. Neumann B, Bogdanoff P, Tributsch H et al (2005) Electrochemical mass spectroscopic and surface photovoltage studies of catalytic water photooxidation by undoped and carbon-doped titania. J Phys Chem B 109:16579–16586

45. Raja KS, Misra M, Mahajan VK et al (2006) Photo-electrochemical hydrogen generation using band-gap modified nanotubular titanium oxide in solar light. J Power Sources 161:1450

46. Fujishima A (2003) Comment on "Efficient photochemical water splitting by a chemically modified n-TiO_2" (I) Science 301:1673a

47. Hägglund C, Grätzel M, Kasemo B (2003) Comment on "Efficient photo-chemical water splitting by a chemically modified n-TiO_2" (II) Science 301:1673b

48. Lackner SK (2003) Comment on "Efficient photochemical water splitting by a chemically modified n-TiO_2" (III) Science 301:1673c

49. Murphy AB (2008) Does carbon doping of TiO_2 allow water splitting in visible light? Comments on "Nanotube enhanced photoresponse of carbon modified (CM)-n-TiO_2 for efficient water splitting". Sol Energy Mater Sol Cells 92:363–367

50. Di Valentin C, Pacchioni G, Selloni A (2005) Theory of carbon doping of titanium dioxide. Chem Mater 17:6656–6665

51. Barborini E, Conti AM, Kholmanov I et al (2005) Nanostructured TiO_2 films with 2 eV optical gaps. Adv Mater 17:1842–1846

52. Bak T, Nowotny J, Rekas M, Sorrell CC (2002) Photo-electrochemical hydrogen generation from water using solar energy. Materials related aspects. Int J Hydrogen Energy 27:991–1022

53. Kudo A, Miseki Y (2009) Heterogeneous photocatalyst materials for water splitting. Chem Soc Rev 38:253–278

54. Alexander BD, Kulesza PJ, Rutkowska I et al (2008) Metal oxide photoanodes for solar hydrogen production. J Mater Chem 18:2298–2303

55. Anderman M, Kennedy JH (1988) In semiconductor electrodes. In: Finklea HO (ed) Elsevier: New York

56. Candea RM (1981) Photoelectrochemical behavior of iron oxides thermally grown on Fe Ni alloys. Electrochim Acta 26:1803–1808

57. Leland JK, Bard AJ (1987) Photochemistry of colloidal semiconducting iron oxide polymorphs. J Phys Chem 91:5076–5083

58. Morin FJ (1954) Electrical properties of α-Fe$_2$O$_3$. Phys Rev 93:1195–1199
59. Sartoretti CJ, Ulmann M, Alexander BD et al (2003) Photoelectrochemical oxidation of water at transparent ferric oxide film electrodes. Chem Phys Lett 376:194–200
60. Sartoretti CJ, Alexander BD, Solarska R et al (2005) Photoelectrochemical oxidation of water at transparent ferric oxide film electrodes. J Phys Chem B 109:13685–13692
61. Kumari S, Singh AP, Sonal et al (2010) Spray pyrolytically deposited nanoporous Ti^{4+} doped hematite thin films for efficient photoelectron chemical splitting of water. Int J Hydrogen Energy 35:3985–3990
62. Morin FJ (1950) Magnetic susceptibility of α-Fe$_2$O$_3$ and α-Fe$_2$O$_3$ with added titanium. Phys Rev 78:819–820
63. Morin FJ (1951) Electrical properties of α-Fe$_2$O$_3$ and α-Fe$_2$O$_3$ containing titanium. Phys Rev 83:1005–1010
64. De Cogan D, Lonergan GA (1974) Electrical conduction in Fe$_2$O$_3$ and Cr$_2$O$_3$. Solid State Commun 15:1517–1519
65. Gardner RFG, Sweett F, Tanner DW (1963) The electrical properties of alpha ferric oxide II: ferric oxide of high purity. J Phys Chem Solids 24:1183–1186
66. Iordanova N, Dupuis M, Rosso KM (2005) Charge transport in metal oxides: a theoretical study of hematite α-Fe$_2$O$_3$. J Chem Phys 122:144305–144310
67. Thimsen E, Biswas S, Lo CS, Biswas P (2009) Predicting the band structure of mixed transition metal oxides: theory and experiment. J Phys Chem C 113:2014–2021
68. Glasscock JA, Barnes PRF, Plumb IC, Savvides N (2007) Enhancement of photoelectrochemical hydrogen production from hematite thin films by the introduction of Ti and Si. J Phys Chem C 111:16477–16488
69. Bjorksten U, Moser J, Gratzel M (1994) Photoelectrochemical studies on nanocrystalline hematite films. Chem Mater 6:858–863
70. Hu YS, Shwarsctein AK, Forman AJ et al (2008) Pt doped α-Fe$_2$O$_3$ thin films active for photoelectrochemical water splitting. Chem Mater 20:3803–3805
71. Duret A, Gratzel M (2005) Visible light induced water oxidation on mesoscopic α-Fe$_2$O$_3$ films made by ultrasonic spray pyrolysis. J Phys Chem B 109:17184–17191
72. De Faria DLA, Silva SV, de Oliveira MT (1997) Raman microspectroscopy of some iron oxides and oxyhydroxides. J Raman Spectrosc 28:873–878
73. Aroutiounian VM, Arakelyan VM, Shahnazaryan GE et al (2006) Photo-electrochemistry of semiconductor electrodes made of solid solutions in the system Fe$_2$O$_3$:Nb$_2$O$_5$. Sol Energy 80:1098–1111
74. Morton CD, Slipper IJ, Thomas MJK, Alexander BD (2010) Synthesis and characterisation of Fe-V-O thin film photoanodes. J Photochem Photobiol A 216:209–214
75. Kleiman-Shwarsctein A, Hu YS, Forman AJ et al (2008) Electrodeposition of α-Fe$_2$O$_3$ doped with Mo or Cr as photoanodes for photocatalytic water splitting. J Phys Chem C 112: 15900–15907
76. Ingler WB Jr, Baltrus JP, Khan SUM (2004) Photoresponse of p type zinc doped iron(III) oxide thin films. J Am Chem Soc 126:10238–10239
77. Ingler WB, Khan SUM (2004) Photoresponse of spray pyrolytically synthesized magnesium doped iron(III) oxide (p Fe$_2$O$_3$) thin films under solar simulated light illumination. Thin Solid Films 461:301–308
78. Satsangi VR, Kumari K, Singh AP et al (2008) Nanostructured hematite for photoelectrochemical generation of hydrogen. Int J Hydrogen Energy 33:312–318
79. Kumari S, Tripathi C, Singh AP et al (2006) Characterization of Zn doped hematite thin films for photoelectrochemical splitting of water. Curr Sci 91:1062–1064
80. Ingler WB Jr, Khan SUM (2005) Photoresponse of spray pyrolytically synthesized copper doped p-Fe$_2$O$_3$ thin film electrodes in water splitting. Int J Hydrogen Energy 30:821–827
81. Cesar I, Kay A, Gonzalez M, Gratzel M (2006) Translucent thin film Fe$_2$O$_3$ photoanodes for efficient water splitting by sunlight: nanostructure directing effect of Si doping. J Am Chem Soc 128:4582–4583

82. Kay A, Cesar I, Gratzel M (2006) New benchmark for water photooxidation by nano-structured α-Fe$_2$O$_3$ films. J Am Chem Soc 128:15714–15721

83. Cesar I, Sivula K, Kay A, Zboril R, Gratzel M (2009) Influence of feature size, film thickness, and silicon doping on the performance of nanostructured hematite photoanodes for solar water splitting. J Phys Chem C 113:772–782

84. Sivula K, Le Formal F, Gratzel M (2009) WO$_3$-Fe$_2$O$_3$ photoanodes for water splitting: a host scaffold, guest absorber approach. Chem Mater 21:2862–2867

85. Saremi Yarahmadi S, Wijayantha KGU, Tahir AA, Vaidhyanathan B (2009) Nanostructured α-Fe$_2$O$_3$ electrodes for solar driven water splitting: effect of doping agents on preparation and performance. J Phys Chem C 113:4768–4778

86. Liang Y, Enache CS, Krol R (2008) Photoelectrochemical characterization of sprayed α-Fe$_2$O$_3$ thin films: influence of Si doping and SnO$_2$ interfacial layer. Int J Photoenergy 739864:1–7

87. Souza FL, Lopes KP, Nascente PAP, Leite ER (2009) Nanostructured hematite thin films produced by spin coating deposition solution: application in water splitting. Sol Energy Mater Sol C 93:362–368

88. Sivula K, Zboril R, Le Formal F et al (2010) Photoelectrochemical water splitting with mesoporous hematite prepared by a solution-based colloidal approach. J Am Chem Soc 132:7436–7444

89. Scaife DE (1980) Oxide semiconductors in photoelectrochemical conversion of solar energy. Solar Energy 25:41–54

90. Aroutiounian VM, Arakelyan VM, Shahnazaryan GE (2005) Metal oxide photoelectrodes for hydrogen generation using solar radiation-driven water splitting. Solar Energy 78:581–590

91. Krol Rvd, Liang Y, Schoonmann J (2008) Solar hydrogen production with nanostructured metal oxides. J Mater Chem 18:2311–2320

92. Yang X, Wolcott A, Wang G et al (2009) Nitrogen-doped ZnO nanowire arrays for photo-electrochemical water splitting. Nano Lett 9:2331–2336

93. Reyes-Gil KR, Sun Y, Reyes-Garća E, Raftery D (2009) Characterization of photoactive centers in N-doped In$_2$O$_3$ visible photocatalysts for water oxidation. J Phys Chem C 113:12558–12570

94. Livraghi S, Paganini MC, Giamello E et al (2006) Origin of photoactivity of nitrogen-doped titanium dioxide under visible light. J Am Chem Soc 128:15666–15671

95. Sun Y, Murphy CJ, Reyes-Gil KR et al (2008) Carbon-doped In$_2$O$_3$ films for photoelec-trochemical hydrogen production. Int J Hydrogen Energy 33:5967–5974

96. Sayama K, Nomura A, Arai T et al (2006) Photoelectrochemical decomposition of water into H$_2$ and O$_2$ on porous BiVO$_4$ thin-film electrodes under visible light and significant effect of Ag ion treatment. J Phys Chem B 110:11352–11360

97. Su J, Guo L, Yoriya S, Grimes CA (2010) Aqueous growth of pyramidal-shaped BiVO$_4$ nanowire arrays and structural characterization: application to photoelectrochemical water splitting. Crystal Growth Design 10:856–861

98. Iwase A, Kudo A (2010) Photoelectrochemical water splitting using visible-light-responsive BiVO$_4$ fine particles prepared in an aqueous acetic acid solution. J Mater Chem 20:7536–7542

99. Li M, Zhao L, Guo L (2010) Preparation and photoelectrochemical study of BiVO$_4$ thin films deposited by ultrasonic spray pyrolysis. Int J Hydrogen Energy 35:7127–7133

100. Santato C, Odziemkowski M, Ulmann M, Augustynski J (2001) Crystallographically oriented mesoporous WO$_3$ films: synthesis characterization and applications. J Am Chem Soc 123:10639–10649

101. Butcher DP Jr, Gewirth AA (2010) Photoelectrochemical response of TlVO$_4$ and InVO$_4$: TlVO$_4$ composite. Chem Mater 22:2555–2562

102. Tahir AA, Wijayantha KGU (2010) Photoelectrochemical water splitting at nanostructured ZnFe$_2$O$_4$ electrodes. J Photochem Photobiol A 216:119–125

103. Banerjee S, Mohapatra SK, Misra M (2009) Synthesis of TaON nanotube arrays by sonoelec-trochemical anodization followed by nitridation: a novel catalyst for photoelectrochemical hydrogen generation from water. Chem Commun 46:7137–7139

104. Abe R, Higashi M, Domen K (2010) Facile fabrication of an efficient oxynitride TaON photoanode for overall water splitting into H_2 and O_2 under visible light irradiation. J Am Chem Soc 132:11828–11829
105. Paven-Thivet CL, Ishikawa A, Ziani A, Gendre LL et al (2009) Photoelectrochemical properties of crystalline perovskite lanthanum titanium oxynitride films under visible light. J Phys Chem C 113:6156–6162
106. Fuertes A (2010) Synthesis and properties of functional oxynitrides – from photocatalysts to CMR materials. Dalton Trans 39:5942–5948
107. Hitoki G, Takata T, Kondo JN et al (2002) An oxynitride, TaON, as an efficient water oxidation photocatalyst under visible light irradiation ($\lambda < 500$ nm). Chem Commun 16:1698–1699
108. Abe R, Takata T, Sugihara H, Domen K (2005) Photocatalytic overall water splitting under visible light irradiation by TaON and WO_3 with an IO3-/I-shuttle redox mediator. Chem Commun 30:3829–3831
109. Maeda K, Teramura K, Lu D et al (2006) Photocatalyst releasing hydrogen from water. Nature 440:295
110. Uno M et al (2005) Photoelectrochemical study of lanthanide titanium oxides, $Ln_2Ti_2O_7$ (Ln = La, Sm, and Gd). J Alloys Compd 400:270–275
111. Arai T, Konishi Y, Iwasaki Y et al (2007) High-throughput screening using porous photo-electrode for the development of visible-light-responsive semiconductors. J Comb Chem 9:574–581
112. Arai T, Yanagida M, Konishi Y et al. (2008) AIP Conf. Proc. 2008, 987:26–29
113. Kusama H, Wang N, Miseki Y, Sayama K (2010) Combinatorial search for iron/titanium-based ternary oxides with a visible-light response. J Comb Chem 12:356–362
114. Sun J, Zhong DK, Gamelin DR (2010) Composite photoanodes for photoelectrochemical solar water splitting. Energy Environ Sci 3:1252–1261
115. Zhong DK, Gamelin DR (2010) Photoelectrochemical water oxidation by cobalt catalyst ("Co-Pi")/α-Fe_2O_3 composite photoanodes: oxygen evolution and resolution of a kinetic bottleneck. J Am Chem Soc 132:4202–4207

Hydrogen Production with Nanostructured and Sensitized Metal Oxides

Stefano Caramori, Vito Cristino, Laura Meda, Roberto Argazzi, and Carlo Alberto Bignozzi

Abstract Recent advances in the field of photoelectrochemical cells (PECs) applied to solar water and H_2S splitting and hydrogen production are reviewed with meaningful examples and case studies. At the molecular level, significant recent efforts have been directed towards the development of stable dye sensitizers/water oxidation catalyst assemblies. In the field of photoactive nanostructured materials and interfaces, novel highly ordered semiconductors nanostructures (i.e., anodically grown titania nanotubes) are drawing an increasing interest, under both the fundamental and applicative points of view, due to improved charge transfer kinetics with respect to more conventional sintered nanoparticle substrates. These features, coupled with low cost and ease of fabrication, stand as a good promise for the realization of solar devices capable of solar hydrogen production at a useful rate.

Contents

S. Caramori (✉), V. Cristino, and C.A. Bignozzi (✉)
Dipartimento di Chimica dell'Università di Ferrara, Università di Ferrara, Via Luigi Borsari 46, 44121 Ferrara, Italy
e-mail: cte@unife.it, g4s@unife.it

L. Meda
ENI, Istituto Guido Donegani, Via Fauser 4, 28100 Novara, Italy

R. Argazzi
ISOF-CNR, c/o Dipartimento di Chimica dell'Università di Ferrara, Via Luigi Borsari 46, 44121 Ferrara, Italy

1 Introduction

The phenomenology of semiconductor–liquid interfaces represents a very interesting and important area in science and technology [1], involving principles of electrochemistry, photochemistry, solid state theory, and surface and interface science. The applications are varied, but most are focused on solar energy conversion schemes, through the use of regenerative photoelectrochemical cells (PECs), which convert sunlight to electricity, or photoelectrolytic or photoelectrosynthetic cells in which solar energy is stored in chemical fuels [2]. Other important applications involve the development of photocatalytic processes for selective photooxidation of organic compounds and for environmental remediation.

Photoelectrolysis of water using sunlight [3–5] is extremely attractive for a number of reasons: (1) photoproduced hydrogen is a valuable fuel and energy carrier which can be stored more easily than electricity or heat; (2) it is nonpolluting, inexhaustible, and flexible with respect to energy conversion in heat (combustion) or electricity (in fuel cells); (3) hydrogen is a valuable chemical by itself, being used in large quantities by industry in chemical processing such as ammonia synthesis and petroleum refining.

A central concept in describing the interaction of a semiconductor with an electrolyte is the equilibration of the Fermi level of the solution and of the semiconductor. Although the concept of Fermi level has been initially introduced for an electronically conducting phase, as a level for which the probability of electron occupation of a given state is 1/2, in our discussion the Fermi level can be conveniently identified with the electrochemical potential of electrons in the solid and of a given redox couple (O,R) in solution, where the usual free energy relationships hold. Obviously, the solution phase does not contain free electrons, but contains available electronic states [in the form of oxidized (O) and reduced species (R)] which can equilibrate with free electrons in the solid. As a consequence, $\overline{\mu_{\text{redox}}} = \mu^0 + KT \ln(C_O/C_R)$, where $\overline{\mu_{\text{redox}}}$ and μ^0 are the electrochemical and standard electrochemical potential of the electron and C_O and C_R are the concentrations of the oxidized and reduced form, respectively. Under equilibrium conditions, $E_F(\text{solid}) = E_F(\text{solution}) = \overline{\mu_{\text{redox}}} = neU_{\text{redox}}$, where U is the redox potential of the couple, n is the number of exchanged electrons (e) and e is the electron charge. Thus when an n-type semiconductor is brought into contact with a
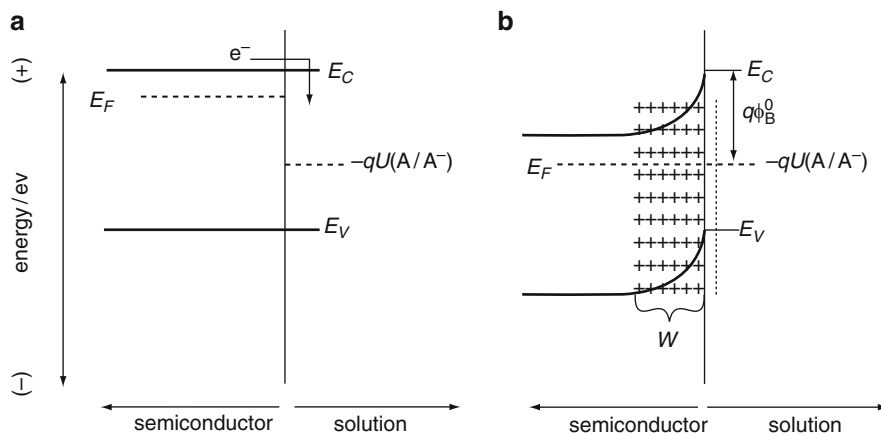
Fig. 1 Before (**a**) and after (**b**) dark equilibration of an n type semiconductor with the electrolyte containing a redox couple of potential U

redox couple, electrons (majority charge carriers) from the solid pass to the solution until the two Fermi levels are identical. Due to the relatively small charge carrier density in the solid, a positive space charge layer of typical thickness 10^{-6} to 10^{-8} m [6] is formed near the surface which is balanced by negative charges in the "compact" Helmholtz layer. The field generated by these negative charges causes an upward bending of the energy band (Fig. 1b). A conceptually similar situation is established for a p-type semiconductor, in which the majority carriers are holes instead of electrons. In that case a space charge layer of opposite sign (negative) would be created by hole transfer to the electrolyte.

The thermodynamic upper limit to the energy that can be extracted by the semiconductor/liquid junction is given by $e\Phi_B^0 = E_c - E_F = E_c + qU_{redox}$, which is called the equilibrium barrier height. For all semiconductor/liquid junctions the condition $qU_{redox} \sim Ev$ gives a barrier height approximately equal to the band gap, maximizing the power output of the system.

For semiconductors under illumination, the quantity related to Φ is the open circuit photovoltage (V_{oc}) which reflects the maximum free energy that can be harnessed by the junctions. However, the usable free energy collected across a semiconductor/electrolyte junction is not limited purely by thermodynamic quantities, but also by electron transfer kinetics and transport of the photogenerated charge carriers (Fig. 2). The electric field inside the space charge region may play a relevant role in assisting the charge separation at the interface. Holes are attracted towards the electrolyte by the negative charge layer, while electrons are repelled from the surface. As a consequence, photooxidation reactions can take place under illumination at the surface of an n-type semiconductor, while photoreduction can be carried out at a counter electrode (either p type semiconductor or metal electrode) wired to the photoactive material. However, in many nanostructured photoelectrodes the small size of the nanocrystals and a lower charge carrier density cannot
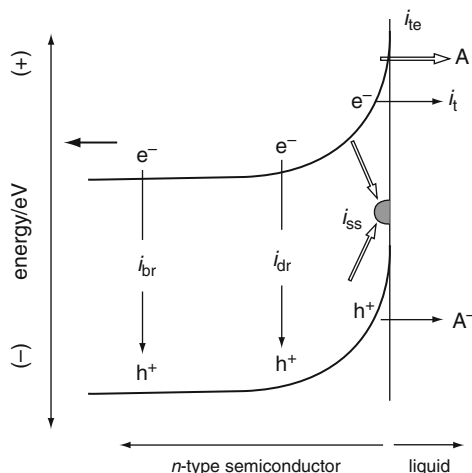
Fig. 2 Recombination pathways of photogenerated charge carriers (e$^-$ and h+) in an n-type semiconductor in the presence of a space charge region and of a A/A$^-$ redox couple. The electron/hole pair can recombine in bulk (ibr), depletion layer (idr), or through surface states (iss). Electron can also tunnel to the electrolyte through the barrier layer (it) or across the interface (ite). The *bold arrows* indicate processes favorable to the functioning of the photoelectrochemical cell:hole transfer to the electrolyte and electron migration/diffusion through the bulk of the solid to the charge collector. From [6]

sustain a relevant electric field [7] and the charge separation is mainly determined by kinetic reasons related to the chemical nature of the redox processes at the semiconductor/electrolyte interface: the efficiency of charge separation is thus essentially determined by the different overpotentials for the oxidation and reduction reactions taking place at the semiconductor surface and by the kinetic competition between recombination and successful transfer of the charge carriers [8, 9].

Several approaches to photoelectrolysis are possible, involving a photoactive semiconductor electrode electrically connected to a metal electrode, or photoactive anode (n-type) and cathode (p-type) acting either as separate electrodes, or coupled to form a monolithic structure called a photochemical diode.

A common photoelectrolysis configuration, useful for the general scope of our discussion, is represented by the wiring of an n-type semiconductor, acting as a photoanode, to a metal counter electrode (Fig. 3).

The Fermi level in the electrolyte has been left undefined since it depends on the initial relative concentrations of H_2 and O_2 in solution. Figure 3b shows the situation at equilibrium in the dark once the semiconductor and the metal are brought into contact with the electrolyte and a depletion layer is formed near the semiconductor surface. Fermi levels of the three phases equilibrate, giving rise to a band bending in the semiconductor. When the semiconductor is irradiated with photons of energy corresponding to the band gap, electron–hole pairs are created and the Fermi level in the semiconductor is raised towards the flat band potential V_{fb} by an amount V_{ph} which is the photopotential generated. The maximum value the

a

b

c

d
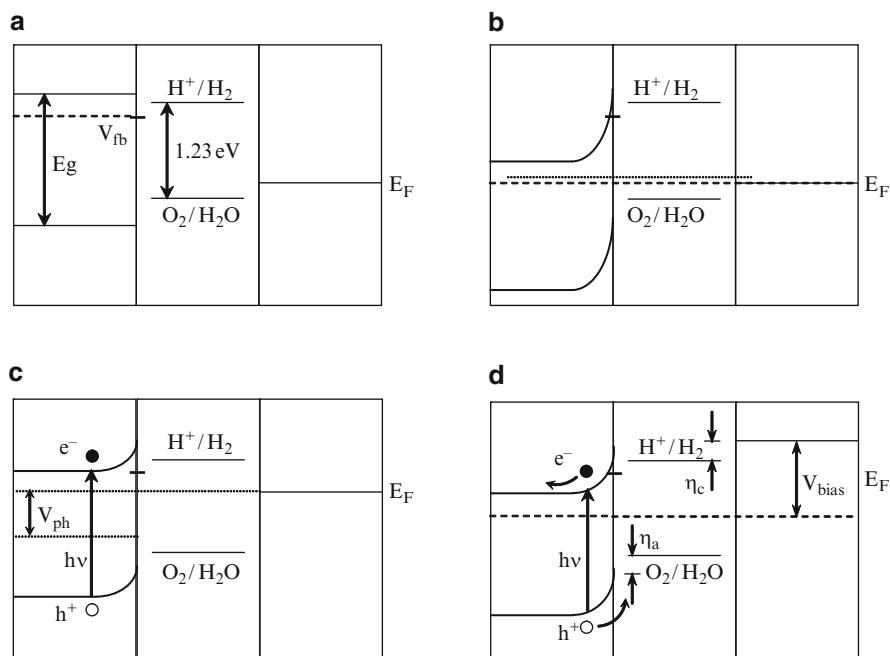
Fig. 3 Energy level diagrams for a semiconductor-metal photoelectrolysis cell: (a) no contact, (b) equilibrium in the dark, (c) high intensity irradiation, (d) high intensity irradiation with anodic bias

Fermi level can reach in the semiconductor is the flat band potential V_{fb} which, in the case shown, is lower with respect to the H^+/H_2 redox couple. This means that hydrogen evolution cannot take place at the metal electrode even at the highest irradiation intensity. For hydrogen evolution to occur, a positive bias must be applied to the semiconductor electrode as shown in Fig. 3d. This bias, which is usually provided by an external voltage source, should also account for the necessary cathodic (η_c) and anodic (η_a) overvoltages in order to sustain the current flow. This situation represents a condition which is frequently met with visible absorbing semiconductor metal oxides photochemically stable in aqueous environment, like WO_3 or Fe_2O_3.

The ideal situation would be to operate with metal oxides in which, like $SrTiO_3$ [10] or $KTaO_3$, the flat band potential is above the H^+/H_2 potential (Fig. 4); therefore no external bias is required to generate H_2 and O_2. Unfortunately most of these materials have large band gaps (3.2–3.5 eV) which result in very low solar absorptivity and are inefficient for solar energy conversion.

With PECs made of n-type and p-type semiconductors in contact with an electrolyte, the requirement of an external bias can be eliminated [11]. A first example of these p–n photoelectrolysis cells was reported by Nozik in 1976 [12] with an n-TiO_2/p-GaP heterotype device whose efficiency at zero bias was 0.25%. The energy diagram of such a cell, also called photochemical diode, is
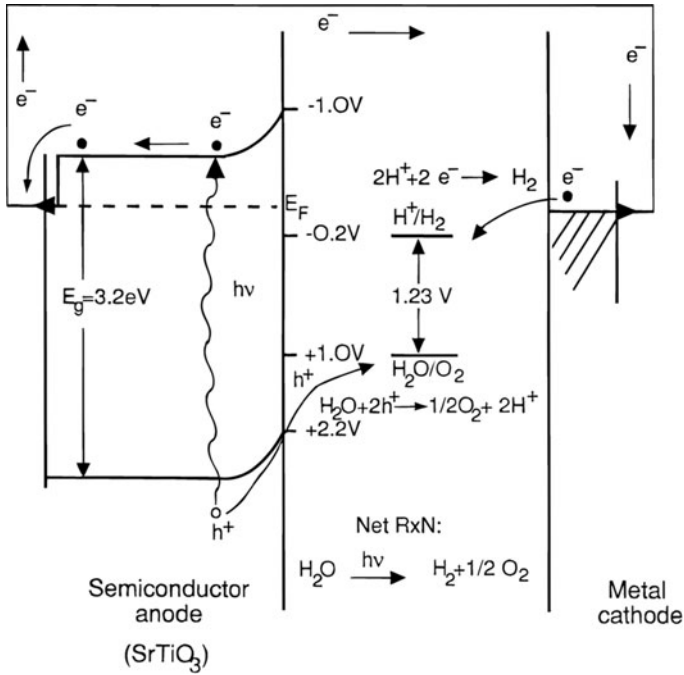
Fig. 4 Photoelectrolysis of water using an $SrTiO_3$ photoanode. Due to the position of conduction and valence band edges hydrogen and oxygen are evolved without need of external bias. From [4]
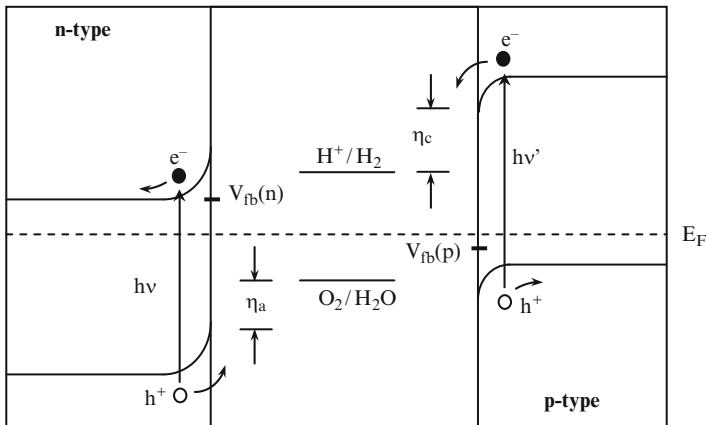
**Fig. 5** Energy level diagram for a p–n type photoelectrolysis cell

shown in Fig. 5. Several other systems have been studied including n-TiO_2/p-CdTe, n-$SrTiO_3$/p-CdTe, n-$SrTiO_3$/p-GaP, n-Fe_2O_3/p-Fe_2O_3, and n-TiO_2/p-$LuRhO_3$ [13]. However, many visible absorbing p type semiconductors have shown limited

stability in aqueous solvents [14], and, although power conversion efficiencies exceeding 12% could be achieved in monolithic multijunction systems [15], the durability of many devices was low, with degradation occurring on the time scale of hours.

An interesting approach to overcome limitations arising by the need of a bias while keeping an effective light absorption in the visible region is the absorption of dye molecules on the surface of a wide band gap semiconductor with an appropriate band energy, like TiO_2 for example, which, upon light excitation, can inject electrons (in n-type materials) or holes (in p-type systems) into the acceptor states of the solid. In principle the photooxidized (photoreduced) dye can oxidize (reduce) water, while the complementary redox process can occur at the counter electrode of the cell. Although such an approach has evident limitations related to the demanding four-electron kinetics of water oxidation, some recent fundamental work pointing out the feasibility of molecular dye sensitized solar water splitting by exploiting certain specific hole transfer catalysts is briefly reviewed in Sect. 2. Attention will then focus on the design and characterization of newly developed photoanodes, based on anodically grown wide band gap semiconductors with improved charge transfer kinetics, as well as on the coupling of these substrates to lower band gap semiconductors.

2 Dye Sensitized Photoanodes for Water Oxidation and Hydrogen Evolution

In a generic sensitized PEC design, the molecular excitation and excited state formation are followed by electron transfer injection into the conduction band of a semiconductor. In order to promote multielectron transfer events like water oxidation, multiple redox equivalents must be concentrated in a single site or cluster. The working principles of the cell are schematized in Fig. 6, where solar energy is stored to create a photopotential for water splitting [16, 17]. In principle, at the cathode, water or CO_2 reduction may occur, giving rise to the production of fuels.
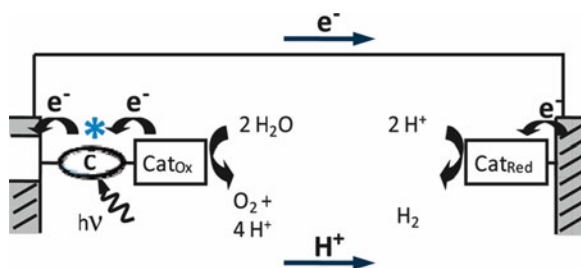
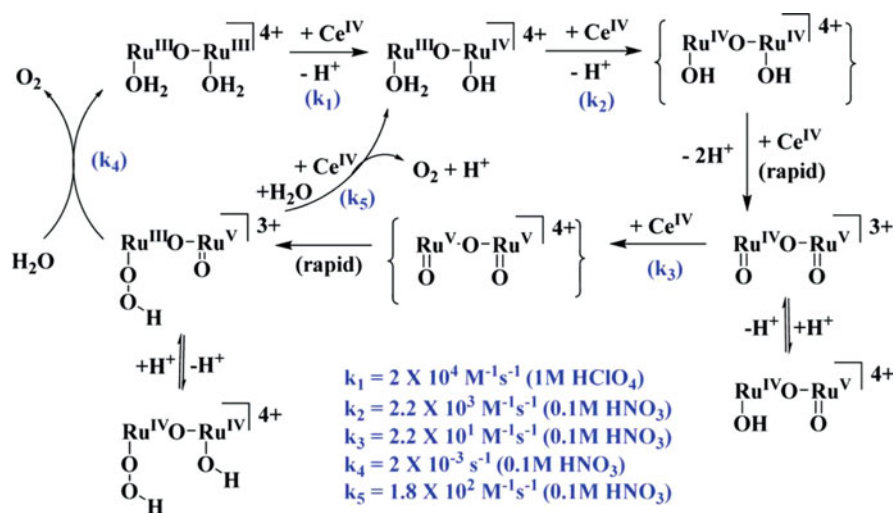**Fig. 6** Working principle of a sensitized PEC cell for water splitting. Cat_{ox} and Cat_{red} are catalyst for water oxidation and reduction [16]

The blue dimer $cis,cis[(bpy)_2(H_2O)Ru(III)ORu(III)(OH_2)bpy)_2]^{4+}$ (Fig. 7) was among the first molecular species to show catalyzed water oxidation by Ce(IV) through a reaction mechanism which has been elucidated in detail by spectroscopic, electrochemical, and chemical mixing experiments [18] (Scheme 1). The key point
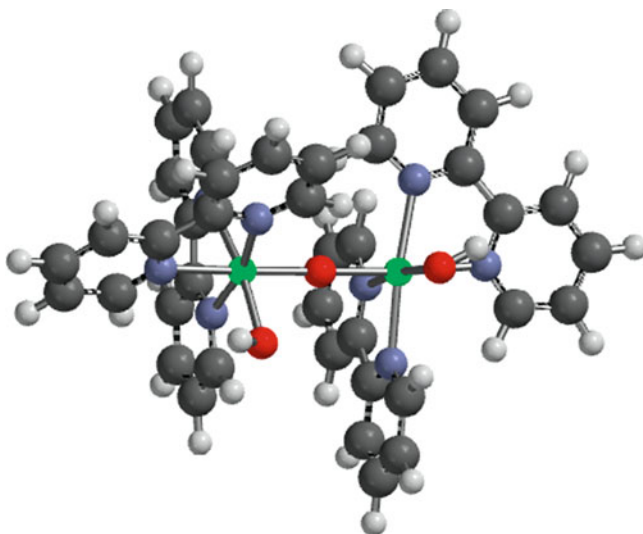
Fig. 7 Energy minimized structure of the "blue Ru dimer" $cis,cis[(bpy)_2Ru(OH)ORu(OH)(bpy)_2]^{4+}$. The *green balls* are the Ru(III) centers


$k_1 = 2 \times 10^4 \ M^{-1}s^{-1}$ (1M HClO$_4$)
$k_2 = 2.2 \times 10^3 \ M^{-1}s^{-1}$ (0.1M HNO$_3$)
$k_3 = 2.2 \times 10^1 \ M^{-1}s^{-1}$ (0.1M HNO$_3$)
$k_4 = 2 \times 10^{-3} \ s^{-1}$ (0.1M HNO$_3$)
$k_5 = 1.8 \times 10^2 \ M^{-1}s^{-1}$ (0.1M HNO$_3$)

Scheme 1 Mechanism of water oxidation by $[(bpy)_2(H_2O)Ru(V)ORu(V)(OH_2)bpy)_2]^{4+}$ [19]

is the 4 e$^-$/4H$^+$ loss to form the activated catalyst [(bpy)$_2$(H$_2$O)Ru(V)ORu(V)(OH$_2$) bpy)$_2$]$^{4+}$ which undergoes water attack on one of the Ru(V)=O sites to give a peroxo intermediate which releases oxygen and gives back the initial Ru(III)–O–Ru(III) species on a millisecond time scale.

As a catalyst, the blue dimer has limitations due to oxidatively induced coordination of anions which slow down the catalytic cycles. Since the O–O bond forming step occurs at a single Ru(V) site, it has been demonstrated that simpler and more robust mononuclear Ru(III) aquo complexes of the type [Ru(tpy)(bpm)(H$_2$O)]$^{2+}$, where tpy is the 2,2′6′2″ terpyridine and bpm is the bipyrimidine ligand, can undergo hundreds of turnovers without showing decomposition according to the cycle schematized in Scheme 2 [20]. It must be noted that the Ru(III) state appears to be a "missing" state due to instability toward the disproportionation to Ru(IV) and Ru(II).

DFT and spectroscopic results indicate that, following the attack of water at the Ru(V)=O sites, one has the formation of a first intermediate described as a terminal peroxide coordinated to Ru(III) which undergoes further oxidation by Ce(IV) to give a 7 coordinated Ru(IV) complex where O$_2^{2-}$ acts as a chelating ligand. Oxygen can be evolved both from [Ru(IV)OO]$^{2+}$ and [Ru(V)OO]$^{3+}$ structures following water attack.

Although the electrocatalytic water oxidation by blue dimer has been demonstrated at FTO and ITO electrodes modified with phosphonated Ru(II)
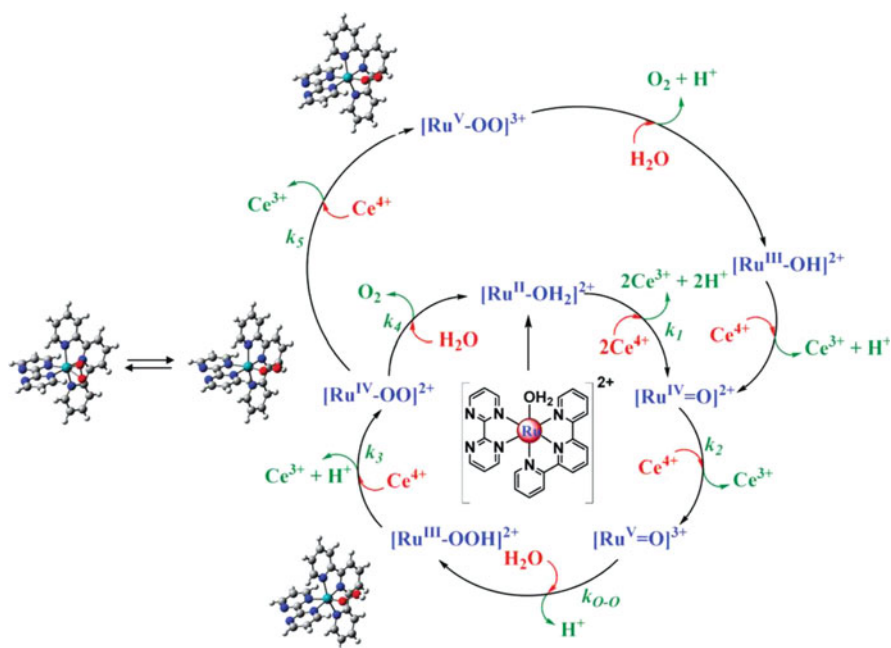

**Scheme 2** Ce(IV) water oxidation catalyzed by [Ru(tpy)(bpm)OH$_2$]$^{2+}$ [16]

tris-bipyridine derivatives working as a redox mediator [19], the realization of an efficient dye sensitized PEC device for water oxidation has yet to be realized, but progress is underway. In fact several issues have to be contemporarily satisfied to realize an efficient solar device: (1) effective visible-NIR absorption by the molecular sensitizer; (2) excited state quenching by electron transfer to the semiconductor; (3) efficient and repeated single photon–single hole transfer to the catalyst to achieve the accumulation of three oxidative equivalents to give Ru(V)–OO which undergoes attack by water giving Ru(III)–OOH; after two further subsequent oxidations, one finally obtains the evolution of molecular oxygen and the recovery of Ru(III)–OH which initiates a new catalytic cycle. While oxidative excited state quenching by Ru(II) chromophores on TiO_2 have been reported to be extremely fast, the subsequent hole transfers are in critical kinetic competition with photo-injected electron (TiO_2)/hole recombination. A further complication arises from the light harvesting competition between the photoactive $Ru(bpy)_3$ type unit and the catalyst, which being relatively remote from the semiconductor surface does not contribute significantly to the photocurrent. In fact, APCEs (absorbed photons to electrons conversion efficiency) of the order of 3–4% (Fig. 8b) and of 1–2% have been achieved in the presence of hydroquinone and pure water, respectively, by using the sensitizer/oxygen evolving catalyst dyad $[(4,4'((HO)_2P(O)CH_2)_2bpy)_2Ru(II)(bpm)Ru(II)(Mebimpy)(OH_2)]^{4+}$ (Fig. 8a), where Mebimpy is 2,6-*bis*(1-methylbenzimidazol-2.yl)pyridine) [16].

Conceptually similar approaches have been based on different molecular catalysts or nanomaterials chemically coupled to the molecular sensitizer.

In a recent interesting design [21], a manganese cage complex catalyst $([Mn_4O_4L_6]^+$, or "*cubium*", L = $MeOPh)_2PO_2^-$), able to undergo multiple proton coupled electron transfer, is encapsulated in a Nafion membrane which has the role of providing both a high local surface concentration of redox active catalyst and
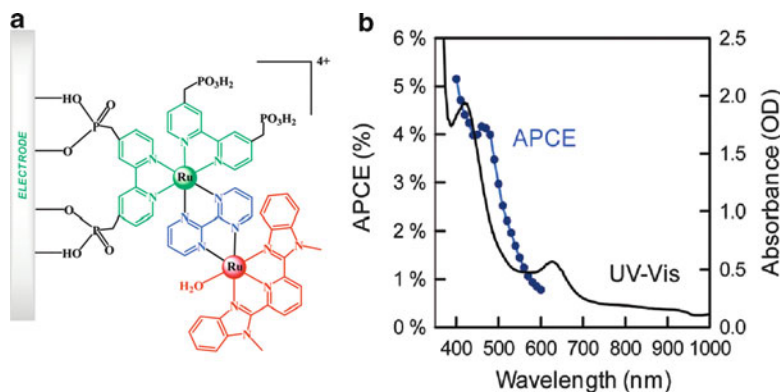

Fig. 8 (**a**) Structure of $[(4,4'((HO)_2P(O)CH_2)_2bpy)_2Ru(II)(bpm)Ru(II)(Mebimpy)(OH_2)]^{4+}$ sensitizer/catalyst assembly anchored to a TiO_2 electrode; (**b**) APCE and absorption spectrum in the presence of 0.5 M hydroquinone acting as an electron donor in 0.1 M $HClO_4$
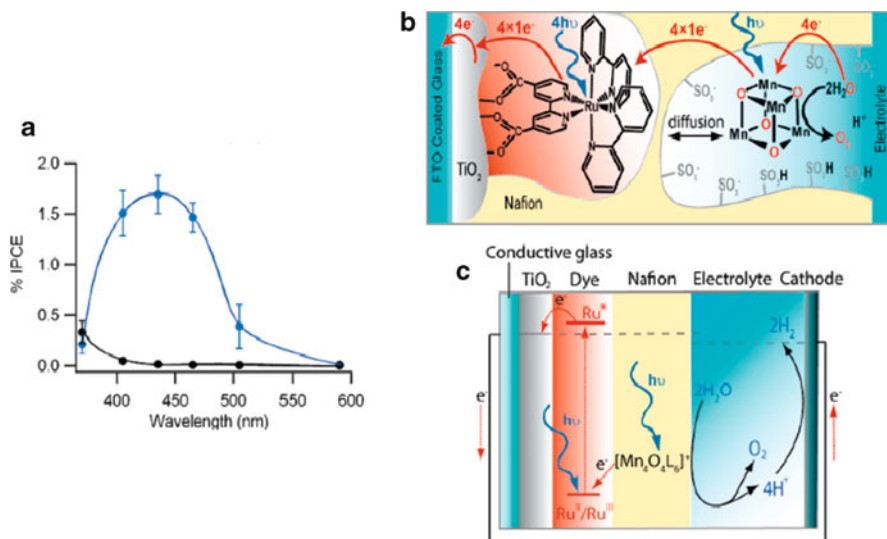
Fig. 9 (**a**) IPCE Spectrum (*blue*) of the sensitizer/catalyst system (**b**) compared to that of the plain Nafion/TiO$_2$ electrodes. (**c**) Pictorial scheme of working principles of the dye sensitized PEC for solar water splitting with no external bias. From [21]

a reasonable coupling with the Ru(II) dye sensitizer (Fig. 9). The molecular level solar water splitting, recalling that occurring in natural photosynthesis, was thus beautifully demonstrated, but also in this case the performances were far from a practical application of the device, with IPCEs (IPCE=number of electrons/number of incident photons) below 2%, corresponding to a stable photocurrent, with no externally applied bias, of the order of 30–5 µA/cm^2 depending on the illumination intensity and spectral bandwidth.

Another interesting configuration, which is discussed in detail in another section of this book (see Bonchio et al.), involves the anchoring of hydrated IrO$_2$ nanoparticles to a phosphonated Ru(II) sensitizer modified with malonate binding groups (Fig. 10) [22, 23]. The hole transfer to the IrO$_2$ takes place on a millisecond (2.2 ms) time scale, while charge recombination occurs on a submillisecond (0.37 ms) time scale. Thus, the competition between hole transfer and recombination is unfavorable to an effective charge separation. Nevertheless, under a small positive bias ($\geq$330 mV) a stable photoanodic current of the order of few tens of microamperes is effectively detected, indicating the occurrence of photoinduced water oxidation under steady state conditions. Although the efficiency is low, the device represents a successful proof of the concept of water splitting in a sensitized PEC device. Possible efficiency improvements could be related to synthetic modifications of the sensitizer/catalyst assembly, aimed at improving the binding between the photoactive dye and the IrO$_2$ nanostructures, to slow down recombination and to speed up the hole transfer to Ir(IV) for improving the turnover number which is now poor (<20).
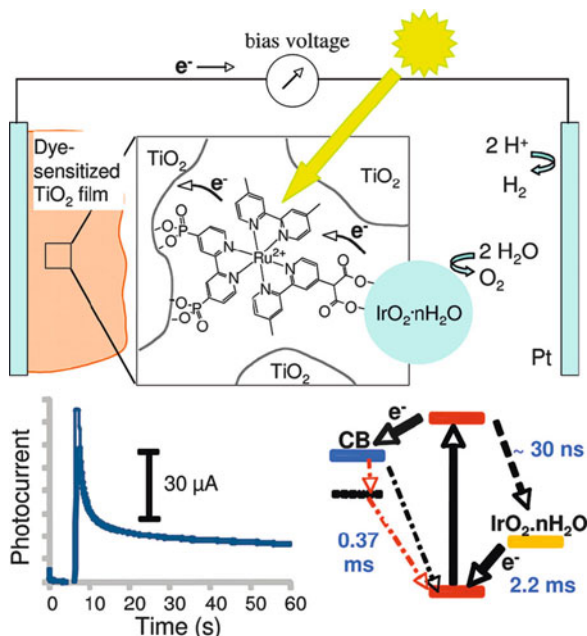
**Fig. 10** *Top*: schematic diagram of an IrO_2 catalyzed water-splitting dye-sensitized solar cell. Following light excitation and oxidative quenching of the excited state of Ru(II), the hole is transferred to Ir(IV), activating the IrO_2 catalyst toward water oxidation. *Bottom left*: photocurrent transient showing a steady state photocurrent. *Bottom right*: energy diagram and time constants for the relevant interfacial electron transfer and excited state deactivation processes

Unless sensitizers capable of performing directly an efficient water oxidation are designed, the use of sacrificial agents, although disadvantageous, cannot be avoided. It must be noted that there is a potentially large number of relatively abundant easily oxidizable ions and organic species that could be consumed to produce hydrogen. This type of conceptually simple sensitized photoelectrolytic cell is schematized in Fig. 11. In principle, photogenerated D^+ could compete with the reduction of H^+ at the counter electrode, thus decreasing the hydrogen yield; however, this process can be avoided, or at least minimized, by an appropriate choice of D (e.g., irreversible couples, non-electroactive oxidized species) or simply by operating the two electrodes in separate compartments connected by a glass frit, a proton permeable membrane, or a salt bridge.

In an aqueous solvent the stability of the linkage between the molecular sensitizer and TiO_2 is crucial and requires the use of multiple anchoring groups. The series of dyes shown in Fig. 12, containing phosphonic acid functions, display a remarkable adsorption stability and allow for visible light harvesting, charge injection, and hydrogen production at a Pt counter electrode in aqueous solutions containing iodide, chloride, isopropanol, or ascorbic acid as sacrificial donors [24].

The Ru(II)/(III) oxidation potentials of the selected dye sensitizers decrease in the order **1** (1.20 V vs SCE) > **2** (1.18 V vs SCE) > **3** (0.94 V vs SCE). The trend is
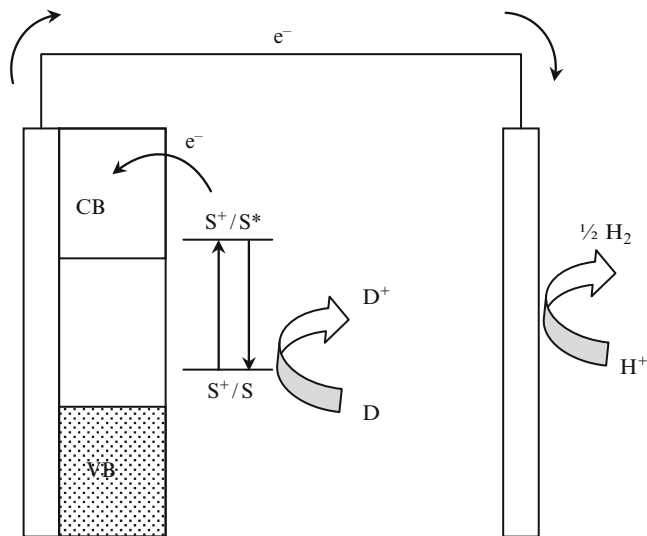
Fig. 11 Working principle of a dye-sensitized photoelectrolytic device based on a sacrificial agent D
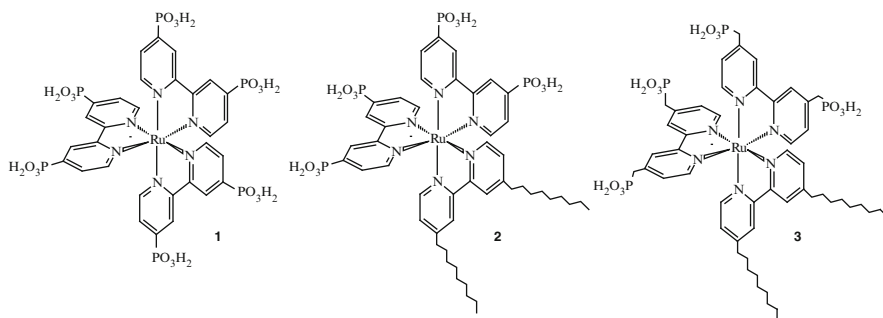

Fig. 12 Phosphonic Ru(II) sensitizers used in water stable PEC cell for solar hydrogen evolution

expected on the basis of the substituents at the 4,4′ positions of the bipyridines: in **3** the methylene spacers attenuate the electron-withdrawing inductive effect of the phosphonates, leading to a destabilization of the metal dπ orbitals which results in an oxidation potential evidently less positive than **1** and **2**, which show energetically close processes. The wave separation is in all cases of the order of 80–100 mV, without cell resistance compensation, indicating a fast electron transfer, expected in the case of redox processes involving Ru(II–III) dπ orbitals [25].

In the most favorable case (complex **1**), it was possible to observe the production of a photoanodic current in the presence of plain water/LiClO$_4$ 0.1 M at pH 5 (HClO$_4$). However, despite a reasonable negative free energy difference for water oxidation (ca. 0.46 V, considering that the thermodynamic potential for oxygen evolution at pH 5 is 0.95 V vs NHE), the photocurrent was extremely small, ca.
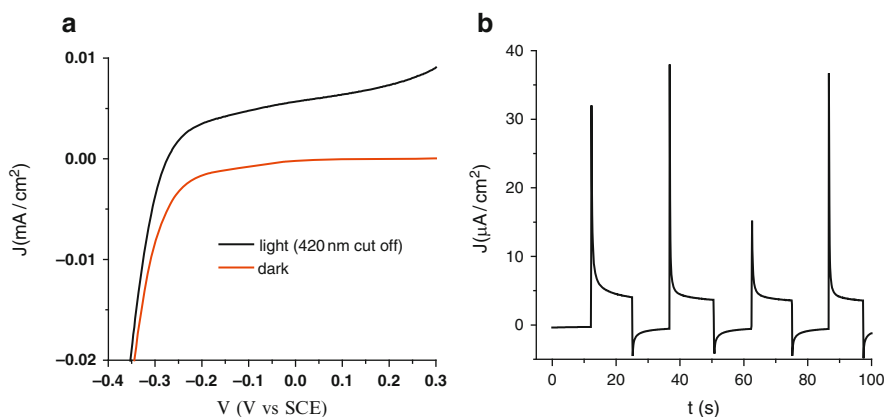
Fig. 13 (**a**) *J–V* curves of **1** in water LiClO$_4$ 0.1 M at pH 5 (HClO$_4$); (**b**) photocurrent transients under 0 mV vs SCE potential bias

5 μA/cm^2 (Fig. 13a). Chronoamperometry under pulsed illumination (Fig. 13b) revealed the presence of a fast relaxation from the initial value, reached as soon as the electrode was exposed to light, and the presence of dark cathodic features. Both characteristics are indicative of an inadequate dye regeneration efficiency which reflects in an interfacial hole accumulation leading to an effective photoinjected electron to Ru(III) recombination.

Addition of isopropanol 20 vol.% leads to a general increase of the performances, allowing for the delivery of a maximum photocurrent density of 300 μA/cm^2 in the case of **1**. The photoanodic current (Fig. 14a) increases in the order **3 < 2 < 1**, in agreement with the relative Ru(II)/Ru(III) oxidation potentials. The photocurrent transients collected in the presence of a 0 mV vs SCE potential bias (Fig. 14b) approach a more ideal rectangular shape, although both the initial relaxation and the cathodic features are still evident. These latter features are, however, barely observable, indicating that isopropanol effectively acts as an electron donor, promoting Ru(III) reduction.

Ascorbic acid was found to be an effective organic electron donor, resulting in a maximum IPCE of 24% in the 430–500 nm region, with a photoaction onset at 675 nm. Correspondingly, under white light irradiation, photocurrents higher than 2 mA/cm^2 were achieved with **1** at 0 mV vs SCE and a photoanodic plateau of ca. 3 mA/cm^2 was observed under a slightly positive bias (0.2 V vs SCE). Hydrogen collection experiments revealed a satisfactory electrolysis yield (96.7%), which resulted in the production of 2.96×10^{-5} mol of H$_2$ in 2,680 s.

Rectangular shaped photocurrent transients (Fig. 14c) indicate a strongly decreased electron back recombination involving Ru(III) and a good reproducibility of the photoanodic processes. In contrast, formic acid, which is known to be an effective hole scavenger for bare TiO$_2$ (upon direct band gap excitation), proved inadequate for regenerating the sensitizer, producing a marginal improvement over the pure water/LiClO$_4$ electrolyte. This evidence is related to the exceedingly
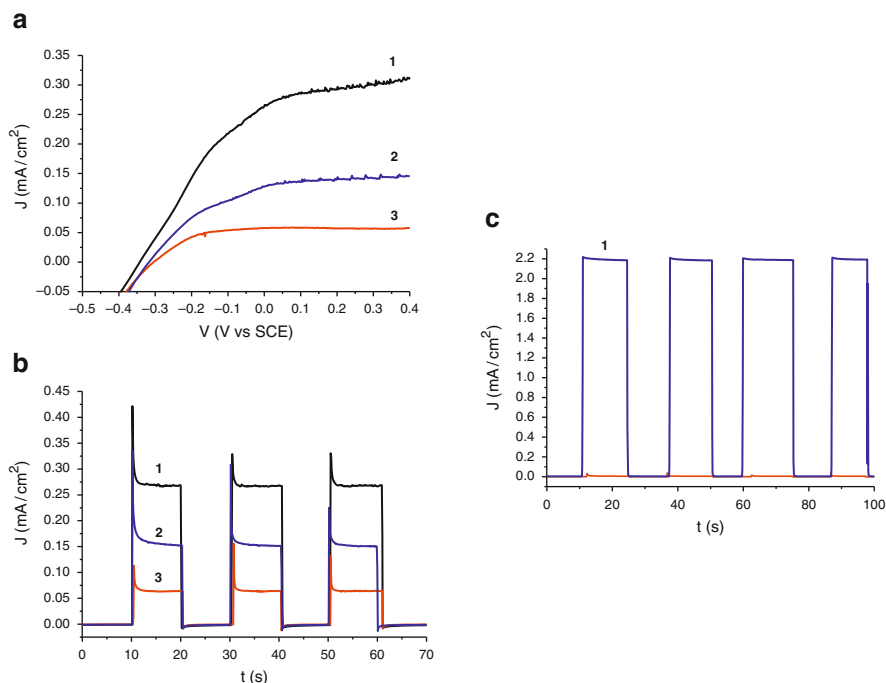
**Fig. 14** (**a**) *J–V* curves for the complexes **1–3** in water/isopropanol 8/2 v/v, LiClO$_4$ 0.1 M at pH 3 (HClO$_4$); (**b**) photocurrent transients under 0 mV vs SCE potential bias; (**c**) photocurrent transients for dye 1 in 1 M ascorbic acid, 0.1 M LiClO$_4$

positive potential for formic acid oxidation, which could not be observed by cyclic voltammetry at a glassy carbon electrode in water/LiClO$_4$ in the interval 0–1.2 V vs SCE; in contrast, under the same conditions, ascorbic acid gave a clear irreversible oxidation wave with a peak at 0.36 V vs SCE.

The use of chlorides as sacrificial agents in either aqueous or organic media did not lead to relevant performances. The best results were obtained with complex **1**: in the presence of a positive bias of 0.4 V vs SCE, photocurrents of (120 ± 20) μA/cm^2 were measured. At 0 mV vs SCE, **2** and **3** produce lower photoanodic currents (ca. 60 μA/cm^2). The photocurrent transients recorded at 0 mV vs SCE (Fig. 14b) indicate for all complexes an inefficient Ru(II) recovery most probably due to the small driving force for the Cl$^-$ oxidation by Ru(III) (E$^{0'}$ (Cl$_2$/Cl$^-$) = 1.1 V vs SCE).

Iodide was expected to be a better hole scavenger since its formal oxidation potential is of the order of 0.4 V vs SCE; however the use of aqueous iodide solutions led to instability of the photoanodic response of the sensitized anodes due to adsorption of triiodide onto the TiO$_2$ surface which, according to evidence gained by both electrochemical and transient spectroscopy techniques, acted as a recombination center, causing a tenfold photocurrent drop from an initial 5 mA/cm^2 to about 0.5 mA/cm^2.
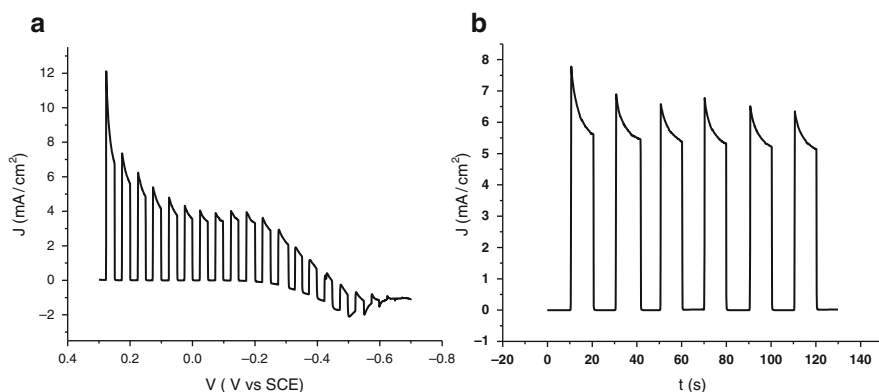
Fig. 15 (**a**) Shuttered *J–V* curve recorded in saturated NaI in ACN/Pt-HCl configuration. Scan-speed 10 mV/s; (**b**) photoanodic response upon subsequent irradiation cycles at 0 mV vs SCE

The photoelectrolysis in a separated compartment cell configuration where the photoanode was immersed in an NaI/ACN solution and the counter electrode was immersed in an aqueous acidic solution (1 M HCl) solved the problem, giving rise to the expected *J–V* characteristics of an n-type semiconductor/electrolyte rectifying junction with a photoanodic current of about 5.5 mA/cm^2 at 0 mV vs SCE showing good stability and reproducibility (Fig. 15). The triiodide production at the anodic compartment was paralleled by the evolution of hydrogen at the Pt cathode, resulting in 1.43×10^{-5} mol of H$_2$ collected in 1,190 s, corresponding to an electrolysis yield of 86.6%.

Due to the outlined practical difficulties and limitations in achieving an efficient and economically viable water photoelectrolysis under visible radiation, the scientific community also turned to the exploration of novel nanostructures, mainly based on well known semiconductor metal oxides, which could optimize the rates of interfacial charge separation leading to the maximization of the rate of hydrogen photoproduction in a given absorption region, determined by the band gap of the material. Significant efforts and results in the development and in the understanding of these new photoactive interfaces are discussed in Sect. 3.

3 Highly Ordered Semiconductor Nanostructures Based on TiO$_2$ and TiO$_2$/Metal Chalcogenides

Highly organized and ordered substrates produced by electrochemical formation or by template synthesis are attracting significant interest from the scientific community [26, 27]. While fundamental efforts are being directed towards the understanding of self organization phenomena, technological implications are arising from the exploitation of structure-related peculiar properties which allow for promising applications in catalysis [28], photonic materials [28], optical waveguides [29], and,
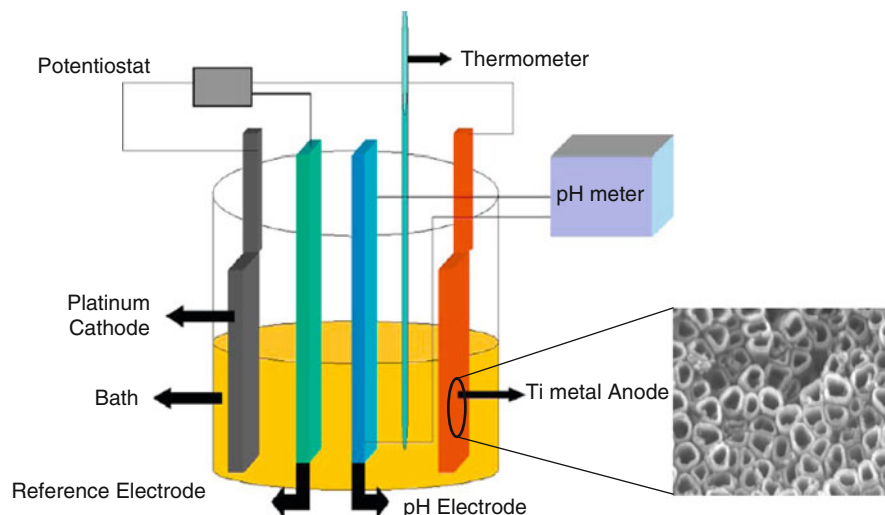
Fig. 16 Schematic apparatus for the electrochemical growth of titania nanotubes (*right*). From [34]

particularly, in photoelectrochemistry [30] and photovoltaics [31], since grain boundary effects, normally occurring between more conventional sintered nanoparticles, can be avoided or reduced.

Although several attempts successfully achieved the production of nanotubes, their relatively short lengths (tens or hundreds of nanometers) [32] somehow limited their applications. However, in recent years, mainly Schmucki and Grimes have shown the possibility of growing high aspect ratio TiO_2 nanotubes of considerable length and uniform pore diameter by tailoring the electrochemical conditions during the anodization of metallic titanium foils [33–35] (Fig. 16).

In general the key process for anodic formation of titania nanotubes are: (1) metal oxide formation due to reaction of titanium with O^{2-} or OH^- – these anions can also migrate through the initially formed oxide layer reaching the metal/metal oxide interface where they react with the metal; (2) Ti^{4+} migration from the metal to the metal oxide interface under the intense electric field; (3) field assisted dissolution of the oxide at the oxide/electrolyte interface – under the intense electric field the Ti–O bonds are polarized and weakened, promoting dissolution of metal cations (Ti^{4+}); (4) chemical dissolution of titania in the HF-containing electrolyte, which plays a key role in the formation of tubes rather than of an irregular mesoporous structure – although the field assisted dissolution is initially dominating, due to the strong field across the initially thin oxide layer, it is the chemical reaction with fluorides that gives rise to localized dissolution of the oxide forming pits that act as a pore forming centers, according to

$$TiO_2 + 6F^- + 4H^+ \rightarrow TiF_6^{2-} + 2H_2O$$
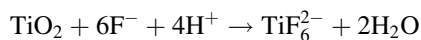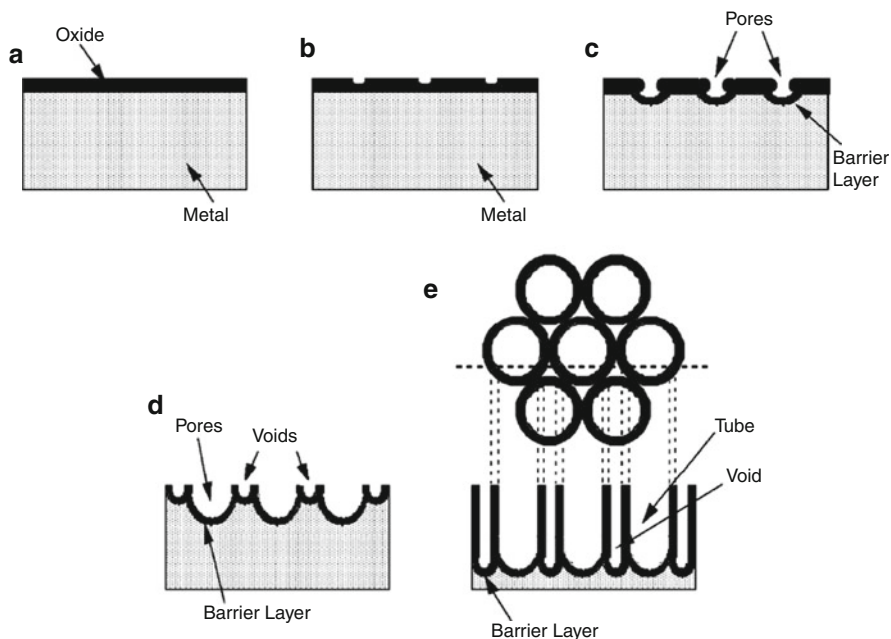
Fig. 17 Schematic diagram showing the nanotube on anodized titanium foil: (**a**) oxide layer formation; (**b**) pit formation; (**c**) growth of pit into pores; (**d**) regions between the pores undergo oxidation and field assisted dissolution; (**e**) developed nanotube array. From [34]

The thinner barrier layer at the bottom of the chemically etched pits leads to a localized increase of the electric field which promotes field assisted dissolution leading to pore deepening and widening, while, at the same time the density of the pits increases finally leading to the full development of a densely packed nanotube array (Fig. 17). When the rate of chemical oxide dissolution at the mouth of the tube (top surface) becomes equal to the rate of inward movement, the thickness of the tubular layer ceases to increase. High anodization voltages increase the oxidation and field assisted dissolution, hence a greater nanotube length can usually be achieved before equilibrating with the chemical dissolution.

As pointed out by Schmucki [33], another key parameter to achieve high aspect ratio nanotubes consists in adjusting the dissolution rate of TiO_2 at the pore bottom while a relatively protecting environment, in which the TiO_2 dissolution is slower compared to the bottom, is maintained at the walls and at the mouth of the tube (Fig. 18). Self acidification of the pore bottom occurs, mainly due to the electro-chemical oxidation of elemental titanium, according to

$$Ti + 2H_2O \rightarrow TiO_2 + 4H^+$$
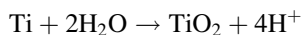
Hence it is possible, by operating in a buffered solution, to produce protons where needed by adjusting the anodic current flow to an ideal value. Thus, while lower pH values can be obtained at the tube bottom, in turn favoring chemical
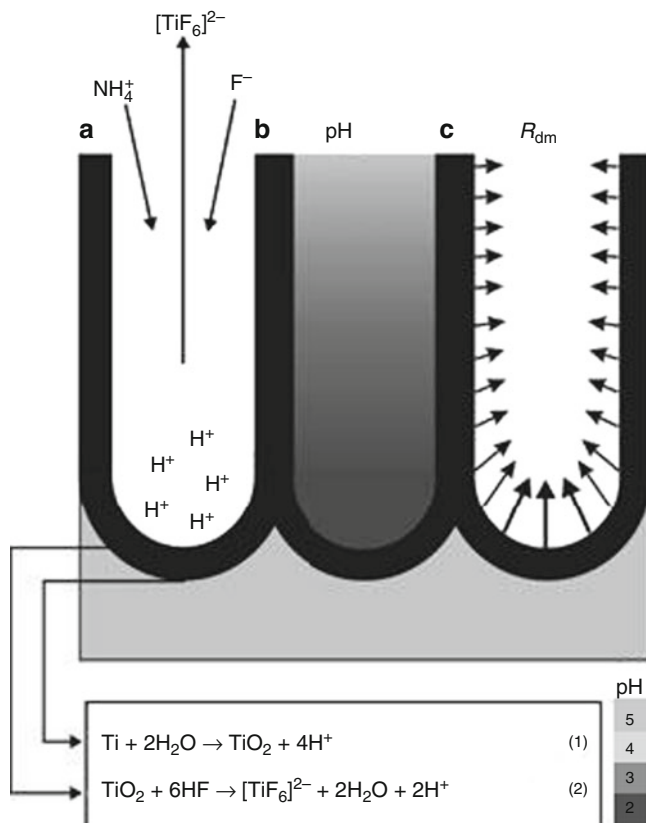
Fig. 18 Schematic representation of: (**a**) oxide formation and dissolution reactions; (**b**) pH profile within the pore; (**c**) dissolution rate (proportional to the *arrow* length). From [33]

dissolution of the oxide due to the "in situ" formation of HF, higher pH values and, consequently, a slower oxide dissolution rate can be established at the top and at the walls of the nanotube, thanks to the presence of pH buffering species (NH_4F, $(NH_4)_2SO_4$). The pH gradient (Fig. 18) has been calculated in great detail by using finite-difference numerical simulation, and it has been shown that a pH variation from 2 to 5 occurs by moving from the bottom to the top of the tube, corresponding to a 20-fold drop in the local chemical etching rate.

3.1 Experimental Conditions for Electrochemical Titania Nanotube Formation

In general, potentiostatic or potential sweep methods are preferred over a galvanostatic approach which has the tendency to oscillate and destabilize the steady state conditions within the pore. A method devised by Schmucki et al. [33] involves the

use of an aqueous electrolyte containing 1 M $(NH_4)_2SO_4$ and smaller amount of NH_4F (0.5–5 wt%). The electrochemical treatment consists in a voltage ramp from open circuit potential to 20 V, adopting various scan rates, followed by a potentio-static treatment at 20 V for different times.

Considering water based electrolytes, Grimes et al. [34] achieved the best results (i.e., nanotubes up to 6 μm long) in a solution containing either fluoride salts (NaF or KF) or HF in the presence of buffer salts like sodium sulfate or sodium or potassium hydrogen phosphate in a pH interval ranging from 3 to 5 (Fig. 19).
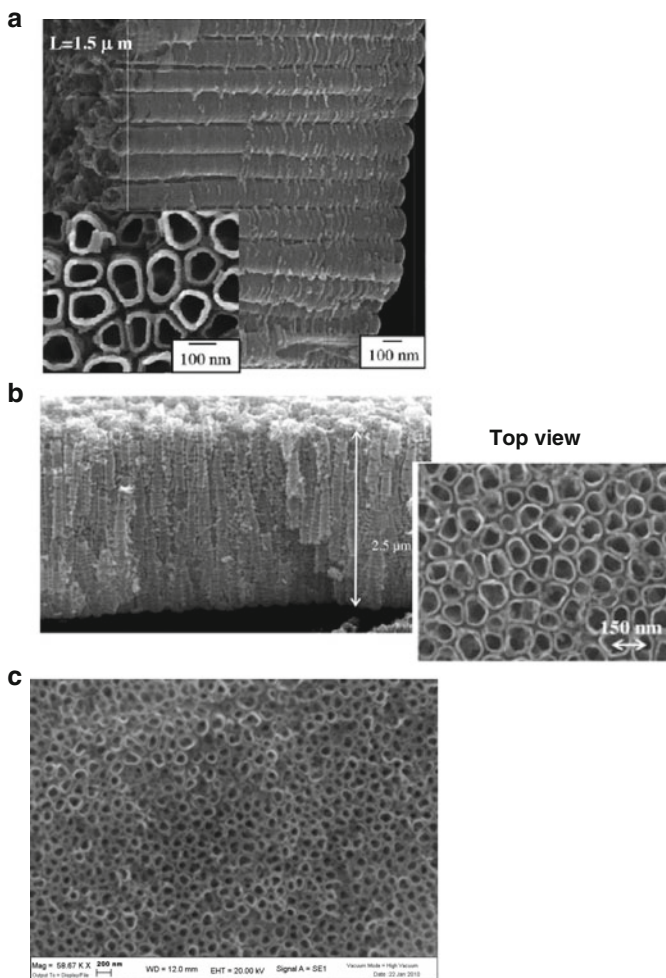
Fig. 19 Titania nanotubular arrays grown in various aqueous fluoride-containing electrolytes. (**a**) 0.1 M F^- + 1 M SO_4^{2-} at pH 2.8 and at 25 V for 20 h; (**b**) 1 M $(NH_4)_2SO_4$ + 0.5 wt% NH_4F by using a potential sweep from OCP to 20 V at 0.1 V/s; (**c**) 1 M KF 0.5 M Na_2SO_4 at pH 4 at 25 V for 24 h

Table 1 Electrolyte composition of KF based electrolytes and relative electrochemical treatment

| No.	Electrolyte				pH	V (V)	t (h)	D (nm)	L (μm)	Q
	F^-	SO_4^{2-}	PO_4^{3-}	Cit						
01	0.1	1.0	–	–	<1	5	1	10 ± 2	–	No NT
02	0.1	1.0	–	–	<1	10	1	40 ± 5	0.28 ± 0.02	NT
03	0.1	1.0	–	–	<1	15	1	80 ± 9	–	NT
04	0.1	1.0	–	–	<1	20	1	100 ± 11	0.48 ± 0.03	NT
05	0.1	1.0	–	–	<1	25	1	110 ± 12	0.56 ± 0.04	NT
06	0.1	1.0	–	–	<1	30	1	–	–	No NT
07	0.1	1.0	–	–	<1	20	6.5	100 ± 11	0.43 ± 0.03	NT
08	0.1	2.0	–	–	<1	20	1	100 ± 11	0.45 ± 0.03	NT
09	0.1	1.0	–	0.2	1.3	10	20	30 ± 5	0.32 ± 0.03	NT
10	0.1	1.0	–	0.2	2.8	10	20	30 ± 5	0.59 ± 0.05	NT
11	0.1	1.0	–	0.2	2.8	15	20	50 ± 5	1.00 ± 0.05	NT
12	0.1	1.0	–	0.2	2.8	25	20	115 ± 10	1.50 ± 0.04	NT
13	0.1	1.0	–	0.2	3.8	10	20	30 ± 5	0.80 ± 0.06	NT
14	0.1	1.0	–	0.2	3.8	10	60	30 ± 5	1.80 ± 0.06	NT
15	0.1	1.0	–	0.2	3.8	10	90	30 ± 5	2.30 ± 0.08	NT
16	0.1	1.0	–	0.2	4.5	10	20	30 ± 5	1.05 ± 0.04	NT
17	0.1	1.0	–	0.2	4.5	25	20	115 ± 5	4.40 ± 0.10	NT
18	0.1	1.0	–	0.2	5.0	10	20	30 ± 5	1.40 ± 0.06	NT
19	0.1	1.0	–	0.2	5.0	25	20	115 ± 5	6.00 ± 0.40	NT
20	0.1	1.0	0.1	0.2	6.4	10	24	–	–	No NT
21	–	2.0	–	–	<1	10	24	–	–	No NT

V is constant voltage and t is the application time. D and L stand for nanotube diameter and length, Q stands for quality of the anodized substrates. NT denotes a homogeneous nanotube coverage, no NT partially developed/porous surfaces. pH was adjusted by addition of sulfuric acid (pH 1–2) sodium hydrogen sulfate or citric acid (2.5–6.5). From [34]

The potential window necessary to induce nanotube formation was 10–25 V which could be maintained for several hours (Table 1). The as made nanotubes present an amorphous structure which crystallizes at high temperature (>280 °C) to give anatase and rutile. The rutile phase becomes dominating at temperatures higher than 620 °C.

Higher aspect ratio (up to an amazing 835 L/d ratio) nanotubes [35] could be obtained in organic electrolytes comprising a high dielectric constant solvent [N-methyl-formamide (NMF), formamide (FA), dimethylsulfoxide (DMSO), ethylene glycol], a small percentage of water, and fluoride salts or hydrofluoric acid. The highly polar FA and NMF increase nanotube length dramatically, probably due to an accelerated growth of the substrate. In fact, the dielectric constants of FA and NMF of respectively 111 and 182.4 are significantly higher than that of water (78.4). As a consequence, for any given potential the higher electrolytic capacitance induces a larger number of charges in the oxide layer, which in turn, promote an enhanced extraction of Ti^{4+}. At the same time a limited presence of water reduces the oxide dissolution rate in the fluoride-containing medium, aiding a longer nanotube formation.

In comparison with aqueous electrolytes, the range of applied anodization potentials over which nanotube arrays are formed is significantly extended, with
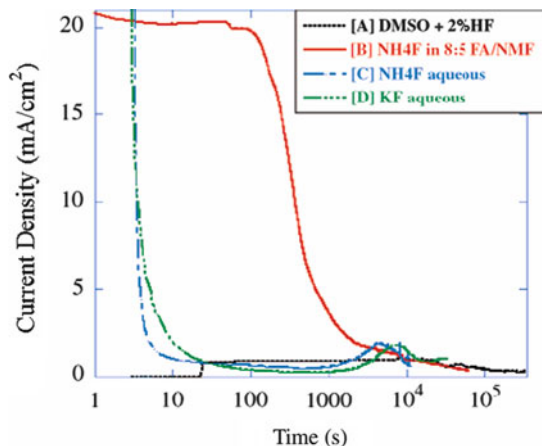
**Fig. 20** Anodization current of Ti foil at constant 25 V in different electrolytic compositions. From [35]

an upper limit of 50 V in FA and NMF electrolytes. This is consistent with a more difficult oxygen donation in comparison with water, requiring higher overvoltages to occur. However, higher anodization potentials also imply a greater driving force for both electronic and ionic conduction within the oxide layer, both factors favoring nanotube formation and growth.

The comparison between the anodization current recorded in an aqueous electrolyte and that obtained in FA-NMF solvents is indeed striking (Fig. 20): while in aqueous environment passivation is almost immediately established, causing a quick drop in current, in FA-NMF the current remains at a high and constant level for at least 100 s, which is consistent with the formation of a thin oxide layer of high conductivity and a low titanium oxidation rate. It is the high conductivity of the oxide layer which enables a faster inward movement of the Ti/TiO$_2$ interface, resulting in an improved nanotube length. Also, DMSO is a suitable solvent for inducing long nanotube growth (Fig. 21), probably due to its protophilic properties which moderate the activity of HF. This minimizes the loss by chemical dissolution from the tube mouth, allowing the tubes to grow deep into the titanium foil.

3.2 Photoelectrochemical Properties of NT Arrays

Although the amount of solar light that can be absorbed by TiO$_2$ is limited by a band gap of about 3.2 eV, nanotubular titania (anatase and rutile) structures display interesting properties with respect to the photocleavage of water. First, due to light scattering within a porous structure, incident photons are more effectively absorbed than from a flat electrode; second, and more important, compared to nanocrystalline electrodes made of sintered nanometer sized

Fig. 21 FESEM images of anodically grown nanotubes in a FA based electrolyte at 35 V for 48 h showing the *cross section* (*top*) and the *top view* (*bottom*) of the surface with nanotube mouths. From [35]
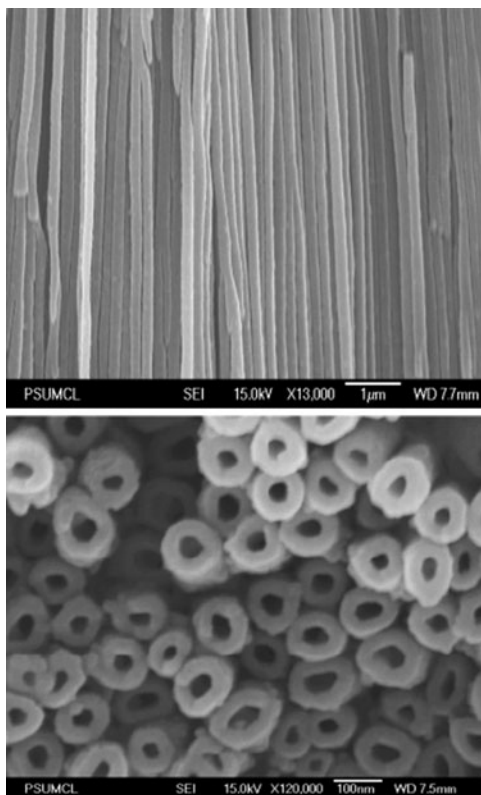
nanoparticles, tubular domains with wall thickness of 30–50 nm may also sustain a relevant electric field, which, inducing a depletion layer, may assist the charge separation at the interface.

This is experimentally indicated by the linearity between the squared photocurrent and the applied potential (particularly under a low potential bias) suggesting that the photogenerated charge carriers are, as a matter of fact, being separated by the electric field in the depletion layer. This feature, coupled with a large effective photoactive area in close proximity to the electrolyte, which enables a shortened diffusional path (ca. 20 nm, compared to a hole diffusion length of about 100 nm) of photogenerated holes to oxidizable species in the electrolyte, stands as a forecast of an efficient photoanode: in fact, all the minority carriers that are generated within a distance equal to the sum of the depletion layer thickness with the hole diffusion length are able to escape from recombination and reach the electrolyte, contributing to the enhancement of external quantum efficiencies which can reach reported values of up to 70% under a strong positive polarization (1 V vs Ag/AgCl) [30].

Transient photovoltage decays (in both 1 M KOH and H_2SO_4) and electrochemical impedance spectroscopy under illumination are also indicative of better
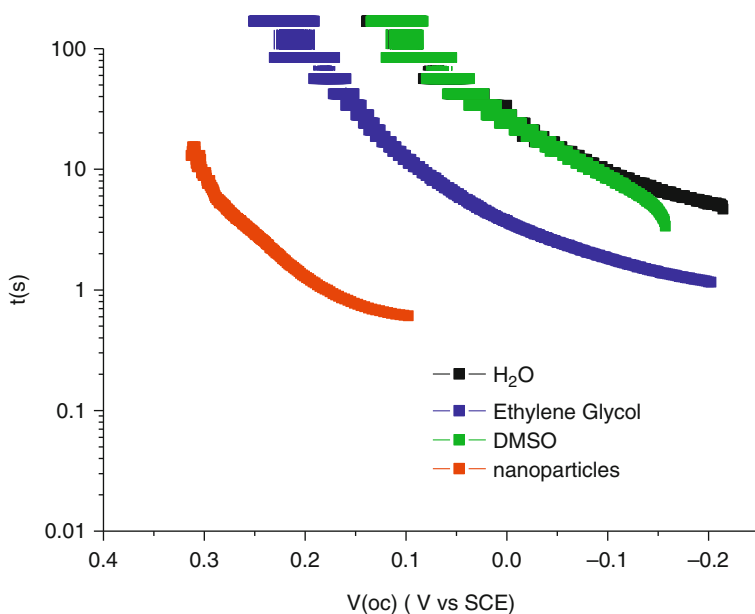
Fig. 22 Electron lifetime calculated from $\tau = \frac{kT}{e} \left(\frac{dV_{oc}}{dt} \right)^{-1}$ for a series of nanotube electrodes obtained by anodization in different solvents compared to a nanoparticle film obtained from a commercial TiO$_2$ paste (Dyesol). Full Xe, 0.3 W/cm^2 illumination

photoelectrochemical properties with respect to more conventional nanoparticle substrates: the electron lifetime [36] found for anodized tubular arrays under intense full Xe illumination (Fig. 22) is in fact from five to ten times longer than in a sintered nanoparticle titania film ca. 6 μm thick, due to less efficient (slower) photogenerated electron/hole recombination processes. At the same time, the interfacial charge transfer resistance (Fig. 23) in nanotube electrodes is strongly reduced (at least by a factor of five), evidencing an improved hole transfer to the electrolyte, leading to remarkable IPCE values (Fig. 24).

All these factors explain water photoelectrolysis efficiencies that have reached values of the order of 15–16% under 0.1 W/cm^2 UV (320–400 nm) illumination, where limiting photocurrents exceeding 20 mA/cm^2 are observed at 1 V vs Ag/AgCl; however, under simulated sunlight (AM 1.5) the performances are obviously lower, due to intrinsic limitations in visible light absorption, and the maximum photocurrents are generally of the order of 1 mA/cm^2.

3.3 Functionalization of Titania Photoelectrodes with Group VI Semiconductors

Group VI semiconductors, where a metal M^{n+} (M = Cd^{2+}, Bi^{3+}, Cu^{2+}, Pb^{2+}) is combined with S^{2-}, Se^{2-}, Te^{2-} to form an M$_2$(S,Se,Te)$_n$ solid, may offer
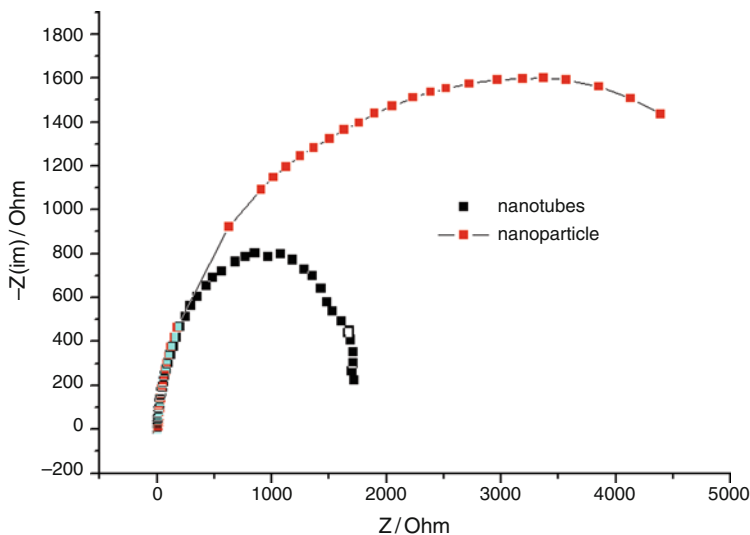
Fig. 23 Nyquist plot at V_{oc} of a titania nanotube electrode obtained in water/KF compared to nanocrystalline electrode in H_2SO_4 1 M. Full Xe, 0.3 W/cm^2
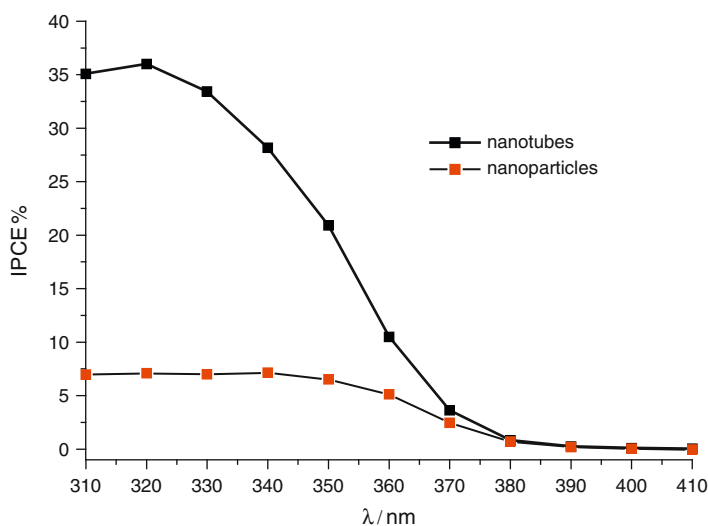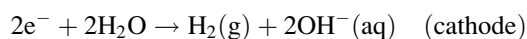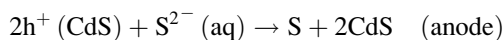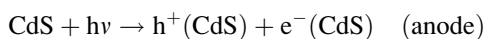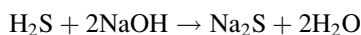

Fig. 24 IPCE spectra of a titania nanotube array obtained by anodization in H_2O/KF (*black*) compared to a sintered nanoparticle electrode (*red*) in 1 M H_2SO_4 under 500 mV vs SCE applied potential bias

interesting possibilities when employed in photoelectrolytic or photoelectrosynthetic devices applied to solar hydrogen production. Although in many of these semiconductors the quasi-Fermi energy of the photogenerated hole is too low to

drive an efficient water oxidation, they can be advantageously used for the photoinduced oxidation of Na_2S or of other easily oxidizable molecules or ions resulting in the concomitant production of hydrogen at the cathode of the PEC [37–39].

It must be noted that H_2S and sulfides are common, abundant, and harmful contaminants present in fossil fuels and in natural gas, where H_2S alone can account for up to 30% of their total volume [40].

Thus, by exploiting solar energy and chalcogenide semiconductors, sulfides can be photoelectrochemically converted to less dangerous oxidized forms (i.e., poly-sulfides, S_n^{2-}) and to molecular hydrogen thanks to an energy storing cycle which can be proposed as an interesting method for the photodegradation of H_2S wastes according to the following simplified photocatalytic scheme, where CdS is chosen as an example of photoactive semiconductor:

$$H_2S + 2NaOH \rightarrow Na_2S + 2H_2O$$

$$CdS + h\nu \rightarrow h^+(CdS) + e^-(CdS) \quad (anode)$$

$$2h^+(CdS) + S^{2-}(aq) \rightarrow S + 2CdS \quad (anode)$$

$$2e^- + 2H_2O \rightarrow H_2(g) + 2OH^-(aq) \quad (cathode)$$

Thus, the overall reaction is the splitting of H_2S into S (or more appropriately in S_x^{2-}, given the excess of S^{2-} in solution) and H_2. At the end of the photoelectrolysis one also retrieves the base which has been initially used to convert H_2S into a water soluble sulfide salt, which is obviously easier and safer to handle.

Generally, group VI semiconductors are characterized by a relatively small band gap (from 2.4 eV for CdS to 1.4 eV for Bi_2S_3) and by intense direct transitions which allow for an efficient visible light absorption from relatively thin (few hundreds nm) layers of photoactive substrate [41]. Since, in the presence of S^{2-} and at an appropriate pH, the Fermi level of these semiconductors is more negative than that of TiO_2, they can be used as photosensitizers to extend the spectral sensitivity and responsivity of TiO_2 electrodes which merely act as electron gathering media (Fig. 25a). The possibility of obtaining interparticle electron transfer has possible important implications: the deposition of group VI semiconductors onto nanocrystalline porous TiO_2 substrates (roughness coefficient 100–1,000) leads to an effective light absorption from a relatively thin absorber layer (Fig. 25b), in which the photogenerated electron (e^-) and hole (h^+) pairs are relatively close to both the electrolytic solution containing S^{2-} (hole acceptor) and to the electron collector, with the subsequent reduction of the probability of charge recombination.

Besides this effect, the coupling to TiO_2 may also have a relevant stabilizing effect against the photochemical degradation of semiconductors like CdS or CdSe. While the self oxidation of the lattice sulfides by photogenerated holes can be
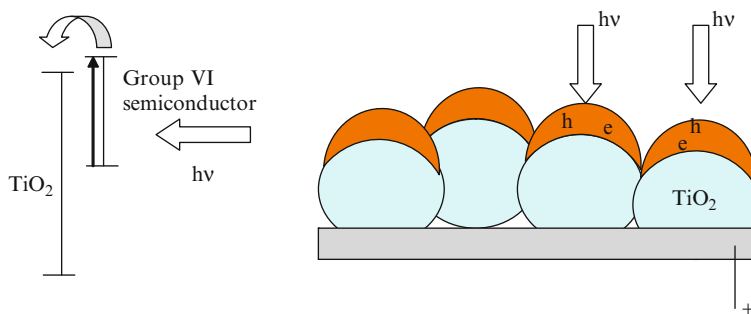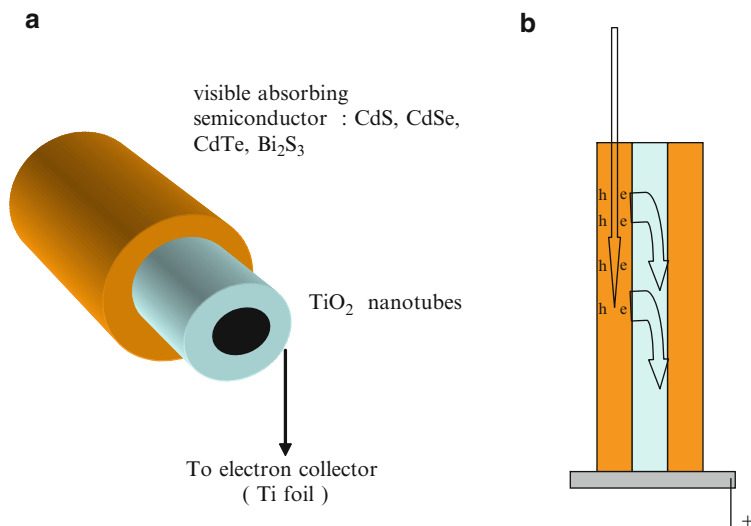
Fig. 25 Sensitization of TiO$_2$ by a visible absorbing semiconductor
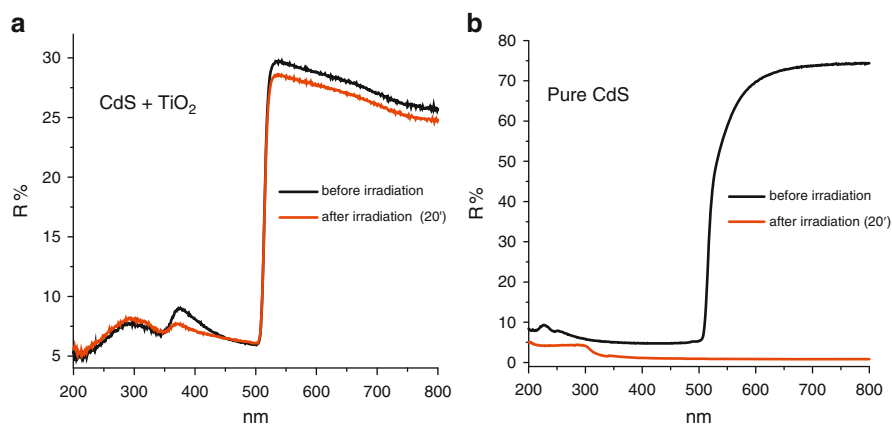
Fig. 26 Diffuse reflectance spectra of CdS based electrodes before (*black*) and after (*red*) 20 min of continuous irradiation under simulated sunlight. (**a**) Mixed electrode: 50 wt% nanocrystalline TiO$_2$ and CdS (Aldrich 99%). (**b**) Pure CdS 99% (Aldrich)

controlled by using a high concentration of hole scavengers, like S^{2-}, the trapping of electrons, responsible for the irreversible Cd$^{2+/0}$ reduction, can be avoided by activating the electron transfer to TiO$_2$. Figure 26 can be taken as an illustrative example of the improvement in the photoelectrode stability obtained by coupling CdS to a TiO$_2$ substrate: while the fundamental CdS absorption at 500 nm is maintained in CdS/TiO$_2$ systems, it is lost in pure CdS substrates after 20 min of intense irradiation in a sulfide-containing electrolyte. The decreased reflectance at longer wavelength is indicative of the development of a gray coloration of the photoelectrode, consistent with the formation of Cd^0.

In a similar way, the sensitization of tubular titania structures could be equally promising, since the cylindrical geometry of the TiO$_2$ core may allow for the generation of the charge carriers at a short distance from the electron collector,

a

visible absorbing
semiconductor : CdS, CdSe,
CdTe, Bi$_2$S$_3$

TiO$_2$ nanotubes

To electron collector
(Ti foil)

b

Fig. 27 (**a**) TiO$_2$ nanotubes functionalized with group VI semiconductors; (**b**) generation and collection of charge carriers

regardless of the penetration depth of the radiation, leading to an enhancement in electron collection efficiency as is pictorially illustrated in Fig. 27.

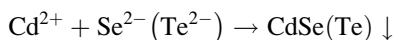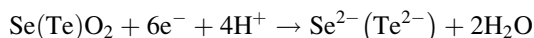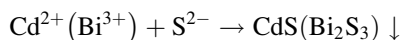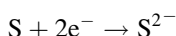## 3.4 Methods of Functionalization of Titania Substrates

Sulfur, selenium and tellurium have very similar chemical properties: many sulfides and selenides are insoluble compounds (ks(CdS) $= 10^{-26}$, ks(Bi$_2$S$_3$) $= 10^{-98}$ e k$_s$(CdSe) $= 10^{-33}$), hence it is possible to obtain the functionalization of titania electrodes by a simple chemical bath deposition.

Many methods of obtaining a CdS deposition on a variety of substrates have been devised [42–44] and all of these reside in the in situ reaction of S^{2-} with Cd^{2+}, which can be obtained by alternated repeated immersion of the photoelectrodes in separate solutions containing Na$_2$S and Cd(NO$_3$)$_2$ or CdCl$_2$. An analogous procedure can be adopted for depositing Bi$_2$S$_3$, starting from Bi(NO$_3$)$_3$ or Bi(Ac)$_3$ (Ac = acetate) solutions. A convenient and stable selenide source for CdSe deposition can be represented by sodium selenosulfite (Na$_2$SeSO$_3$) which can be obtained by reaction of elemental selenium with a fourfold excess of Na$_2$SO$_3$ at 70–80 °C. In the presence of Cd^{2+}, SeSO$_3^{2-}$ gives a grayish precipitate which quickly decomposes, particularly under moderate heating (ca. 50 °C), to give red-brown CdSe [45, 46].

In general, a thermal treatment in air improves the performance and the stability of the photoelectrodes, leading to an enhancement in crystallinity, in electrical connections between the nanostructures, and to an increased hole diffusion length. In the case of CdSe, a partial sublimation of the photoactive film is observed starting from 260 °C. A post treatment with CdS can be helpful for encapsulating CdSe, making it more stable at elevated temperatures, at the same time improving the photon to electron conversion at shorter wavelengths.

Bi_2S_3 (bismuthinite, orthorhombic) electrodes thermally degrade in air at $T > 260\,°C$ to form white bismuth oxide sulfate ($Bi_{28}O_{32}(SO_4)_{10}$) due to reaction with atmospheric oxygen. In nitrogen atmosphere the annealing can be carried out at 400 °C without observing decomposition. However, the best photoelectrochemical results were observed with photoelectrodes annealed in air at 220 °C for 15–20 min, in agreement with conditions reported by other authors in the preparation of TiO_2 (Degussa P25) supported Bi_2S_3 nanoparticles for environmental remediation [47].

The electrochemical methods of TiO_2 surface modification by growth of lower band gap semiconductors rely on principles analogous to the chemical deposition, i.e., the electrochemical generation, of the anion (S^{2-}, Se^{2-}, Te^{2-}) in a cation (Cd^{2+}, Bi^{2+}) containing electrolyte, according to the following reactions:

$$S + 2e^- \rightarrow S^{2-}$$

$$Cd^{2+}\left(Bi^{3+}\right) + S^{2-} \rightarrow CdS(Bi_2S_3) \downarrow$$

$$Se(Te)O_2 + 6e^- + 4H^+ \rightarrow Se^{2-}\left(Te^{2-}\right) + 2H_2O$$

$$Cd^{2+} + Se^{2-}\left(Te^{2-}\right) \rightarrow CdSe(Te) \downarrow$$

Compared to chemical impregnation methods, the electrodeposition may lead to more homogeneous surfaces and to a better control of the sensitizing semiconductor growth, since the anions are directly electrogenerated on the oxide surface with the desired rate.

The precursor electrolytes for CdS and Bi_2S_3 deposition are very similar, consisting in a saturated sulfur solution in DMSO to which 0.3 M $Cd(NO_3)_2$ or Bi $(NO_3)_3$ are added. The CdSe precursor is composed by a selenium oxide solution in sulfuric acid in the presence of $Cd(NO_3)_2$ [48]. Our preferred concentrations were 10^{-2} M SeO_2 and 0.3 M $Cd(NO_3)_2$ in 4×10^{-3} M H_2SO_4.

The deposition can be performed by either potentiostatic, potentiodynamic (multiple scan) or galvanostatic procedures. In our case we have adopted a multiple scan deposition technique where the potential was linearly varied on subsequent cycles at cathodic potentials, usually between −0.3 and −1.1 V vs SCE, with a scan rate of 50 mV/s until strongly colored electrodes were obtained.

The deposition was considered complete when the maximum optical density (absorbance or, in the case of opaque substrates, spectral absorption) allowed for

the absorption of at least 70% of the incident photons. A direct reliable estimate of the amount of deposited material from the integration of voltammetric waves was either difficult or impossible due to the capacitive TiO_2 contribution, to the irreversible nature of the electrochemical process, and to the lack of any clearly defined diffusion limited peak.

3.5 Bi_2S_3/TiO_2 Photoelectrodes

The absorption spectrum of Bi_2S_3 chemically deposited on TiO_2 nanoparticles shows a featureless continuous absorption in the whole visible region, with an estimated optical band gap of 1.4 eV (Fig. 28) [47, 49]. Repeated (up to 40) chemical bath deposition from $Bi(Ac)_3$ and Na_2S leads to intensely colored electrodes with a maximum absorbance of the order of 4, allowing for an almost quantitative light absorption. Despite this, the chemical impregnation appears to be characterized by a scarce reproducibility, even by considering the same number and duration of the deposition steps, and the photoelectrochemical response in 0.1 M Na_2S is promising but also highly variable: in the presence of a 0 V vs SCE potential bias, photocurrents ranging from 7 to 4 mA/cm^2 (Fig. 29) were observed under a 0.2 W/cm^2 visible light irradiation (HID lamp). A modest positive polarization results, however, in a strong enhancement of the photocurrent, which is superimposed to the contribution of the direct electrochemical oxidation of sulfides, whose onset is located at about 0.2 V vs SCE.

The electrodeposition process quickly leads (two to four potential scans) to good quality Bi_2S_3 films with a good reproducibility. Although the optical density is
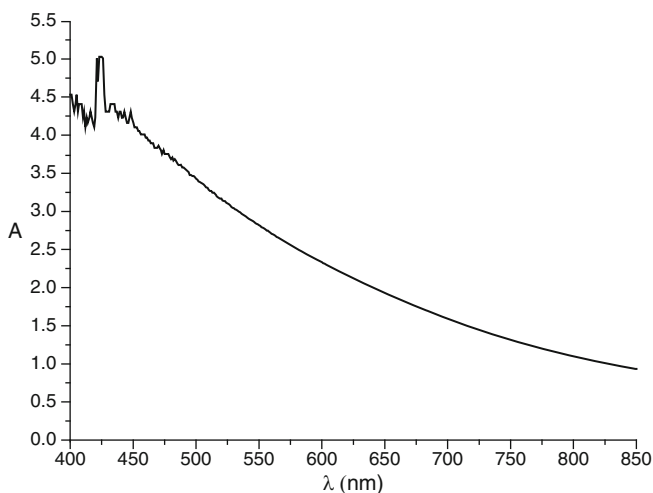

Fig. 28 Absorption spectrum of Bi_2S_3 chemically deposited on a TiO_2 nanoparticle film

lower than that obtained by chemical impregnation (Fig. 30), the light harvesting efficiency (LHE) of the photoelectrodes varies between 95 and 50% in the spectral region between 400 and 850 nm, with a sharp rise below 400 nm due to TiO_2 absorption. The maximum photocurrent at 0 mV vs SCE is in the order of 5 ± 1 mA/cm^2 in the presence of an incident irradiance of 0.12 W/cm^2 (AM 1.5 G).
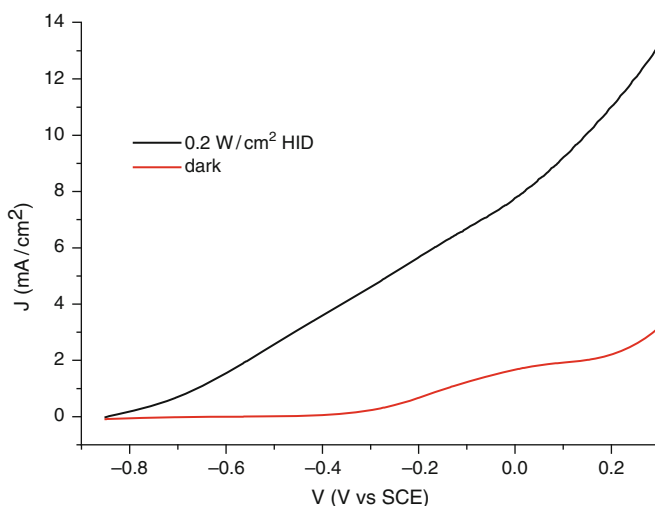
Fig. 29 *J–V* characteristics under illumination (*black*) (0.2 W/cm^2 HID lamp) and in the dark (*red*) of a Bi_2S_3/TiO_2 electrode in 0.1 M Na_2S
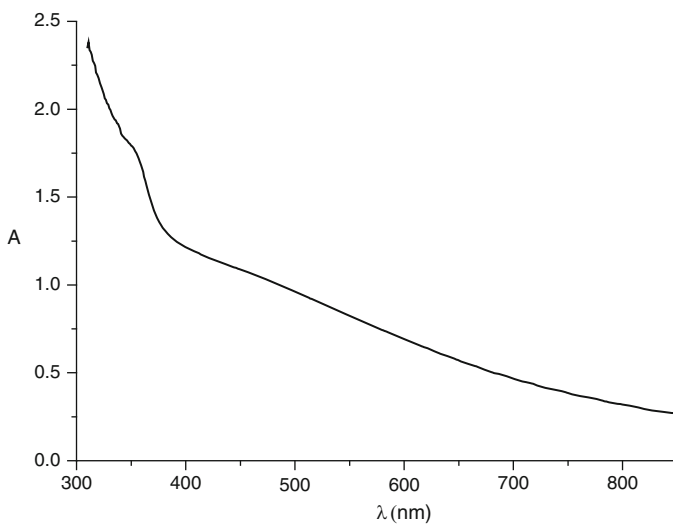
Fig. 30 Typical absorption spectrum of electrodeposited Bi_2S_3 on a nanocrystalline titania electrode
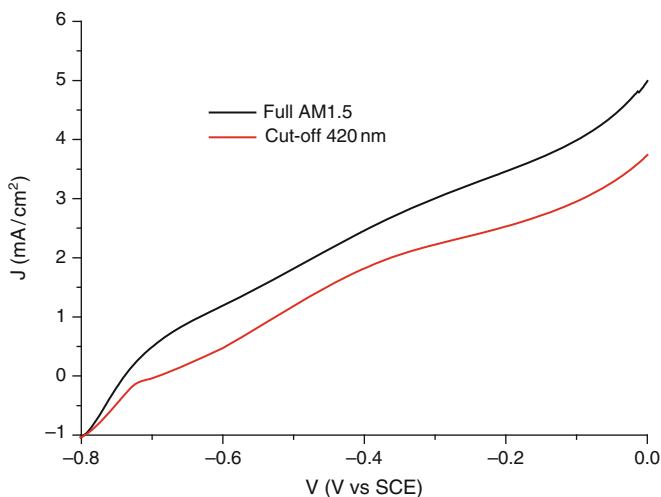
**Fig. 31** JV curves of electrodeposited Bi_2S_3 with (*red*) and without (*black*) 420 nm cut-off filter. 0.1 M Na_2S

The advantage of having a panchromatic absorber is clearly evident from Fig. 31, where the UV component has been completely removed from the excitation light with a 420-nm cut-off filter. Under these conditions the photoelectrode does not undergo a substantial decrease in its performance, still reaching values of more than 3 mA/cm^2 at 0 V vs SCE, showing that Bi_2S_3 is effectively injecting into the conduction band of TiO_2.

Interestingly, despite the good performances, the *J–V* curves recorded under shuttered illumination show a notable difference between front (electrolyte) side and backside (FTO contact) illumination, evidence of a more effective photocurrent generation by backside illumination (Fig. 32). The effect is even more dramatic in thick electrodes, where the transients in front irradiation are about half of those recorded in backside mode, corroborating the indication of limitations arising from charge transport and collection. Although the *J–V* curves do not show dark cathodic features, usually originated from charge recombination mediated by surface states, the existence of a certain amount of electron recombination is also clearly suggested by the nonideally rectangular shape of the transients.

The IPCE under a potential bias of −0.5 V vs SCE is relevant when the photoelectrode is illuminated through the FTO (collector) side (backside) reaching values in the order of 30–10% in the 350–450 nm region and extending to 830 nm (Fig. 33). Although the UV contribution of TiO_2 cannot be completely neglected, the sharp decrease in IPCE is in contrast with the absorption spectrum of Bi_2S_3, which declines smoothly and maintains high LHE values by moving from shorter to longer wavelengths, suggesting that high energy photons with a smaller penetration depth, being absorbed in closer proximity of the back contact, are more effectively converted into electrons flowing through the external circuit.
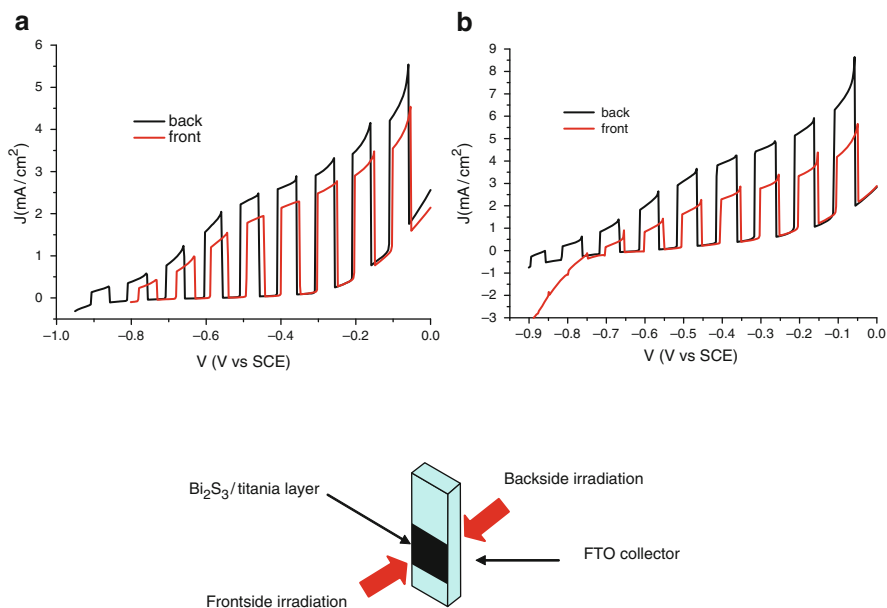
Fig. 32 Shuttered J–V curves of Bi_2S_3/TiO_2 systems in 0.1 M Na_2S under AM 1.5 G illumination. (**a**) Thinner layer (20 deposition scans from 10^{-3} Bi^{3+} solution); (**b**) thicker Bi_2S_3 layer (100 deposition scans from 10^{-3} Bi^{3+} solution)
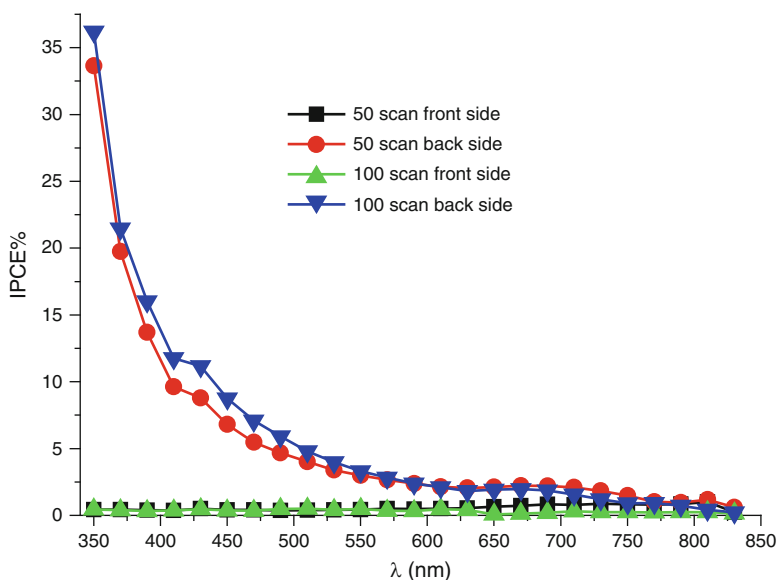

Fig. 33 IPCE spectra of Bi_2S_3/TiO_2 system biased at -0.5 V vs SCE. The negative bias is chosen from minimizing the dark background from electrochemical oxidation of sulfides

By contrast, illumination to the front side leads to an almost negligible photon to current conversion, indicating that only a small fraction of electron/hole pairs generated in the outer Bi_2S_3 layer is effectively capable of escaping from recombination. Actually, the difference between the photocurrent measured in front and back illumination mode under full AM 1.5 (~100 mW/cm^2) is smaller than what could be anticipated by observing the photoaction spectra recorded under a low intensity (~1 mW/cm^2) monochromatic light. The reason is most probably related to the fact that, due to the low excitation intensity, nearly all of the monochromatic photons in the incident beam are absorbed by the most external layers of the black absorber, where the charge collection is poor, and by a lower conductivity of Bi_2S_3 itself, which, under a sufficiently high light intensity, exhibits a photoconductor behavior object of recent investigations in the field of sensor devices [50, 51].

In order to improve charge collection, the electrodeposition of Bi_2S_3 on titania nanotubes can be successfully performed, as demonstrated by the SEM images of the top Bi_2S_3/nanotube structure (Fig. 34). The multiple scan deposition at 10 mV/s from a diluted (10^{-3} M Bi^{3+}) precursor electrolyte in DMSO leads to a quite homogeneous decoration of tubular nanostructures with Bi_2S_3, clearly evidenced by a considerable thickening of the nanotube walls, reaching a size of about 50 nm, resulting, in many cases, in the complete occlusion of the nanotube mouth. The presence of some spherical agglomerates of Bi_2S_3 with a diameter variable between 200 nm and 1 μm is also evident.

The photoaction spectra of the Bi_2S_3/nanotubes photoelectrodes (Fig. 35) have distinct characteristics when compared to those found for Bi_2S_3/nanoparticle systems: although the absolute IPCE are of the same order of magnitude, with values of
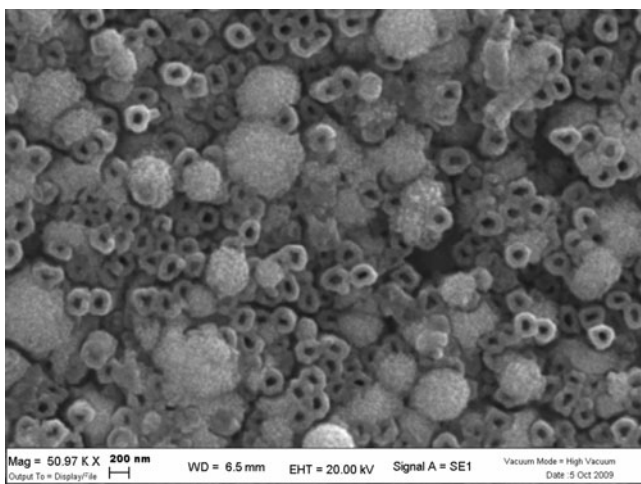
Fig. 34 Bi_2S_3/titania nanotubes surface obtained by multiple scan (45, 10 mV/s) electrodeposition of Bi_2S_3 from 10^{-3} M Bi^{3+} electrolytes. Sample annealed in air at 220 °C for 30 min
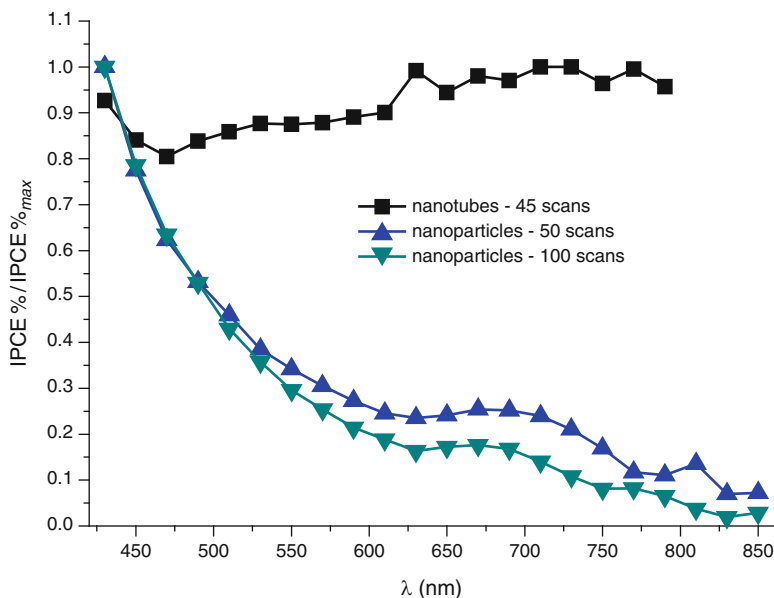
Fig. 35 Normalized photoaction spectra: Bi_2S_3/titania nanotubes (*black*) compared to Bi_2S_3/TiO_2 nanoparticle substrates (*blue* and *green*)

10–15% under -0.5 V vs SCE potential bias, a substantially constant photoconversion in the whole visible region is observed, as would reasonably be expected for a black absorber in which the LHE approaches unity. In other words, while in the planar Bi_2S_3/TiO_2 electrodes the light collection efficiency drops dramatically, depending on the photon penetration depth and ultimately on the distance from the collector at which electron/hole pairs are generated, in Bi_2S_3/nanotubes the electrons are collected with analogous efficiency in both the blue and red parts of the spectrum. This is consistent with the coated nanotube geometry where, without respect to the penetration depth of the visible radiations, the charge carriers diffuse or migrate orthogonally to the tube axis [52], traversing in all cases nearly the same thickness of Bi_2S_3 before reaching the charge collector.

3.6 CdS and CdSe/TiO₂ Photoelectrodes

The chemical bath deposition of CdS on titania nanotubes leads to photoelectrodes characterized by satisfactory photoelectrochemical properties. SEM micrographs taken at ×9,700 and at ×51,370 indicate that, after the annealing at 400 °C, chemically deposited CdS forms a nanocrystalline network which covers and incorporates the anatase nanotubes which have a mouth diameter of about 100 nm
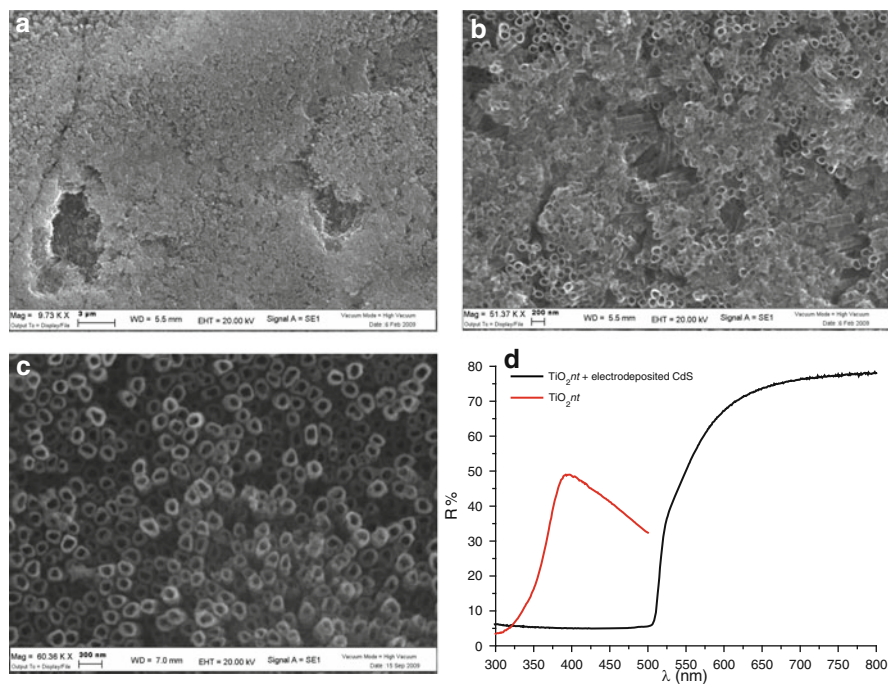
Fig. 36 CdS modified nanotubes by (**a**, **b**) chemical bath deposition and (**c**) electrodeposition. (**d**) Diffuse reflectance spectrum of the electrodeposited CdS/titania nanotubes (NT) surface compared to the unmodified titania NT surface. Titania NT were obtained from DMSO/HF anodization procedures

(Fig. 36). Single CdS nanostructures cannot be resolved in SEM mode; however, higher resolution transmission microscopy (HRTEM) studies carried out by Sun et al. have confirmed that the initially formed CdS network consists of quantum dots the size of which varies between 2 and 10 nm [53]. By contrast, the electrodeposition of CdS produces a much more homogeneous coating, which is actually difficult to detect in SEM imaging, simply resulting in a thickening of nanotube walls (Fig. 36c). Nevertheless, the diffuse reflectance spectrum (Fig. 36d) confirms without any doubt the presence of CdS, showing the typical steep and intense transition with onset located at about 600 nm, leading to a significant extension of the spectral sensitivity of the photoanode, with an effective absorption (75–80%) of the photons in the 510–300 nm range.

The photoaction spectrum of the CdS sensitized nanotubes recorded in 0.1 M Na_2S at 0 V vs SCE shows a good conversion, approaching 50% at 500 nm, in good agreement with the absorption spectrum of CdS, testifying an effective charge injection into TiO_2 (Fig. 37a). The good performance is confirmed under AM 1.5 irradiation, where photocurrents of the order of 6–9 mA/cm^2 are recorded in 0.1 M Na_2S (Fig. 37b). The electrodeposited CdS substrates generate higher currents (ca. 20% higher with respect to chemically deposited substrates), but display
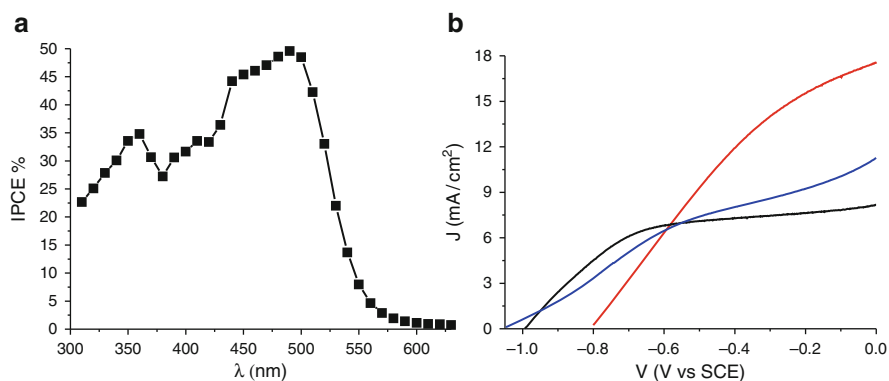
Fig. 37 (**a**) Photoaction spectrum of chemically impregnated CdS/TiO$_2$ nanotubes at 0 V vs SCE. (**b**) *J*–*V* curves under AM 1.5 illumination (0.12 W/cm^2) in the presence of Na$_2$S (*black* chemically deposited CdS, *blue* electrochemically deposited CdS) and in 1 M 1/1 formate buffer (*red*)

a lower fill factor. In both cases the open circuit photovoltage is ≥1 V vs SCE. In the presence of a formate buffer as a sacrificial donor, the photocurrents are more than doubled, reaching 16–18 mA/cm^2 due both to a more effective hole scavenging which can be originated by HCOOH/HCOO$^-$ adsorption onto the CdS/TiO$_2$ surface, and by secondary electron injection by highly reducing HCOO· intermediates which are known to inject into the conduction band of TiO$_2$.

Although in this case the sensitization of nanotubes with CdS produces good performances, comparable photocurrent densities ($J \sim 6 \pm 1$ mA/cm^2) can be found through the sensitization via electrochemical deposition of more conventional transparent nanocrystalline electrodes made of sintered titania nanoparticles. The use of transparent CdS based electrodes has the advantage of allowing for the assembly of tandem configurations, in which two spectrally complementary photoelectrodes can be connected in parallel to sum the photocurrents (Fig. 38a). For example, a tandem photoanode made by a CdS/TiO$_2$ and by Bi$_2$S$_3$/TiO$_2$ heterointerfaces biased at 0 V vs SCE can generate photocurrents in the order of 12–14 mA/cm^2 in 0.1 M Na$_2$S (Fig. 38b) thanks to the simultaneous exploitation of the high photon to current conversion of CdS in the blue part of the spectrum (300–550 nm) and of the extended spectral sensitivity of Bi$_2$S$_3$, which is able to capture and convert photons where CdS does not absorb, starting from 830 nm.

A panchromatic sensitization as well as a considerable efficiency in photon to electron conversion can be obtained by functionalizing titania nanostructures (nanotubes as well as nanoparticles) with CdSe. In this case both chemical and electrochemical deposition leads to morphologically similar surfaces where CdSe can be observed to decorate each nanotube. As previously observed, the electrodeposition is the preferred method for obtaining a more homogeneous coating of each nanostructure, where CdSe covers almost completely the entire length of every nanotube, also occluding their mouths (Fig. 39).
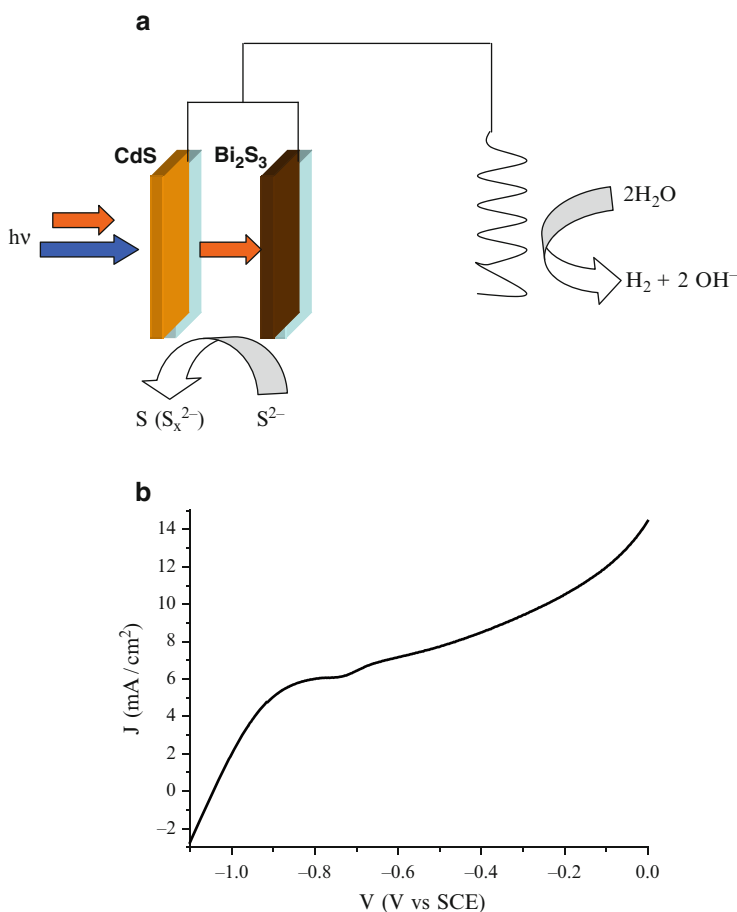
Fig. 38 (**a**) Scheme of a tandem photoelectrochemical cell based on CdS/TiO$_2$ and Bi$_2$S$_3$/TiO$_2$ heterointerfaces; (**b**) resulting *J–V* characteristic

Although a relevant loss of photoactive CdSe coating occurs by sublimation during the 400 °C annealing stage in air or under inert atmosphere (N$_2$), the thermal treatment was found to be beneficial for both performance and stability of the photoelectrode. The optical band gap evaluated from the absorption spectrum (Fig. 40a) was found to be 1.65 eV, in good agreement with the literature reported values [54, 55]. The IPCE extends from 310 to 750 nm, keeping an almost constant plateau value which, with the annealed samples, can reach 40% (Fig. 40b). The red shift in IPCE onset between untreated and annealed substrates is in agreement with the absorption spectra where, upon 400 °C treatment, a bathochromic shift of the absorption threshold to about 750 nm can be observed. The increased IPCE indicate an efficient charge carrier transfer and a suitable band alignment at the CdSe/TiO$_2$
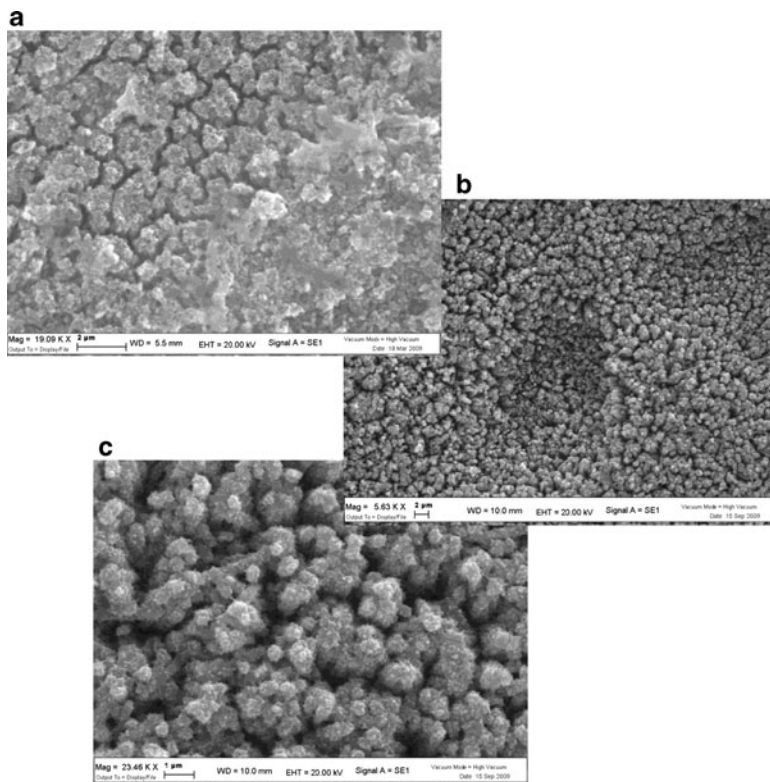
Fig. 39 SEM micrographs of (**a**) CdSe/titania nanotube heterostructures obtained by chemical bath deposition ~×19,000; (**b**) CdSe functionalized nanotubes from electrochemical deposition at ×5,630; (**c**) higher magnification (×23,460) of (**b**)
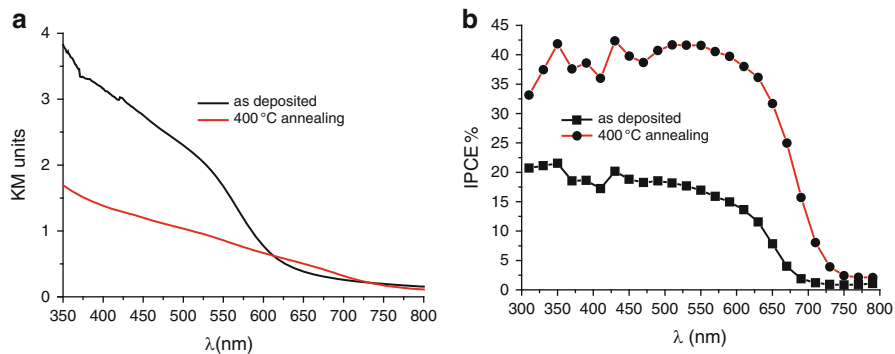
Fig. 40 (**a**) Diffuse reflectance spectra (KM units) of chemically deposited CdSe on titania nanotubes; (**b**) IPCE spectra. 0.1 M Na$_2$S, 0 V vs SCE
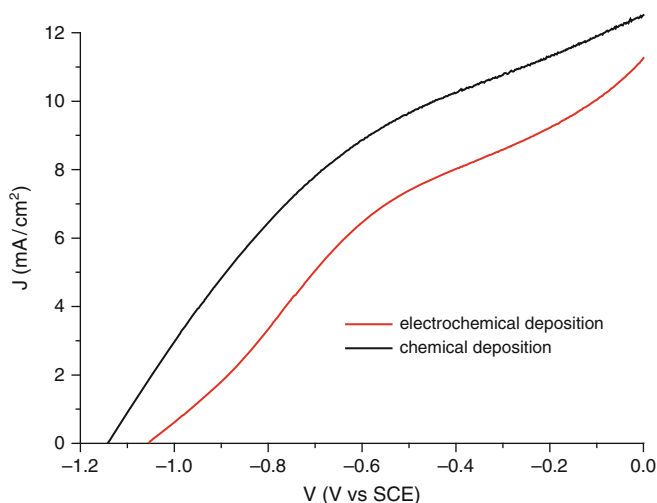
Fig. 41 JV curve under AM1.5 G illumination (0.12 W/cm^2) of CdSe/TiO$_2$ NT photoanodes in 0.1 M Na$_2$S

interface. These features have been observed by other authors in CdSe/ZnO hetero-interfaces [56], and have been explained by the loss of quantum confinement in CdSe nanoparticles which, due to the thermal formation of larger crystals, might facilitate the charge transport through the CdSe coating to the inner nanotube collector. Besides thermal sintering of the CdSe nanocrystals, other authors have attributed the increased reproducibility and durability of the photoelectrochemical response in cadmium chalcogenide-based PEC cells to the transition from cubic zinc blende to wurtzite structures, which becomes the dominating phase at temperatures >350 °C [57].

The performances under white light are satisfactory for both chemically and electrochemically deposited CdSe substrates, showing photocurrents in the 10–11 mA/cm^2 range at 0 V vs SCE and a $V_{oc} > 1$ V (Fig. 41).

Sensitization by sequential electrodeposition of CdSe and CdS can be achieved with both colloidal (TiO$_2$ nanoparticles) and nanotube surfaces; however, as previously observed with Bi$_2$S$_3$/TiO$_2$ heterointerfaces, the comparison with the IPCE spectrum recorded for colloidal substrates in back (FTO collector) side illumination is consistent with a more favorable electron collection in nanotubular substrates, causing a broader photon to electron conversion and a significant IPCE maximum in the red part of the spectrum (650–700 nm) clearly absent in colloidal electrodes, which, in contrast, show a rather steep decrease in IPCE by moving from shorter to longer wavelengths (Fig. 42). Thus, also in this case, limitations arising from the relatively short hole diffusion length (~1 μm in air annealed samples) [58] in CdSe may be overcome by exploiting the geometry of nanotube arrays.
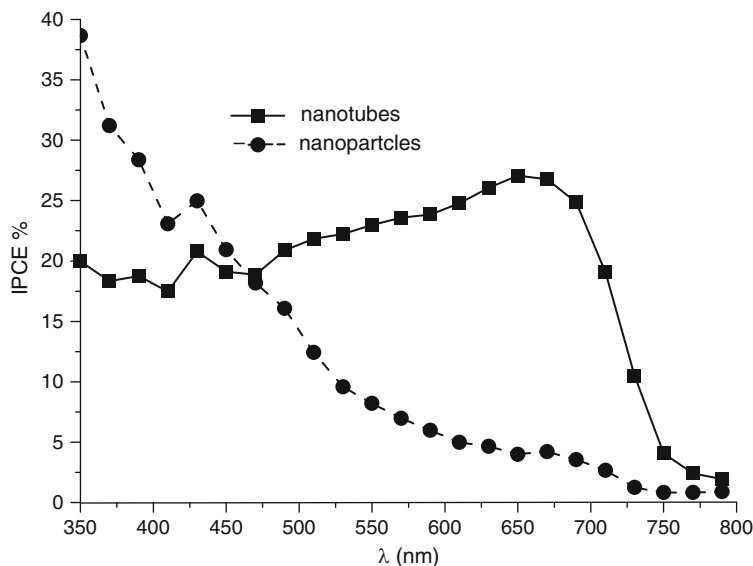
Fig. 42 IPCE spectra in mixed CdS/CdSe/TiO$_2$ interfaces: nanotubes (*squares*) compared to nanoparticles (*circles*). 0 V vs SCE, 0.1 M Na$_2$S

3.7 CdTe/TiO$_2$

The interest in CdTe arises from its ideal band gap for solar photoconversion (1.5 eV) which, coupled with nanotube arrays, thanks to an improved charge separation and collection and to a large junction area, may lead to interesting advancements in the light to electricity (and ultimately to hydrogen) conversion. It has already been shown that in many cases, being diffusionally favored, the electrodeposition of cadmium chalcogenides results in the clogging of the pores before attaining a complete coverage of the internal surface of the tube with the photoactive material, thus limiting the active area which would be otherwise available for the photoelectrochemical reactions. For this reason, Grimes and coworkers devised a deposition method [59] which, in principle, can be generally applied every time that a certain selectivity in the deposition of a given material has to be attained on conductive porous substrates.

Essentially, the new approach (Fig. 43) consists in the dipping of the nanotube electrodes in the precursor electrolytes (0.1 M CdSO$_4$ and 0.1 mM TeO$_2$ in dilute sulfuric acid at pH 1.4), where the capillary forces draw the electrolyte inside the pores. The electrode is then transferred in an inert supporting electrolyte where the electrodeposition is carried out at constant cathodic potential (−0.4 V). The procedure can be repeated until a desired amount of CdTe is deposited into the pores (Fig. 44).
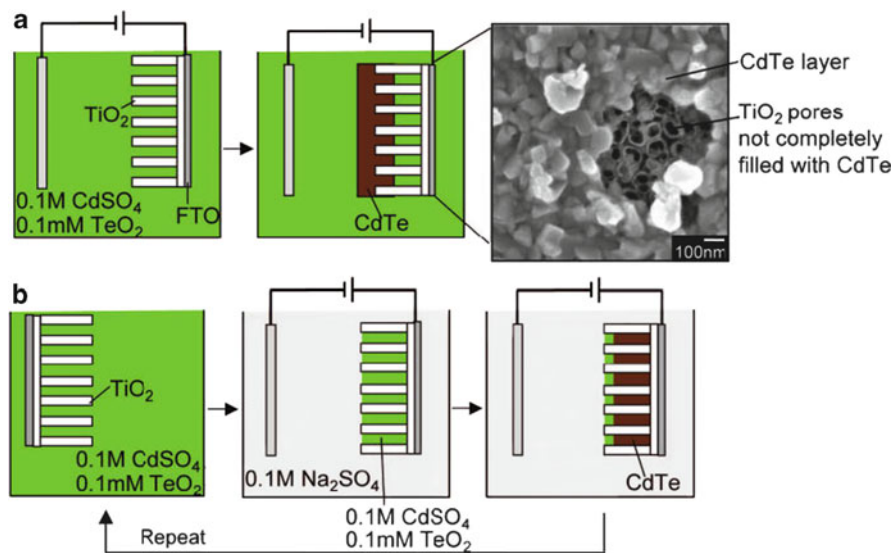
Fig. 43 Schematic procedure of nanotube functionalization with CdTe: (**a**) conventional approach; (**b**) dipping and deposition approach. From [59]
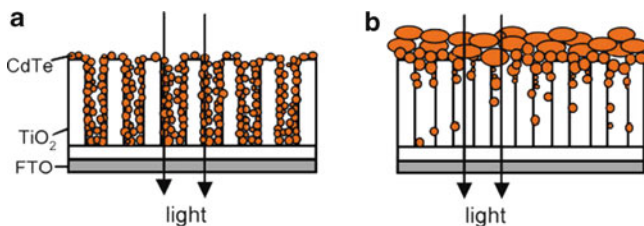
Fig. 44 Schematic comparison of CdTe/TiO$_2$ heterojunctions created by dipping and deposition (**a**) and conventional electrodeposition (**b**)

The successful formation of a CdTe/TiO$_2$ nanotube heterojunction is testified by its n-type behavior, suggesting that electrons are more effectively transferred to the TiO$_2$ than to the electrolyte. The stability and the magnitude of the photoanodic current generated by the interfaces built with the newly modified procedure undergoes a general improvement, reaching 0.44 mA/cm^2 and nearly doubling the photoresponse of the conventional interfaces (Fig. 45).

Given that both (a) and (b) interfaces in Fig. 45 display a similar light absorption capability, the observed improvement is attributed to a reduced electron–hole recombination resulting from a thinner CdTe layer with a more even and more intimate contact with titania nanotube. For the same reason the improvement in photostability would result from the minimization of the self photooxidation of CdTe (CdTe + 2OH$^-$ + 2h$^+$ → HCdO$_2$$^-$ + H$^+$ + Te) which would follow from

Fig. 45 Photocurrent transients in 0.6 M Na$_2$S under short circuit conditions and visible light illumination: (**a**) dipping/deposition (20 cycles); (**b**) regular deposition (30 min at −0.4 V vs Ag/AgCl)

a more effective hole transfer to the electrolyte, as a result of the enhanced electrolyte/CdTe/TiO$_2$ junction areas.

4 Photoelectrodes Based on Anodically Grown WO$_3$

4.1 Formation of Anodic WO$_3$ Films by Electrochemical Oxidation of Metallic Tungsten

Tungsten (together with Al, Ti, Zr, Bi, Ta, and Nb) belongs to the group of the so-called valve metals, which passivate and show a very high corrosion resistance in most common aqueous media. The composition of naturally or anodically produced oxide films is essentially identical to WO$_3$.

Due to its electrochromic properties, i.e., a reversible color change upon application of suitable electric potential, tungsten trioxide has been employed and widely used in electronic displays, smart windows, sunroofs, and rear and side view mirrors [60–63]. More recently, due to its chemical stability in acidic aqueous media and interesting photoelectrochemical properties, it has been proposed as a promising candidate in water photoelectrolysis processes [64–68].

Thanks to its many possible technological applications, considerable work has been carried out to investigate the detailed mechanistic aspects of electrochemical tungsten oxide growth in aqueous media, but there is no universally accepted model that accounts completely for the experimental evidence [69]. The typical voltammograms obtained for tungsten in 1 M HCl in the −0.5 to +3 V region are shown in Fig. 46.
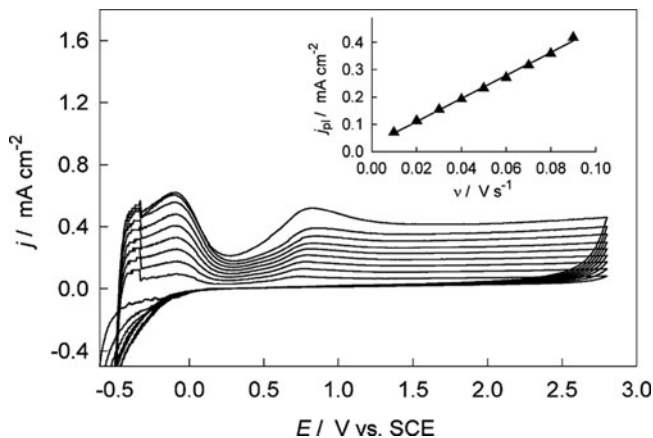
Fig. 46 CV of a tungsten electrode in 1 M HCl at various scan rates (10–90 mV/s). From [69]

At least two anodic peaks depicting the initial stages of oxide formation are observed, followed by a very wide plateau at potentials >1 V.

According to the electrochemical and XPS evidence [70], it has been proposed that the anodic oxidation of tungsten may result in the initial formation of a mixture of oxides, namely WO_2, W_2O_5, and WO_3, according to the equations

$$W + H_2O \rightarrow WO_2 + 4H^+ + 4e^-$$

$$2WO_2 + H_2O \rightarrow W_2O_5 + 2H^+ + 2e^-$$

$$W_2O_5 + H_2O \rightarrow 2WO_3 + 2H^+ + 2e^-$$

However, at higher anodization potentials, corresponding to the plateau of Fig. 46, the dominating species is W^{6+}. After the anodic peak, the current densities are practically constant, indicating that the thickening of the amorphous barrier layer takes place during the positive sweep. The fact that passivity can still be observed in the absence of an outer/precipitated oxide layer indicates that passivation of tungsten can be attributed to a barrier layer between the metal and the outer layer in which transmission of ions occurs essentially by vacancy motion. EIS analysis performed during the potentiostatic anodization also suggests that the migration of oxygen vacancies is the main charge transport mechanism across the growing WO_3 oxide film and that it is eventually enhanced by the accumulation of negative charges (corresponding to cation vacancies) at the film/solution interface.

Thus, electrochemical anodization of metallic tungsten can be a convenient method for preparing porous photoactive substrates in which the oxide structures are tightly interconnected and strongly bound to the metal collector, both factors concurring to increase the photogenerated charge collection efficiency. It has already been shown that, by this approach, it is indeed possible to obtain interesting

nanostructures that can find application in the field of solar energy conversion. The most common route for the anodic preparation of porous films involves the application of a constant potential to a metallic tungsten lamina in the presence of aqueous electrolytes containing fluoride anions which establish mild oxide dissolution conditions. It is the achievement of a steady state between oxide dissolution and formation which leads to nanotubular or nanoporous structures. Some authors [71] also achieved a porous oxide structure (and even some small nanotubular WO_3 domains) by careful application of an appropriate overvoltage intended to reach oxide breakdown conditions in fluoride free electrolytes. Basically, in order to reach breakdown conditions, made possible by the presence of a strong applied field strength, a harsh treatment consisting in the application of a sudden step potential of several tens of volts has to be adopted. Electrolyte temperature and compositions are, however, also important for reaching reproducible results and a reasonable surface coverage.

Nevertheless, from the photoelectrochemical point of view, most literature reports deal with nanocrystalline WO_3 substrates which display a high photoactivity in the UV region but give a limited response in the visible frequencies. This is consistent with reported WO_3 band gaps ranging from 3.25 to 2.9 eV [72, 73]. Indeed, we have also experimentally verified in our laboratories that, by following or slightly modifying literature approaches, relevant IPCEs in the order of 50% could be reached in the UV region, but no substantial photoactivity could be observed beyond 430 nm. However, by following the pioneering work of Grimes et al. (see Sect. 3), it has also been found that, among many solvents and electrolytic compositions, efficient WO_3 substrates characterized by an extended spectral response could be obtained by potentiostatic anodization in a two W electrode cell in the 30–40 V range by using an electrolyte comprised of N-methyl-formamide (NMF)/water 8:2 in the presence of 0.05 wt% NH_4F. Also, in this electrolytic composition, water is required to act as an oxygen donor and allow for oxide formation, as indicated by the cyclic voltammograms reported below. From Fig. 47a, during the first scan at 1 V/s an anodic current is clearly observable
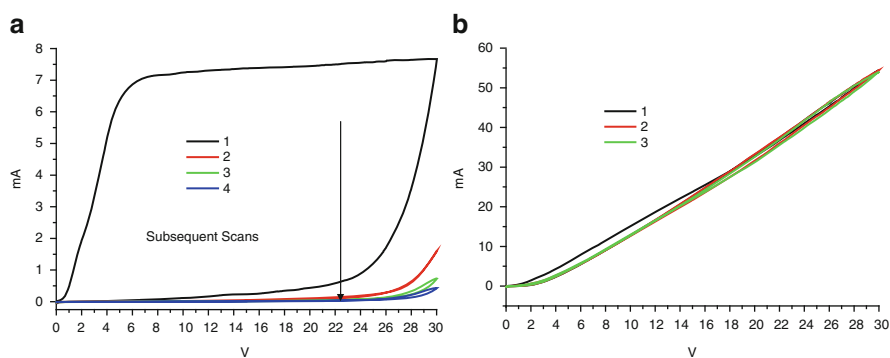

Fig. 47 Cyclic voltammograms of metallic W in the electrolyte comprised of (**a**) NMF/water 8/2 + 0.05% NH_4F; (**b**) NMF + 0.05% NH_4F. The solutions were not purged with inert gas

which drops dramatically on subsequent scans as a result of the metal surface passivation induced by the formation of an oxide layer, whereas different behavior is observed in the water free electrolyte, where a current, about one order of magnitude higher (Fig. 47b), assigned to the anodic dissolution of the metal is recorded with no appreciable changes upon subsequent scans.

The potentiostatic anodization is usually carried out with an unstirred solution at room temperature ($20 \pm 5\,°C$) for several hours (48–72). At present, in our conditions, 72 h at a constant applied voltage of 40 V constitutes the longest practical and convenient anodization time, since it has been observed that no photoelectrochemical improvement results from prolonging the electrolysis beyond this limit. Figure 48 is indicative of the typical behavior of the current recorded during an anodization in NMF/H_2O 8/2 and 0.05 wt% NH_4F at room temperature (17 °C). The anodization current shows alternating minima and maxima probably determined by the competition between oxide formation and dissolution rates: when the oxide formation overcomes the dissolution the current drops due to a more complete passivation of the metal surface. In contrast, the oxide dissolution leads to the exposure of fresh metal surface, which undergoes oxidation causing a new increment in the anodic current. The typical average current density during the anodization is 8–10 mA and the total charge exchanged, obtained by integration of the i–t curve, is 150 ± 18 C.

The anodization procedure results, after 72 h, in the formation of an irregular porous oxide layer 3–5 μm thick, with bundled up structures (Fig. 49), particularly evident in AFM imaging, ca. 300 nm wide, longitudinally crossed by cracks which
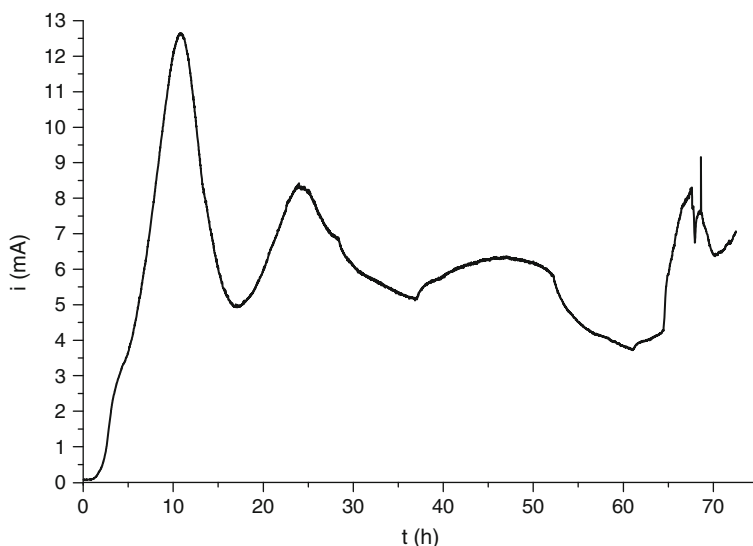
Fig. 48 Anodization current recorded during electrochemical tungsten oxide formation in NMF/ H_2O 8/2 and 0.05% NH_4F at 40 V
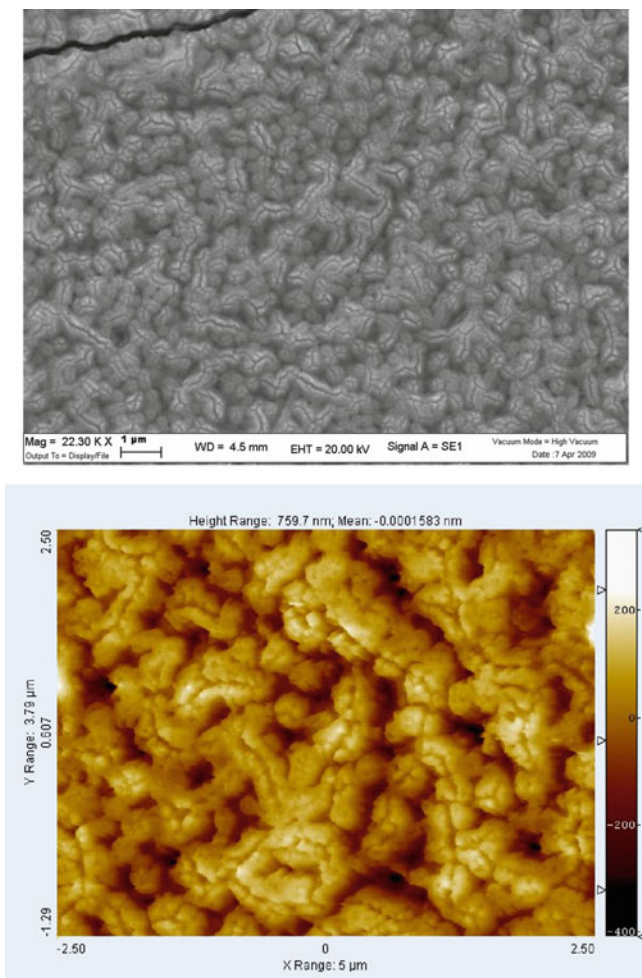
Fig. 49 SEM (*top*) and AFM (*bottom*) micrographs of anodically formed WO$_3$ after the annealing process at 550 °C for 1 h in air

give to the surface an overall worm-like appearance. After a thermal treatment at 550 °C in air, necessary both to induce crystallinity and to establish good electrical connections between the nanostructures, small angle XRD confirmed the presence of the expected monoclinic phase of WO$_3$ (Fig. 50). In many samples a strong morphological anisotropy manifests itself as a preferential orientation of the oxide along crystallographic planes (111 and 200). Although this feature has also been documented by other authors in different anodization conditions [72], at present we have not been able to establish any clear correlation between crystallographic anisotropy and photoelectrochemical properties of the metal oxide which, within experimental error, do not vary appreciably.
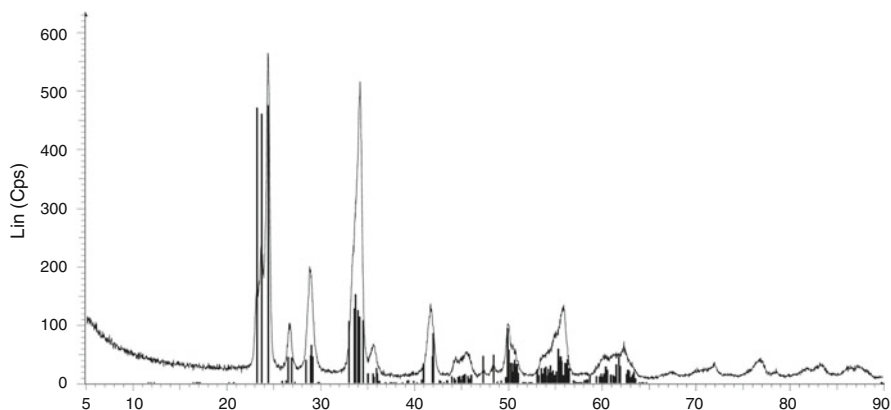
Fig. 50 Small angle XRD pattern of the anodically grown WO_3 film obtained in NMF/water 8/2 + NH_4F 0.05%

4.2 Photoelectrochemistry

As demonstrated by the *J–V* characteristic recorded in 1 M H_2SO_4 (Fig. 51), the typical photoelectrochemical performances of the anodically grown oxides are relevant: under varying AM 1.5 G incident irradiation the photocurrent, whose threshold at pH 0 is located at +0.3 V vs SCE, varies in a reasonably linear fashion with the incident irradiance, showing maximum values exceeding 9 mA/cm^2 under 0.37 W/cm^2 with an average slope of 0.013 A/(cm^2 V). The advantage of the electrochemically grown WO_3 over a more conventional WO_3 electrode, obtained by standard sol–gel methods (colloidal) made by sintered nanoparticles, can be clearly appreciated from Fig. 51b: while the performances of the two electrodes are quite similar at low power intensities, under strong illumination the anodically grown substrate does not show saturation and clearly outperforms the colloidal almost fourfold.

In the presence of an electrolyte composed of 1 M H_2SO_4/CH_3OH 8/2 the plateau photocurrents are nearly doubled, approaching, under strong illumination (ca. 0.3 W/cm^2), 16 mA/cm^2. Concomitantly, a negative shift of the photoanodic onset of ca. 100 mV can be observed: both effects are consistent with an improved hole scavenging by CH_3OH and/or by a known mechanism of secondary electron injection from surface adsorbed highly reducing $CH_3O\cdot$ intermediates. The *J–V* curves were found nearly independent from the scan rate in an ample interval ranging from 2 to 500 mV/s (Fig. 52): although this is a typical behavior of a kinetically controlled process, it is also indicative of a relatively facile interfacial charge transfer, in which the steady state is maintained, even in the presence of a rapidly changing potential.

Referring to Fig. 52, the diffusional "bell" shaped peak at low potential (0–0.2 V interval) which, in contrast, shows a marked scan rate dependence, is ascribed to the
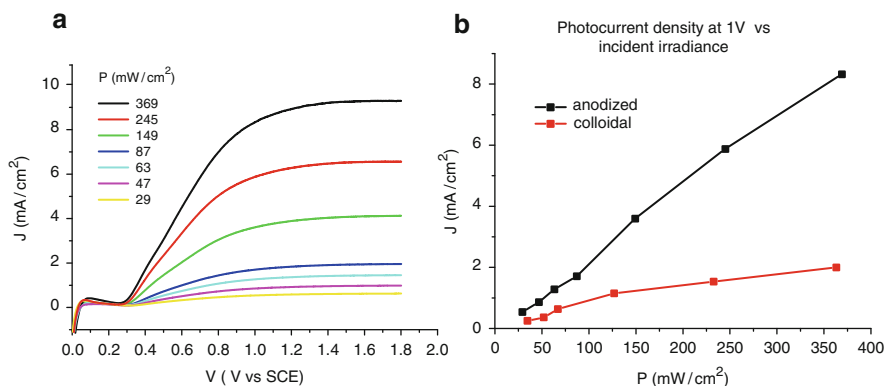
Fig. 51 *J–V* curves in 1 M H$_2$SO$_4$ *black* (**a**) as a function of the incident irradiance (AM 1.5 G); (**b**) photocurrent density taken at 1 V vs SCE vs incident irradiance: anodically grown (*black*); sol/gel (*red*)
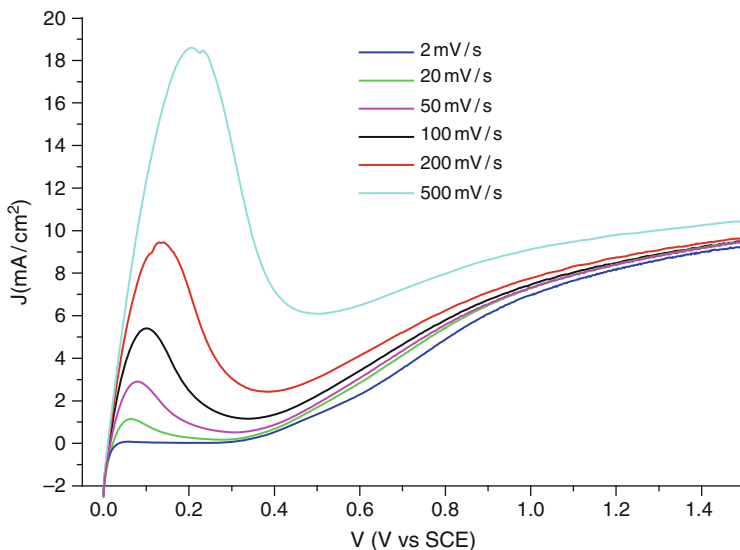
Fig. 52 *J–V* curves of anodically grown WO$_3$ in 1 M H$_2$SO$_4$ under 0.3 W/cm^2 AM 1.5 G irradiation as a function of the scan rate (2–500 mV/s interval)

reversible W^{+5} → W^{6+} oxidation, responsible for the known electrochromism of the WO$_3$: in fact, since the flat band of WO$_3$ at pH < 1 is located at positive potential (ca. 0.2 V vs SCE, in reasonable agreement with the photocurrent onset at 300 mV vs SCE), a certain amount of W^{5+} is created each time the cell is switched on at 0 V vs SCE, a potential at which light electron accumulation conditions in the oxide are established. W^{5+} is then reoxidized as the potential is increased towards more positive values.
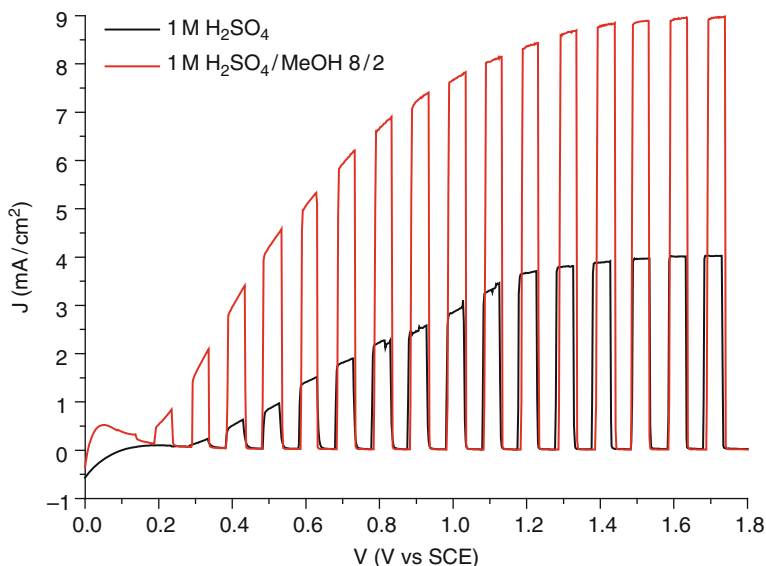
Fig. 53 Manually shuttered J–V curves in 1 M H_2SO_4 (*black*) and 1 M H_2SO_4/CH_3OH 8/2 (*red*). Incident irradiance 0.120 W/cm^2

Further evidence of effective charge transfer to the electrolyte, as well as of photocurrent doubling in the presence of methanol, which is a known hole scavenger, can be obtained from the J–V curves recorded under modulated (on/off) ~0.1 W/cm^2 intensity, in which the rectangular shape of the transients, the presence of small photoanodic transients in the immediate proximity of the flat band potential, and the lack of cathodic features are all indicative of efficient photoinduced charge separation and transport [74] (Fig. 53). The evolution of hydrogen from the cathode of the PEC can be visually assessed in the presence of photocurrents ≥1 mA/cm^2. Under such conditions it is easy to collect hydrogen in a pneumatic syringe and calculate the electrolysis yield ($R\%$) from the ratio of the moles of collected hydrogen and those theoretically predicted on the basis of the Faraday law. The rate of production of hydrogen in 1 M sulfuric acid can be calculated as 2 mL/(cm^2 h), which is nearly tripled in the presence of CH_3OH [~6 mL/(cm^2 h)], in agreement with the enhanced photocurrent and the higher electrolysis yield which approaches 100%. It must be noted that in the presence of MeOH, due to a decreased surface tension, the detachment of hydrogen bubbles from the Pt surface of the counter electrode was faster than in pure water/sulfuric acid, where at the end of the electrolysis bubbles were still observed to adhere to the platinum spiral.

The photocurrent spectrum (Fig. 54) recorded under monochromatic light under a potential bias of 1 V shows a maximum of 380 μA/cm^2 around 390 nm and its subtended area gives an integrated photocurrent in the order of 2.5 mA/cm^2, consistent with the photoanodic plateau observed under polychromatic light under 1 sun illumination.
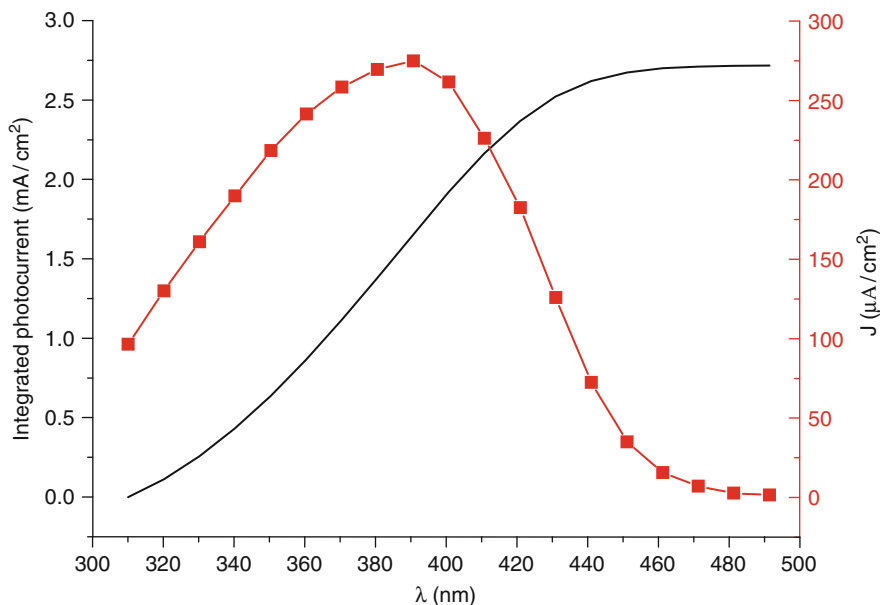
Fig. 54 Photocurrent spectrum of a typical anodically grown WO_3 film (*red*) and the relative integrated photocurrent (*black*). 1 M H_2SO_4, 1 V vs SCE
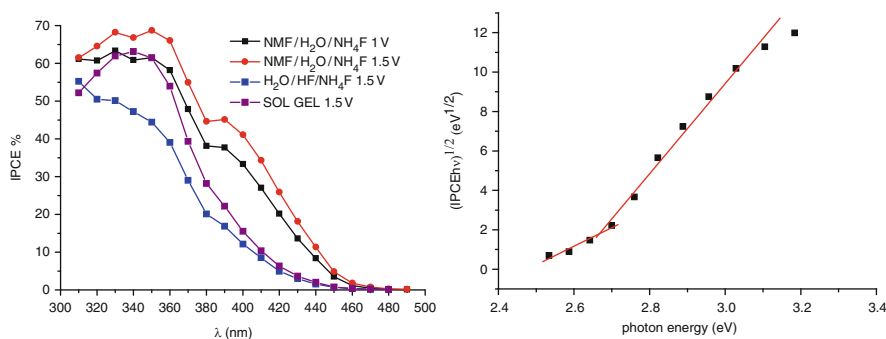
Fig. 55 *Left*: Photoaction spectra (IPCE vs λ) in 1 M H_2SO_4 of a WO_3 film grown in NMF under 1 V (*black*) and 1.5 V (*red*) potential bias, compared to a WO_3 substrate electrochemically formed in water (1.5 V) (*blue*) and to a nanocrystalline electrode produced by sol–gel methods (*violet*) (1.5 V). Voltage referred to SCE. Values not corrected for the transmittance of the electrochemical cell. *Right*: Band gap determination from the relation $(IPCE h\nu)^{1/2} = A(h\nu - E_g)$ where E_g is the band gap energy

The photocurrent action spectra (IPCE = number of electrons/number of incident photons) (Fig. 55) recorded in sulfuric acid indicate a high photon to current conversion, approaching 70% in a broad region in the UV and extending deeply into the visible region, thanks to a secondary maximum at 400 nm ($IPCE_{max} = 45\%$ at
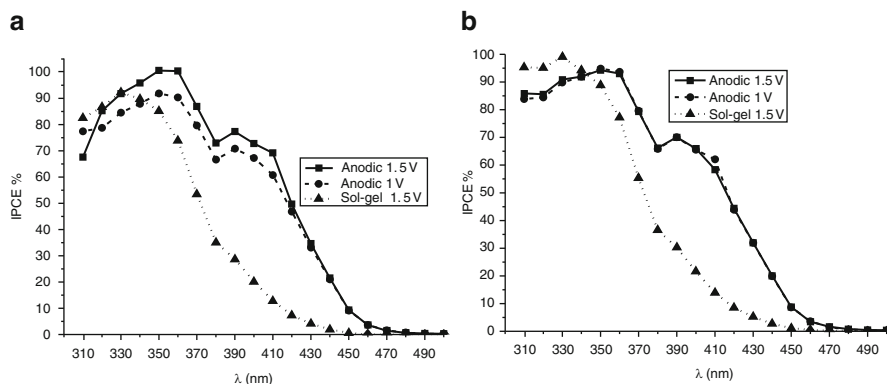
Fig. 56 Photoaction spectra of WO$_3$ in the presence of sacrificial electron donors: (**a**) 20% methanol in 1 M sulfuric acid; (**b**) 1 M formic acid/1 M sodium formate; *squares* and *circles*: anodically grown WO$_3$ films in the presence of a bias equal to, respectively, 1.5 and 1 V vs SCE compared to a sol/gel WO$_3$ film biased at 1.5 V vs SCE (*triangles*)

1.5 V vs SCE) whose onset is located at 490 nm. This leads to a calculated indirect band gap of 2.66 eV, which is significantly lower (by at least 0.15–0.3 eV) than values commonly reported for other nanostructured anodically grown WO$_3$ substrates and approaches those reported for monoclinic WO$_3$ films obtained by exploiting high vacuum technologies like thermal evaporation or radio frequency sputtering [75, 76]. As a comparison, WO$_3$ films electrochemically produced in water/HF/NH$_4$F according to a procedure described by Guo et al. or by sol gel methods do not show a relevant photoconversion beyond 430–440 nm.

The IPCE undergoes a significant enhancement in the presence of sacrificial hole scavengers like methanol or formic acid, reaching a value close to 100% in the UV region, where the light absorption is complete (Fig. 56). The secondary maximum nearly doubles in intensity, approaching values of the order of 80%. Since, to a first approximation, the presence of a scavenger cannot influence the charge transport through the solid phase to the interface, the observed increase in IPCE is most probably the result of a more facile charge (hole) transfer process to the electrolyte (expressed by the interfacial charge transfer efficiency term η_i). This also implies an almost unitary charge transport efficiency (η_{tr}) at the interface given that, at least in the UV region, APCE $= 1 = \eta_{tr}\,\eta_i$ [77] and that, in pure water, limitations in interfacial kinetics may eventually represent, in this case, the primary loss mechanism.

In fact, the impedance spectroscopy of the WO$_3$ photoanodes under strong illumination (ca. 0.3 W/cm^2) reveals that the photoelectrode is essentially dominated, in the complex plane, by a kinetic loop: the single semicircle with a maximum in the 1–10 Hz interval (depending on the potential) can be reasonably attributed to the charge transfer across the semiconductor–electrolyte interface (Fig. 57). It can be well fitted by a single $R(QR')$ equivalent circuit [78], where R is the ohmic contribution, Q is the constant phase element which takes into account

non-idealities in the capacitance of the Helmholtz layer, and R' is the charge transfer resistance. The inverse of the charge transfer resistance (cm^2/ohm) plotted as a function of the applied potential (Fig. 58) is in good agreement in both shape and magnitude with the derivative (slope) of the J–V curve, corroborating the correctness of our assignment. Moreover, as would be expected in the case of an
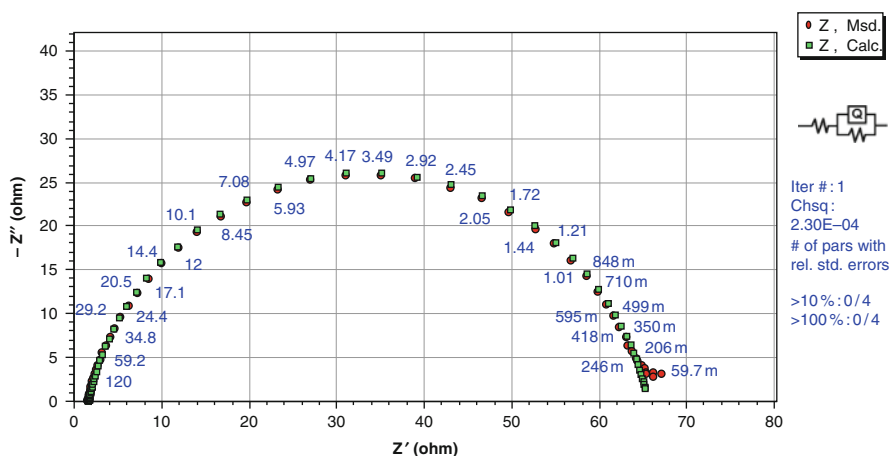
Fig. 57 Nyquist plot of an anodically grown WO$_3$ photoelectrode in 1 M H$_2$SO$_4$ at 0.7 V vs SCE. *Red dots* experimental data, *green dots* calculated. AM 1.5 G irradiation, 0.3 W/cm^2
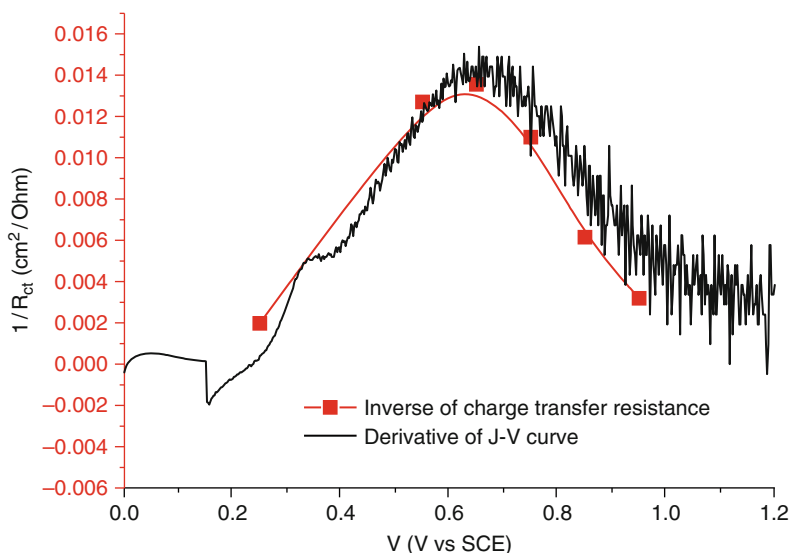
Fig. 58 Derivative of a typical J–V curve in 1 M H$_2$SO$_4$ compared with the inverse of the charge transfer resistance (*red*) obtained from fitting of EIS data a different applied potentials. 0.3 W/cm^2 AM1.5 G irradiation
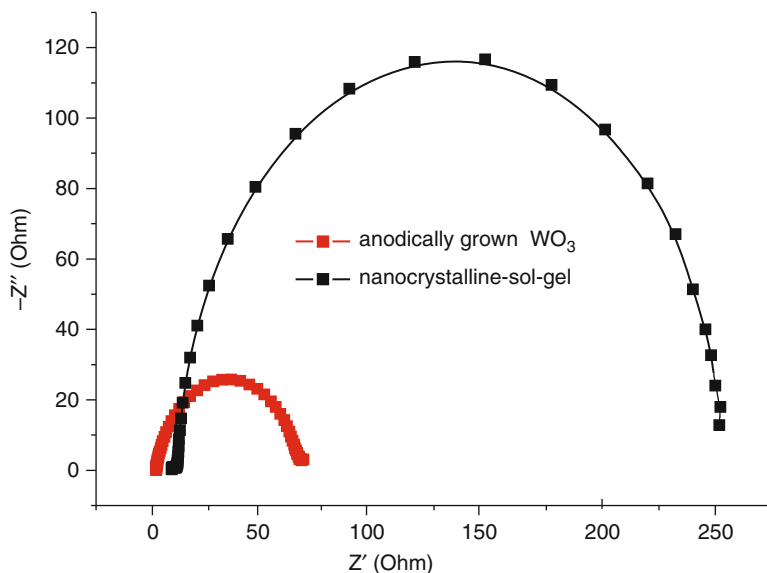
Fig. 59 Nyquist plot of anodically grown WO_3 (*red*) and nanocrystalline WO_3 (*black*) obtained from a sol–gel route (*black*) under 0.3 W/cm^2 AM 1.5 G illumination and 0.7 V vs SCE potential bias in 1 M H_2SO_4

interfacial process, the charge transfer resistance is dependent upon electrolyte composition, and decreases in the presence of methanol acting as an electron donor, confirming that, effectively, the observed impedance loop is originated by the hole transfer to the electrolyte. When compared to a sol–gel nanocrystalline WO_3 substrate sintered on FTO [79] (Fig. 59), the anodically grown substrate exhibits substantially decreased interfacial hole transfer resistance (64 vs 240 ohm) and lack of the small high frequency loop ($>10^4$ Hz) attributed to the FTO/WO_3 interface, suggesting an excellent ohmic contact with the metal electron collector. Besides its higher spectral sensitivity, both factors contribute to explain the good performance of the anodically grown WO_3 electrodes, when compared to more conventional WO_3 films obtained from sol–gel routes: a smaller charge transfer resistance can be particularly important under intense illumination, when, in order to sustain the photocurrent, large number of photogenerated minority charge carriers have to be injected efficiently into the electrolyte.

To conclude, the potentiostatic anodization of metallic tungsten in an appropriate electrolytic composition provides a simple wet electrochemical tool [80] to produce highly efficient WO_3 photoanodes, which, combining spectral sensitivity, highly electrochemically active surface, and improved charge transfer kinetics outperform, under simulated solar illumination, most of the reported nanocrystalline substrates produced by sol gel methods and are, at the very minimum, comparable to substrates produced with vacuum technologies (i.e., RF sputtering) recently reported in the literature.

References

1. Ni M, Leung MKH, Leung DYC, Sumathy K (2007) Renew Sustain Energy Rev 11:401
2. Lewis NS (2005) Inorg Chem 44:6900–6911
3. Eisenberg R, Nocera GD (2005) Inorg Chem 44:6799–6801
4. Nozik AJ, Memming RJ (1996) Phys Chem 100:13061–13078
5. Fujishima A, Honda K (1972) Nature 238:37
6. Maldonado S, Fitch AG, Lewis NS (2008) Nanostructured and photoelectrochemical systems for solar photon conversion. Imperial College Press, London
7. Sodergren S, Hagfeldt A, Olsson J, Lindquist S-E (1994) J Phys Chem 5552–5556
8. Gregg BA (2004) Coord Chem Rev 248:1215–1224
9. Gregg BA, Pichot F, Ferrere S, Fields CR (2001) J Phys Chem B 105:1422–1429
10. Kumar A, Santangelo PG, Lewis NS (1992) J Phys Chem 834–842
11. Fornarini L, Nozik AJ, Parkinson BAJ (1984) Phys Chem 88:3238–3243
12. Nozik AJ (1976) Appl Phys Lett 29:150–153
13. Kainthla RC, Zelenay B, Bockris JOMJ (1987) Electrochem Soc 134:841–845
14. Grimes CA, Varghese OK, Ranjan S (2008) Light, water, hydrogen. Springer, New York
15. Khaselev O, Turner JA (1998) Science 280:425–427
16. Concepcion JJ, Jurss JW, Brennaman MK, Hoertz PG, Patrocionio AOT, Murakami Iha NY, Templeton JL, Meyer TJ (2009) Acc Chem Res 42:1954–1965
17. Alstrum-Acevedo JH, Brennaman MK, Meyer TJ (2005) Inorg Chem 44:6802–6827
18. Liu F, Concepcion JJ, Jurss JW, Cardolaccia T, Templeton JL, Meyer TJ (2008) Inorg Chem 47:1727–1752
19. Jurss JW, Concepcion JJ, Norris MR, Templeton JL, Meyer TJ (2010) Inorg Chem 49:3980–3982
20. Concepcion JJ, Jurss JW, Norris MR, Chen Z, Templeton JL, Meyer TJ (2010) Inorg Chem 49:1277–1279
21. Brimblecombe R, Koo A, Dismukes CG, Swiegers GF, Spiccia LJ (2010) Am Chem Soc 132:2892–2864
22. Youngblood JW, Anna Lee S-H, Maeda K, Mallouk TE (2009) Acc Chem Res 42:1966–1973
23. Youngblood JM, Seung-Hyun AL, Kobayashi Y, Ernandez Pagan EA, Hoertz PG, Moore TA, Moore LA, Gust D, Mallouk TEJ (2009) Am Chem Soc 131:926–927
24. Caramori S, Cristino V, Argazzi R, Meda L, Bignozzi CA (2010) Inorg Chem 49:3320–3328
25. Balzani V, Juris A (1988) Coord Chem Rev 84:85–277
26. Kayes BM, Richardson CE, Lewis NS, Atwater HA (2005) IEEE Photo Spec Conf 55–58
27. Kayes BM, Atwater HA, Lewis NSJ (2005) Appl Phys 97(114302):1–11
28. Clarke J, Hill DR, Roberts JJ (1997) Chem Technol Biotechnol 68:397
29. Haginoya C, Ishibashi M, Koike K (1997) Appl Phys Lett 71:2934
30. Mor KG, Shankar K, Paulose M, Varghese OK, Grimes CA (2005) Nano Lett 5:191–195
31. Grimes CA, Mor GK (2009) TiO_2 nanotube arrays: synthesis, properties and applications. Springer, Dordrecht
32. Varghese OK, Gong D, Paulose M, Ong KG, Dickey EC, Grimes CA (2003) Adv Mater 15:624
33. Macack JM, Tsuchiya H, Schmucki P (2005) Angew Chem Int Ed 44:2100–2102
34. Mor GK, Varghese OK, Paulose M, Shankar K, Grimes CA (2006) Solar Energy Mater Solar Cells 90:2011–2075
35. Paulose M, Shankar K, Yoriya S, Prakasam EH, Varghese OK, Mor GK, Latempa TA, Fitzgerald A, Grimes CA (2006) J Phys Chem B Lett 110:16179–16184
36. Zaban A, Greenshtein M, Bisquert J (2003) ChemPhysChem 4:859–864

37. Kamat PV (2007) J Phys Chem C 111:2834–2860
38. Robel I, Subramanian V, Kuno M, Kamat PVJ (2006) Am Chem Soc 128:2385–2393
39. Gopidas KR, Bohorquez M, Kamat PVJ (1990) Phys Chem 94:6435–6440
40. Bessekhuad Y, Mohammedi M, Trari M (2002) Solar Energy Mater Solar Cells 73:339–350
41. Ortuno-Lopez MB, Sotelo-Lerma M, Mendoza-Galvan A, Ramirez-Bon R (2004) Vacuum 76:181–184
42. Blackburn JL, Selmarten DC, Nozik AJJ (2003) Phys Chem B 107:14154–14157
43. Boyle DS, O'Brien P, Otway DJ, Robbe OJ (1999) Mater Chem 9:725–729
44. Baranski AS, Fawcett WR, McDonald AC, De Nobriga RM, MacDonald AC (1981) J Electrochem Soc Electrochem Sci Technol 128:963–968
45. Raevskaya AE, Stroyuk AL, Kuchmiy SY (2006) J Colloid Interface Sci 302:133–141
46. Cocivera M, Darkowski A, Love BJ (1984) Electrochem Soc 131:2514–2517
47. Bessekhuad Y, Robert D, Weber JVJ (2004) Photochem Photobiol A Chem 163:569–580
48. Liu D, Kamat PVJ (1993) Phys Chem 97:10769–10773
49. Medles M, Benramdane N, Bouzidi A, Nakrela A, Nakrela A, Tabet-Derraz H, Kebbab Z, Mathieu C, Khelifa B, Desfeux R (2006) Thin Solid Films 497:58–64
50. Ahire RR, Deshpande NG, Gudage YG, Sagade AA, Chavhan SD, Phase DM, Sharma R (2007) Sensor Actuators A 140:207–214
51. Bao H, Cui X, Ming Li C, Gan Y, Zhang J, Guo J (2007) J Phys Chem C 111:12279–12283
52. Spurgeon JM, Atwater HA, Lewis NS (2008) J Phys Chem C 112:6186–6193
53. Sun W-T, Yu Y, Pan H-Y, Gao X-F, Chen Q, Peng L-MJ (2008) Am Chem Soc 130:1124–1125
54. Kale RB, Lokhande CD (2005) J Phys Chem B 109:20288–20294
55. Soloviev VN, Eichhofer A, Fenske D, Banin UJ (2000) Am Chem Soc 122:2673–2674
56. Tena-Zaera R, Katty A, Bastside S, Lévy-Clément C (2007) Chem Mater 19:1626–1632
57. Hodes G, Manassen J, Cahen DJ (1980) Am Chem Soc 102:5964
58. Szabo JP, Cociviera MJ (1987) Appl Phys 61:4820
59. Seabold JA, Shankar K, Wilke RHT, Paulose M, Varghese OK, Grimes CA, Choi K-S (2008) Chem Mater 20:5266–5273
60. Reichmann B, Bard AJJ (1979) Electrochem Soc 126:586
61. Bellac DL, Azens A, Granqvist CG (1995) Appl Phys Lett 1715–1176
62. Niklasson GA, Klasson J, Olson E (2001) Electrochim Acta 46:1967
63. Pennisi A, Simone F, Lampert CM (1992) Solar Energy Mater Solar Cells 28:233–247
64. Wang H, Lindgren T, He J, Hagfeldt A, Lindquist S-E (2000) J Phys Chem B 104:5686–5696
65. Santato C, Odziemkowski M, Ulmann M, Augustynski JJ (2001) Am Chem Soc 123:10639–10649
66. Santato C, Ulmann M, Augustynski J (2001) J Phys Chem B 105:936–940
67. Finlayson AP, Glowacki BA (2006) Proc SPIE 6340:L1–L10
68. Bard AJ, Park JH (2006) Electrochem Solid State Lett 9:E5–E8
69. Metikos-Hukovic M, Grubac Z (2003) J Electroanal Chem 556:167–178
70. Yoshioka H, Habazaki H, Kawashima I, Asami K, Hashimoto K (1991) Corros Sci 32:313
71. Hahn R, Macak JM, Schmuki P (2007) Electrochem Commun 9:947–952
72. Guo Y, Quan X, Huimin Zao NL, Chen S (2007) Environ Sci Technol 41:4422–4427
73. Berger S, Tsuchiya H, Ghicov A, Schmucki P (2006) Appl Phys Lett 88:203119–203121
74. Sivula K, Zboril R, Le Formal F, Robert R, Weidenkaff A, Tucek J, Frydrych J, Graetzel M (2010) J Am Chem Soc 132:7436–7444
75. Gillet M, Aguir K, Lemire C, Gillet E, Schierbaum K (2004) Thin Solid Films 467:239–246
76. Ottaviano L, Lozzi L, Passacantando M, Santucci S (2001) Surf Sci 475:73–82
77. Chen Z, Jaramillo TF, Deutsch TG, Shwarscstein AK, Forman AJ, Gaillard N, Garland R, Takanabe K, Heske C, Sunkara M, McFarland EW, Domen K, Miller EL, Turner JA, Dinh HNJ (2010) Mater Res 25:3–16
78. Wang Q, Moser J-E, Graetzel M (2005) J Phys Chem B 109:14945–14953
79. Meda L, Tozzola G, Tacca A, Marra GL, Caramori S, Cristino V, Bignozzi CA (2010) Solar Energy Mater Solar Cells 94:788–796
80. Cristino V, Caramori S, Argazzi R, Meda L, Marra GL, Bignozzi CA (2011) Langmuir (in press)

Surface Nanostructures in Photocatalysts for Visible-Light-Driven Water Splitting

Kazuhiko Maeda and Kazunari Domen

Abstract Overall water splitting to form hydrogen and oxygen over a heterogeneous (particulate) photocatalyst with solar energy is a promising process for clean and recyclable hydrogen production on a large-scale. In recent years, numerous attempts have been made for the development of photocatalysts that work under visible-light to utilize solar energy efficiently. This chapter describes recent research progress on heterogeneous photocatalysis for water splitting with visible light, particularly focusing on the development of nanostructured cocatalysts made by the authors' group.

Contents

K. Maeda (✉) and K. Domen
Department of Chemical System Engineering, The University of Tokyo, 7-3-1 Hongo, Bunkyo-ku,
Tokyo 113-8656, Japan
e-mail: kmaeda@chemsys.t.u-tokyo.ac.jp; domen@chemsys.t.u-tokyo.ac.jp

1 Introduction

Hydrogen has attracted considerable interest as a clean and renewable energy carrier offering both high-energy capacity and minimal environmental impact. Large-scale hydrogen production using solar energy is therefore an ultimate goal for the supply of clean and renewable energy, and several types of reaction schemes have been proposed [1–4]. Direct overall water splitting to form hydrogen and oxygen using a particulate photocatalyst is one of the most promising candidates, and is also potentially applicable over a wide area. The first step in the development of a technology that makes efficient use of solar energy is the discovery of a photocatalyst that becomes highly active under visible light ($\lambda > 400$ nm). Extensive efforts have already been made in the search for such a material [5–8], and some have achieved overall water splitting, although the quantum efficiency still remains low.

Our group has recently reported the discovery and refinement of a new material for stable overall water splitting under visible light – a solid solution of GaN and ZnO that is expressed as $(Ga_{1-x}Zn_x)(N_{1-x}O_x)$ [9–29]. Both GaN and ZnO are well-known III–V and II–VI semiconductors that have been the target of extensive research as functional materials in light-emitting diodes and laser diodes [30–32]. As shown in Fig. 1, the $(Ga_{1-x}Zn_x)(N_{1-x}O_x)$ solid solution possesses a wurtzite crystal structure similar to GaN and ZnO, and is typically synthesized by nitriding a mixture of Ga_2O_3 and ZnO powders. As both GaN and ZnO have band-gap energies of greater than 3 eV, neither can absorb visible light in the pure form. Interestingly, however, the solid solution $(Ga_{1-x}Zn_x)(N_{1-x}O_x)$ has a band gap smaller than 3 eV and a steep absorption onset in the visible region. As shown in Fig. 2, the band-gap energy (light absorption edge) is dependent on the compositional parameter (x) that is controllable by modifying the preparation parameters, and the decrease in band-gap energy in the solid solution is due to the electronic behavior of the constituent Zn and O species [19, 33, 34].

As shown in Fig. 3, overall water splitting on a semiconductor photocatalyst occurs in three steps: (1) the photocatalyst absorbs photon energy greater than the
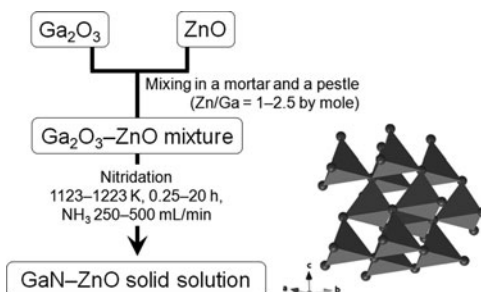
Fig. 1 Preparation scheme of a GaN–ZnO solid solution with its crystal structure

Fig. 2 UV–visible diffuse reflectance spectra for $(Ga_{1-x}Zn_x)(N_{1-x}O_x)$ with various compositions (x)
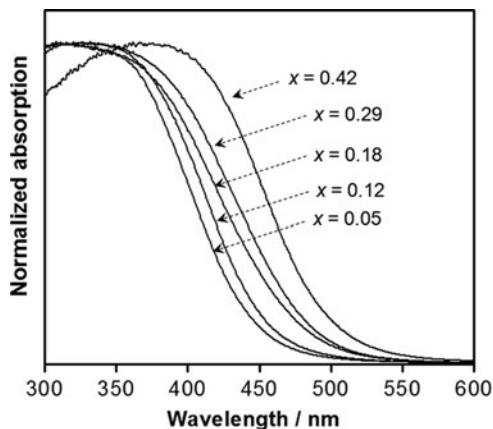
Fig. 3 Processes involved in photocatalytic overall water splitting on a heterogeneous photocatalyst. E_g indicates the band gap energy of a given photocatalyst
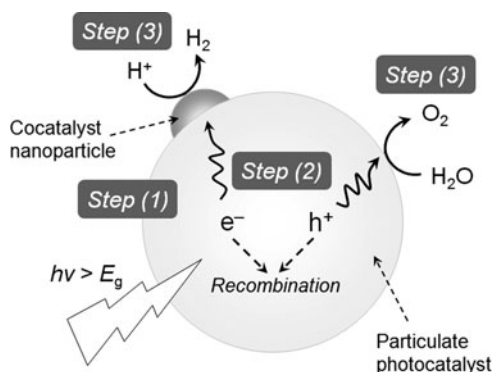
band gap energy of the material and generates photoexcited electron–hole pairs in the bulk, (2) the photoexcited carriers separate and migrate to the surface without recombination, and (3) adsorbed species are reduced and oxidized by the photogenerated electrons and holes to produce H_2 and O_2, respectively. The first two steps are strongly dependent on the structural and electronic properties of the photocatalyst. In general, high crystallinity has a positive effect on activity, since the density of defects, which act as recombination centers between photogenerated carriers, decreases with increasing crystallinity. The third step, on the other hand, is promoted by the presence of a solid cocatalyst. The cocatalyst is typically a noble metal (e.g., Pt, Rh) or transition metal oxide (e.g., NiO_x, RuO_2) and is loaded onto the photocatalyst surface as a dispersion of nanoparticles to produce active sites and reduce the activation energy for gas evolution. It is thus important to design both the bulk and surface properties of the material carefully so as to obtain high photocatalytic activity for this reaction.

For $(Ga_{1-x}Zn_x)(N_{1-x}O_x)$, much effort has been devoted to improve the preparation method that allows one to produce high-quality $(Ga_{1-x}Zn_x)(N_{1-x}O_x)$ samples [10, 20, 22, 24, 28]. Although the preparation conditions of $(Ga_{1-x}Zn_x)(N_{1-x}O_x)$ have been shown to be critically important for obtaining enhanced photocatalytic activity, the activity of this photocatalyst can also be improved significantly by loading a proper cocatalyst. In this chapter, therefore, we would like to focus on nanostructured cocatalysts loaded on the $(Ga_{1-x}Zn_x)(N_{1-x}O_x)$ surface. In the following sections we start with some basic aspects of cocatalysts for photocatalytic water splitting and then introduce new types of cocatalysts that have recently been developed by our group. For simplicity, $(Ga_{1-x}Zn_x)(N_{1-x}O_x)$ will be referred to as "GaN:ZnO" hereafter.

2   General Role of Cocatalysts in Photocatalytic Water Splitting

Figure 4 shows a schematic illustration of a photocatalyst loaded with a cocatalyst, where the H_2 evolution reaction process is assumed. It is believed that the loaded cocatalysts play the roles of extracting photogenerated electrons from the photocatalyst (process 1) and of hosting active sites for gas evolution (process 2). Therefore, the overall efficiency of a given photocatalytic system is dependent on the loaded cocatalyst. In particular, structural characteristics and the intrinsic catalytic property for hydrogen (or oxygen) evolution are important factors. For example, Pt is well known as an excellent catalyst for reduction of protons to give hydrogen molecules. However, a photocatalyst loaded with Pt cocatalyst does not always exhibit the highest activity among analogs loaded with other metals (e.g., Ru and Rh). This is the evidence that the contribution of process (1) to the overall efficiency is more important than that of process (2). For example, Ru-loaded TaON exhibits higher activity for H_2 evolution from aqueous alcohol solution than Pt-loaded TaON [35]. Although it has been reported that various factors (e.g., band edge potential [36] and work function [37] of the photocatalyst and the loaded
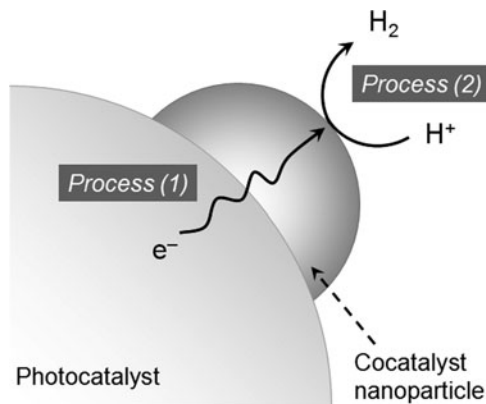
Fig. 4 A schematic illustration of the electron transfer from a photocatalyst to the loaded cocatalyst (*Process 1*) and H_2 evolution (*Process 2*) in overall water splitting

species) affect the efficiency of process (1), none have yielded a systematic understanding. Anyway, one has to consider both process (1) and (2) when designing a more efficient photocatalytic system.

3   Preparation of a Cocatalyst/Photocatalyst Composite

As shown in Fig. 5, there are two representative methods for introducing cocatalysts onto a semiconductor photocatalyst. One is an impregnation method, where proper precursor species are impregnated with a photocatalyst, followed by thermal annealing at a given condition to produce a desired form of cocatalyst. In this method there are a lot of choices of precursors and solvents for the impregnation procedure as well as final treatment conditions. This kind of loading method is well known in the field of heterogeneous catalysis. The other is an in situ photochemical deposition method, originally developed by Bard and Kraeutler who demonstrated that nanoparticles of metals (e.g., Pt, Pd) can be prepared by irradiation of aqueous solution containing semiconductor powder (e.g., TiO_2, WO_3), metal ions, and an electron donor [38]. Metal cations with appropriate redox potentials can be reduced by electrons generated through the photoexcitation of a semiconductor powder. Such photochemical deposition has been studied extensively over the past 30 years for applications in photocatalysis [39–41], catalysis [42–44], the recovery of noble metals [45], and the removal of heavy metals from waste water [46].

In general, photocatalytic activity of a given material (cocatalyst/photocatalyst composite) for water splitting is dependent on the loading method of cocatalysts, as it determines the physicochemical characteristics of the loaded cocatalyst
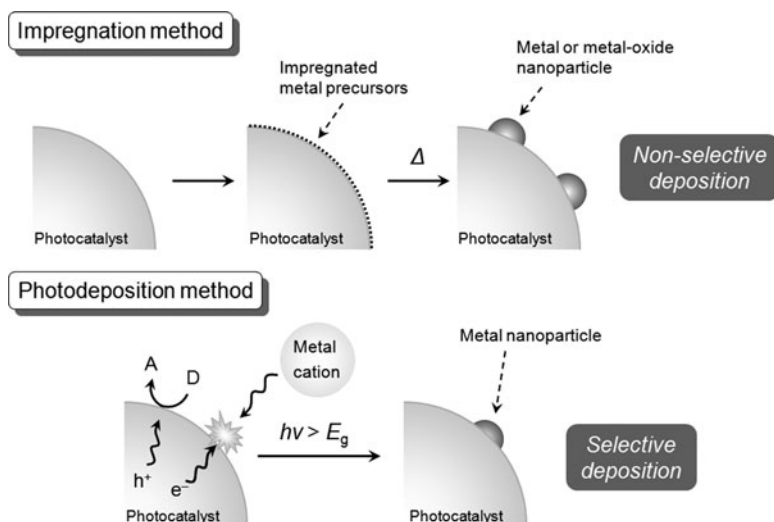

Fig. 5 Schematic illustrations of an impregnation and a photodeposition method

(e.g., valence state and dispersion). It is a general trend in heterogeneous (photo) catalysis that highly dispersed nanoparticles contribute to increasing the rate of catalytic reactions, and an excess loading leads to lowering catalytic activity. In the case of photocatalysis, excessively loaded cocatalysts hinder light absorption by the base photocatalyst and can also work as recombination centers for photogenerated electrons and holes. Accordingly, there is a volcano-type trend between the loading amount of a given cocatalyst and the activity in most cases (regardless of the kind of preparation method, the base photocatalyst, and the loaded cocatalyst). Therefore, refinement of the preparation condition that allows for optimal distribution of cocatalysts on a photocatalyst is an important aim to construct a highly efficient photocatalytic system for overall water splitting.

4 Nanoparticulate Mixed Oxides as New Cocatalysts

4.1 Motivation for Applying Mixed-Oxides as Cocatalysts

Although some of the photocatalysts developed to date (e.g., layered compounds and tantalates) can decompose water without a cocatalyst [7], most require the loading of a suitable cocatalyst (such as NiO_x and RuO_2) to obtain a high activity and reasonable reaction rates. It is believed that the cocatalysts provide reaction sites and decrease the activation energy for gas evolution. Noble metals such as Pt and Rh are excellent promoters for H_2 evolution, but can also catalyze a backward reaction, forming water from H_2 and O_2, limiting their usefulness as cocatalysts for photocatalytic overall water splitting. To avoid the backward reaction, transition metal oxides that do not exhibit activity for water formation from H_2 and O_2 are usually applied as cocatalysts for overall water splitting. However, no cocatalyst more effective than NiO_x or RuO_2 had been found, until recently.

Our group has previously reported that the photocatalytic activity of Ni-loaded $K_2La_2Ti_3O_{10}$ for overall water splitting is improved by coloading with Cr, while modification with Cr alone did not result in appreciable evolution of H_2 or O_2 [47]. This result suggests that the increase in activity is attributable to interaction between Ni and Cr in the cocatalyst, motivating further investigation of Cr as a cocatalyst in combination with other transition metals [13–16].

The cocatalyst, a combination of Cr and one other metal component, was loaded onto the as-prepared GaN:ZnO by a co-impregnation method. In a typical preparation, the co-impregnation was performed by suspending 0.3–0.4 g of the photocatalyst powder in an aqueous solution containing an appropriate amount of Cr $(NO_3)_3 \cdot 9H_2O$ and the nitrate or chloride of the paired metal. The solution was then evaporated to dryness over a water bath followed by calcination in air at 623 K for 1 h. In the case of Ni or Ni–Cr cocatalysts, the impregnated catalyst was reduced by exposure to H_2 (20 kPa) at 573 K for 2 h and then oxidized by exposure to O_2 (10 kPa) at 473 K for 1 h in a closed gas circulation system to produce an Ni/NiO (core/shell) double structure [48].

Table 1 lists the photocatalytic activities of GaN:ZnO loaded with Cr and another transition metal for overall water splitting under UV irradiation ($\lambda > 300$ nm), along with data for samples loaded with just one transition metal. Although loading the cocatalysts by this method is expected to produce the oxide form, the cocatalyst components are simply referred to here by the respective transition metal. The photocatalytic activity of the transition metal-loaded catalysts was markedly improved by coloading with Cr. All of the examples except for the Ag–Cr system achieved stoichiometric evolution of H_2 and O_2 from pure water. The photocatalytic activity of GaN:ZnO loaded with Cr and a transition metal was found to be strongly dependent on the amount of loaded Cr. Taking Ni–Cr and Rh–Cr systems for example, the activities increased with Cr content to a maximum at a certain loading amount, above which the activity decreased. The highest activities were obtained at 0.125 wt% Cr with 1.25 wt% Ni, and 1.5 wt% Cr with 1 wt% Rh. These results suggest that the optimal Cr loading differs according to the coloaded transition metal, and it is expected that a similar enhancement of photocatalytic activity will be realized by other transition metal/Cr combinations as cocatalysts for GaN:ZnO, because the loading amount of Cr in Table 1 may not be optimal except for Ni–Cr and Rh–Cr systems. The improvement in activity is attributed to the formation of suitable reaction sites by intimate interaction between Cr and the paired metal component. The largest improvement in activity was obtained by loading the base catalysts with a combination of 1 wt% Rh and 1.5 wt% Cr. The activity of this catalyst system was two orders of magnitude higher than for the catalysts loaded with 1 wt% Rh under the same reaction conditions. It should be noted that even though loading with Fe, Co, Cu, Pd, or Ag alone did not activate the GaN:ZnO catalyst for overall water splitting (see Table 1), coloading with Cr and one of these

Table 1 Photocatalytic activities of GaN:ZnO loaded with a transition metal oxide and Cr oxide for overall water splitting under UV irradiation ($\lambda > 300$ nm)[a]

Entry	Cocatalyst		Activity/μmol h^{-1}		Coloading amount of Cr/wt%	Activity of coloaded catalysts/μmol h^{-1}	
	Element[b]	Loading amount/wt%	H_2	O_2		H_2	O_2
1	None		0	0			
2	Cr	1.0	0	0			
3	Fe	1.0	0	0	1.0	73	36
4	Co	1.0	2.0	0	1.0	48	24
5	Ni	1.25	126	57	0.125	685	336
6	Cu	1.0	2.0	0	1.0	585	292
7	Ru	1.0	71	27	0.1	181	84
8	Rh	1.0	50	1.6	1.5	3,835	1,988
9	Pd	1.0	1.0	0	0.1	205	96
10	Ag	1.0	0	0	1.0	11	2.3
11	Ir	1.5	9.3	3.1	0.1	41	17
12	Pt	1.0	0.9	0.4	1.0	775	357

[a]Catalyst (0.3 g); distilled water (370–400 mL); light source, high-pressure mercury lamp (450 W); inner irradiation-type reaction vessel made of Pyrex

[b]Transition metal species are expressed as metallic form for simplicity

Fig. 6 A typical HR-TEM
image of GaN:ZnO loaded
with $Rh_{2-y}Cr_yO_3$ cocatalyst
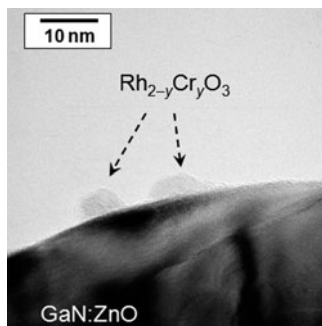
inactive metal components resulted in measurable photocatalytically activity. Coloading Cr is considered to facilitate charge transfer from the GaN:ZnO bulk to the cocatalyst, and/or promote the creation of catalytic gas evolution sites on the cocatalyst surface.

Scanning electron microcopy (SEM), high-resolution transmission electron microscopy (HR-TEM), energy dispersive X-ray spectroscopy (EDS), X-ray photo-electron spectroscopy (XPS), and X-ray absorption fine-structure spectroscopy (XAFS) analyses confirmed that the loaded Rh and Cr species interact to form mixed-oxide ($Rh_{2-y}Cr_yO_3$) nanoparticles of 10–30 nm in size with a trivalent electronic state [16]. A typical HR-TEM image of $Rh_{2-y}Cr_yO_3$/GaN:ZnO is shown in Fig. 6. The photocatalytic performance of the $Rh_{2-y}Cr_yO_3$-loaded GaN:ZnO is strongly dependent on the pH of the reactant solution [15], as in the case of RuO_2-loaded GaN:ZnO [9]. The photocatalyst exhibits stable and high photocatalytic activity in an aqueous solution at pH 4.5 for as long as 3 days. The photocatalytic performance at pH 3.0 and pH 6.2 is much lower, attributable to corrosion of the cocatalyst and hydrolysis of the catalyst. It has also been confirmed by XRD, XPS, and XAFS that the crystal structure of the catalyst and the valence state of both the surface and bulk do not change even after reaction for 3 days at optimal pH (4.5).

4.2 Unique Property of $Rh_{2-y}Cr_yO_3$ Cocatalyst for Photocatalytic Overall Water Splitting

The performance of the $Rh_{2-y}Cr_yO_3$ catalyst for overall water splitting is an order of magnitude higher than that obtained by the previously optimized catalyst consisting of a conventional RuO_2 cocatalyst, giving an apparent quantum yield of ~5% at 410 nm under the optimal preparation and reaction condition. To investigate the origin of the higher activity of the $Rh_{2-y}Cr_yO_3$ catalyst, the photocatalytic activity of $Rh_{2-y}Cr_yO_3$/GaN:ZnO for H_2 or O_2 evolution from aqueous solutions containing methanol and silver nitrate was examined. For comparison, the same experiments were carried out using an RuO_2-loaded sample. The reactions using sacrificial reagents are not "overall" water splitting reactions, but are often carried out as

Fig. 7 Basic principle of photocatalytic reactions in the presence of sacrificial reagents
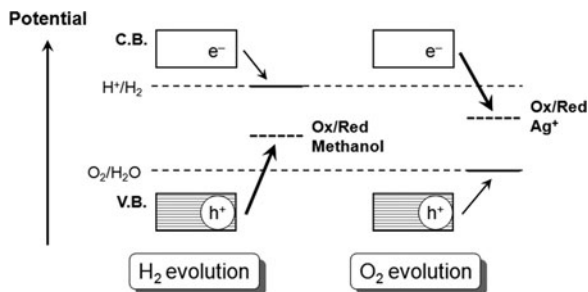
Table 2 Photocatalytic activities of GaN:ZnO loaded with various cocatalysts at various reaction conditions under visible light ($\lambda > 400$ nm)[a]

Entry	Cocatalyst	Reactant solution	Activity/μmol·h^{-1}	
			H$_2$	O$_2$
1	None	10 vol.% MeOH aq.	0	–
2	Rh$_{2-y}$Cr$_y$O$_3$	10 vol.% MeOH aq.	358	–
3	RuO$_2$	10 vol.% MeOH aq.	35	–
4	Rh[b]	10 vol.% MeOH aq.	280	–
5	None	0.01 M AgNO$_3$ aq.	–	548
6	Rh$_{2-y}$Cr$_y$O$_3$	0.01 M AgNO$_3$ aq.	–	307
7	RuO$_2$	0.01 M AgNO$_3$ aq.	–	597
8	Rh$_{2-y}$Cr$_y$O$_3$	H$_2$SO$_4$ (pH 4.5)	264	132
9	Rh$_{2-y}$Cr$_y$O$_3$	HNO$_3$ (pH 4.5)	255	127
10	Rh$_{2-y}$Cr$_y$O$_3$	HCl (pH 4.5)	166	83
11	RuO$_2$	H$_2$SO$_4$ (pH 3.0)	58	29
12	RuO$_2$	HNO$_3$ (pH 3.0)	6.7	24
13	RuO$_2$	HCl (pH 3.0)	60	30

[a]Catalyst (0.3 g); reactant solution (370–400 mL); light source, high-pressure mercury lamp (450 W); inner irradiation-type reaction vessel made of Pyrex with aqueous NaNO$_2$ solution (2 M) filter
[b]0.25 wt% loaded by an in situ photodeposition method

test reactions for overall water splitting [6, 7]. The basic principle of photocatalytic reactions using sacrificial reagents is depicted schematically in Fig. 7. When the photocatalytic reaction is conducted in the presence of an electron donor such as methanol, photogenerated holes in the valence band irreversibly oxidize methanol instead of H$_2$O, thus facilitating water reduction by conduction-band electrons if the bottom of the conduction band of the photocatalyst is located at a more negative potential than the water reduction potential. On the other hand, in the presence of an electron acceptor such as silver cations, photogenerated electrons in the conduction band irreversibly reduce electron accepters instead of H$^+$, thereby promoting water oxidation by valence-band holes if the top of the valence band of the photocatalyst is positioned at a more positive level than the water oxidation potential.

The photocatalytic activities of loaded and unloaded GaN:ZnO in the presence of sacrificial reagents under visible light irradiation ($\lambda > 400$ nm) are summarized in Table 2. GaN:ZnO alone exhibited no activity for H$_2$ evolution even in the

presence of methanol as a sacrificial electron donor (Entry 1). H_2 evolution was observed after modification with $Rh_{2-y}Cr_yO_3$ (Entry 2) and RuO_2 nanoparticles (Entry 3). Rh-loaded GaN:ZnO also evolved H_2 from an aqueous methanol solution (Entry 4). It is thus clear that the loaded $Rh_{2-y}Cr_yO_3$ and RuO_2 nanoparticles have the same function as Rh that is a well-known H_2 evolution cocatalyst, and that GaN: ZnO itself can oxidize methanol on its surface, but does not possess an H_2 evolution site. Accordingly, loading of cocatalysts that work as an H_2 evolution site is indispensable for achieving the H_2 evolution by GaN:ZnO. The rate of H_2 evolution observed on the $Rh_{2-y}Cr_yO_3$-loaded sample (Entry 2) was ten times higher than that achieved on the RuO_2-loaded sample (Entry 3), indicating that the $Rh_{2-y}Cr_yO_3$ cocatalyst functions more efficiently as a H_2 evolution site. In contrast, GaN:ZnO displayed the activity for O_2 evolution from an aqueous silver nitrate solution without modification (Entry 5), whereas the $Rh_{2-y}Cr_yO_3$-loaded sample achieved lower O_2 evolution than the bare sample (Entry 6). Interestingly, the RuO_2-loaded sample exhibited slightly higher activity for O_2 evolution from an aqueous silver nitrate solution compared to the bare sample (Entry 7). In this case, it appears that RuO_2 nanoparticles on the GaN:ZnO have some positive effect on the O_2 evolution reaction, presumably due to the functionality as a water oxidation catalyst [49, 50].

On the basis of these results, it is most likely that the $Rh_{2-y}Cr_yO_3$ loaded on the GaN:ZnO catalyst functions not as an O_2 evolution site but rather as a H_2 evolution site. Considering the inactivity of bare GaN:ZnO for H_2 evolution and appreciable activity for O_2 evolution in the presence of sacrificial reagents, the relatively slow step for overall water splitting on GaN:ZnO is considered to be the water reduction process. Therefore, one of the reasons for the improvement in photocatalytic activity achieved by loading the GaN:ZnO catalyst with $Rh_{2-y}Cr_yO_3$ is the promotion of the H_2 evolution reaction, that is, an increase in the activity of the rate-determining step for overall water splitting.

The reaction behavior was also dependent on pH-adjusting reagents [23]. Table 2 also lists the rates of H_2 and O_2 evolution (average over 5 h) in overall water splitting using $Rh_{2-y}Cr_yO_3$- and RuO_2-loaded GaN:ZnO under visible light ($\lambda > 400$ nm) from various aqueous solutions. The pH of the solutions was adjusted by the reagent shown. As mentioned earlier, the optimal reaction pH for overall water splitting is 4.5 for $Rh_{2-y}Cr_yO_3$-loaded GaN:ZnO and 3.0 for the RuO_2-loaded catalyst (when adjusted with H_2SO_4) [15], with both catalysts exhibiting steady and stoichiometric H_2 and O_2 evolution [9]. The present reactions were therefore carried out at these respective pH levels. The $Rh_{2-y}Cr_yO_3$-loaded GaN:ZnO produced H_2 and O_2 steadily and stoichiometrically (i.e., overall water splitting) regardless of the pH-adjusting reagent employed. Almost identical activity was obtained when the pH was adjusted using H_2SO_4 (Entry 8) and HNO_3 (Entry 9). However, the use of HCl as the pH-adjusting reagent resulted in an approximately 60% drop in activity (Entry 10) compared to the reactions performed using H_2SO_4 (Entry 8) or HNO_3 (Entry 9). In contrast, RuO_2-loaded GaN:ZnO displayed almost the same activity in aqueous HCl solution (Entry 13) as in aqueous H_2SO_4 solution (Entry 11), although stoichiometric H_2 and O_2 evolution was not achieved over any period of reaction when the reaction pH was adjusted using HNO_3 (Entry 12). As mentioned earlier,

the higher activity of $Rh_{2-y}Cr_yO_3$-loaded GaN:ZnO in aqueous H_2SO_4 solution compared to the RuO_2-loaded catalyst is attributable to the superior H_2 evolution ability of $Rh_{2-y}Cr_yO_3$. It was thus found that the photocatalytic activity of GaN:ZnO for overall water splitting is dependent not only on the cocatalyst employed but also on the reagent used to adjust the pH.

These characteristic gas evolution properties can be explained in terms of the different reactivities of each catalyst with respect to redox-active species in the aqueous solution. Inorganic ions can react with photogenerated electrons and/or holes on photocatalysts, thereby inhibiting the efficiency of overall water splitting, which is primarily dependent on the redox potential of ions and the band-edge positions of the photocatalyst. Photoelectrochemical measurements using a porous GaN:ZnO anode suggest that the bottom of the conduction band of GaN:ZnO lies at ca. -0.92 V vs NHE (at pH 4.5) [51]. Accordingly, electrons photogenerated in the conduction band of GaN:ZnO are unable to reduce SO_4^{2-} to SO_3^{2-} thermodynamically, since the thermodynamic reduction potential of SO_4^{2-} (SO_4^{2-}/SO_3^{2-}, -1.22 V vs NHE at pH 4.5) is more negative than the conduction band bottom of GaN:ZnO [52]. Therefore, the reduction of SO_4^{2-} by GaN:ZnO does not take place.

NO_3^-, which is more susceptible to reduction than H^+ (NO_3^-/NO_2^-, $+0.54$ V; H^+/H_2, -0.27 V vs NHE at pH 4.5) [52], can compete with the reduction of H^+ by conduction-band electrons, thereby lowering the overall water splitting activity. It has been reported that NO_3^- can be catalytically reduced during the water splitting reaction when using a semiconductor photocatalyst [53]. The non-stoichiometric evolution of H_2 and O_2 by the RuO_2-loaded catalyst in HNO_3 solution (Entry 12) is thus attributable to the competition between the reduction of NO_3^- and the reduction of H^+ to H_2. Analysis of the reactant solution by ion chromatography indicates that NO_2^- and NH_3 are generated as reaction products in the reaction over RuO_2-loaded GaN:ZnO. In contrast, the reduction of NO_3^- does not appear to occur over the $Rh_{2-y}Cr_yO_3$-loaded catalyst, as indicated by the similarity of the overall water splitting activity for the HNO_3 (Entry 9) and H_2SO_4 (Entry 8) solutions and the stoichiometric ratio of H_2 to O_2 evolution achieved using this system. It was also confirmed that the H_2/O_2 evolution ratio remains stoichiometric even in the presence of 10 mM NO_3^- (pH 4.5), although the absolute rates of gas evolution are 10–15% lower. This result indicates that the photoreduction of NO_3^- over $Rh_{2-y}Cr_yO_3$-loaded GaN:ZnO proceeds very slowly compared to the reduction of H^+.

Another difference between these two catalysts is the drop in activity of $Rh_{2-y}Cr_yO_3$-loaded GaN:ZnO in HCl-adjusted solution (Entry 10), whereas the activity of the RuO_2-loaded catalyst using HCl (Entry 13) remained similar to that of the H_2SO_4-adjusted solution (Entries 11 and 13). Chloride ions in the reactant solution thus appear to have a negative effect on the activity of $Rh_{2-y}Cr_yO_3$-loaded GaN:ZnO, but not on the RuO_2-loaded catalyst. In the case of $Rh_{2-y}Cr_yO_3$-loaded GaN:ZnO, water reduction takes place on $Rh_{2-y}Cr_yO_3$ nanoparticles and oxidation occurs on GaN:ZnO, as mentioned earlier. Although the oxidation of Cl^- is thermodynamically more difficult than the oxidation of H_2O (Cl_2/Cl^-, 1.39 V; O_2/H_2O, 0.96 V vs NHE at pH 4.5) [52], the photooxidation of Cl^- to Cl_2 involves a relatively simple two-electron redox process and is thus likely to

proceed more readily than the photooxidation of H_2O to O_2, which involves a complex four-electron redox process. If Cl_2 is produced as a result of the photooxidation of Cl^- in photocatalytic overall water splitting, the ratio of H_2 to O_2 evolution should become larger than that expected from the stoichiometry (i.e., $H_2/O_2 = 2$) at the normal rate of H_2 evolution. However, the ratio of H_2 to O_2 evolution over $Rh_{2-y}Cr_yO_3$-loaded GaN:ZnO in aqueous HCl solution satisfies the stoichiometry (Entry 10), with the rates of both H_2 and O_2 evolution obviously lower than in the H_2SO_4-adjusted solution (Entry 8). The concentration of HCl in the solution (pH 4.5) is approximately 0.03 mM, corresponding to 12 μmol Cl^-. Assuming that all of the Cl^- in the solution undergoes oxidation to produce Cl_2, the maximum rate of Cl_2 production is only 1.2 μmol·h^{-1} (average over 5 h), which is much lower than the observed rate of O_2 evolution. Competitive Cl_2 production therefore does not appear to affect the rate of O_2 evolution. The stoichiometry of the H_2/O_2 ratio would thus be maintained even if the photooxidation of Cl^- proceeds in this system. Given this situation, the suppression of the rates of H_2 and O_2 evolution in the HCl-adjusted solution indicates that solved Cl^- in the reactant solution hinders not only water oxidation but also water reduction. Although the detailed action of Cl^- in this reaction is not well understood, one possible explanation is the reduction by photogenerated electrons of intermediates produced by the photooxidation of Cl^-. Such a process would result in lower water reduction activity, and explains the simultaneous suppression of the rates of both H_2 and O_2 evolution while maintaining stoichiometry. There are some reports describing a negative effect of Cl^- on photocatalytic oxidation of organic compounds, which are claimed to be attributable to hindrance of active sites in the catalyst surface by adsorption of Cl^- [54, 55]. In contrast, the fact that the activity of RuO_2-loaded GaN:ZnO in an aqueous HCl solution is almost the same (Entry 13) as that in an aqueous H_2SO_4 solution (Entry 11) indicates that there is no negative effect of Cl^-, and implies that oxidation of Cl^- does not take place on this catalyst. RuO_2 is well known as a good oxidation catalyst for O_2 evolution. In the case of water splitting, RuO_2 has been demonstrated by many researchers to be effective as an oxidation site for the evolution of O_2 [49, 50]. In the GaN:ZnO, however, the primary role of nanoparticulate RuO_2 is to provide catalytic active sites for H_2 evolution, as mentioned earlier [15]. It therefore appears that nanoparticulate RuO_2 functions as both an H_2 evolution site and an efficient O_2 evolution site in the presence of Cl^-. This is also supported by the results of photocatalytic reactions using sacrificial reagents.

4.3 Effect of Gases in the Reaction System on Activity

It is known that gaseous oxygen can suppress water splitting over a photocatalyst, as exemplified by NiO-loaded $SrTiO_3$ [56], Pt-loaded TiO_2 [57], and ZrO_2 [58]. This is because oxygen molecules can act as an electron acceptor that reacts with photogenerated electrons in the conduction band of a photocatalyst. The

thus-reduced O_2 species (e.g., $\cdot O_2{}^-$) are presumably oxidized by the valence band holes, thereby lowering the utilization efficiency of photogenerated charge carriers for water splitting. This phenomenon is known as photoreduction of oxygen.

To investigate the possibility of O_2-photoreduction, overall water splitting reactions were conducted using GaN:ZnO modified with RuO_2 or $Rh_{2-y}Cr_yO_3$ nanoparticles in the presence of various gases. In advance, it was confirmed that water formation from H_2 and O_2 does not occur on these catalysts. As shown in Fig. 8, the introduction of Ar gas (30 kPa) into the reaction system before irradiation suppressed the photocatalytic activity of the RuO_2-loaded sample by about 30%, which can be explained as due to the effect of gas pressure. The introduction of O_2 gas (30 kPa) had an even more pronounced suppression effect. It is thus clear that the activity of the RuO_2-loaded sample is suppressed by the effects of gas pressure and O_2, suggesting that photoreduction of O_2 occurred on the RuO_2-loaded sample during the overall water splitting reaction. In contrast, the photocatalytic activity of the $Rh_{2-y}Cr_yO_3$-loaded sample remained largely unchanged with respect to gas pressure and gas composition, indicating that O_2-photoreduction on this sample is negligibly slow, which should contribute to the higher activity of the $Rh_{2-y}Cr_yO_3$-loaded sample than the RuO_2 sample. The inertness of $Rh_{2-y}Cr_yO_3$-loaded GaN:ZnO for the photoreduction of O_2 also suggests that the catalyst is suitable for use at atmospheric pressure. In fact, gas evolution from the reactant suspension dispersed
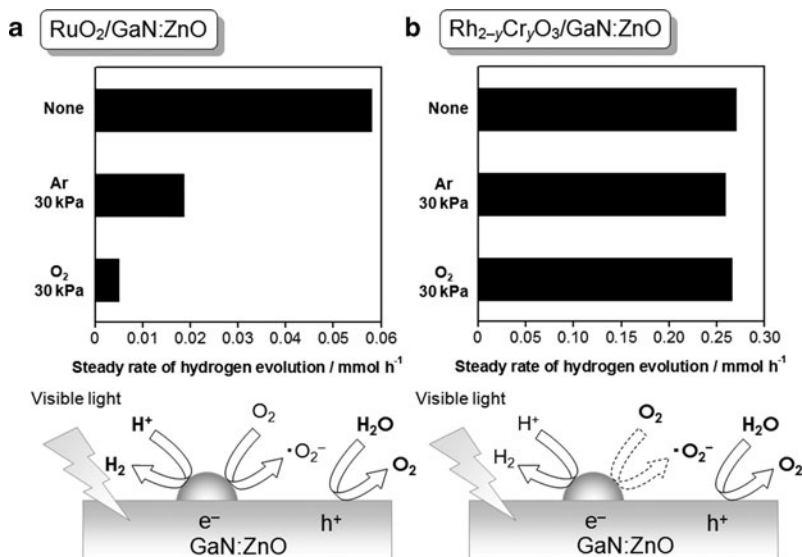
Fig. 8 Effect of gases in the reaction system on photocatalytic activity of (**a**) RuO_2- and (**b**) $Rh_{2-y}Cr_yO_3$-loaded GaN:ZnO for overall water splitting under visible light ($\lambda > 400$ nm), with schematic illustrations of reaction mechanism for each system. Catalyst (0.3 g); an aqueous H_2SO_4 solution adjusted at pH 3.0 for RuO_2-loaded sample and at pH 4.5 for $Rh_{2-y}Cr_yO_3$-loaded sample (370 mL); light source, high-pressure mercury lamp (450 W); inner irradiation-type reaction vessel made of Pyrex with an aqueous $NaNO_2$ solution (2 M) filter

with $Rh_{2-y}Cr_yO_3$-loaded GaN:ZnO powder was observable as bubbles at atmospheric pressure under irradiation by a high-pressure mercury lamp via Pyrex glass, as reported previously [13]. This is a very useful property for the purpose of practical application.

5 Noble Metal/Chromia (Core/Shell) Nanoparticles

5.1 Initial Concept for Designing Core/Shell-Structured Nanoparticles as Cocatalysts

A noble metal in general functions as an efficient cocatalyst for H_2 evolution due to the high exchange current density and low overvoltage for the H_2 evolution reaction. However, it also catalyzes water formation from H_2 and O_2, limiting its usefulness as a cocatalyst for overall water splitting on a particulate photocatalyst [59]. Several approaches have been taken in attempts to solve this problem. Sayama and Arakawa [57] and Abe et al. [60] reported that water formation on a Pt-loaded TiO_2 catalyst during overall water splitting is suppressed by conducting the reaction in Na_2CO_3 or NaI aqueous solution.

At that time, we thought that the reverse reaction would be suppressed if nanoparticulate noble metal cocatalysts could be coated by a certain shell, forming a core/shell-like configuration, as shown in Fig. 9. More specifically, it was expected that the access of H_2 and O_2 molecules to the noble metal core would be suppressed upon such a shell coating. As such a shell component, we paid attention to Cr_2O_3 that has been reported to function as catalyst for some hydrogen-related reactions (e.g., (de)hydration) [61, 62] and to be deposited through photochemical reduction process from Cr(VI) species as the precursor. Photoreduction of Cr(VI) ions over
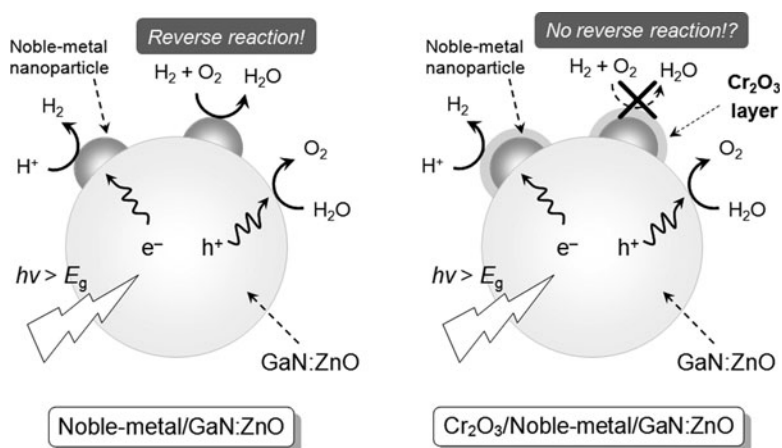

Fig. 9 Initial concept for designing a core/shell-structured noble-metal/Cr_2O_3 cocatalyst

a photocatalyst has been reported by several researchers as a potential method for detoxification of hexavalent chromium species in environmental water [63]. The thermodynamic potential for the reduction of Cr(VI) into Cr(III) is more positive than that for water reduction, meaning that reductive deposition of Cr(III) species onto noble metals is possible when a photocatalyst having band gap positions suitable for water splitting is employed.

5.2 Preparation, Characterization, and Functionality

Preparation of noble metal/Cr_2O_3 (core/shell) nanostructures on GaN:ZnO was conducted through a stepwise photodeposition under oxygen-free conditions [17, 18]. The scheme is shown in Fig. 10. First, noble metal nanoparticles were deposited using a proper metal salt complex under band gap irradiation of GaN:ZnO ($\lambda > 400$ nm). The as-prepared noble metal/GaN:ZnO sample was then treated with K_2CrO_4 in a similar manner. The final product was washed thoroughly with distilled water and dried overnight at 343 K.

Figure 11 shows TEM images of GaN:ZnO loaded with Rh nanoparticles followed by treatment with K_2CrO_4 and visible light. The primary particle size of the introduced Rh nanoparticles is 2–3 nm, although some of them aggregate to form larger secondary particles. On the other hand, the HR-TEM images of the samples after K_2CrO_4 treatment show that the noble metal nanoparticles have been coated with a shell layer about 2 nm thick to form a core/shell nanostructure. Although some of them form large agglomerates, the shell thickness is almost constant (ca. 2 nm). The same phenomenon was observed regardless of the kind of the noble metal nanoparticle and the size of such nanoparticles. Examining over 50 particles irradiated with visible light in an aqueous K_2CrO_4 solution showed that all the particles had a core/shell structure. In the case of Rh as the core, it was confirmed by XAFS and XPS that the core and the shell consist of metallic Rh and Cr_2O_3, respectively.
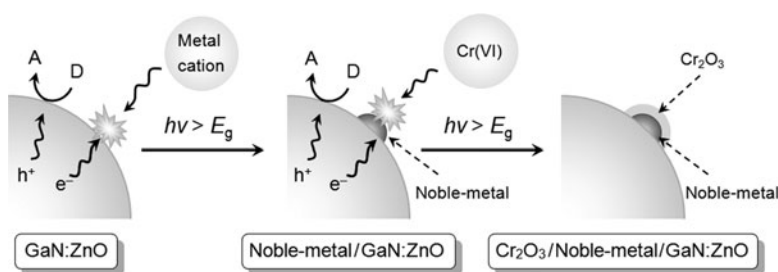
Fig. 10 A schematic illustration of the preparation of noble-metal/Cr_2O_3 (core/shell) nanoparticles through a stepwise deposition of metal cations and Cr(VI) ions (E_g represents the band gap energy of GaN:ZnO, while D and A indicate electron donor and acceptor, respectively)
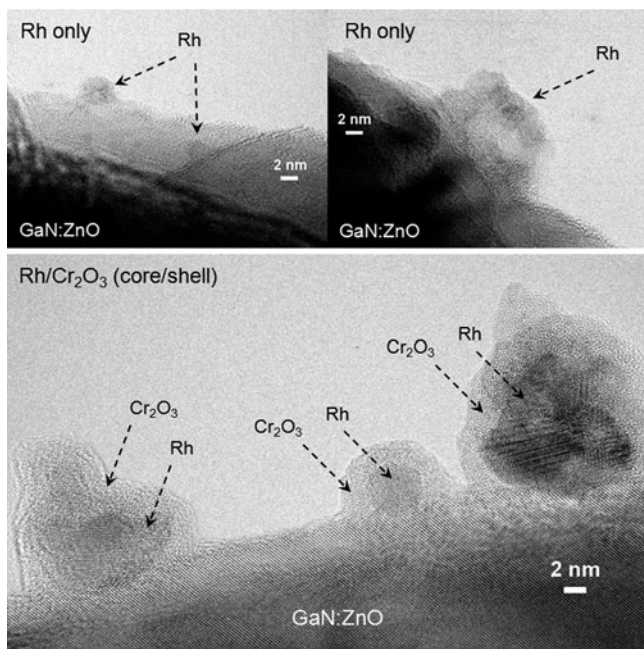
Fig. 11 HR-TEM images of GaN:ZnO loaded with photodeposited Rh and Rh/Cr$_2$O$_3$ (core/shell) nanoparticles

Figure 12 shows water splitting activity of some GaN:ZnO samples under visible light ($\lambda > 400$ nm), with schematic illustrations. Rh-loaded GaN:ZnO exhibited little photocatalytic activity for overall water splitting even for extended periods of irradiation, most likely due to rapid water formation on Rh nanoparticles [59]. However, GaN:ZnO loaded with the Rh-core/Cr$_2$O$_3$-shell cocatalyst exhibited stoichiometric H$_2$ and O$_2$ evolution from pure water, indicating the occurrence of overall water splitting. Addition of the Rh-loaded catalyst to the reactant suspension containing the Rh/Cr$_2$O$_3$-loaded catalyst, however, resulted in a marked decrease in the rates of both H$_2$ and O$_2$ evolution. It is thus clear that water formation from H$_2$ and O$_2$ on unmodified Rh nanoparticles is significant in the overall water splitting reaction, and that the suppression of water formation is essential for achieving efficient evolution of H$_2$ and O$_2$ in this system. It was confirmed that the use of other noble metals, such as Pd and Pt, as a core with the Cr$_2$O$_3$ shell in the same manner achieves the same function as observed here for Rh.

The thickness of the Cr$_2$O$_3$ shell could be controlled by changing the initial concentration of K$_2$CrO$_4$ in the preparation process, although the precise control remained a challenge [18]. With increasing the K$_2$CrO$_4$ concentration, the shell thickness became thicker and more homogeneous and the water splitting rate was enhanced. After the thickness reached ca. 2 nm, further shell deposition did not occur and the activity was saturated. The thickness of the Cr$_2$O$_3$ shell was also dependent on the pH of the solution in which the photoreduction of K$_2$CrO$_4$ was
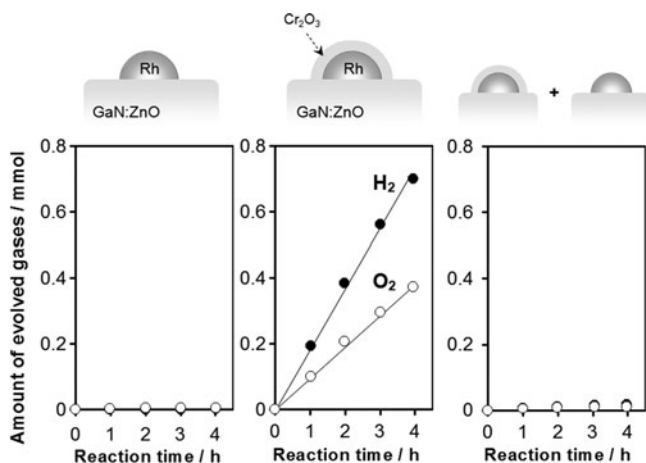
Fig. 12 Time courses and schematic illustrations of overall water splitting under visible light ($\lambda >$ 400 nm) using modified GaN:ZnO samples. Catalyst (0.15 g); distilled water (370 mL); light source, high-pressure mercury lamp (450 W); inner irradiation-type reaction vessel made of Pyrex with an aqueous $NaNO_2$ solution filter. For the reaction data shown in the right panel, a mixture of 0.15 g of the Rh/Cr_2O_3 (core/shell) loaded catalyst and 0.15 g of a sample loaded with only Rh was used

conducted [27]. As a result, the water splitting activity of samples prepared at different pH were different. When the deposition pH ranged from 3.0 to 7.5, there was almost no change in activity, and stoichiometric H_2 and O_2 were produced under visible light. As the pH decreased from 3.0 to 2.0, however, the rates of H_2 and O_2 evolution both decreased significantly. TEM observations showed that, in the Rh-photodeposited GaN:ZnO treated with K_2CrO_4 and visible light at pH 2.0, almost no core/shell-like structure could be identified, in contrast to the sample treated at pH 7.5. At pH below 3.0, the photoreduction of Cr(VI) ions did occur, judging from the fact that the yellow color of the initial solution, which was due to K_2CrO_4, disappeared completely, and turned a faint dark-blue, the typical color of Cr(III) sulfate. At this pH condition, the Cr(III) ions could not precipitate as Cr(III) hydroxide or oxide. Therefore, a relatively neutral pH is a better choice when coating nanoparticulate cores with Cr_2O_3 shells.

It is very important to understand the reaction mechanism at the nanometer scale in order to design better photocatalytic systems. The mechanism of hydrogen evolution on core/shell-structured nanoparticles was therefore investigated using electrochemical and in situ spectroscopic measurements of model electrodes that consisted of Rh and Pt plates with electrochemically deposited 1.8- to 3.5-nm-thick Cr_2O_3 [64]. For both Cr_2O_3-coated and bare electrodes, proton adsorption/desorption and H_2 evolution currents were observed, and an infrared absorption band assigned to Pt-H stretching was apparent. Therefore, the Cr_2O_3 layer did not interfere with proton reduction or hydrogen evolution, and proton reduction took place at the Cr_2O_3/Pt interface. However, the reduction of oxygen to water was suppressed only in the Cr_2O_3-coated samples. It was concluded that the Cr_2O_3 layer

Fig. 13 A schematic illustration of H_2 evolution on core/shell-structured nanoparticles (with a noble metal core and a Cr_2O_3 shell) as a cocatalyst for photocatalytic overall water splitting
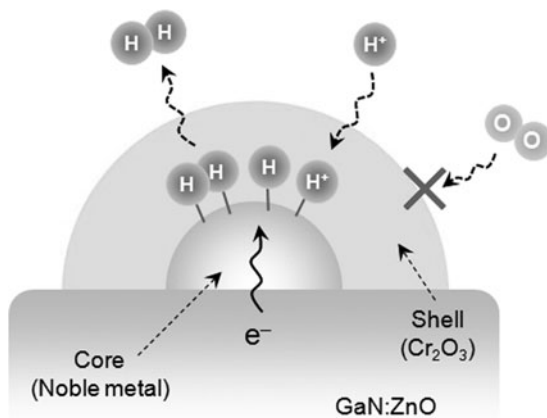
is permeable to protons and evolved hydrogen molecules, but not to oxygen. The reaction mechanism of H_2 evolution on core/shell-structured nanoparticles (with a noble metal or metal oxide core and a Cr_2O_3 shell) in photocatalytic overall water splitting is illustrated in Fig. 13.

5.3 Reason for the Successful Preparation of the Core/Shell Structure

Since CrO_4^{2-} is a strong oxidizing reagent [52], it had been expected that the anions would act as efficient electron acceptors to facilitate O_2 evolution on the GaN:ZnO catalyst (Fig. 7). However, when bare GaN:ZnO was used instead of the Rh-loaded sample, no appreciable O_2 evolution was detected in aqueous K_2CrO_4 solution. On the other hand, appreciable O_2 evolution as well as H_2 evolution was observed when Rh/GaN:ZnO was reacted in the presence of K_2CrO_4, indicating the occurrence of overall water splitting. These results indicate that no catalytic active sites are available for the reduction of CrO_4^{2-} anions on the bare GaN:ZnO surface, and that Rh nanoparticles are the active sites for reduction of CrO_4^{2-} anions.

GaN:ZnO exhibits relatively high photocatalytic activity for water oxidation in the presence of Ag^+ cations as an electron acceptor [21], indicating that electrons photogenerated in the conduction band of GaN:ZnO can efficiently reduce Ag^+ cations. It is thus of interest that GaN:ZnO is unable to reduce CrO_4^{2-} anions even though, thermodynamically, CrO_4^{2-} anions are more readily reduced than Ag^+ cations (Cr^{6+}/Cr^{3+}, 1.33 V; Ag^+/Ag, 0.8 V vs NHE) [52]. To clarify the origin of the inactivity for CrO_4^{2-} reduction by GaN:ZnO, the adsorption of K_2CrO_4 on the GaN:ZnO surface under conditions similar to that of the photocatalytic reaction was examined [18]. However, no adsorption was observed at K_2CrO_4 concentrations lower than ca. 0.4 mM, which is the preparation condition of the core/shell-structured nanoparticles. It has been reported that the adsorption of CrO_4^{2-} anions

on a photocatalyst is essential for achieving the reduction of CrO_4^{2-} anions [65], as this process requires direct electron transfer from the photocatalyst to CrO_4^{2-}. Therefore, reduction of CrO_4^{2-} anions onto the GaN:ZnO surface will be unable to take place due to the lack of adsorption sites, contributing to the successful preparation of Rh/Cr_2O_3 (core/shell) nanoparticles on the GaN:ZnO.

Another noticeable feature of this Rh/Cr_2O_3 (core/shell) system is that Cr_2O_3 shell deposition only occurs up to a thickness of ca. 2 nm, and is independent of the Rh core size [18]. The reason for the inhibition of CrO_4^{2-} reduction onto Cr_2O_3 shells of more than 2 nm thickness remains unclear, and the detailed mechanism by which the Cr_2O_3 shell is formed is complex and requires further investigation. One possible explanation for the self-limiting nature of the Cr_2O_3 shell formation is the difference in reduction process between Cr^{6+}/Cr^{3+} and H^+/H_2. It appears that the photoreduction of Cr^{6+} into Cr^{3+} involving a complex three-electron redox process [66] is more difficult to achieve than kinetically simpler processes, such as H^+ reduction. Bard et al. reported that electron tunneling can take place across an electrochemically passivated oxide layer with a thickness of 0.5–2.5 nm on a Cr electrode, and the tunneling electron transfer is hindered as the thickness of the passivated oxide layer increases [67]. The same tendency has been observed in an Rh/Cr_2O_3 model electrode system [64]. It is therefore considered that the present electron penetration through the Cr_2O_3 shell is due to such a tunneling electron transfer phenomenon, but the efficiency of electron transfer from the Rh core to the external surface of Cr_2O_3 shell decreases with increasing the thickness of the Cr_2O_3 shell. As a result, with increasing the thickness of Cr_2O_3 shell, the reduction of CrO_4^{2-} into Cr_2O_3, involving three-electron transfer, would be difficult to achieve. Finally, when the thickness of Cr_2O_3 shell reaches about 2 nm, the reduction of CrO_4^{2-} ceased and the H_2 evolution as a result of H^+ reduction proceeded preferentially.

5.4 Enhancement of Activity of the Noble Metal/Cr_2O_3 Core/Shell System by Improving the Dispersion of the Core Component

Among the noble metals examined as nanoparticulate cores, Rh was the most effective for enhancing activity. However, in the original preparation method, the Rh-based nanoparticles tended to aggregate on the catalyst [17, 18]. As the activity of a catalytic system is, in general, dependent on the surface area available for reaction, the activity of this system should improve further if aggregation of the cocatalyst nanoparticles can be prevented. Therefore, attempting to increase the dispersion of cocatalysts in a given system is a reasonable strategy for improving the photocatalytic activity.

Highly dispersed Rh nanoparticles were successfully loaded on GaN:ZnO without aggregation by adsorbing Rh nanoparticles that were stabilized by 3-mercapto-1-propanesulfuric acid (prepared by a liquid-phase reduction method) onto GaN:
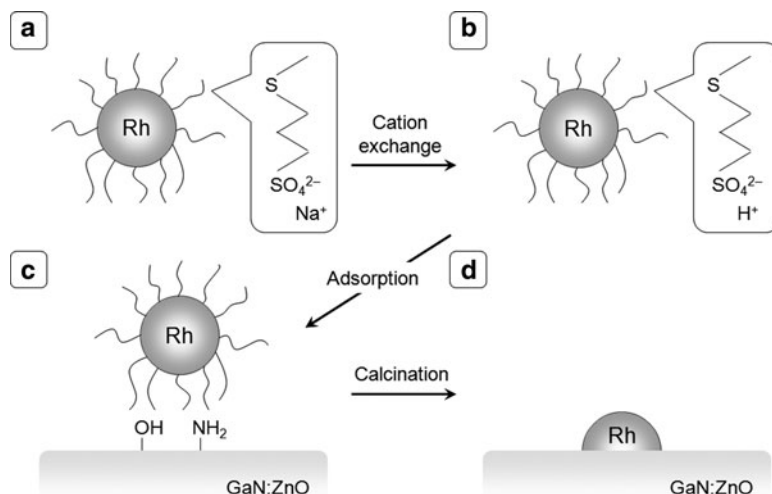
Fig. 14 Procedural flow of proposed LPR-based method. (**a**) Rh nanoparticles are stabilized by organic ligand molecules before cation exchange. (**b**) Stabilized Rh nanoparticles after cation exchange. (**c**) Electrostatic adsorption on GaN:ZnO catalyst. (**d**) Removal of organic ligand
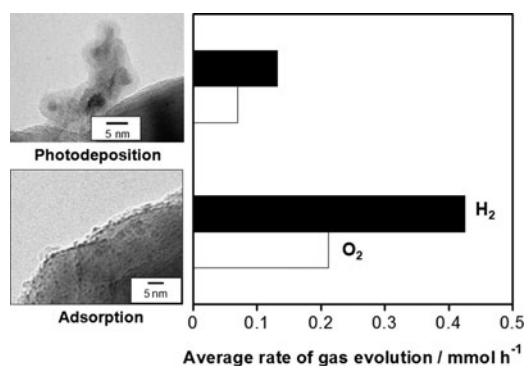
Fig. 15 Rates of H_2 and O_2 evolution under visible light ($\lambda > 400$ nm) over Cr_2O_3/Rh/GaN:ZnO prepared by the adsorption method, and the previous photodeposition method. Almost the same amount of Rh (0.3–0.4 wt%) is loaded on each catalyst. Catalyst (0.15 g); distilled water (400 mL); light source, high-pressure mercury lamp (450 W); inner irradiation-type reaction vessel made of Pyrex with an aqueous $NaNO_2$ solution (2 M) filter

ZnO, followed by calcination under vacuum at 673 K for 30 min [26]. The scheme of introducing highly dispersed Rh nanoparticles onto the surface of GaN:ZnO is shown in Fig. 14. The average size of these Rh nanoparticles was calculated to be 1.9 ± 0.6 nm, approximately one-fourth the size of particles prepared by photodeposition. After the Rh nanoparticles were coated with a Cr_2O_3-shell, the photocatalytic activity for overall water splitting was tested under visible-light irradiation.

Figure 15 displays the rates of H_2 and O_2 evolution over GaN:ZnO modified with the as-prepared highly dispersed Rh nanoparticles and Cr_2O_3 shell under visible

Fig. 16 Dependence of the rates of H_2 and O_2 evolution under visible light ($\lambda > 400$ nm) over Cr_2O_3/Rh/GaN:ZnO on the amount of Rh added in the preparation. The amount of loaded Rh is also shown. Catalyst (0.15 g); distilled water (400 mL); light source, high-pressure mercury lamp (450 W); inner irradiation-type reaction vessel made of Pyrex with an aqueous $NaNO_2$ solution (2 M) filter
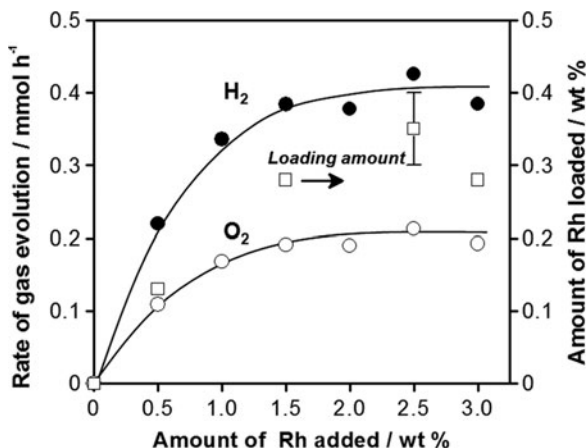
light, with the HR-TEM image of the catalyst. As expected, the sample with a better dispersion of Rh exhibited activity three times higher than an analog containing poorly dispersed Rh nanoparticles. This follows the general trend in heterogeneous (photo)catalysis; highly dispersed catalytic species generally provide higher reaction rates. It is also noted that the activity increased with the amount of Rh added, with the maximum activity obtained with Rh addition of 45 μmol (1.5 wt%) or higher, as shown in Fig. 16. The saturation behavior observed with Rh additions higher than 45 μmol (1.5 wt%) suggests that adsorption–desorption equilibrium is achieved in the preparation procedure. In fact, it was confirmed by inductively coupled plasma atomic emission spectroscopy (ICP-AES) analysis that the actual loading amount of Rh remains unchanged (0.3–0.4 wt%) at addition levels higher than 45 μmol (1.5 wt%). Therefore, during the loading process, Rh nanoparticles stabilized by organic ligands are introduced onto GaN:ZnO via adsorption–desorption. Specifically, hydrogen bonding and/or acid–base interaction between sulfonic acid groups on the Rh nanoparticles and surface hydroxyl and amino groups on the GaN:ZnO both play important roles. XPS analysis for GaN:ZnO suggested that the material possesses N–H groups on the surface [10]. Therefore, it is reasonable to presume that sulfonic acid groups on the Rh nanoparticles interact with hydroxyl and/or amino groups on the GaN:ZnO surface via hydrogen bonding and/or acid–base interaction. This idea is further supported by the observation that sulfonate-terminated Rh nanoparticles do not adsorb onto GaN:ZnO. As a result, the amount of Rh thus introduced onto the surface of GaN:ZnO is limited to a certain level.

5.5 Application of Cr_2O_3-Modification to Metal Oxide Core Systems

It was thus found that the "core/shell" strategy is promising for noble-metal/photocatalyst systems to allow for H_2 and O_2 evolution from water, because H_2–O_2 recombination is effectively suppressed by Cr_2O_3 shell surrounding noble

metals. Although this functionality is essential for a noble metal loaded photocatalyst to achieve overall water splitting [17, 18], it is not necessarily required for metal oxide loaded photocatalysts because metal oxide cocatalysts generally exhibit negligible catalytic activity for water formation [15]. In some cases, however, metal oxide cocatalysts sometimes undergo degradation due to a change in the cocatalyst state by exposure to the reactant solution, and catalyze O_2-photoreduction (another backward reaction of water splitting), which leads to a decrease in activity [15, 68]. Some examples were also shown in early sections. When the loaded metal oxide nanoparticles are covered with Cr_2O_3, this deactivation and O_2-photoreduction should be suppressed by a reduced accessibility of the loaded metal oxides to the reactants. This idea stimulated our investigation of the activity of a metal oxide-loaded photocatalyst modified with Cr_2O_3 photodeposits for overall water splitting.

Three metal oxide/photocatalyst systems (GaN:ZnO loaded with NiO_x, Rh_2O_3, and RuO_2) are briefly introduced here to demonstrate the effectiveness of Cr_2O_3-modification toward the enhancement of water splitting rate [27]. It has been pointed out that the activity of NiO_x-loaded photocatalyst for overall water splitting can be degraded in some cases because of the hydrolysis of NiO_x into $Ni(OH)_2$ and/or peeling off [68]. Actually, the rates of H_2 and O_2 evolution over NiO_x-loaded GaN:ZnO were decreased with reaction time. Interestingly, however, modification of NiO_x/GaN:ZnO with Cr_2O_3 resulted in suppressing deactivation, yielding stable H_2 and O_2 evolution with enhanced rates, although uniform deposition of Cr_2O_3 shell, as observed in noble metal/Cr_2O_3 systems, was not observed. In the case of Rh_2O_3 cocatalyst, while the deposition of this cocatalyst onto GaN:ZnO did not lead to any activity for water splitting, Cr_2O_3/Rh_2O_3/GaN:ZnO produced measurable amounts of H_2 and O_2 with a stoichiometric ratio. Experimental results showed that the enhancement of activity by Cr_2O_3-modification is attributed to the suppression of O_2-photoreduction. A similar activity enhancement was also observed for Cr_2O_3-modified RuO_2-loaded GaN:ZnO that was demonstrated to catalyze O_2-photoreduction (Fig. 8).

Thus, photodeposition of Cr_2O_3 was shown to be an effective approach to improve the activity for overall water splitting under visible light. Suppressing undesirable chemical changes of a cocatalyst and/or O_2 photoreduction is likely to contribute to this enhanced photocatalytic activity. Therefore, Cr_2O_3 photodeposition can improve H_2 evolution, not only on noble metals but also on metal oxides. Another core/shell cocatalyst for photocatalytic overall water splitting, Ni-core/NiO-shell nanoparticles, has been applied to many heterogeneous photocatalytic systems [7, 48, 56]. Compared with Ni/NiO, the present core/shell cocatalyst has several advantages, including (1) the possibility of using various noble metals and metal oxides as a core for the extraction of photogenerated electrons from the photocatalyst bulk, (2) the possibility of selectively introducing active species for overall water splitting at reduction sites on the photocatalyst, and (3) elimination of the need for activation treatment by oxidation or reduction. The latter two advantages are effective when the core is introduced by an in situ photodeposition method. The elimination of activation procedures involving heat treatment is especially beneficial for non-oxide photocatalysts, which tend to be less heat-resistant.

6 Summary and Future Outlook

Recent research on nanostructured cocatalysts with GaN:ZnO for visible light-driven water splitting, developed by our group, has been highlighted. Experimental results have revealed that the water splitting activity is significantly enhanced by combining a proper H_2 evolution cocatalyst with GaN:ZnO. Since our report on nanoparticulate Rh and Cr mixed-oxide with a solid solution of GaN:ZnO in 2006 highlighted the important role of cocatalysts in photocatalytic water splitting, additional research on such cocatalysts was stimulated, increasing the variety of effective cocatalysts especially for water reduction [69–72]. In the case of GaN:ZnO photocatalyst, however, the apparent quantum yield is at most ~5% in the visible light region, necessitating more research not only on cocatalysts but also on the improvement of GaN:ZnO itself. The latter subject is of course now ongoing in our laboratory.

In future research on water splitting cocatalysts, it is expected that not only searching for a new cocatalyst material and improving the preparation method but also elucidating the reaction mechanism and interaction of the loaded cocatalyst with the base photocatalyst will become more important. Some attempts to investigate the mechanistic aspect on water splitting and the cocatalyst/photocatalyst interface by means of kinetic analysis, spectroscopic and (photo)electrochemical measurements, and computational approach have been reported so far [19, 25, 73, 74]. Specifically, understanding the interfacial property between a photocatalyst and the loaded cocatalyst would be the major challenge in this research field.

It is also considered that facilitating both H_2 and O_2 evolution by introducing two different cocatalysts onto a given photocatalyst is an important subject for enhancing water splitting activity. As described earlier, most cocatalysts developed so far function as water reduction sites. However, it would be natural to expect that loading both H_2 and O_2 evolution cocatalysts onto the same photocatalyst would improve water splitting activity, compared to photocatalysts modified with either an H_2 or O_2 evolution cocatalyst. Very recently we demonstrated a proof of concept, using GaN:ZnO loaded with Rh/Cr_2O_3 (core/shell) and Mn_3O_4 nanoparticles as H_2 and O_2 evolution promoters, respectively, under visible light irradiation ($\lambda > 420$ nm) [29]. The activity of GaN:ZnO modified with both Rh/Cr_2O_3 and Mn_3O_4 provided a higher activity than modification with either Rh/Cr_2O_3 or Mn_3O_4. This demonstrates the validity of the above idea, and suggests a new strategy for improving photocatalytic activity for overall water splitting.

References

1. Khaselev O, Turner JA (1998) Science 280:425
2. Grätzel M (2001) Nature 414:338
3. Cortright RD, Davda RR, Dumesic JA (2002) Nature 418:964
4. Kamat PV (2007) J Phys Chem C 111:2834
5. Lee JS (2005) Catal Surv Asia 9:217
6. Maeda K, Domen K (2007) J Phys Chem C 111:7851
7. Kudo A, Miseki Y (2008) Chem Soc Rev 38:253
8. Youngblood WJ, Lee S-HA, Maeda K, Mallouk TE (2009) Acc Chem Res 42:1966
9. Maeda K, Takata T, Hara M, Saito N, Inoue Y, Kobayashi H, Domen K (2005) J Am Chem Soc 127:8286
10. Maeda K, Teramura K, Takata T, Hara M, Saito N, Toda K, Inoue Y, Kobayashi H, Domen K (2005) J Phys Chem B 109:20504
11. Yashima M, Maeda K, Teramura K, Takata T, Domen K (2005) Chem Phys Lett 416:225
12. Teramura K, Maeda K, Saito T, Takata T, Saito N, Inoue Y, Domen K (2005) J Phys Chem B 109:21915
13. Maeda K, Teramura K, Lu D, Takata T, Saito N, Inoue Y, Domen K (2006) Nature 440:295
14. Maeda K, Teramura K, Saito N, Inoue Y, Domen K (2006) J Catal 243:303
15. Maeda K, Teramura K, Masuda H, Takata T, Saito N, Inoue Y, Domen K (2006) J Phys Chem B 110:13107
16. Maeda K, Teramura K, Lu D, Takata T, Saito N, Inoue Y, Domen K (2006) J Phys Chem B 110:13753
17. Maeda K, Teramura K, Lu D, Saito N, Inoue Y, Domen K (2006) Angew Chem Int Ed 45:7806
18. Maeda K, Teramura K, Lu D, Saito N, Inoue Y, Domen K (2007) J Phys Chem C 111:7554
19. Hirai T, Maeda K, Yoshida M, Kubota J, Ikeda S, Matsumura M, Domen K (2007) J Phys Chem C 111:18853
20. Sun X, Maeda K, Le Faucheur M, Teramura K, Domen K (2007) Appl Catal A Gen 327:114
21. Maeda K, Hashiguchi H, Masuda H, Abe R, Domen K (2008) J Phys Chem C 112:3447
22. Maeda K, Teramura K, Domen K (2008) J Catal 254:198
23. Maeda K, Masuda H, Domen K (2009) Catal Today 147:173
24. Hisatomi T, Maeda K, Lu D, Domen K (2009) Chem Sus Chem 2:336
25. Hisatomi T, Maeda K, Takanabe K, Kubota J, Domen K (2009) J Phys Chem C 113:21458
26. Sakamoto N, Ohtsuka H, Ikeda T, Maeda K, Lu D, Kanehara M, Teramura K, Teranishi T, Domen K (2009) Nanoscale 1:106
27. Maeda K, Sakamoto N, Ikeda T, Ohtsuka H, Xiong A, Lu D, Kanehara M, Teranishi T, Domen K (2010) Chem Eur J 16:7750
28. Maeda K, Domen K (2010) Chem Mater 22:612
29. Maeda K, Xiong A, Yoshinaga T, Ikeda T, Sakamoto N, Hisatomi T, Takashima M, Lu D, Kanehara M, Setoyama T, Teranishi T, Domen K (2010) Angew Chem Int Ed 49:4096
30. Nakamura S, Mukai T, Senoh M (1994) Appl Phys Lett 64:1687
31. Nakamura S (1998) Science 281:956
32. Tsukazaki A, Ohtomo A, Onuma T, Ohtani M, Makino T, Sumiya M, Ohtani K, Chichibu SF, Fuke S, Segawa Y, Ohno H, Koinuma H, Kawasaki M (2005) Nat Mater 4:42
33. Jensen LL, Muckerman JT, Newton MD (2008) J Phys Chem C 112:3439
34. Wei W, Dai Y, Yang K, Guo M, Huang B (2008) J Phys Chem C 112:15915
35. Hara M, Nunoshige J, Takata T, Kondo JN, Domen K (2003) Chem Commun 3000
36. Kato H, Kudo A (2003) Catal Today 78:561
37. Nosaka Y, Norimatsu K, Miyama H (1984) Chem Phys Lett 106:128
38. Kraeutler B, Bard AJ (1978) J Am Chem Soc 100:4317
39. Nakamatsu H, Kawai T, Koreeda A, Kawai S (1986) J Chem Soc Faraday Trans 1 82:527
40. Tada H, Teranishi K, Ito S, Kobayashi H, Kitagawa S (2000) Langmuir 16:6077

41. Einaga H, Harada M (2005) Langmuir 21:2578
42. Sato S (1985) J Catal 92:11
43. Zhang F, Chen J, Zhang X, Gao W, Jin R, Guan N, Li Y (2004) Langmuir 20:9329
44. Yamashita H, Miura Y, Mori K, Ohmichi T, Sakata M, Mori H (2007) Catal Lett 114:75
45. Hemnann JM, Disdier J, Pichat P (1986) J Phys Chem 90:6028
46. Tanaka K, Harada K, Murata S (1986) Sol Energy 36:159
47. Thaminimulla CTK, Takata T, Hara M, Kondo JN, Domen K (2000) J Catal 196:362
48. Domen K, Kudo A, Onishi T, Kosugi N, Kuroda H (1986) J Phys Chem 90:292
49. Kalyanasundaram K, Grätzel M (1979) Angew Chem Int Ed 18:701
50. Harriman A, Pickering IJ, Thomas JM, Christensen PA (1988) J Chem Soc Faraday Trans 1 84:2795
51. Hashiguchi H, Maeda K, Abe R, Ishikawa A, Kubota J, Domen K (2009) Bull Chem Soc Jpn 82:401
52. Dean JA (1985) Lange's handbook of chemistry, 13th edn. McGraw-Hill, New York
53. Kato H, Kudo A (2002) Phys Chem Chem Phys 4:2833
54. Abdullah M, Low GKC, Matthews RW (1990) J Phys Chem 94:6820
55. Chen D, Ray AK (1998) Water Res 32:3223
56. Domen K, Kudo A, Onishi T (1986) J Catal 102:92
57. Sayama K, Arakawa H (1997) J Chem Soc Faraday Trans 93:1647
58. Sayama K, Arakawa H (1996) J Photochem Photobiol A 94:67
59. Yamaguti K, Sato S (1985) J Chem Soc Faraday Trans 1 81:1237
60. Abe R, Sayama K, Arakawa H (2003) Chem Phys Lett 371:360
61. Lugo HJ, Lunsford JH (1985) J Catal 91:155
62. Busca G (1989) J Catal 120:303
63. Sun B, Reddy EP, Smirniotis PG (2005) Environ Sci Technol 39:6251
64. Yoshida M, Takanabe K, Maeda K, Ishikawa A, Kubota J, Sakata Y, Ikezawa Y, Domen K (2009) J Phys Chem C 113:10151
65. Fu H, Lu G, Li S (1998) J Photochem Photobiol A 114:81
66. Testa JJ, Grela MA, Litter MI (2001) Langmuir 17:3515
67. Moffat TP, Yang H, Fan FF, Bard AJ (1992) J Electrochem Soc 139:3158
68. Kato H, Kudo A (2001) J Phys Chem B 105:4285
69. Hata H, Kobayashi Y, Bojan V, Youngblood WJ, Mallouk TE (2008) Nano Lett 8:794
70. Zong X, Yan H, Wu G, Ma G, Wen F, Wang L, Li C (2008) J Am Chem Soc 130:7176
71. Jang JS, Ham DJ, Lakshminarasimhan N, Choi W, Lee JS (2008) Appl Catal A Gen 346:149
72. Tabata M, Maeda K, Ishihara T, Minegishi T, Takata T, Domen K (2010) J Phys Chem C 114:11215
73. Shimodaira Y, Kudo A, Kobayashi H (2007) Chem Lett 36:170
74. Yoshida M, Yamakata A, Takanabe K, Kubota J, Osawa M, Domen K (2009) J Am Chem Soc 131:13218

Artificial Photosynthesis Challenges: Water Oxidation at Nanostructured Interfaces

Mauro Carraro, Andrea Sartorel, Francesca Maria Toma, Fausto Puntoriero, Franco Scandola, Sebastiano Campagna, Maurizio Prato, and Marcella Bonchio

Abstract Innovative oxygen evolving catalysts, taken from the pool of nanosized, water soluble, molecular metal oxides, the so-called polyoxometalates (POMs), represent an extraordinary opportunity in the field of artificial photosynthesis. These catalysts possess a highly robust, totally inorganic structure, and can provide a unique mimicry of the oxygen evolving center in photosynthetic II enzymes. As a result POMs can effect H_2O oxidation to O_2 with unprecedented efficiency. In particular, the tetra-ruthenium based POM $[Ru^{IV}_4(\mu\text{-OH})_2(\mu\text{-O})_4(H_2O)_4(\gamma\text{-SiW}_{10}O_{36})_2]^{10-}$, **Ru$_4$(POM)**, displays fast kinetics, electrocatalytic activity powered by carbon nanotubes and exceptionally light-driven performance. A broad perspective is presented herein by addressing the recent progress in the field of metal-oxide nano-clusters as water oxidation catalysts, including colloidal species. Moreover,

M. Carraro, A. Sartorel, and M. Bonchio (✉)
ITM-CNR and Dipartimento di Scienze Chimiche, Università di Padova, via Marzolo 1, 35131 Padova, Italy
e-mail: marcella.bonchio@unipd.it

F.M. Toma and M. Prato
Center of Excellence for Nanostructured Materials (CENMAT), INSTM, Università di Trieste, Piazzale Europa 1, 34127 Trieste, Italy
and
Dipartimento di Scienze Farmaceutiche, Università di Trieste, Piazzale Europa 1, 34127 Trieste, Italy

F. Puntoriero and S. Campagna
Dipartimento di Chimica Inorganica, Chimica Analitica e Chimica Fisica, Università di Messina, via Sperone 31, 98166 Messina, Italy
and
Centro Interuniversitario per la Conversione Chimica dell'Energia Solare, Sezione di Messina, via Sperone 31, 98166 Messina, Italy

F. Scandola
Dipartimento di Chimica, Università di Ferrara, via Borsari 49, 49100 Ferrara, Italy
and
Centro Interuniversitario per la Conversione Chimica dell'Energia Solare, sezione di Ferrara, via Borsari 49, 49100 Ferrara, Italy

the shaping of the catalyst environment plays a fundamental role by alleviating the catalyst fatigue and stabilizing competent intermediates, thus responding to what are the formidable thermodynamic and kinetic challenges of water splitting. The design of nano-interfaces with specifically tailored carbon nanostructures and/or polymeric scaffolds opens a vast scenario for tuning electron/proton transfer mechanisms. Therefore innovation is envisaged based on the molecular modification of the hybrid photocatalytic center and of its environment.

Contents

1   Introduction

1.1   *Water Splitting*

Photosynthesis is a light driven process in which carbon dioxide and water are converted into sugar and dioxygen:

$$nCO_2 + nH_2O \xrightarrow{h\nu} (CH_2O)_n + nO_2$$
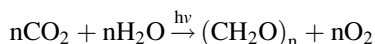
In this process, H_2O is the renewable multi-electron source, providing a total of four electrons/mol by the oxidative half reaction ($2H_2O \rightarrow O_2 + 4H^+ + 4\ e^-$; $E^0 = 1.23$ V vs NHE). Although this multi-electron pathway generates O_2 at the lowest thermodynamic barrier, if compared to the stepwise one-electron, it poses severe kinetic and thermodynamic challenges.

In green plants and some bacteria, water oxidation occurs with unmatched efficiency at the heart of the Photosystem II (PSII) enzyme, a homodimer protein of 650 KDa, where O_2 evolution is catalyzed by a polynuclear metal-oxo cluster with four manganese and one calcium atom held together by oxygen bridges ($CaMn_4O_x$). The structure of the Oxygen Evolving Centre in PSII has been recently addressed by

a combined crystallographic, spectroscopic and computational approach (Fig. 1) [1–3]. The more recent topology involves a $CaMn_3O_4$ fragment, with a trigonal pyramidal arrangement, featuring a "fused-twist" motif, with the fourth "dangling" Mn center bridged via three Mn-di-μ-oxo-Mn (Fig. 1).

The adoption of such a catalytic core, featuring adjacent multi-transition metal centers and multiple-μ-hydroxo/oxo bridging units, is thus the winning strategy to master a four-electron/four-proton mechanism through sequential redox steps with high efficiency and minimal energy cost. Although several mechanistic details still need to be clarified, a light induced four electron process, involving five oxidation states S_n ($n = 0$–4), seems to be responsible for the catalytic cycling of the oxygenic $CaMn_4O_x$ core [4–7]. In this scheme, S_0 is the most reduced state and S_4 the four-electron oxidized state, whereby the latter reacts quickly (1 ms) to release O_2, returning to the initial S_0 form of the enzyme (Kok cycle, Fig. 2) [8].

The global photo-oxidation cycle is driven by P_{680}^+, a chlorophyll pigment radical cation, generated upon illumination (680 nm is the optimal absorption wavelength) and which is by far the strongest oxidizing agent known in living systems ($P_{680}/P_{680}^+ \approx 1.2$–1.25 V). In the natural system, P_{680}^+ is generated in close proximity to a redox active tyrosine (TyrZ), in turn located at ca. 7 Å distance from the manganese cluster. Such a donor–acceptor sequence is pivotal to ensure a photo-induced electron flow in the sequence $P_{680}^+ \leftarrow$ TyrZ $\leftarrow CaMn_4O_x$, to power the $S_0 \rightarrow S_4$ evolution within a nano- to microsecond time domain. On the other hand, the coupled four proton release, compensating for charge increase, involves water molecules coordinated at the manganese core and via hydrogen-bonding within the organic domains of the surrounding proteins.

In such an optimally merged hybrid nano-environment, oxygenic photosynthesis turns out to effect successfully a solar-activated $4e^-/4H^+$ catalytic routine at a moderate overpotential (ca. 0.3–0.4 V at physiological pH), with multi-turnover (TON) efficiency yielding up to ca. 400 TON per second and an overall quantum

Fig. 1 Schematic view of the oxygen evolving center in PSII. The figure was kindly provided by Professor James Barber (Imperial College, London, UK) based on the coordinates PDB file 1S5L for the crystal structure of PSII isolated from the cyanobacterium, *Thermosynechococcus elongatus* [2]
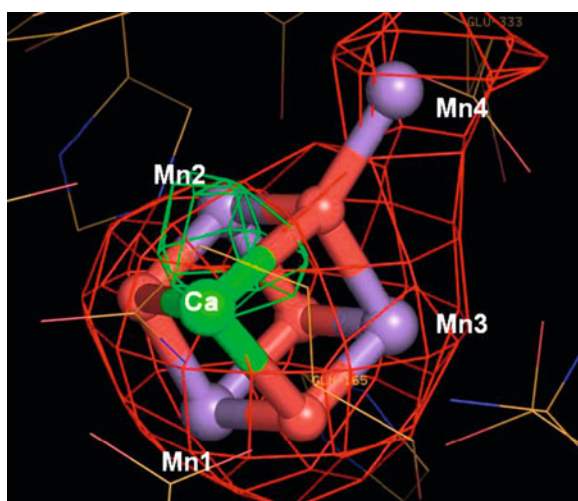
Fig. 2 The Kok cycle of the oxygen evolving center in PSII
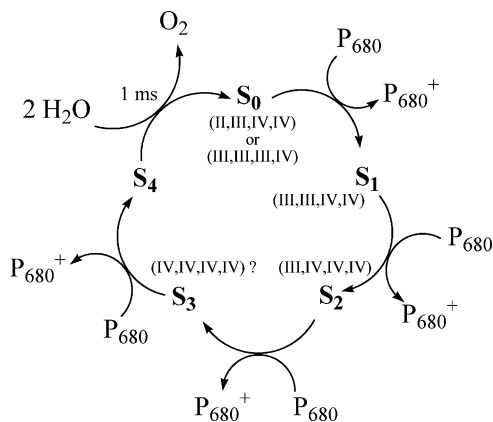
yield close to 10%. However, despite some elaborate control/protection strategies, under turnover regime the PSII enzyme undergoes to fatal damage, thus requiring a perpetual self-healing reconstruction, occurring every 30–60 min.

Artificial photosynthesis is a Holy Grail of modern science [9–14]. Actually, the effective production of high-energy content chemical species, to be used as fuels, by exclusively using solar irradiation would revolutionize modern society, giving access to a virtually inexhaustible energy source, equally distributed on Earth [15].

A major goal is to convert solar energy into chemical energy, by means of the light-driven splitting of water into its high-energy constituents, that are molecular oxygen and hydrogen ($2H_2O \rightarrow O_2 + 2H_2$), an endoergonic process by 4.92 eV (113.38 kcal). In analogy to the natural photosynthetic scheme, an artificial system should thus integrate the following functional components, *in a "modular" approach*: (1) light-harvesting antennae; (2) charge separation units; (3) multi-electron transfer catalysts [16, 17]. Whereas the design of light-harvesting antenna systems, as well as of charge separation units, has been extensively pursued in the last few decades [13, 18–23], the bottleneck of research in artificial photosynthesis remains the design of synthetic catalysts able to drive efficiently light-induced multielectron transfer processes, in particular for the water oxidation semi-reaction [5, 24–27].

2 Oxygen Evolving Catalysts

Suitable oxygen evolving catalysts (OECs) must respond to the requirements of (1) availability of different oxidation states, (2) ability of transferring protons, and (3) possibility to form metallo-oxo species, responsible for the oxygen–oxygen bond formation.

Since robust molecular OECs have been elusive species for a long time, most research has been focused on metal oxides, including their colloidal form, and some results are presented below.

2.1 Metal Oxides

Ruthenium based catalysts have attracted interest as water oxidation systems, since the discovery, by J. Kiwi and M. Grätzel [28, 29], that nano-RuO_2 particles with average hydrodynamic radius of 28 nm, stabilized by polyvinyl alcohol as additive, exhibit oxygen evolution activity when added to a solution of cerium(IV) as oxidant. The resulting oxidation rate exceeded by two orders of magnitude that achieved with RuO_2 powder, despite an excess of about 40 times being used in the latter case. RuO_2 colloids were then integrated in a redox system to allow catalytic light driven splitting of water into hydrogen and oxygen, in the presence of $[Ru^{II}(bpy)_3]^{2+}$ (bpy = 2,2'-bipyridine) as the photosensitizer and dimethylviologen as the electron acceptor, responsible for H_2 production [30]. Colloidal RuO_2 was also co-deposited on nanoparticles of TiO_2, with Pt(0) as the hydrogen evolving catalyst [31].

A crucial parameter affecting RuO_2 activity is the hydration grade, to be assessed at ~12–14%, to avoid (1) anodic corrosion of highly hydrated samples or (2) decreasing of surface area in the poorly hydrated batches. This is generally controlled upon heating at 150 °C for 2–5 h [32–35]. Mills et al. reported a simple procedure for photodeposition of RuO_2 nanoparticles onto TiO_2, starting from a perruthenate solution. The resulting material, featuring evenly distributed coverage with 2–3 nm catalyst particles was tested as a catalyst for water oxidation in the presence of Ce(IV), where it exhibited a fairly low TON > 16 for oxygen evolution.

Interaction with visible light of Ru(II) polypyridine sensitizers [36], and in particular $[Ru(bpy)_3]^{2+}$, has been achieved both in homogeneous solution and under heterogeneous conditions [37, 38].

Pillai et al. reported electrocatalytic water oxidation by using an electrode prepared by deposition of a dilute Nafion solution containing colloidal RuO_2, and subsequent dipping of the electrode surface in an $[Ru(bpy)_3]^{2+}$ solution, resulting in a composite containing 0.1–1% of RuO_2 and 0.03% of $[Ru(bpy)_3]^{2+}$ [38]. Water oxidation in acetate buffer (pH = 4.6), was observed at 0.9 V vs SCE, corresponding to 0.2 V overpotential.

Yoshida et al. reported oxygen evolution by a soft material containing RuO_2 nanoparticles dispersed by sodium dodecyl sulfate and embedded into a polymer of poly(*N*-isopropylacrylamide), cross-linked and sensitized with $[Ru(bpy)_3]^{2+}$ derivatives, in the presence of $[Co(NH_3)_5Cl]^{2+}$ as the sacrificial oxidant [37].

The gel structure allows the organization of the catalytic and sensitizer domains into a functional material with high surface area where trapped water pools are faced to such catalytic domains.

Colloidal *iridium* oxide IrO_x is still one of the most efficient catalysts for water oxidation to date [39]. Bulk IrO_2 powder and colloidal $IrO_2 \cdot xH_2O$ have been found

to be more stable than RuO_2, which suffers for anodic corrosion in the presence of strong oxidants [40–42]. Nanostructured IrO_2 presents an implemented surface area, and exhibits a low overpotential once deposited on ITO [43]. In this case, citrate-stabilized nanoparticles (50–100 nm) can form a monolayer upon formation of ester bonds between the carboxylate groups and hydroxyl groups on the ITO surface. Water oxidation occurred at 1 V vs SCE (pH 5.3), the overpotential observed was 0.325 V, with an estimate TOF up to 6.9 s^{-1} at $\eta = 0.625$ V. Smaller nanoparticles (1.6 $\pm$ 0.6 nm) were used to prepare an IrO_x film (2 nm thickness) on glassy carbon electrodes upon controlled potential electro-flocculation at pH 13 [44, 45]. Overpotentials of $0.15 - 0.25$ V were observed in a wide pH range, showing a 100% current efficiency at $\eta = 0.25$ V.

In 2000, T. E. Mallouk and coworkers reported the combination of citrate stabilized colloidal IrO_2 and $[Ru(bpy)_3]^{2+}$ photosensitizer to achieve water oxidation in aqueous Na_2SiF_6-$NaHCO_3$ buffer [41]. A heterogeneous setup was obtained by anchoring the sensitizer to a cationic polymer [40, 46]. At high concentration of the photosensitizer and low loading of the IrO_2 catalyst, a turnover frequency of 160 s^{-1} per surface iridium atom was observed [40]. A further improvement of the system was achieved by using well dispersed, small (1–5 nm) IrO_2 nanoparticles, stabilized by bidentate carboxylates, which can also be introduced on the ancillary ligands of the sensitizer [42]. The photoinduced electron transfer from Ir(IV) to $[Ru(bpy)_3]^{3+}$ occurs concomitantly with oxygen production in the milliseconds timescale, following second order kinetics with $k = 1.3 \times 10^6$ M^{-1} s^{-1} [40], and therefore this has been recognized as the rate determining step of the process. Direct tethering of the IrO_2 nanoparticles to the sensitizer molecules containing pendant succinate or malonate groups results in an improvement of the electron transfer rate, occurring with a first-order rate constant $k = 8 \times 10^2$ s^{-1}.

These results have set the basis for an advanced proof-of-principle concerning the artificial leaf functional assembly (Fig. 3). In this case, the photosensitizer-IrO_2 assembly was covalently bound to nanoparticulate TiO_2 (anatase) through phosphate ester bonds [47]. Nevertheless, despite the covalent binding between the photosensitizer and the catalyst, the electron transfer between the Ir(IV) and the oxidized photosensitizer remains slow, occurring in the milliseconds timescale, still limiting the production of intense photocurrents.

In comparison with $[Ru(bpy)_3]^{2+}$, the tetranuclear Ru(II) dendrimer $[Ru\{(\mu\text{-dpp})Ru(bpy)_2\}_3]^{8+}$ (dpp = 2,3-bis(2′-pyridyl)pyrazine) features higher molar absorptivity, with a significant extension towards the red portion of the visible of the spectrum, as well as a more positive redox potential (1.70 V and 1.26 V vs NHE in water, for the tetranuclear compound and $[Ru(bpy)_3]^{2+}$, respectively) [48]. Upon irradiating ($\lambda > 550$ nm) a solution of $[Ru\{(\mu\text{-dpp})Ru(bpy)_2\}_3]^{8+}$ and iridium oxide nanoparticles (20 nm diameter), stabilized by citrate anions, in the presence of $Na_2S_2O_8$ as the sacrificial electron acceptor, the observed oxygen evolution was six times higher with respect to that obtained by an equimolar solution of $[Ru(bpy)_3]^{2+}$, with overall quantum yield, $\phi = 0.015$ (expressed as mol O_2/photon). By using malonate-stabilized IrO_2 nanoparticles and $[Ru\{(\mu\text{-dpp})Ru(bpy)_2\}_3]^{8+}$, the photochemical quantum yield for oxygen production, calculated at the fixed excitation wavelength of 550 nm,
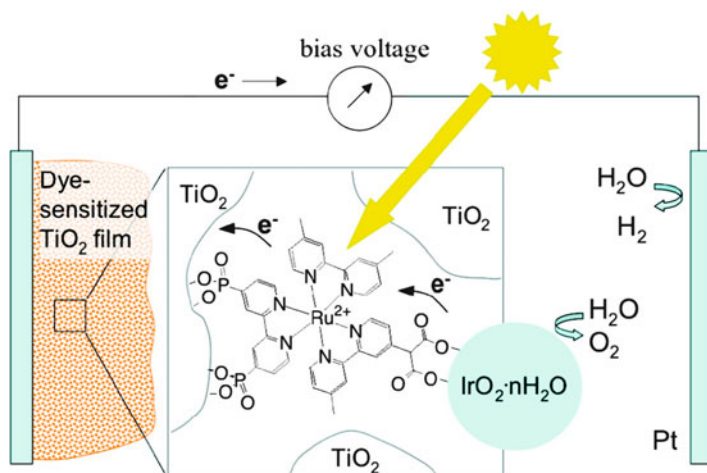
Fig. 3 The water splitting dye sensitized solar cell proposed by Mallouk et al. (reproduced from [47] with authorization from ACS)

was 0.055 [48]. Moreover, it could be inferred that the system using $[Ru\{(\mu\text{-dpp})Ru(bpy)_2\}_3]^{8+}$ as the sensitizer instead of $[Ru(bpy)_3]^{2+}$ should be more stable, due to the more efficient hole scavenging on the oxidized photosensitizer, thus leading to a decreased attack of the oxidized photosensitizer by the produced O_2 [49]. Actually, lower irradiation energy and faster ET rates could be pivotal to avoid sensitizer degradation.

In 2008, H. Han and H. Frei reported the assembly of Ir oxide nanoclusters within a totally inorganic photocatalytic unit on mesoporous silica AlMCM-41, where the sensitizer is a binuclear TiOCr charge-transfer chromophore [50]. When exciting the chromophore with visible light ($\lambda = 460$ nm), a metal-to-metal charge-transfer Ti(IV)OCr(III) $\rightarrow$ Ti(III)OCr(IV) occurs. Cr(IV) is then reduced by Ir oxide, and in the presence of persulfate as sacrificial acceptor, oxygen evolution is observed with an estimated quantum efficiency of 13%.

IrO_2 nanoparticles of 2 nm diameter were also deposited by electrophoresis onto an Fe_2O_3 photoanode, yielding an unprecedented 3 mA cm^{-2} value of photocurrent at 1.23 V vs reversible hydrogen electrode, under simulated sunlight conditions. However, decreased performances were observed after repetitive scans, likely due to the degradation of the electrode surface and loss of the catalytic components [51].

The interest in *cobalt* as a water oxidation catalyst stems from its abundance on Earth and its low cost, compared to second row transition metals.

Cobalt oxide and soluble aquo or hydroxo complexes have been known as water oxidation catalysts since the early 1980s, under heterogeneous and homogeneous conditions [52, 53]. However, cobalt ions in aqueous solution present poor stability, showing detrimental separation as insoluble oxides, these latter being characterized by very low activity.

D. Nocera and M. Kanan reported the in situ formation of a catalytic film composed by Co(III) phosphates, hydroxides, and oxides (with Co:P ratio of ca 2:1) upon application of positive potentials to indium tin oxide (ITO) and fluorine tin oxide (FTO) electrodes in neutral aqueous solutions containing Co(II) and phosphate ions [54–56]. At pH = 7, room temperature and in air atmosphere, electrochemical oxygen generation is observed at 280 mV overpotential, while 8 h of electrolysis at 1.29 V (corresponding to 470 mV overpotential) leads to prolonged oxygen generation, corresponding to 5.2 turnovers per Co center.

X-Ray Absorption Near-Edge Structure (XANES) experiments indicated an octahedral coordination environment for the cobalt centers, with six oxygen ligands, Co(III) being the major oxidation state [57]. Extended X-Ray Absorption Fine Structure (EXAFS) revealed four metal–metal interactions per Co ion with a mean Co–Co distance of 2.81 Å, typical of a di-µ-oxo bridge connection, specifically in Co-oxo cubanes that share Co corners with phosphate not directly bound to Co.

The authors proposed a catalytic cycle in which Co(II)-water moieties undergo proton coupled oxidation, with phosphate being the proton acceptor, to form adjacent Co(IV)-oxo units, finally responsible for oxygen generation [58]. Important insights on the reaction mechanism come from Electron Paramagnetic Resonance (EPR) evidence of low-spin Co(IV) formation (g_{eff} = 2.27) upon preparation of the film at potentials of 1.14 and 1.34 V [59].

An outstanding feature of Nocera's catalyst is its self-healing attitude, in the presence of proton accepting electrolytes, in analogy with the oxygen evolving center in Photosystem II enzyme [60]. Furthermore, oxygen evolution is not limited by the presence of chloride anions (no Cl^- oxidation to chlorine is observed), also allowing efficient oxygen evolution from sea water.

More recently, Nocera's catalyst was electrodeposited onto mesostructured hematite (α-Fe_2O_3) [61], and photochemically deposited, as 10–30 nm nanoparticles, on a semiconductor photoanode of ZnO [62], leading to performance and fabrication improvements. The resulting photoanodes show >0.35 V and 0.23 V reduction, respectively, of the bias voltage required for promoting water oxidation, with respect to bare oxides [63].

Another excellent example of an inorganic Co-based water oxidation catalyst was recently reported by Jiao and Frei [64] dealing with immobilization of nanostructured Co_3O_4 clusters in mesoporous silica (SBA-15) by means of wet impregnation methods. Transmission electron microscopy (TEM) confirmed the integrity of the silica structure, after formation of the Co_3O_4 nanoclusters inside the channels of 8 nm diameter. Structural characterization revealed spheroid-shaped bundles of parallel Co_3O_4 nanorods of spinel structure inside the silica. Light driven oxygen evolving catalysis was performed in aqueous suspension (pH = 5.8, with laser at 476 nm), using the $[Ru(bpy)_3]^{2+}$/$S_2O_8^{2-}$ system described above. The nanostructured material (4.2% loading) showed an increased catalytic activity with respect to commercially available micrometer sized Co_3O_4 particles, with estimated turnover frequencies TOF = 0.01 s^{-1} per Co surface center compared to TOF = 0.0006 s^{-1} for the commercial catalysts. The much larger surface area provided by the internal structure of the silica channels is probably a major factor for the high turnover

frequency observed for the nanoclusters. The quantum yield of the process, reported as the number of oxygen molecules per photons, was 18%.

A third selected example of cobalt based water oxidation material was reported by Wu et al., with the growth of $Ni_xCo_{3-x}O_4$ nanowire arrays on conductive titanium foils, showing the advantage of great surface area and improved conduction [65]. While pure Co_3O_4 nanowires have a 400 nm diameter and 15–20 μm length, increasing the nickel amount they become thicker and rougher, providing an increase in surface area. The spinel crystal structure of Co_3O_4 was maintained after doping. Such deposited materials were used as oxygen evolving anodes in basic conditions (1 M NaOH), and water oxidation was observed at ca. 0.4 V overpotential. At the same overpotential value the current is six times higher with doped nanowires with respect to pure Co_3O_4. Besides the increase in the number of active sites on the nanowires surface, the electrical conductivity was also increased up to five orders of magnitude.

Being the metal present in the natural oxygen evolving center of Photosystem II, *manganese* oxides have been widely investigated as catalysts for water oxidation [32, 33, 66]. Manganese is about 30 times more abundant than cobalt, while displaying a decreased toxicity. Mn_2O_3 exhibits oxygen evolution activity under photochemical conditions, coupled with the light/$[Ru(bpy)_3]^{2+}/S_2O_8^{2-}$ system, but the particles display a low surface area (1.1 m^2 g^{-1}). Using a similar procedure adopted for the Co_3O_4 nanoclusters described above, Frei et al. were able to prepare nanostructured Mn oxide clusters (70–90 nm diameter) in mesoporous KIT-6 silica (8% loading) [67]. The Mn_2O_3 clusters were formed inside the silica upon calcinations at 600 °C, with retention of the cubic mesoporous structure. Oxygen evolution was performed by irradiation with visible light of an aqueous solution ($Na_2SiF_6/NaHCO_3$ buffer, pH = 5.8) of $Na_2S_2O_8$ and $[Ru(bpy)_3]^{2+}$ as the photosensitizer, in the presence of the Mn oxide nanoclusters. Oxygen evolution was observed until total consumption of the persulfate sacrificial oxidant, while restoring the initial reaction conditions showed unchanged activity of the catalyst, confirming no-deactivation of the Mn centers.

A bio-inspired, all inorganic, OEC based on calcium–manganese oxide particles was proposed by Kurz et al. [68]. Particles of α-Mn_2O_3 and $CaMn_2O_4 \cdot H_2O$ with high surface area were obtained by careful oxidation of Mn(II) ions in basic aqueous solution, with or without Ca, respectively, after calcination at 600 and 400 °C. Scanning electron microscopy (SEM) analysis confirmed the formation of particles of 5–50 μm size and surface area of 16.6 and 205–303 m^2 g^{-1} were measured for α-Mn_2O_3 and $CaMn_2O_4 \cdot H_2O$, respectively. Both α-Mn_2O_3 and $CaMn_2O_4 \cdot H_2O$ were observed to catalyze oxygen evolution in the presence of sacrificial oxidants and also in the light driven $[Ru(bpy)_3]^{2+}/[Co(NH_3)_5Cl]^{2+}$ system (acetate buffer at pH 4). Observed rates, expressed in $mmol_{O2}mol_{Mn}^{-1}s^{-1}$, were 0.325 and 0.350 for $CaMn_2O_4 \cdot 4H_2O$ and $CaMn_2O_4 \cdot H_2O$. The high surface area of the $CaMn_2O_4 \cdot H_2O$ samples is not the only factor enhancing the catalytic properties of these materials, since a sample of $CaMn_2O_4 \cdot H_2O$ with low surface area (14.8 m^2 g^{-1}) still yielded an impressive oxygen evolution rate of 0.225 $mmol_{O2}$ mol_{Mn}^{-1} s^{-1}. Drawbacks are the poor stability of the calcium manganese oxide catalysts in acetate buffer, and the strong influence of the hydration grade on the turnover performance, as the anhydrous $CaMn_2O_4$ obtained after extensive calcination (marokite) is inactive.

2.2 Polyoxometalates

Catalysts based on metal oxides have several related drawbacks, including low turnover frequencies since the active metal sites are usually on the surface of the material, slow electron transfer to photogenerated oxidants, limited possibility of tuning the electronic properties of the catalyst, and inherent difficulties in the comprehension of the reaction mechanism. This is why the development of molecular OECs has attracted much attention over the last few decades.

The first synthetic, non-proteic molecular catalyst capable to oxidize water was reported about 30 years ago [69]. This was the so-called "blue dimer," [(bpy)$_2$Ru (H$_2$O)(μ-O)Ru(H$_2$O)(bpy)$_2$]$^{4+}$. Once electrochemically or chemically activated, the blue dimer undergoes the stepwise loss of four electrons and four protons, producing an intermediate reactive species that oxidizes water [70, 71]. Unfortunately, the blue dimer loses its catalytic efficiency after a few cycles due to the degradation of the organic ligands. However, the blue dimer paved the way to the discovery of other water oxidation catalysts, most of them still based on ruthenium centers [72–78]. In the last few years, molecular catalysts based on iridium centers [79] as well as on cheaper metals such as manganese [80–84], cobalt [85], and iron [86] were also developed.

In recent years, a breakthrough in this field concerned the adoption of totally inorganic transition metal substituted polyoxometalates (POMs) as molecular catalysts for water oxidation.

POMs are characterized by molecular, discrete, nanosized multi-metal oxide polyanionic scaffolds, with a structural motif being at the interface between molecular complexes and extended oxides. Therefore, they show the reactivity of metal oxides with, in addition, the tunability of a molecular species.

The first paper dealing with POMs in Oxygen Evolving Catalysis was reported in 2004 [87] when Shannon et al. observed electrochemical oxygen generation at low potentials, ($E^0 = 0.756$ V vs NHE), from a 2 μM aqueous solution of Na$_{14}$[Ru$_2$Zn$_2$(H$_2$O)$_2$(ZnW$_9$O$_{34}$)$_2$] in phosphate buffer at pH = 8.0, using pulsed voltammetry. The proximity of the two ruthenium centers was considered a key factor, but studies concerning the reaction mechanism were not performed.

In 2008, simultaneously and independently, two groups reported the tetra-ruthenium POM {Ru$_4$(μ-OH)$_2$(μ-O)$_4$(H$_2$O)$_4$[γ-SiW$_{10}$O$_{36}$]}$^{10-}$ (**Ru$_4$(POM)**) as a high efficient water oxidation catalyst [77, 78]. The structure of **Ru$_4$(POM)** is reported in Fig. 4, being two staggered γ-[SiW$_{10}$O$_{36}$]$^{8-}$ units which coordinate an adamantane like tetraruthenium-oxo core, which evidences strict analogies with the tetramanganese oxygen evolving site of Photosystem II. Indeed, in both cases, four redox-active transition metals are connected through μ-oxo or μ-hydroxo bridges, with the metal centers coordinating a water molecule as the terminal ligand.

Activity of **Ru$_4$(POM)** in water oxidation catalysis was initially studied in the presence of sacrificial oxidants such as Ce(IV) and [Ru(bpy)$_3$]$^{3+}$[77, 78].
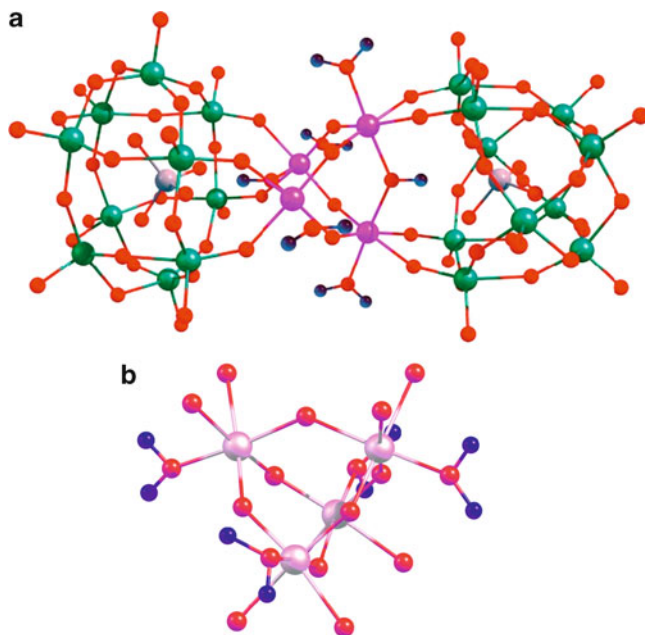
Fig. 4 (**a**) Structure of **Ru$_4$(POM)**. (**b**) Representation of the tetraruthenium-oxo core in **Ru$_4$(POM)**

In the presence of excess of Ce(IV), up to 500 catalytic cycles for oxygen evolution were observed (calculated as moles of oxygen produced per mole of catalyst employed), with an initial turnover frequency of 0.125 s^{-1}, while a second recharge in Ce(IV) induces an equivalent oxygen production.

When [Ru(bpy)$_3$]$^{3+}$ is used as the sacrificial oxidant, up to 18 turnovers are obtained in 30–40 s of reaction, corresponding to a turnover frequency of 0.45–0.60 s^{-1}.

The full comprehension of the reaction mechanism of water oxidation catalyzed by **Ru$_4$(POM)** is still under investigation [88–90]. A common conclusion among the studies reported to date is that this species undergoes several consecutive single electron oxidation steps, finally yielding a high valent intermediate responsible for oxygen production in a single four electron step. From the cyclic voltammetry held in acidic aqueous solution, the shift of the redox potentials by changing the pH of the media seems to confirm a contemporary exchange of one proton per redox event [89]. The proton coupled electron transfer also seems to be supported by resonant Raman spectroscopy of high valent derivatives of **Ru$_4$(POM)**, generated in situ by stoichiometric addition of Ce(IV): indeed, bands in the 450–550 cm^{-1} spectral region were attributed to stretchings of Ru^V-OH moieties, generated upon oxidation of the Ru^{IV}-OH$_2$ in the parent species [88]. It is worth noting that these studies were performed in acidic aqueous solution (pH = 0.6–2.0), and then the related conclusions cannot also be directly transferred for the catalysis held at neutral pH.
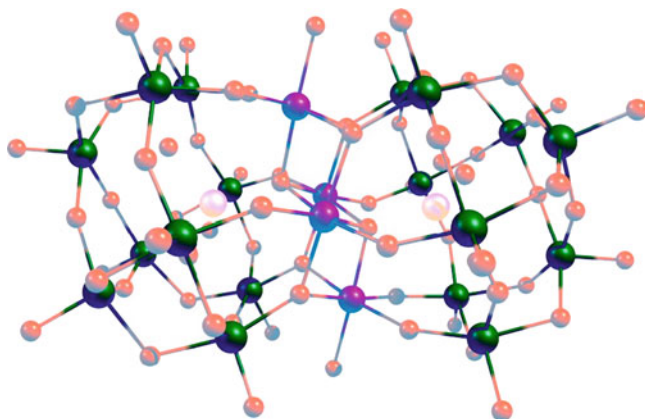
Fig. 5 Representation of the structure of $[Co_4(H_2O)_2(\alpha\text{-}PW_9O_{34})_2]^{10-}$

The species **Ru$_4$(POM)** has also been extensively studied in light driven water oxidation that will be presented in the next paragraph.

The iridium based POM $[(IrCl_4)KP_2W_{20}O_{72}]^{14-}$ was prepared upon isomerization of $[\alpha_2\text{-}P_2W_{17}O_{61}]^{10-}$ in the presence of $IrCl_3$ and WO_4^{2-} at pH 6.8, followed by addition of 1M NaOH, resulting in one $IrCl_4$ unit supported on one of the two bridged $PW_{10}O_{36}$ subunits. The complex catalyzes the reduction of $[Ru(bpy)_3]^{3+}$ in a 20 mM sodium phosphate buffer solution (pH 7.2), with 30% O_2 yield. However, the similar reactivity of $IrCl_3$ suggests that the complex dissociates into $[IrCl_4(H_2O)_2]^-$ and $[KP_2W_{20}O_{72}]^{13-}$ [91].

The tetracobalt substituted POM $[Co_4(H_2O)_2(\alpha\text{-}PW_9O_{34})_2]^{10-}$ was recently reported to be an actual water oxidation catalyst [85]. This species features a Co_4O_4 core, again resembling the active site of the natural enzyme Photosystem II (Fig. 5). Water oxidation was studied in phosphate buffer (pH = 7.5–8.0), using $[Ru(bpy)_3]^{3+}$ as sacrificial oxidant: despite a reduced reactivity of the POM with respect to $Co(NO_3)_2$ (19.5 and 23.4 turnovers per cobalt atom, respectively), the complex presents an interesting structural stability. Using very dilute catalyst concentrations, up to 1,000 turnovers were observed in 3 min, corresponding to an outstanding turnover frequency >5 s^{-1}.

2.3 Light Driven Water Oxidation by POMs

Most of the molecular OECs reported to date have been investigated by electrochemical or chemical activation, while only a few of them take advantage of photoactivation [92–99].

The following equations illustrate a possible general scheme for photoinduced water oxidation assisted by a sacrificial electron acceptor. In such equations, P and SA are the photosensitizer and the sacrificial oxidizing agent (primary electron

acceptor), respectively. Once formed by sunlight (1), *P undergoes oxidative electron transfer in the presence of a primary acceptor, the sacrificial agent SA, which can be a molecular species as well as a semiconducting surface, leading to the formation of the oxidized photosensitizer, P^+ (2). Equation (3), decay of *P to the ground state P, is a competing reaction, and the ratio between (2) and (3) rate constants determines the efficiency of P^+ production, which can be optimized (i.e., made close to 1) by adjusting the concentration of SA. Equation (4), back electron transfer between P^+ and SA^-, is a poisoning reaction for the overall process; however, it can be eliminated if the sacrificial agent decomposes quickly upon reduction, as is the case with the persulfate anion ($S_2O_8^{2-}$).

$$P + h\nu \rightarrow {}^*P \tag{1}$$

$$^*P + SA \rightarrow P^+ + SA^- \tag{2}$$

$$^*P \rightarrow P + h\nu' \text{and/or heat} \tag{3}$$

$$P^+ + SA^- \rightarrow P + SA \tag{4}$$

$$SA^- \rightarrow \text{products} \tag{5}$$

$$P^+ + OEC \rightarrow P + OEC^+ \tag{6}$$

Once formed, P^+ reacts with OEC, leading to the restoration of the ground state P, which is ready for another cycle, and to the formation of the mono-oxidized catalyst (6).

$$P^+ + OEC^+ \rightarrow P + OEC^{2+} \tag{7}$$

$$P^+ + OEC^{2+} \rightarrow P + OEC^{3+} \tag{8}$$

$$P^+ + OEC^{3+} \rightarrow P + OEC^{4+} \tag{9}$$

$$^*P + OEC^{n+} \rightarrow P^+ + OEC^{(n-1)+} \tag{10}$$

$$OEC^{4+} + 2H_2O \rightarrow OEC + O_2 + 4H^+ \tag{11}$$
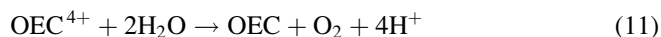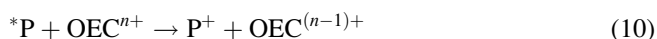
Equations (7)–(9) are the successive, stepwise oxidations of OEC^+ by P^+ ultimately leading to OEC^{4+}, the needed active catalyst that can oxidize water (11). Thermodynamics factors are expected to be different for the various stepwise mono-oxidation processes shown in (6)–(9). Equation (10) is another poisoning reaction, which can involve any OEC^{n+} species (with $n = 1$–3) and could compete with (2); (10) can be minimized by keeping low the concentration of OEC.

It has to be noted that, since four photoinduced cycles are needed to produce the active OEC^{4+} catalyst form, the photochemical quantum yield of molecular oxygen produced, $\Phi(O_2)$, per moles of adsorbed photons, can reach a limiting value of 0.25, unless some radicalic process is involved. Actually, in the specific (but quite common) case when persulfate ion is used as the sacrificial agent SA, the limiting value can reach 0.5, as the product of the reaction in (2) is the sulfate radical anion, which can promptly react with P to generate another molecule of oxidized photosensitizer P^+ or could directly react with $OEC^{(n-1)+}$ to form OEC^{n+}. In both cases, two photons are needed for producing a molecule of oxygen.

In light driven water oxidation, the first requirement of a good photosensitizer P is that it absorbs as much visible light as possible. Then it has to undergo a fast and efficient photoinduced electron transfer leading to its oxidized form P^+. To this end, a long-lived excited state of $^*P$ is highly desired. It is also required that the reducing power of $^*P$ and the oxidizing power of P^+ must be thermodynamically favorable to accomplish the electron transfers.

In this regard, the most common photosensitizer used is $[Ru(bpy)_3]^{2+}$, although porphyrins have also been employed [100]. The choice of $[Ru(bpy)_3]^{2+}$ as the photosensitizer is due to the quite interesting and convenient properties of such a species, including absorption in the visible region, relatively long-lived excited-state lifetime, reversible redox processes, and stability in the ground and excited states [101, 102]. Actually, the excited state of $[Ru(bpy)_3]^{2+}$ is a triplet metal-to-ligand charge-transfer (^3MLCT) state, having an excited-state energy of about 2.12 eV with a lifetime close to 0.5 µs and a luminescence quantum yield of 0.028 in air-equilibrated aqueous solution [101, 103]. Such excited-state properties indicate that the decay processes leading to the ground state in $[Ru(bpy)_3]^{2+}$ are relatively slow. In fact, the ^3MLCT state of $[Ru(bpy)_3]^{2+}$ can be involved in many efficient electron transfer processes, also owing to the mild and reversible redox properties of the compound. Noticeably, the oxidation potential of $[Ru(bpy)_3]^{2+}$ in aqueous solution is + 1.26 V vs NHE, high enough to access catalytic water oxidation.

In the first example of light driven water oxidation catalyzed by **Ru₄(POM)**, [Ru(bpy)₃]²⁺ was used as the photosensitizer ($\lambda_{max} = 454$ nm, $\varepsilon = 14{,}000$ M^{-1} cm^{-1}) with persulfate as sacrificial acceptor in phosphate buffer [104]. With this system, up to 350 turnovers and an initial turnover frequency of 8×10^{-2} s^{-1} were observed for the tetraruthenium POM, while the quantum yield was found to be 0.045. Similar results were observed for the isostructural catalyst $\{Ru_4(\mu\text{-}O)_5(\mu\text{-}OH)(H_2O)_4(\gamma\text{-}PW_{10}O_{36})_2\}^{9-}$, where phosphorus instead of silicon is present as the central heteroatom of the POM units. The reaction with photogenerated [Ru(bpy)₃]³⁺ in the presence of peroxodisulfate in $Na_2SiF_6/NaHCO_3$ buffer (pH 5.8) affords O_2 with 25% yield (vs 50% with the silicon analog), with turnover frequency reaching 0.13 s^{-1} and total turnover number up to 120 [105].

Besides the excellent features of **Ru₄POM** as an OEC, its good performance in light driven water oxidation with $[Ru(bpy)_3]^{2+}$ as the photosensitizer is also ascribable to fast reaction kinetics of the electron transfer from the catalyst to the photogenerated oxidant (6). This was investigated by using $[Ru(bpy)_3]^{3+}$, photochemically generated by $[Ru(bpy)_3]^{2+}$ in the presence of persulfate anions [106]. In a typical nanosecond

laser flash photolysis experiment (excitation, 355 nm; FWHM, 8 ns), the recovery of the bleach at 450 nm, due to the regeneration of $[Ru(bpy)_3]^{2+}$, is accelerated by increasing **Ru$_4$(POM)** concentration. The kinetics of the hole scavenging, see (6), are pseudo-first order when $[[Ru(bpy)_3]^{3+}] << [$**Ru$_4$(POM)**$]$, depending on the catalyst concentration, and are characterized by a bimolecular rate constant of $(2.1 \pm 0.4) \times 10^9$ M^{-1} s^{-1}, close to the diffusion-controlled limiting rate.

A serious drawback of $[Ru(bpy)_3]^{2+}$ as a photosensitizer is its limited absorption in the visible region. In order to take full advantage of solar radiation, sensitizers having a larger cross section with solar light are desired. In the last 20 years, promising multinuclear Ru(II) and Os(II) dendrimers based on 2,3-bis(2'-pyridyl) pyrazine (dpp) and other related bridging ligands have also been developed [107–113].

First, second, and third generation dendrimers – containing 4, 10, and 22 metal centers, respectively – based on Ru(II) metal centers, bpy as peripheral ligands, and dpp as bridging ligands have been prepared (Fig. 6). For this series of compounds, the absorption spectrum extends beyond 700 nm, due to MLCT bands involving both peripheral bpy and bridging dpp ligands as acceptors, with molar absorption increasing accordingly to the number of chromophores. Interestingly, the first oxidation potential of such compounds occurs around +1.70 V vs NHE, and involves the practically simultaneous one-electron oxidation of all the equivalent peripheral metal centers.

Coupling $[Ru\{(\mu-dpp)Ru(bpy)_2\}_3]^{8+}$ with **Ru$_4$(POM)** has given quite interesting results [114]. The time-profile of oxygen evolution during continuous irradiation of a phosphate-buffered solution (pH = 7.2) containing $[Ru\{(\mu-dpp)Ru(bpy)_2\}_3]^{8+}$,
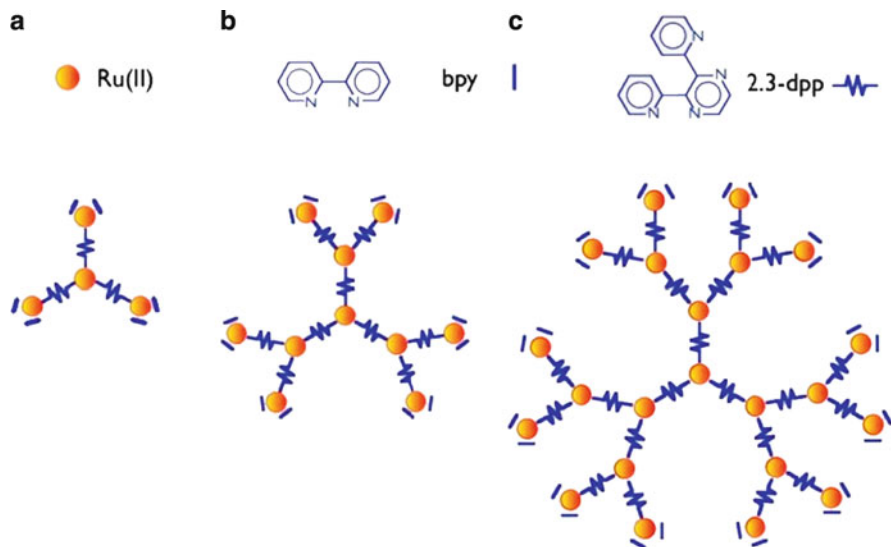

Fig. 6 Schematic representations of dendrimeric ruthenium based polypyridine photosensitizers

Ru$_4$(POM), and persulfate is represented by linear kinetics, maintained up to ca. 80% reaction within the overall experimental time (180 min), achieving 80 turnovers with an initial turnover frequency of $8 \times 10^{-3} \, s^{-1}$. In this time frame, the O$_2$ evolution accounts for a persulfate conversion >90% (average yield over three runs). Similar results are obtained by using different buffers and pH conditions (Na$_2$SiF$_6$, 2.6×10^{-3} M/Na$_2$B$_4$O$_7$, 1.14×10^{-2} M; pH = 5.8).

Besides the outstanding stability of the system (about 5% of photosensitizer degradation within the overall experimental time takes place), the most intriguing result obtained by this experiment is probably the photoreaction quantum yield. Indeed, a quite impressive quantum yield for oxygen production of 0.3 was calculated by irradiating at 550 nm [114]. This value, to the best of our knowledge, is the highest photoreaction quantum yield ever reported for photoinduced water oxidation. The ion pairing between the positively charged Ru-polypyridine sensitizers and the negatively charged **Ru$_4$(POM)** catalyst could favor the rate constant of hole scavenging processes.

3 Carbon Nanotubes Potential in Water Splitting Catalysis

A key component for the preparation of Oxygen Evolving (Photo)Anodes is the templating and conductive substrate which is expected to drive the electron flow from the OEC toward the electrode. A wide surface area, displaying multiple sites for the grafting of the OEC as well as of the sensitizer is a fundamental requisite to allow easy assembly of the molecular components in a modular approach. With this aim, carbon nanotubes have been extensively used [115, 116]. An overview of their use to manage charge transfer processes, including their successful applications in water splitting, will be presented in the next paragraphs.

3.1 Carbon Nanotubes as Active Components in Charge Separation Dyads

Very soon after their discovery both fullerene and carbon nanotubes (CNT), thanks to their extended π-system, were employed for photonic applications spanning from photochemical activated water splitting to CO$_2$ reduction. Light driven water splitting and reduction of CO$_2$ still represent some of the main challenges in the field of renewable energy; but, as far as CNTs are concerned, one of the major obstacles to their use is represented by the complete lack of solubility in most organic and aqueous solvent. Many different attempts to produce chemical modification of CNT skeletons are still a hot topic in carbon nanostructure chemistry [117–119]. Two main pathways, involving non-covalent and covalent chemistry (fig. 7), are pursued, but it is renowned that 1,3 dipolar cycloaddition of azomethine

ylides [120, 121] has paved the way towards the fabrication of CNT-based donor–acceptor ensembles (Fig. 7).

Besides the first report by Nakashima et al. [122] using porphyrins to solubilize single-walled CNTs (SWCNTs), Guldi et al. reported the functionalization of carbon nanotubes employing a ferrocenyl derivative [123]. Ferrocene is a well-known electron donor that is able to promote multi-electron charge transfers. Afterwards, the same group worked on the non-covalent immobilization of porphyrins onto CNTs [124, 125]. In this case, the first step is represented by the solubilization of single-walled CNTs (SWCNTs) upon grafting a poly(sodium 4-styrenesulfonate) polymer (PSS), followed by the immobilization through electrostatic binding of an octapyridinium free base porphyrin salt (SWCNT–PSS$^-$/H$_2$P$^+$). This compound was investigated by cyclic voltammetry and fluorescence, pointing out the possibility to produce, upon excitation, long- (10.2 ns) and short-lived (0.3 ns) charge separation intermediates [124]. On the other hand, porphyrins can be trapped onto the CNTs surface exploiting supramolecular chemistry [125]. Water soluble pyrene salts are known to promote solubilization of CNTs in aqueous solvent thanks to π–π intermolecular interactions. Indeed, trimethyl ammonium acetyl pyrene can be used to suspend CNTs and tailor the binding of an anionic electron donor Zn-porphyrin (ZnP) systems in a hierarchical fashion (SWCNT/pyrene$^+$/ZnP^{8-}). A complete spectroscopic characterization highlights the potential of CNTs for light driven systems as efficient electron acceptors. Both systems were proposed to realize a device for solar energy conversion [126]; SWCNT–PSS$^-$/H$_2$P$^+$ and SWCNT/pyrene$^+$/ZnP^{8-} were deposited onto ITO electrodes and the internal photoconversion efficiencies (IPCE) were measured. The material was deposited exploiting electrostatic interaction and sodium ascorbate was employed to restore the oxidized porphyrins in order to increase the photocurrent. The maximum values of ICPE obtained for the SWCNT-PSS$^-$/H$_2$P$^+$ and SWCNT/pyrene$^+$/ZnP^{8-} are 1.0% and 4.2% respectively, compared with 0.15% and 0.08% for a PDDA^{n+}/C$_{60}$$^{9-}$/ZnP^{8+} cell (where PDDA stands for poly diallyl dimethyl ammonium) or PSS^{n-}/ZnP^{8+} respectively.

Admittedly, covalent functionalization may strongly affect the extended π-system, dramatically changing the electronic properties of SWCNTs. Therefore, in order to maintain the contact between the donor and the acceptor and, at the same time, to preserve the electronic structure of SWCNTs, polymer wrapping constitutes an eligible alternative. Interestingly, with this idea, Guldi et al. proposed the functionalization
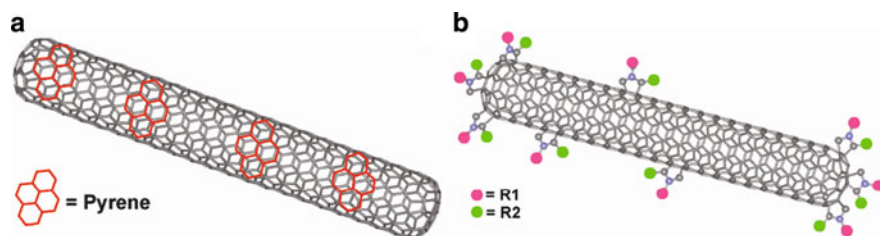
Fig. 7 Examples of modification of CNT skeleton by (**a**) non covalent or (**b**) covalent approaches

of CNTs via the supramolecular association of SWCNTs with linear porphyrin polymers and found efficient charge separation [127]. The polymer was obtained via transesterification of 5-(4-hydroxyphenyl)-10,15,20-tris (4-sulfonatophenyl)porphyrin (H_2P) with methyl methacrylic acid, and subsequent polymerization occurred in the presence of methyl methacrylate (polyH_2P). Purified SWCNT were mixed with the polymer at high temperature with different intervals. Then SWCNT-polyH_2P was characterized by means of several techniques, such as transmission electron microscopy (TEM) or atomic force microscopy (AFM) and absorption spectroscopy. Using the latter technique, the authors proved that the Van Hove absorptions are still preserved, while new characteristics in the spectra appeared, due to mutual interactions between the π electrons of the porphyrin and SWCNT. Porphyrin Q bands underwent a red shift and the Soret band became weaker and broader. Therefore, the excited-state interactions were investigated by means of time-resolved fluorescence, finding the coexistence of two components with different lifetimes, one long-lived (10 ± 1 ns) and one short-lived (0.8 ± 0.4 ns).

Similar studies using differently functionalized pyrene and iron or cobalt porphyrins were proposed to obtain integrated SWCNT nanohybrids [128] and, very interestingly, the use of multi-walled CNTs (MWCNTs) produced remarkable results as well [129, 130]. Complexes of MWCNTs and pyrene were obtained and combined with metallo-porphyrins, giving rise to charge separated species upon photoexcitation. MWCNTs are easier to process and their electronic structure is more suitable to achieve charge transfer and transport due to the presence of concentric internal graphitic layers.

On the other hand, in order to reduce the number of functional groups attached onto the CNT surface, a more elegant procedure involves the synthesis of SWCNTs functionalized polyamidoamide dendrimers. In this way, the extended conjugated π-system is not irreversibly perturbed and it is possible to modify further the periphery of the dendrimer with electron donor molecules to mediate the electron transfer process [131]. Also in this case, the fluorescence kinetic studies brought about the existence of short-lived (0.04 ± 0.01 ns) and long-lived (8.6 ± 1.2 ns) excited states. This kind of construct plays the unambiguous role of antenna system on the nanotube surface.

Control over the electron transfer process has been achieved by binding tetrathiafulvalene derivatives to shortened SWCNTs through their esterification, using spacers with different length [132]. In this way, a fine-tuned donor acceptor conjugate was produced with successful control over the recombination process, as a function of the donor–acceptor separation.

Two different approaches were also adopted to bind phthalocyanines to carbon nanotubes using 1,3-dipolar cycloaddition reaction [133] or amidation of carboxylic residues [134] with the same goal to achieve efficient charge separation mimicking the PSII.

Stemming out of this background, there are several contributions by Ito and D'Souza and collaborators who also proposed the functionalization of SWCNTs using porphyrins to promote the photoinduced electron transfer and charge separation. In 2007, these authors proposed an elegant nanohybrid system fully based on

supramolecular chemistry: SWCNTs were solubilized with an alkyl ammonium derivatized pyrene which interacts through H-bonds with an [18]crown-6 ether porphyrin derivative [135]. In detail, porphyrins were modified with one up to four crown ether substituents, which interact with alkyl ammonium pyrene attached, in turn, to SWCNTs (Fig. 8a). In this assembly, the ammonium ion-crown ether motif displays high importance in the formation of H-bonds, thus tailoring the interaction of porphyrin-SWCNT system and the consequent photoinduced electron transfer and charge separation (Fig. 8b).

It was found that the radical ion pair lifetime was around 100 ns and it was possible to use the nanohybrids to perform the reduction of hexyl viologen dication and the consequent oxidation of 1-benzyl-1,4-dihydronicotinamide in an electron-pooling experiment. In a very similar manner, SWCNTs were also functionalized through the use of a modified imidazole pyrene, with Zn-naphthalocyanine or Zn-porphyrin to achieve donor–acceptor nanohybrids for photoinduced electron transfer [136]. In this case, the authors used the imidazole moiety on pyrene to tailor the axial coordination to the Zn atom. Other assemblies relate to the use of positively or negatively charged pyrene moieties, namely pyrene-COO^- or pyrene-NH_3^+, linked to SWCNTs by means of π–π interactions and, in turn, positively or negative charged porphyrin, respectively. Porphyrins were substituted with N-methyl-pyridyl (positive) or sulfonatophenyl (negative) moieties and interacted with (opposite) charged pyrene by means of electrostatic interactions [137]. Recently D'Souza and coworkers proposed the use of similar functionalization utilizing chiral enriched semiconductor SWCNTs [138]. They also fabricated a solar cell employing a pyrene-tetrasubstituted porphyrin able to link SWCNTs, the higher efficiency being obtained with CNT bearing a narrower band gap. Noteworthy, even though the electron transfer could occur on both the chiralities tested (7,6 narrow band gap
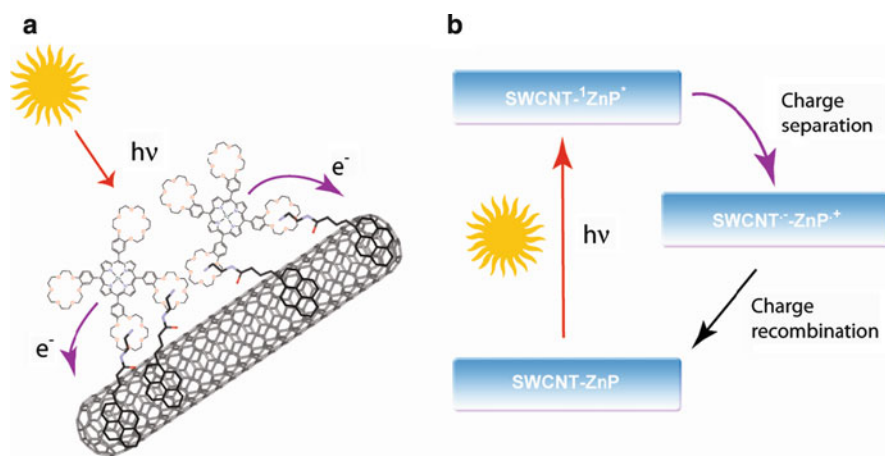
Fig. 8 Schematic representation of a carbon nanotube dyad: (**a**) a possible structure of porphyrin–CNT complex and (**b**) generation mechanism of photoexcited species [135]

and 6,5 wide band gap), the tetra-substituted pyrene porphyrin likely acts as a tweezer and maximizes its interactions with a selected CNT chirality.

Other attempts have recently been proposed regarding the use of phthalocyanine or complex systems of phthalocyanines and/or porphyrins. Phthalocyanines absorb in the red spectral region and phthalocyanine–pyrene conjugates were used to propose new carbon nanotube-based solar cells [139]. SWCNTs were functionalized with a phthalocyanine unit bearing a pyrene moiety and used to build a solar cell with a stable and reproducible photocurrent, among the highest reported with this kind of system (ICPE = 15% and 23% without and with an applied bias of 0.1 V, respectively). To achieve higher yields, other complex systems were evaluated, such as CNTs functionalized with diporphyrin moieties [140]. Lin et al. reported the covalent functionalization of SWCNTs with meso–meso linked diporphyrins, proving the photoinduced electron transfer through steady state emission spectroscopy and calculating the lifetime (145 ns) of the transient ($[H_2P]_2^{\bullet+}$–SWCNTs$^{\bullet-}$) through transient absorption spectroscopy. Finally, Zn-porphyrin/Zn-phthalocyanine dendron functionalized SWCNTs have also been reported in order to increase the absorption spectra of chromophores to achieve higher performance in light harvesting [141].

Towards the fabrication of a device for the efficient light harnessing and harvesting, the possibility to obtain an electrophoretically deposited optically transparent electrode based on SWCNTs for photoelectrochemical cells was reported. After exciting with visible light ($\lambda = 400$ nm), the generation of photocurrent was observed with an IPCE of 0.15%. A threefold increase in the yield was obtained by adding a layer of SnO_2 to increase the surface area of the electrode. In this system, the generation of the photocurrent is due to the conductive properties of SWCNTs, while the photogenerated holes at the CNT electrode surface are transported to the counter electrode through an external circuit [142]. Based on the work proposed by Nakashima and collaborators [122], the supramolecular assembly of SWCNTs with protonated porphyrin through non-covalent interaction [143] was successfully achieved, followed by deposition onto nanostructured SnO_2 [144]. The authors first proved the electron transfer between porphyrin and SWCNTs enabling efficient charge separation. Then the electrochemical deposition of a photoanode was accomplished, using an optically transparent electrode/SnO_2/SWCNT-protonated porphyrin together with the redox couple I^-/I_3^- and a Pt counter electrode. An IPCE of 13% was obtained under an applied voltage of 0.2 V. Besides the use of the chromophore, semiconductor particles can be dispersed on the CNT surface generating photocurrents. Interestingly, upon excitation, charge separation was facilitated by the presence of CNT for charge collection and transport. This material was then supported onto an electrode surface with an IPCE of 14% and of 16% using functionalized (COOH) SWCNTs [145]. In a similar work, TiO_2 nanoparticles were employed to obtain an SWCNT composite material with a nominal ICPE of 16% [146]. More recently, Kamat and collaborators proposed a nanohybrid architecture composed of Ru(II) trisbipyridyl complex onto TiO_2, where SWCNTs reduce charge

recombination. However, the conversion efficiency was not very high because of a more positive Fermi level of SWCNT/TiO_2 composite with respect to pure TiO_2 [147].

## 3.2   Carbon Nanotubes Applied to Water Splitting

CNTs are also widely used to fabricate nanostructured electrodes, due to the possibility (1) to increase the (active) surface area, and (2) to act as electrical wires owing to their conductive properties. Indeed, two recent relevant contributions have been reported concerning the use of CNTs as electrodes in water splitting reaction.

In 2009 Le Goff et al. [148] produced an electrode based on CNT functionalized with a catalyst for H_2 production. This work is based on two main challenges: the first is related to the general need to find high performance substrates to put forward in the research for inter-conversion of water and H_2 in fuel cells, the second is focused on the use of synzymes to avoid Pt based catalysts for hydrogen production. Bioinspired catalysis represents an emerging approach to address this latter issue and enzyme catalytic centers may offer a source of inspiration to design new synthetic catalytic systems. Microorganisms able to metabolize H_2 are known as hydrogenases, and in principle they could be used in fuel cells. Despite their high efficiency, they are oxygen sensitive and consequently present a low stability. In addition, even if several advantages arise from recent developments in biotechnology for enzyme production and purification, their use could be hardly scaled up.

For example, in this case the authors proposed the synthesis of a bisdiphosphine nickel complex inspired to the NiFe hydrogenases and, binding this synzyme to CNTs, they were able to achieve high yield in electrochemical H_2 production. The catalyst was covalently attached to MWCNTs and cyclic voltammetry was extensively employed to characterize fully the performance of the resulting nanostructured electrode. First of all, they were able to immobilize a twofold quantity of catalyst using CNTs with respect to a non-nanostructured electrode, then they also achieved a low overvoltage (200 mV) with a TON for H_2 evolution of 20,000 ($\pm$30%) in 1 h. Moreover, they reproduced the same condition of state-of-the-art proton exchange membrane (PEM) electrolyzers, usually obtained with Pt. In this case, the authors ran the experiments for 10 h with 100,000 ($\pm$30%) TON. Finally, the possibility to employ the same derivative in the reverse reaction for hydrogen oxidation was investigated. Again, after 10 h, they obtained a high TON, 35,000 ($\pm$30%). All in all, this is an example of a promising result for PEM technology and for biomimetic catalysis as well.

More recently, positively functionalized carbon nanotubes were modified by a covalent synthetic route with polycationic dendrimeric chains, fostering the successive decoration with a multi-metallic and polyanionic water oxidation catalyst, the **Ru$_4$(POM)**, with a complementary combination of covalent/non-covalent approaches (Fig. 9) [149].
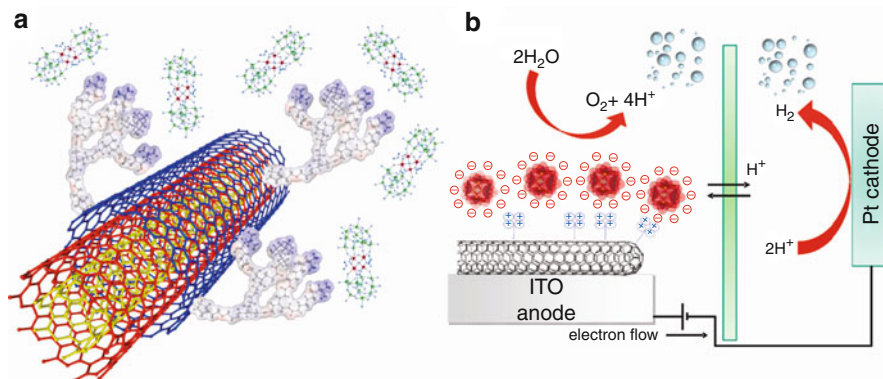
Fig. 9 (**a**) Dendron functionalized-MWCNT complexed with **Ru₄(POM)** molecules and (**b**) scheme of a complete electrochemical cell. Adapted from [149]

Using this methodology, the conjugated π-system of CNTs remained basically unperturbed. In addition, in contrast to SWNTs, MWCNTs allow one to exploit the conductive properties of the CNT internal layers. Thanks to this approach, CNTs conserved their electrical properties and were in close contact with **Ru₄(POM)**, enabling electrocatalytic water splitting and leading to high efficiency at low overpotentials. In detail, the authors proceeded with the divergent growth of a polyamidoamine dendrimer onto MWCNTs achieving second generation bearing free amino groups, further functionalized with positively charged ammonium moieties. Prior to the deposition with polyoxometalates, the CNT derivatives were fully characterized by means of several techniques (TEM, TGA, Raman spectroscopy, AFM), proving the efficiency of functionalization. Afterwards, owing to the resident positive charges, functionalized MWCNTs could serve to scavenge efficiently polyanions via electrostatic interactions. Straightforward techniques in water solutions were adopted to anchor the catalytically active **Ru₄(POM)** to the positively charged PAMAM-modified MWCNTs. By rRaman (resonant Raman) spectra, it was demonstrated that the catalyst maintains its own structure once immobilized onto the CNT surface, while, by means of high-resolution TEM analysis, the presence of metal-centered domains ascribed to **Ru₄(POM)** on CNTs was confirmed. These **Ru₄(POM)**-CNTs were deposited onto ITO electrodes to probe the catalytic activity by cyclic voltammetry. Electrodes doped with **Ru₄(POM)** derivatives exhibited an oxidation at 0.9 V, followed by the onset of a catalytic wave at applied voltages >1.10 V, due to water oxidation. The superior performance of the nanostructured electrode is likely due to coupling of the redox features of **Ru₄(POM)** with the MWCNT, enabling electrical wiring of the hybrid material. Indeed, turnover frequency values in the range 36–306 h^{-1} were achieved depending on the applied overpotential: an appreciable catalytic current with a remarkable TOF (36 h^{-1}) was observed beginning at $\eta = 0.35$ V, and reached a peak performance of 306 h^{-1} at $\eta = 0.60$ V. These results address the importance of hybrid interfaces/contacts to control and promote electron transfer events at heterogeneous surfaces.

4 Conclusions and Outlook

Artificial photosynthetic methods represent the future of solar fuel production. The key concept is not to reproduce the exact copy of the natural system in vitro. This is too complex and inefficient to some extent; our mission is rather to capture and transpose the same principles in smaller, simpler, more robust, and more efficient man-made arrays. According to bio-inspired guidelines, H_2 photo-production requires a modular organization of functional molecules/materials solving some fundamental tasks: (1) collection/harvesting of solar light, (2) light-to-"electricity" conversion by a charge separation center, and (3) scavenging of the separated charges by catalytic manifolds where H_2 and O_2 evolution occur separately. In this chemistry, H_2O is the renewable multi-electron source, providing a total of four electrons/mol by the oxidative half reaction. The key question around the artificial solar-to-energy equation ($2H_2O + 4$ hv $\rightarrow 2H_2 + O_2$) stems from the multi-electron/photon requirement, while any photo-induced charge separation occurs generally as a one electron/photon step. Therefore, the crucial points are: (1) the repetition of light absorption/electron transfer events and (2) the interplay of efficient/robust catalysts managing such sequential evolution at a sustainable rate that is fast enough to overcome the competing charge recombination/deactivation dead-end. In this vision, the sequence of light collection, charge separation, and catalytic events calls for a precise architectural control and manipulation at the nanoscale level. The final aim is to devise the optimal matching of catalytic domains/photoactive and conductor materials, integrated in a functional geometry/multi-arrays, so as to boost the catalytic performance and enhance the interfacial charge transfer rate. The engineering of these diverse components in a single operating device is one of the greatest challenges in contemporary chemistry and remains one of the most ambitious goals towards a sustainable hydrogen economy.

References

1. Yano J, Kern J, Sauer K, Latimer MJ, Pushkar Y, Biesiadka J, Loll B, Saenger W, Messinger J, Zouni A, Yachandra VK (2006) Where water is oxidized to dioxygen: structure of the photosynthetic Mn$_4$Ca cluster. Science 314:821–825
2. Ferreira KN, Iverson TM, Maghlaoui K, Barber J, Iwata S (2004) Architecture of the photosynthetic oxygen-evolving center. Science 303:1831–1838
3. Loll B, Kern J, Saenger W, Zouni A, Biesiadka J (2005) Towards complete cofactor arrangement in the 3.0 Å resolution structure of Photosystem II. Nature 438:1040–1044
4. Haumann M, Liebisch P, Müller C, Barra M, Grabolle M, Dau H (2005) Photosynthetic O$_2$ formation tracked by time-resolved X-ray experiments. Science 310:1019–1021

5. McEvoy JP, Brudvig GW (2006) Water-splitting chemistry of Photosystem II. Chem Rev 106:4455–4483

6. Brudvig GW (ed) (2008) Special issue on the role of manganese in Photosystem II. Coord Chem Rev 252:231–468

7. Hammarstrom L, Hammes-Schiffer S (eds) (2009) Special issue on artificial photosynthesis and solar fuels. Acc Chem Res 42:1859–2029

8. Kok B, Forbush B, McGloin M (1970) Cooperation of charges in photosynthetic O_2 evolution-I, a linear four step mechanism. Photochem Photobiol 11:457–475

9. Bard AJ, Fox MA (1995) Artificial photosynthesis: solar splitting of water to hydrogen and oxygen. Acc Chem Res 28:141–145

10. Lewis NS, Nocera DG (2006) Powering the planet: chemical challenges in solar energy utilization. Proc Natl Acad Sci USA 103:15729–15735

11. Armaroli A, Balzani V (2007) The future of energy supplies: challenges and opportunities. Angew Chem Int Ed 46:52–66

12. Gray HB (2009) Powering the planet with solar fuel. Nat Chem 1:7

13. Gust D, Moore TA, Moore AL (2009) Solar fuels via artificial photosynthesis. Acc Chem Res 42:1890–1898

14. Nocera DG, Guldi DM (eds) (2009) Special issue on renewable energy. Chem Soc Rev 38:1–293

15. Krassen H, Ott S, Heberle J (2011) In vitro hydrogen production using energy from the sun. Phys Chem Chem Phys 13:47–57

16. Huynh MHV, Dattelbaum DM, Meyer TJ (2005) Exited state electron and energy transfer in molecular assemblies. Coord Chem Rev 249:457–483

17. Balzani V, Credi A, Venturi M (2008) Photochemical conversion of solar energy. Chem-SusChem 1:26–58

18. Wasielewski M (2009) Self-assembly strategies for integrating light harvesting and charge separation in artificial photosynthetic systems. Acc Chem Res 42:1910–1921

19. Albinsson B, Mårtensson J (2008) Long-range electron and excitation energy transfer in donor–bridge–acceptor systems. J Photochem Photobiol C 9:138–155

20. Magnuson A, Anderlund M, Johansson O, Lindblad P, Lomoth R, Polivka T, Ott S, Stensjö K, Styring S, Sundström V, Hammarström L (2009) Biomimetic and microbial approaches to solar fuel generation. Acc Chem Res 42:1899–1909

21. Gust D, Moore TA, Moore AL (2001) Mimicking photosynthetic solar energy transduction. Acc Chem Res 34:40–48

22. Hambourger M, Kodis G, Vaughn MD, Moore GF, Gust D, Moore AL, Moore TA (2009) Solar energy conversion in a photoelectrochemical biofuel cell. Dalton Trans 9979–9989

23. Benniston AC, Harriman A (2008) Artificial photosynthesis. Mater Today 11:26–34

24. Huynh MHV, Meyer TJ (2007) Proton-coupled electron transfer. Chem Rev 107:5004–5064

25. Meyer TJ, Huynh MHV, Thorp HH (2007) The possible role of proton-coupled electron transfer (PCET) in water oxidation by Photosystem II. Angew Chem Int Ed 46:5284–5304

26. Eisenberg R, Gray HB guest editors (2008) Special issue on forum on making oxygen. Inorg Chem 47:1697–1861

27. Meyer TJ (2008) Catalysis: the art of splitting water. Nature 451:778–779

28. Kiwi J, Grätzel M (1979) Ruthenium oxide, a suitable redox catalyst to mediate oxygen production from water. Chimia 33:289–291

29. Kiwi J, Grätzel M (1979) Colloidal redox catalysts for evolution of oxygen and for light-induced evolution of hydrogen from water. Angew Chem Int Ed 18:624–626

30. Kalayanasundaram K, Grätzel M (1979) Cyclic cleavage of water into H_2 and O_2 by visible light with coupled redox catalysts. Angew Chem Int Ed 18:701–702

31. Kiwi J, Borgarello E, Pellizzetti E, Visca M, Grätzel M (1980) Cyclic water cleavage by visible light: drastic improvement of yield of H_2 and O_2 with bifunctional redox catalysts. Angew Chem Int Ed 19:646–648

32. Harriman A, Richoux MC, Christensen PA, Mosseri S, Neta P (1987) Redox reactions with colloidal metal oxides. Comparison of radiation-generated and chemically generated $RuO_2 \cdot 2H_2O$. J Chem Soc Faraday Trans 1 83:3001–3014

33. Harriman A, Pickering IJ, Thomas JM, Christensen PA (1988) Metal oxides as heterogeneous catalysts for oxygen evolution under photochemical conditions. J Chem Soc Faraday Trans 1 84:2795–2806

34. Mills A (1989) Heterogeneous redox catalysts for oxygen and chlorine evolution. Chem Soc Rev 18:285–316

35. Mills A, Duckmanton PA, Reglinski J (2010) A simple, novel method for preparing an effective water oxidation catalyst. Chem Commun 46:2397–2398

36. Puntoriero F, Sartorel A, Orlandi M, La Ganga G, Serroni S, Bonchio M, Scandola F, Campagna S (2011) Photoinduced water oxidation using dendrimeric Ru(II) complexes as photosensitizers. Coord Chem Rev. doi:10.1016/j.ccr.2011.01.026

37. Okeyoshi K, Yoshida R (2010) Oxygen-generating gel systems induced by visible light. Adv Funct Mater 20:708–714

38. Pillai KC, Kumar AS, Zen JM (2000) J Mol Cat A Chem 160:277–285

39. Kiwi J, Grätzel M (1978) Oxygen evolution from water via redox catalysis. Angew Chem Int Ed 17:860–861

40. Morris ND, Suzuki M, Mallouk TE (2004) Kinetics of electron transfer and oxygen evolution in the reaction of $[Ru(bpy)_3]^{3+}$ with colloidal iridium oxide. J Phys Chem A 108:9115–9119

41. Hara M, Waraksa CC, Lean JT, Lewis BA, Mallouk TE (2000) Photocatalytic water oxidation in a buffered tris(2,2'-bipyridyl)ruthenium complex-colloidal IrO_2 system. J Phys Chem A 104:5275–5280

42. Hoertz PG, Kim YI, Youngblood WJ, Mallouk TE (2007) Bidentate dicarboxylate capping groups and photosensitizers control the size of IrO_2 nanoparticle catalysts for water oxidation. J Phys Chem B 111:6845–6856

43. Yagi M, Tomita E, Salita S, Kuwabara T, Nagai K (2005) Self-assembly of active IrO_2 colloid catalyst on an ITO electrode for efficient electrochemical water oxidation. J Phys Chem B 109:21489–21491

44. Nakagawa T, Bjorge NS, Murray RW (2009) Electrogenerated IrO_x nanoparticles as dissolved redox catalysts for water oxidation. J Am Chem Soc 131:15578–15579

45. Nakagawa T, Beasley CA, Murray RW (2009) Efficient electro-oxidation of water near its reversible potential by a mesoporous IrOx nanoparticle film. J Phys Chem C 113:12958–12961

46. Hara M, Lean JT, Mallouk TE (2001) Photocatalytic oxidation of water by silica-supported tris(4,4'-dialkyl-2,2'-bipyridyl)ruthenium polymeric sensitizers and colloidal iridium oxide. Chem Mater 13:4668–4675

47. Youngblood WJ, Lee SHA, Kobayashi Y, Hernandez-Pagan EA, Hoertz PG, Moore TA, Moore AL, Gust D, Mallouk TE (2009) Photoassisted overall water splitting in a visible light-absorbing dye-sensitized photoelectrochemical cell. J Am Chem Soc 131:926–927

48. La Ganga G, Nastasi F, Campagna S, Puntoriero F (2009) Dalton Trans 9997–9999

49. Youngblood JW, Lee SHA, Maeda K, Mallouk TE (2009) Visible light water splitting using dye-sensitized oxide semiconductors. Acc Chem Res 42:1966–1973

50. Han H, Frei H (2008) In situ spectroscopy of water oxidation at Ir oxide nanocluster driven by visible TiOCr charge-transfer chromophore in mesoporous silica. J Phys Chem C 112:16156–16159

51. Tilley SD, Cornuz M, Sivula K, Grätzel M (2010) Light-induced water splitting with hematite: improved nanostructure and iridium oxide catalysis. Angew Chem Int Ed 49:6405–6408

52. Shafirovich VY, Khannanov NK, Strelets VV (1980) Chemical and light-induced catalytic water oxidation. Nouv J Chim 4:81–84

53. Brunschwig BS, Chou MH, Creutz C, Ghosh P, Sutin N (1983) Mechanisms of water oxidation to oxygen: cobalt(IV) as an intermediate in the aquocobalt(II)-catalyzed reaction. J Am Chem Soc 105:4832–4833

54. Kanan MW, Nocera DG (2008) In situ formation of an oxygen-evolving catalyst in neutral water containing phosphate and Co^{2+}. Science 321:1072–1075

55. Kanan MW, Surendranath Y, Nocera DG (2009) Cobalt–phosphate oxygen-evolving compound. Chem Soc Rev 38:109–114

56. Surendranath Y, Dincă M, Nocera DG (2009) Electrolyte-dependent electrosynthesis and activity of cobalt-based water oxidation catalysts. J Am Chem Soc 131:2615–2620

57. Kanan MW, Yano J, Surendranath Y, Dincă M, Yachandra VK, Nocera DG (2010) Structure and Valency of a Cobalt-Phosphate Water Oxidation Catalyst Determined by in Situ X-ray Spectroscopy. J Am Chem Soc 132:13692–13701

58. Surendranath Y, Kanan MW, Nocera DG (2010) Mechanistic studies of the oxygen evolution reaction by a cobalt-phosphate catalyst at neutral pH. J Am Chem Soc 132:16501–16509

59. McAlpin JG, Surendranath Y, Dincă M, Stich TA, Stoian SA, Casey WH, Nocera DG, Britt RD (2010) EPR evidence for Co(IV) species produced during water oxidation at neutral pH. J Am Chem Soc 132:6882–6883

60. Lutterman DA, Surendranath Y, Nocera DG (2009) A self-healing oxygen-evolving catalyst. J Am Chem Soc 131:3838–3839

61. Zong DK, Gamelin DR (2010) Photoelectrochemical water oxidation by cobalt catalyst ("Co−Pi")/α-Fe_2O_3 composite photoanodes: oxygen evolution and resolution of a kinetic bottleneck. J Am Chem Soc 132:4202–4207

62. Steinmiller EMP, Choi KS (2009) Photochemical deposition of cobalt-based oxygen evolving catalyst on a semiconductor photoanode for solar oxygen production. Proc Natl Acad Sci USA 106:20633–20636

63. Kay A, Cesar I, Grätzel M (2006) New benchmark for water photooxidation by nanostructured α-Fe_2O_3 films. J Am Chem Soc 128:15714–15721

64. Jiao F, Frei H (2009) Nanostructured cobalt oxide clusters in mesoporous silica as efficient oxygen-evolving catalysts. Angew Chem Int Ed 48:1841–1844

65. Li Y, Hasin P, Wu Y (2010) $Ni_xCo_{3−x}O_4$ nanowire arrays for electrocatalytic oxygen evolution. Adv Mater 22:1926–1929

66. Okuno Y, Yonemitsu O, Chiba Y (1983) Manganese dioxide as specific redox catalyst in the photosensitized oxygen generation from water. Chem Lett 12:815–818

67. Jiao F, Frei H (2010) Nanostructured manganese oxide clusters supported on mesoporous silica as efficient oxygen-evolving catalysts. Chem Commun 46:2920–2922

68. Najafpour MM, Ehrenberg T, Wiechen M, Kurz P (2010) Calcium manganese(III) oxides ($CaMn_2O_4.xH_2O$) as biomimetic oxygen-evolving catalysts. Angew Chem Int Ed 49:2233–2237

69. Gersten SW, Samuels GJ, Meyer TJ (1982) Catalytic oxidation of water by an oxo-bridged ruthenium dimer. J Am Chem Soc 104:4029–4030

70. Liu F, Conception JJ, Jurss JW, Cardolaccia T, Templeton JL, Meyer TJ (2008) Mechanisms of water oxidation from the blue dimer to Photosystem II. Inorg Chem 47:1727–1752

71. Jurss JW, Concepcion JC, Norris MR, Templeton JL, Meyer TJ (2010) Surface catalysis of water oxidation by the blue ruthenium dimer. Inorg Chem 49:3980–3982

72. Deng Z, Tseng HW, Zong R, Wang D, Thummel RP (2008) Preparation and study of a family of dinuclear Ru(II) complexes that catalyze the decomposition of water. Inorg Chem 47:1835–1848

73. Wada T, Tsuge K, Tanaka K (2001) Syntheses and redox properties of bis(hydroxoruthenium) complexes with quinone and bipyridine ligands. Water-oxidation catalysis. Inorg Chem 40:329–337

74. Duan L, Xu Y, Zhang P, Wang M, Sun L (2010) Visible light-driven water oxidation by a molecular ruthenium catalyst in homogeneous system. Inorg Chem 49:209–215

75. Xu Y, Duan L, Tong L, Akermark B, Sun L (2010) Visible light-driven water oxidation catalyzed by a highly efficient dinuclear ruthenium complex. Chem Commun 46:6506–6508

76. Borzoglian F, Mola J, Rodriguez M, Romero I, Nenet-Buchholtz J, Fontrodona X, Cramer CJ, Gagliardi L, Llobet A (2009) The Ru−Hbpp water oxidation catalyst. J Am Chem Soc 131:15176–15187

77. Sartorel A, Carraro M, Scorrano G, De Zorzi R, Geremia S, McDaniel ND, Bernhard S, Bonchio M (2008) Polyoxometalate embedding of a tetraruthenium(IV)-oxo-core by template-directed metalation of $[\gamma\text{-SiW}_{10}O_{36}]^{8-}$: a totally inorganic oxygen-evolving catalyst. J Am Chem Soc 130:5006–5007

78. Geletii YV, Botar B, Köegerler P, Hillesheim DA, Musaev DG, Hill CL (2008) An all-inorganic, stable, and highly active tetraruthenium homogeneous catalyst for water oxidation. Angew Chem Int Ed 47:3896–3899

79. McDaniel ND, Coughlin MJ, Tinker LL, Bernhard S (2008) Cyclometalated iridium(III) aquo complexes: efficient and tunable catalysts for the homogeneous oxidation of water. J Am Chem Soc 130:210–217

80. Limburg J, Vrettos JS, Liable-Sands LM, Rheingold AL, Crabtree RH, Brudvig GW (1999) A functional model for O–O bond formation by the O_2-evolving complex in Photosystem II. Science 283:1524–1527

81. Cady CW, Crabtree RH, Brudvig GW (2008) Functional models for the oxygen-evolving complex of Photosystem II. Coord Chem Rev 252:444–455

82. Tagore R, Crabtree RH, Brudvig GW (2008) Oxygen evolution catalysis by a dimanganese complex and its relation to photosynthetic water oxidation. Inorg Chem 47:1815–1823

83. Dismukes GC, Brimblecomb R, Felton GA, Pryadun RS, Sheats JE, Spiccia L, Swiegers GF (2009) Development of bioinspired Mn_4O_4−cubane water oxidation catalysts: lessons from photosynthesis. Acc Chem Res 42:1935–1943

84. Robinson DM, Go YB, Greenblatt M, Dismukes CG (2010) Water oxidation by λ-MnO_2: catalysis by the cubical Mn_4O_4 subcluster obtained by delithiation of spinel $LiMn_2O_4$. J Am Chem Soc 132:11467–11469

85. Yin Q, Tan JM, Besson C, Geletii YV, Musaev DG, Kuznetsov AE, Luo Z, Hardcastle KI, Hill CL (2010) A fast soluble carbon-free molecular catalyst based on abundant metals. Science 328:342–345

86. Ellis WC, McDaniel ND, Bernhard S, Collins TJ (2010) Fast water oxidation using iron. J Am Chem Soc 132:10990–10991

87. Howells AR, Sankarraj A, Shannon C (2004) A diruthenium-substituted polyoxometalate as an electrocatalyst for oxygen generation. J Am Chem Soc 126:12258–12259

88. Sartorel A, Mirò P, Salvadori E, Romain S, Carraro M, Scorrano G, Di Valentin M, Llobet A, Bo C, Bonchio M (2009) Water oxidation at a tetraruthenate core stabilized by polyoxometalate ligands: experimental and computational evidence to trace the competent intermediates. J Am Chem Soc 131:16051–16053

89. Geletii YV, Besson C, Hou Y, Yin Q, Musaev DG, Quiñonero D, Cao R, Hardcastle KI, Proust A, Kögerler P, Hill CL (2009) Structural, physicochemical, and reactivity properties of an all-inorganic, highly active tetraruthenium homogeneous catalyst for water oxidation. J Am Chem Soc 131:17360–17370

90. Quiñonero D, Kaledin AL, Kuznetsov AE, Geletii YV, Besson C, Hill CL, Musaev DG (2010) Computational studies of the geometry and electronic structure of an all-inorganic and homogeneous tetra-Ru-polyoxotungstate catalyst for water oxidation and its four subsequent one-electron oxidized forms. J Phys Chem A 114:535–542

91. Cao R, Ma H, Geletii YV, Hardcastle KI, Hill CL (2009) Structurally characterized Iridium (III)-containing polytungstate and catalytic water oxidation activity. Inorg Chem 48:5596–5598

92. Kohl SW, Weiner L, Schwartsburd L, Konstantinovski L, Shimon LJW, Ben-David Y, Iron MA, Milstein D (2009) Consecutive thermal H_2 and light-induced O_2 evolution from water promoted by a metal complex. Science 324:74–77

93. Gorlin Y, Jamarillo TF (2010) A bifunctional nonprecious metal catalyst for oxygen reduction and water oxidation. J Am Chem Soc 132:13612–13614

94. Yamazaki H, Shouji A, Kajita M, Yagi M (2010) Electrocatalytic and photocatalytic water oxidation to dioxygen based on metal complexes. Coord Chem Rev 254:2483–2491

95. Yagi M, Toda M, Yamada S, Yamazaki H (2010) An artificial model of photosynthetic Photosystem II: visible-light-derived O_2 production from water by a di-μ-oxo-bridged manganese dimer as an oxygen evolving center. Chem Commun 46:8594–8596

96. Cape JL, Hurst JK (2008) Detection and mechanistic relevance of transient ligand radicals formed during $[Ru(bpy)_2(OH_2)]_2O^{4+}$-catalyzed water oxidation. J Am Chem Soc 130:827–829

97. Brimblecomb R, Koo A, Dismukes GC, Swiegers GF, Spiccia L (2010) Solar driven water oxidation by a bioinspired manganese molecular catalyst. J Am Chem Soc 132:2892–2894

98. Li L, Duan L, Xu Y, Gorlov M, Hagfeldt A, Sun L (2010) A photoelectrochemical device for visible light driven water splitting by a molecular ruthenium catalyst assembled on dye-sensitized nanostructured TiO_2. Chem Commun 46:7307–7309

99. Xu Y, Fischer A, Duan L, Tong L, Gabrielsson E, Akermark B, Sun L (2010) Chemical and light-driven oxidation of water catalyzed by an efficient dinuclear ruthenium complex. Angew Chem Int Ed 49:8934–8937

100. Nam YS, Magyar AP, Lee D, Kim JW, Yun DS, Park H, Pollom TS, Weitz DA, Belcher AM (2010) Biologically templated photocatalytic nanostructures for sustained light-driven water oxidation. Nat Nanotechnol 5:340–344

101. Juris A, Balzani V, Barigelletti F, Campagna S, Belser P, von Zelewsky A (1988) Ru(II) polypyridine complexes: photophysics, photochemistry, eletrochemistry, and chemilumines-cence. Coord Chem Rev 84:85–277

102. Meyer TJ (1986) Photochemistry of metal coordination complexes: metal to ligand charge transfer excited states. Pure Appl Chem 58:1193–1206

103. Balzani V, Scandola F (1991) Supramolecular photochemistry. Horwood, Chichester

104. Geletii YV, Huang Z, Hou Y, Musaev DG, Lian T, Hill CL (2009) Homogeneous light-driven water oxidation catalyzed by a tetraruthenium complex with all inorganic ligands. J Am Chem Soc 131:7522–7523

105. Besson C, Huang Z, Geletii YV, Lense S, Hardcastle KI, Musaev DG, Lian T, Proust A, Hill CL (2010) $Cs_9[(γ-PW_{10}O_{36})_2Ru_4O_5(OH)(H_2O)_4]$, a new all-inorganic, soluble catalyst for the efficient visible-light-driven oxidation of water. Chem Commun 46:2784–2786

106. Orlandi M, Argazzi R, Sartorel A, Carraro M, Scorrano G, Bonchio M, Scandola F (2010) Ruthenium polyoxometalate water splitting catalyst: very fast hole scavenging from photo-generated oxidants. Chem Commun 46:3152–3154

107. Campagna S, Denti G, Serroni S, Juris A, Venturi M, Ricevuto V, Balzani V (1995) Dendrimers of nanometer size based on metal complexes: luminescent and redox-active polynuclear metal complexes containing up to twenty-two metal centers. Chem Eur J 1: 211–221

108. Serroni S, Juris A, Venturi M, Campagna S, Resino IR, Denti G, Credi A, Balzani V (1997) Polynuclear metal complexes of nanometre size. A versatile synthetic strategy leading to luminescent and redox-active dendrimers made of an osmium(II)-based core and ruthenium (II)-based units in the branches. J Mater Chem 7:1227–1236

109. Balzani V, Campagna S, Denti G, Juris A, Serroni S, Venturi M (1998) Designing dendri-mers based on transition-metal complexes. Light-harvesting properties and predetermined redox patterns. Acc Chem Res 31:26–34

110. Venturi M, Serroni S, Juris A, Campagna S, Balzani V (1998) Electrochemical and photo-chemical properties of metal-containing dendrimers. Top Curr Chem 197:193–228

111. Serroni S, Campagna S, Puntoriero F, Di Pietro C, Loiseau F, McClenaghan ND (2001) Dendrimers based on ruthenium(II) and osmium(II) polypyridine complexes and the approach of using complexes as ligands and complexes as metals. Chem Soc Rev 30: 367–375

112. Puntoriero F, Serroni S, Galletta M, Juris A, Licciardello A, Chiorboli C, Campagna S, Scandola F (2005) A new heptanuclear dendritic ruthenium(II) complex featuring photoin-duced energy transfer across high-energy subunits. Chemphyschem 6:129–138

113. Larsen J, Puntoriero F, Pascher T, McClenaghan N, Campagna S, Åkesson E, Sundström V (2007) Extending the light-harvesting properties of transition-metal dendrimers. Chemphyschem 8:2643–2951
114. Puntoriero F, La Ganga G, Sartorel A, Carraro M, Scorrano G, Bonchio M, Campagna S (2010) Photo-induced water oxidation with tetra-nuclear ruthenium sensitizer and catalyst: a unique 4×4 ruthenium interplay triggering high efficiency with low-energy visible light. Chem Commun 46:4725–4727
115. Guldi DM (2007) Nanometer scale carbon structures for charge-transfer systems and photovoltaic applications. Phys Chem Chem Phys 9:1400–1420
116. Guldi DM, Rahman GMA, Sgobba V, Ehli C (2006) Multifunctional molecular carbon materials – from fullerenes to carbon nanotubes. Chem Soc Rev 35:471–487
117. Tasis D, Tagmatarchis N, Bianco A, Prato M (2006) Chemistry of carbon nanotubes. Chem Rev 106:1105–1136
118. Hirsch A (2002) Functionalization of single-walled carbon nanotubes. Angew Chem Int Ed 41:1853–1859
119. Singh P, Campidelli S, Giordani S, Bonifazi D, Bianco A, Prato M (2009) Organic functionalisation and characterisation of single-walled carbon nanotubes. Chem Soc Rev 38:2214–2230
120. Georgakilas V, Tagmatarchis N, Pantarotto D, Bianco A, Briand J, Prato M (2002) Amino acid functionalisation of water soluble carbon nanotubes. Chem Commun 24:3050–3051
121. Georgakilas V, Kordatos K, Prato M, Guldi DM, Holzinger M, Hirsch A (2002) Organic functionalization of carbon nanotubes. J Am Chem Soc 124:760–761
122. Murakami H, Nomura T, Nakashima N (2003) Noncovalent porphyrin-functionalized single-walled carbon nanotubes in solution and the formation of porphyrin-nanotube nanocomposites. Chem Phys Lett 378:481–485
123. Guldi DM, Marcaccio M, Paolucci D, Paolucci F, Tagmatarchis N, Tasis D, Vázquez E, Prato M (2003) Single-wall carbon nanotube–ferrocene nanohybrids: observing intramolecular electron transfer in functionalized SWNTs. Angew Chem Int Ed 42:4206–4209
124. Guldi DM, Rahman GMA, Ramey J, Marcaccio M, Paolucci D, Paolucci F, Qin S, Ford WT, Balbinot D, Jux N, Tagmatarchis N, Prato M (2004) Donor–acceptor nanoensembles of soluble carbon nanotubes. Chem Commun 18:2034–2035
125. Guldi DM, Rahman GMA, Jux N, Tagmatarchis N, Prato M (2004) Integrating single-wall carbon nanotubes into donor-acceptor nanohybrids. Angew Chem Int Ed 43:5526–5530
126. Guldi DM, Rahman GMA, Prato M, Jux N, Qin S, Ford W (2005) Single-wall carbon nanotubes as integrative building blocks for solar-energy conversion. Angew Chem Int Ed 44:2015–2018
127. Guldi DM, Taieb H, Rahman GMA, Tagmatarchis N, Prato M (2005) Novel photoactive single-walled carbon nanotube-porphyrin polymer wraps: efficient and long-lived intracomplex charge separation. Adv Mater 17:871–875
128. Guldi DM, Rahman GMA, Jux N, Balbinot D, Hartnagel U, Tagmatarchis N, Prato M (2005) Functional single-wall carbon nanotube nanohybrids associating SWNTs with water-soluble enzyme model systems. J Am Chem Soc 127:9830–9838
129. Guldi DM, Rahman GMA, Jux N, Balbinot D, Tagmatarchis N, Prato M (2005) Multiwalled carbon nanotubes in donor-acceptor nanohybrids towards long-lived electron transfer products. Chem Commun 15:2038–2040
130. Guldi DM, Rahman GMA, Zerbetto F, Prato M (2005) Carbon nanotubes in electron donor−acceptor nanocomposites. Acc Chem Res 38:871–878
131. Campidelli S, Sooambar C, Diz E, Ehli C, Guldi D, Prato M (2006) Dendrimer-functionalized single-wall carbon nanotubes: synthesis, characterization, and photoinduced electron transfer. J Am Chem Soc 128:12544–12552
132. Herranz MÁ, Martín N, Campidelli S, Prato M, Brehm G, Guldi DM (2006) Control over electron transfer in tetrathiafulvalene-modified single-walled carbon nanotubes. Angew Chem Int Ed 45:4478–4482

133. Ballesteros B, de la Torre G, Ehli C, Rahman GMA, Agulló-Rueda F, Guldi DM, Torres T (2007) Single-wall carbon nanotubes bearing covalently linked phthalocyanines−photoinduced electron transfer. J Am Chem Soc 129:5061–5068

134. Zhang X, Cui X, Liu Q, Zhang F (2009) Photoinduced multi-electron transfer in the D_n–A system consisting of multi-phthalocyanines linked to one carbon nanotube. Phys Chem Chem Phys 11:3566–3572

135. D'Souza F, Chitta R, Sandanayaka ASD, Subbaiyan NK, D'Souza L, Araki Y, Ito O (2007) Self-assembled single-walled carbon nanotube:zinc–porphyrin hybrids through ammonium ion–crown ether interaction: construction and electron transfer. Chem Eur J 13:8277–8284

136. Chitta R, Sandanayaka ASD, Schumacher AL, D'Souza L, Araki Y, Ito O, D'Souza F (2007) Donor−acceptor nanohybrids of zinc naphthalocyanine or zinc porphyrin noncovalently linked to single-wall carbon nanotubes for photoinduced electron transfer. J Phys Chem C 111:6947–6955

137. Sandanayaka ASD, Chitta R, Subbaiyan NK, D'Souza L, Ito O, D'Souza F (2009) Photoinduced charge separation in ion-paired porphyrin−single-wall carbon nanotube donor−acceptor hybrids. J Phys Chem C 113:13425–13432

138. Maligaspe E, Sandanayaka ASD, Hasobe T, Ito O, D'Souza F (2010) Sensitive efficiency of photoinduced electron transfer to band gaps of semiconductive single-walled carbon nanotubes with supramolecularly attached zinc porphyrin bearing pyrene glues. J Am Chem Soc 132:8158–8164

139. Bartelmess J, Ballesteros B, de la Torre G, Kiessling D, Campidelli S, Prato M, Torres T, Guldi DM (2010) Phthalocyanine−pyrene conjugates: a powerful approach toward carbon nanotube solar cells. J Am Chem Soc 132:16202–16211

140. He L, Zhu Y, Zheng J, Ma Y, Chen Y (2010) Meso-meso linked diporphyrin functionalized single-walled carbon nanotubes. J Photochem Photobiol A Chem 216:15–23

141. Le Ho KH, Rivier L, Jousselme B, Jégou P, Filoramo A, Campidelli S (2010) Zn-porphyrin/Zn-phthalocyanine dendron for SWNT functionalisation. Chem Commun 46:8731–8733

142. Barazzouk S, Hotchandani S, Vinodgopal K, Kamat PV (2004) Single-wall carbon nanotube films for photocurrent generation. A prompt response to visible-light irradiation. J Phys Chem B 108:17015–17018

143. Hasobe T, Fukuzumi S, Kamat PV (2005) Ordered assembly of protonated porphyrin driven by single-wall carbon nanotubes. J- and H-aggregates to nanorods. J Am Chem Soc 127:11884–11885

144. Hasobe T, Fukuzumi S, Kamat PV (2006) Organized assemblies of single wall carbon nanotubes and porphyrin for photochemical solar cells: charge injection from excited porphyrin into single-walled carbon nanoubes. J Phys Chem B 110:25477–25484

145. Vietmeyer F, Seger B, Kamat PV (2007) Anchoring ZnO particles on functionalized single wall carbon nanotubes. Excited state interactions and charge collection. Adv Mater 19:2935–2940

146. Kongkanand A, Martínez Domínguez R, Kamat PV (2007) Single wall carbon nanotube scaffolds for photoelectrochemical solar cells. Capture and transport of photogenerated electrons. Nano Lett 7:676–680

147. Brown P, Takechi K, Kamat PV (2008) Single-walled carbon nanotube scaffolds for dye-sensitized solar cells. J Phys Chem C 112:4776–4782

148. Le Goff A, Artero V, Jousselme B, Dinh Tran P, Guillet N, Métayé R, Fihri A, Palacin S, Fontecave M (2009) From hydrogenases to noble metal-free catalytic nanomaterials for H_2 production and uptake. Science 326:1384–1387

149. Toma FM, Sartorel A, Iurlo M, Carraro M, Parisse P, Maccato C, Rapino S, Rodriguez Gonzalez B, Amenitsch H, Da Ros T, Casalis L, Goldoni A, Marcaccio M, Scorrano G, Scoles G, Paolucci F, Prato M, Bonchio M (2010) Efficient water oxidation at carbon nanotube/polyoxometalate electrocatalytic interfaces. Nat Chem 2:826–831

Photocatalytic Reduction of CO$_2$: From Molecules to Semiconductors

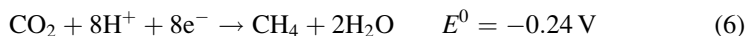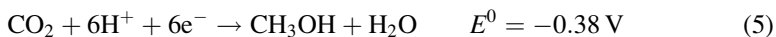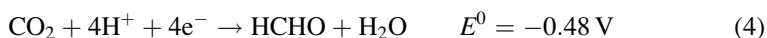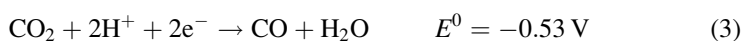**Tatsuto Yui, Yusuke Tamaki, Keita Sekizawa, and Osamu Ishitani**

Abstract We are facing three serious problems related to fossil resources, i.e., shortage of energy, shortage of carbon resources, and the global worming problem. Development of practical systems for converting CO$_2$ to useful chemicals using solar light, i.e., photocatalytic CO$_2$ reduction systems, should be one of the best solutions for these problems. In this article, we review photocatalytic CO$_2$ reduction systems, which are classified in two categories: (1) homogeneous reaction systems mainly using transition metal complexes, and (2) heterogeneous systems mainly using inorganic semiconductor as a light absorber.

Keywords Electron transfer · Metal complex photocatalyst · Photocatalytic CO$_2$ reduction · Semiconductor photocatalyst · Supramolecular chemistry

T. Yui
Department of Chemistry, Graduate School of Science and Engineering, Tokyo Institute of Technology, 2-12-1-E1-9 Ookayama, Meguro-ku, Tokyo 152-8551, Japan
and
CREST, Japan Science and Technology Agency (JST), Kawaguchi 332-0012, Saitama, Japan

Y. Tamaki
Department of Chemistry, Graduate School of Science and Engineering, Tokyo Institute of Technology, 2-12-1-E1-9 Ookayama, Meguro-ku, Tokyo 152-8551, Japan
and
Research Fellow of the Japan Society for the Promotion of Science, Tokyo, Japan

K. Sekizawa
Department of Chemistry, Graduate School of Science and Engineering, Tokyo Institute of Technology, 2-12-1-E1-9 Ookayama, Meguro-ku, Tokyo 152-8551, Japan

O. Ishitani (✉)
Department of Chemistry, Graduate School of Science and Engineering, Tokyo Institute of Technology, 2-12-1-E1-9 Ookayama, Meguro-ku, Tokyo 152-8551, Japan
and
Research Seeds Program, Japan Science and Technology Agency (JST), Kawaguchi 332-0012, Saitama, Japan
e-mail: ishitani@chem.titech.ac.jp

Contents

Abbreviations

Φ	Quantum yield
BNAH	1-Benzyl-1,4-dihydronicotinamide
bpy	2,2′-Bipyridine
bpz	Bipyrazine
CB	Conduction band
dmb	4,4′-Dimethyl-2,2′-bipyridine
H$_2$A	Ascorbic acid
MES	2-(N-Morpholino)ethanesulfonic acid
MLCT	Metal-to-ligand charge transfer
OER	One-electron reduced species
phen	1,10-Phenanthroline
Phen	Phenazine
TEA	Triethylamine
TEOA	Triethanolamine
TF	Turnover frequency
TN	Turnover number
TP	p-Terphenyl
H$_2$TPP	5,10,15,20-Tetraphenyl-21H,23H-porphyrin
VB	Valence band

1   Introduction

We human beings are facing three serious problems related to fossil resources, i.e., shortage of energy, shortage of carbon resources, and the global warming problem. In the biosphere, photosynthesis has been employed for both conversion of CO$_2$ to organics and conversion of solar energy to chemical energy. However, human

activities have used a lot of oil, coal, and natural gas, which were produced by photosynthesis in ancient times, as both major energy resources and chemical resources. These are finally burnt, which releases a tremendous amount of CO_2 to the atmosphere. For solving all three of these problems at once, one of the best solutions is the development of practical systems for converting CO_2 to useful chemicals using solar light, i.e., artificial photosynthesis.

Artificial photosynthetic systems for CO_2 utilization have to have the following essential features:

1. They must efficiently utilize visible light because only 5% of the solar light that reaches Earth's surface is in the UV region.
2. Water is used as an electron source.
3. Mechanisms for highly efficient reduction of CO_2 are required because CO_2 represents fully oxidized carbon and is very stable.

Photocatalysts for CO_2 reduction are one of the most important aspects of artificial photosynthesis. Consideration of the thermodynamics of CO_2 reduction gives an important strategy for constructing these photocatalysts [1–3]. Equation (1) indicates that the one-electron reduction of CO_2 (at pH 7 in an aqueous solution, vs NHE) is highly endothermic and that the product ($CO_2^{\cdot-}$) is too reactive to handle with ease. On the other hand, the multi-electron reduction of CO_2 can give stable and useful products with much lower energies, as shown in (2)–(6). However, one photon can usually induce the transfer of only one electron in photochemical reactions. Overcoming this obstacle is a key goal in the design of efficient photocatalysts for CO_2 reduction.

$$CO_2 + e^- \rightarrow CO_2^{\cdot-} \qquad\qquad E^0 = -1.9\,V \qquad\qquad (1)$$

$$CO_2 + 2H^+ + 2e^- \rightarrow HCO_2H \qquad E^0 = -0.61\,V \qquad\qquad (2)$$

$$CO_2 + 2H^+ + 2e^- \rightarrow CO + H_2O \qquad E^0 = -0.53\,V \qquad\qquad (3)$$

$$CO_2 + 4H^+ + 4e^- \rightarrow HCHO + H_2O \qquad E^0 = -0.48\,V \qquad\qquad (4)$$

$$CO_2 + 6H^+ + 6e^- \rightarrow CH_3OH + H_2O \qquad E^0 = -0.38\,V \qquad\qquad (5)$$

$$CO_2 + 8H^+ + 8e^- \rightarrow CH_4 + 2H_2O \qquad E^0 = -0.24\,V \qquad\qquad (6)$$

Many reported photocatalysts are constructed with both a photosensitizer, which initiates photochemical one-electron transfer, and a catalyst which converts one-electron transfer to multi-electron reduction of CO_2. As the photosensitizer component, metal complexes, organic compounds, and semiconductors have been used. These have been combined with various catalysts, such as metal complexes, metal particles, and enzymes. Some exceptional photocatalysts can fill both roles, such as rhenium(I) complexes (see Sect. 2.1.1) and TiO_2 (Sect. 3.2).

In this review, we classify the reported photocatalysts for CO_2 reduction into two categories, i.e., homogeneous and heterogeneous systems. Typically, the former are transition metal complexes and the latter are semiconductors.

The photocatalytic activities for CO_2 reduction can be evaluated by the following factors:

1. Product selectivity. This is usually evaluated as the ratio of the specified product to total amount of all of the products. In many cases, H_2 is generated as a byproduct during the photocatalytic reactions.
2. Quantum yield (Φ). The definition of quantum yield is shown in (7). In some cases, the input number of electrons is used as the numerator in (7). It is noteworthy that stable reduction products of CO_2 require multi-electron transfer, as described above.

$$\Phi = [\text{product/mol}]/[\text{absorbed photons/einstein}] \tag{7}$$

3. Turnover number (TN). The stability of the photocatalyst is given by its TN, which is defined using (8). In the case of TN < 1, this is not a photocatalytic reaction.

$$\text{TN} = [\text{product/mol}]/[\text{photocatalyst/mol or unit mass}] \tag{8}$$

4. Turnover frequencies (TF). The speed of the photocatalytic cycle is given by the photocatalyst's TF, which is defined using (9).

$$\text{TF} = \text{TN}/[\text{reaction time/min or hour}] \tag{9}$$

2 Photochemical CO_2 Reduction by Metal Complexes

2.1 Single-Component Systems

The structures and abbreviations of the compounds discussed in this section are shown in Scheme 1, and the photocatalytic properties of these compounds are summarized in Table 1.

2.1.1 Rhenium(I) Diimine Carbonyl Complexes

Lehn et al. reported for the first time that a rhenium complex can work as a photocatalyst for CO_2 reduction [4, 5]. A solution containing fac-Re(bpy)(CO)$_3$Cl (**1**) and a sacrificial donor, triethanolamine (TEOA), was irradiated using > 400-nm light
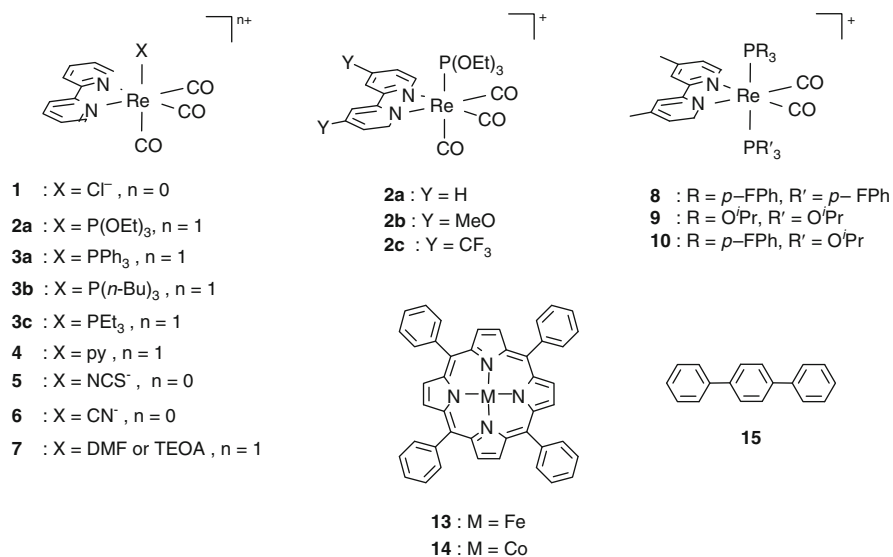
Scheme 1 Structures and abbreviations of the compounds used in single-component systems

Table 1 Products, catalytic activities and quantum yields of photocatalytic CO_2 reduction using single-component systems

Photocatalyst	Donor[a]	Product(s)	Φ	TN	TF/h^{-1}	$E_{1/2}^{red}$/V vs Ag/AgNO₃	Ref.
1	TEOA	CO	0.14	27	11	−1.67	[4, 5]
2a	TEOA	CO	0.38	7.5	–	−1.43	[6, 7]
2b	TEOA	CO	0.33	–	–	−1.67	[8]
2c	TEOA	CO	0.005	0.10	–	−1.03	[9]
3a	TEOA	CO	0.05	–	–	−1.56	[10]
3b	TEOA	CO	0.013	0.65		−1.39	[7]
3c	TEOA	CO	0.023	0.83		−1.39	[7]
4	TEOA	CO	0.03	–	–	–	[11]
5	TEOA	CO	0.30	–	–	−1.61	[8]
6	TEOA		0	–	–	−1.67	[8]
7	TEOA	CO	0.04	–	–	−1.57 (X = DMF), −1.64 (X = TEOA)	[8, 10]
8	TEOA	CO	0.20	–	–	−1.73	[12, 13]
9	TEOA	CO	0.02	–	–	−1.86	[12–14]
10	TEOA	CO	0.09	–	–	–	[12, 13]
13	TEA	CO	–	70	–	–	[15]
14	TEA	HCOOH, CO	–	> 300	–	–	[16]
15	TEA	HCOOH	0.072	4	–	–	[17]

[a]*TEOA* triethanolamine, *TEA* triethylamine

to produce CO efficiently and selectively. The product selectivity was very high, and little HCOOH and H₂ were detected. The quantum yield for CO formation was 0.14, and this was the highest efficiency for CO_2 reduction at the time.

As the Cl^- ligand of **1** can be easily exchanged for various other ligands [18], a number of photocatalytic rhenium(I) mononuclear complexes have been reported [6–11, 19]. For example, fac-[Re(bpy)(CO)$_3$\{P(OEt)$_3$\}]$^+$ (**2a**, bpy = 2,2′-bipyridine) reduces CO_2 with an efficiency ($\Phi_{CO} = 0.38$) more than twice that of **1** [6]. On the other hand, the quantum yield for CO formation using fac-[Re(bpy)(CO)$_3$(PPh$_3$)]$^+$ (**3a**) fell to 0.05 [10]. fac-[Re(bpy)(CO)$_3$(py)]$^+$ (**4**, py = pyridine) also exhibited little photocatalytic ability [11]. Among the complexes with an anionic ligand, fac-Re(bpy)(CO)$_3$(NCS) (**5**) produced CO with a high efficiency ($\Phi_{CO} = 0.30$), while fac-Re(bpy)(CO)$_3$(CN) (**6**) was inactive as a photocatalyst [8].

The substituent groups on the bpy ligand are also important for the photocatalytic properties of these rhenium complexes. The complex **2c**, in which electron-attracting CF_3 groups are introduced to the bpy ligand, exhibited a low photocatalytic ability ($\Phi_{CO} = 0.005$) [9]. By contrast, introducing electron-donating MeO groups (**2b**) did not significantly impact the photocatalytic reaction ($\Phi_{CO} = 0.33$) [8].

It has been found that the one-electron reduced forms of **3a** and **4,** produced by photoinduced electron transfer reaction [(10) and (11)], released their monodentate ligand, i.e., PPh$_3$ or py, to produce rapidly [Re(bpy)(CO)$_3$(S)]$^+$ (**7**, S = DMF or TEOA) by the chain reaction shown in (12) and (13) [10, 11].

$$[Re^I(bpy)(CO)_3X]^+ + h\nu \rightarrow [Re^{II}(bpy^{\cdot-})(CO)_3X]^+ \quad (X = PPh_3 \text{ or } py) \quad (10)$$

$$[Re^{II}(bpy^{\cdot-})(CO)_3X]^+ + TEOA \rightarrow [Re^I(bpy^{\cdot-})(CO)_3X] + TEOA^{\cdot+} \quad (11)$$

$$[Re^I(bpy^{\cdot-})(CO)_3X] + S \rightarrow [Re^I(bpy^{\cdot-})(CO)_3S] + X \quad (12)$$

$$[Re^I(bpy^{\cdot-})(CO)_3S] + [Re^I(bpy)(CO)_3X]^+ \rightarrow 7 + [Re^I(bpy^{\cdot-})(CO)_3X] \quad (13)$$
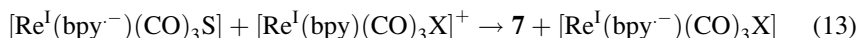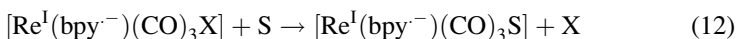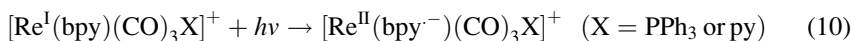
The photocatalytic ability of **7** is low because its excited state lifetime is short. The reason why **6** is catalytically inactive will be discussed later.

The photocatalytic competencies of these rhenium complexes are strongly correlated with their first reversible reduction potentials [9]. Specifically, rhenium complexes whose $E_{1/2}^{red} > -1.4$ V vs Ag/AgNO$_3$, i.e., **2c**, **3b**, and **3c**, exhibited only low photocatalytic quantum yields (Table 1).

The photocatalytic properties of rhenium biscarbonyl bisphosphine complexes $cis,trans$-[Re(dmb)(CO)$_2$(PR$_3$)(PR'$_3$)]$^+$ (dmb = 4,4′-dimethyl-2,2′-bipyridine) have also been reported [12–14]. The complexes with two triphenylphosphine derivatives (**8**, **9**, **10**) are able to reduce CO_2 photocatalytically. Notably, complex **8**, in which electron-attracting F groups are introduced to p-positions of the phenyl groups of the phosphine ligands, efficiently produced CO with a quantum yield of 0.20 [12, 13].

The initial step in the photocatalytic cycle has been illuminated by laser flash photolysis experiments. These experiments have shown that reductive quenching of the triplet metal-to-ligand charge transfer (^{3}MLCT) excited state by a sacrificial donor occurs to generate a one-electron reduced (OER) species of the rhenium
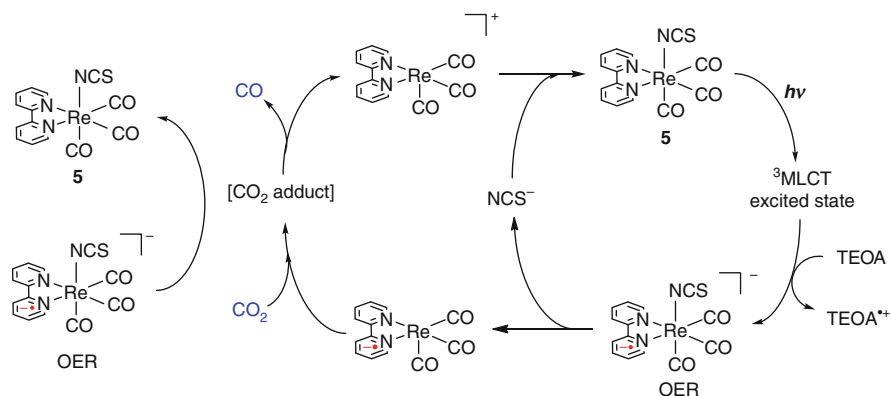
complex [20–22]. The OER species of *fac*-[Re(N^N)(CO)$_3$(PR$_3$)]$^+$ (N^N = α-diimine) complexes are especially stable, and the accumulation of their OER species can be observed in solution, even during photocatalytic CO$_2$ reduction reactions [6, 7, 9, 23].

Three rhenium complexes with different anionic ligands (**1**: L = Cl$^-$, **5**: NCS$^-$, **6**: CN$^-$) have been noted to have similar photophysical and electrochemical properties to each other [8]. However, their photocatalytic abilities differ substantially [8, 19]. The photocatalytic ability of **5** was better than that of **1**, while **6** was not photocatalytically active (Table 1). Such differences can be ascribed to the relative lability of the anionic ligands in the corresponding OER species [8]. The OER species of **1** loses its Cl$^-$ ligand rapidly, and thus can participate in subsequent steps in the catalytic cycle. In contrast, the OER species of **5** and **6** accumulate in considerable concentrations in the reaction solutions since dissociation of the SCN$^-$ or CN$^-$ ligand occurs slowly (**5**) or not at all (**6**). This prevents complex **6** from entering the catalytic cycle. For catalytically-competent complexes, the 17-electron species produced by dissociation of the anionic ligand from the OER species reacts with CO$_2$ giving a CO$_2$ adduct (Scheme 2). The CO$_2$ adduct receives a second electron from another OER species producing CO, and the starting complex recovers by re-coordination of the dissociated anionic ligand.

The structure of the CO$_2$ adduct, an important intermediate for CO$_2$ reduction, has yet to be determined, but some candidates have been proposed, i.e., a CO$_2$ bridging rhenium dimer (CO)$_3$(dmb)Re-CO$_2$-Re(dmb)(CO)$_3$ (**11**) [24, 25] and a rhenium carboxylate complex Re(bpy)(CO)$_3$(COOH) (**12**) [26].

Fujita et al. reported that irradiation of a dry THF solution containing (CO)$_3$(dmb)Re-Re(dmb)(CO)$_3$ under a CO$_2$ atmosphere gave the 17-electron species [Re(dmb)(CO)$_3$], which reacted with CO$_2$ to produce **11**. Irradiation of **11** under a CO$_2$ atmosphere gave CO and CO$_3$$^{2-}$ quantitatively.

12 was produced from the reaction of [Re(bpy)(CO)$_4$]$^+$ and OH$^-$. This reaction is reversible, i.e., the dissociation of OH$^-$ from **12** produces [Re(bpy)(CO)$_4$]$^+$. It is

Scheme 2 Photocatalytic reaction mechanism by **5** [8]

known that irradiation of $[Re(bpy)(CO)_4]^+$ efficiently stimulates the dissociation of a CO ligand to give fac-$[Re(bpy)(CO)_3S]$ (S = solvent).
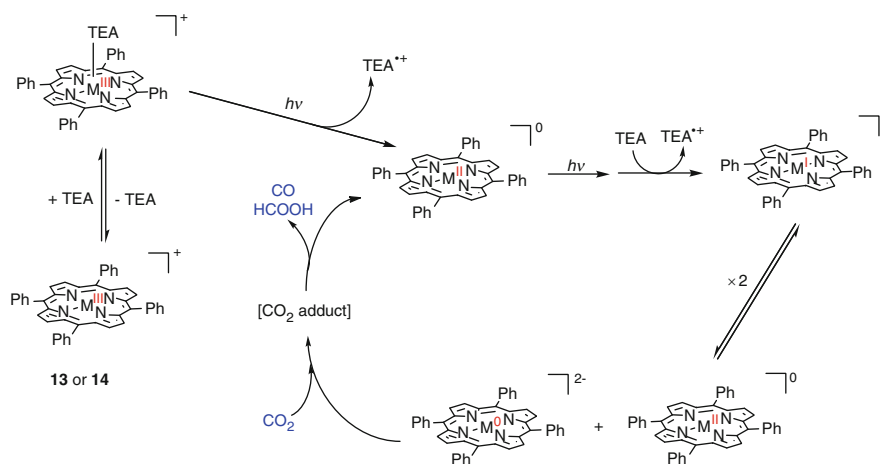
However, these complexes have not been detected in photocatalytic reaction solutions yet.

2.1.2 Metallo Porphyrins

Irradiation of iron and cobalt porphyrins (**13**: Fe(TPP), **14**: Co(TPP), H_2TPP = 5,10,15,20-tetraphenyl-21H,23H-porphyrin) in the presence of triethylamine (TEA) using > 320-nm light caused the photocatalytic reduction of CO_2 [15, 16, 27–31]. When **13** was used as a photocatalyst, CO was detected with $TN_{CO} = 70$ after 180-h irradiation [15]. Formic acid was the main product when **14** was employed as a photocatalyst [16]. The reaction mechanism proposed on the basis of UV–vis absorption changes during photolysis and radiolysis, and electrochemical measurements are shown in Scheme 3. M^{III}(TPP) is reduced to M^I(TPP) by photoinduced electron transfer from TEA, which subsequently disproportionates to M^0(TPP), the proposed catalytically-active species.

2.1.3 *p*-Terphenyl

Irradiation using > 290-nm light of a mixed system of *p*-terphenyl (TP) (**15**) and TEA gives $TP^{\cdot-}$. Because $TP^{\cdot-}$ has a very strong reduction power ($E^0 = -2.2$ V vs NHE), $TP^{\cdot-}$ can directly reduce CO_2 and formation of HCOOH is observed ($\Phi_{HCOOH} = 0.072$, $TN_{HCOOH} = 4$) [17]. This photocatalytic system, however,

Scheme 3 The proposed mechanism of photocatalytic CO_2 reduction by **13** and **14** [15, 16, 32]

was deactivated quickly because **15** itself was reduced to the corresponding dihydro form by photo-Birch reduction.

2.2 Multi-Component System

As described above, photocatalysts for the two-electron reduction of CO$_2$ should have both a photosensitizing component for initiating photoinduced one-electron transfer and a catalyst component for activating and introducing two electrons to CO$_2$. The structures and abbreviations of compounds using for the double-component systems, in which the two functions are carried out by two distinct molecules, are shown in Scheme 4. Data relating to their efficacy as a photo-catalysts for the reduction of CO$_2$ are summarized in Table 2.

2.2.1 Ruthenium(II) Diimine Photosensitizers

Photosensitizers are required to have long-lived excited states and to be stable in either oxidized or reduced form. The photosensitizers most frequently used are $[Ru^{II}(N \wedge N)_3]^{2+}$. These complexes absorb visible light efficiently and the lifetimes

Scheme 4 Structures and abbreviations of the compounds used in multi-component systems

Table 2 Products, catalytic activities, and quantum yields of photochemical CO_2 reduction using multi-component systems

Photosensitizer	Catalyst	Donor	Product(s)	Φ	TN	TF/h^{-1}	Ref.
16	**18, 19**	TEOA	H$_2$, CH$_4$	10^{-3} (H$_2$), 10^{-4} (CH$_4$)	–	–	[33]
17	**18**	TEOA	CH$_4$	10^{-4}	–	–	[33, 34]
16	**20**	TEOA	HCOOH	0.14	155	20	[35, 36]
		BNAH	CO, HCOOH	0.15 (CO), 0.03 (HCOOH)	270	80	[36, 37]
16	**21**	TEOA	HCOOH	–	163	–	[38]
16	**22**	TEOA	HCOOH	0.15	161	–	[38]
16	**23**	H$_2$A	H$_2$, CO	0.001	< 1	–	[39, 40]
16	**24**	H$_2$A	H$_2$, CO	0.005	~ 2	–	[41]
2b	**25**	TEOA	CO	0.59	–	–	[8]
15	**26**	TEOA	CO, HCOOH, H$_2$	0.25	–	–	[42, 43]
15	**27**	TEA	CO, HCOOH, H$_2$	–	–	–	[44]
28	**26**	TEA	HCOOH	0.07	–	–	[45]

TEOA triethanolamine, *TEA* triethylamine, *BNAH* 1-benzyl-1,4-dihydronicotinamide, *H$_2$A* ascorbic acid

of their ^{3}MLCT excited states are usually long, typically 1 µs. Moreover, one-electron oxidized and reduced forms $[Ru^{III}(N^\wedge N)_3]^{3+}$ and $[(N^\wedge N)_2Ru^{II}(N^\wedge N^{\cdot-})]^+$ are comparatively stable.

Mixed systems comprising $[Ru(bpy)_3]^{2+}$ (**16**) or $[Ru(bpz)_3]^{2+}$ (**17**, bpz = bipyrazine) as the photosensitizer, Ru colloid (**18**) or Os colloid (**19**) as the catalyst, TEOA as a sacrificial donor, and a viologen derivative as an electron relay were irradiated with > 400-nm light to produce H$_2$ ($\Phi_{H2} = 10^{-3}$) and CH$_4$ ($\Phi_{CH4} = 10^{-4}$) [33, 34].

Tanaka et al. have reported the electrocatalytic reduction of CO_2 using [Ru(bpy)$_2$(CO)$_2$]$^{2+}$ (**20**) as a catalyst [46–48]. They have also investigated the photocatalytic CO_2 reduction using a mixture of photosensitizer **16** and catalyst **20** [35–37]. The product distribution was strongly dependent on the pH of the reaction solution [36, 48]. The mixed system of **16**, **20** (5:1), and TEOA was irradiated using > 320-nm light giving HCOOH selectively. The quantum yield for HCOOH formation in the initial stages of the conversion was 0.14 [35, 36]. Replacing TEOA by 1-benzyl-1,4-dihydronicotinamide (BNAH) as the sacrificial donor leads to the production of CO and HCOOH. The quantum yields in H$_2$O – DMF (1:9, v/v) were 0.15 for CO production and 0.03 for HCOOH production [36, 37]. Emission from ^{3}MLCT excited state of **16** was quenched by neither CO_2 nor **20**, but it was quenched by both TEOA and BNAH [36]. These results indicate that the photocatalytic reaction cycle is initiated by electron transfer from TEOA or BNAH to ^{3}MLCT excited state of **16** (**14**), not from the ^{3}MLCT state to CO_2 or **20** (**15**).

$$[(bpy)_2Ru^{III}(bpy^{\cdot-})]^{2+} + \text{TEOA or BNAH} \rightarrow [(bpy)_2Ru^{II}(bpy^{\cdot-})]^+$$
$$+ \text{TEOA}^{\cdot+} \text{or BNAH}^{\cdot+} \tag{14}$$

$$[(bpy)_2Ru^{III}(bpy^{\cdot-})]^{2+} + CO_2 \text{ or } \mathbf{20} \not\rightarrow [Ru^{III}(bpy)_3]^{3+} + CO_2^{\cdot-} \text{ or } [(bpy)Ru^{II}(bpy^{\cdot-})(CO)_2]^+ \quad (15)$$

The reduction of CO_2 is thought to proceed via electron transfer from the OER species $[(bpy)_2Ru^{II}(bpy^{\cdot-})]^+$ to **20**. However, the source of the second electron, which is necessary for CO or HCOOH production, has not been clarified yet. These photocatalytic systems have a problem of generating a black precipitate, which is presumed to be $[Ru(bpy)(CO)_2]_n$ [49], upon prolonged irradiation (16). This process deactivates the catalyst.

$$\mathbf{20} \xrightarrow{e^-} \quad \overset{\text{bpy}}{\nearrow} \quad \xrightarrow{(\times n)} [Ru(bpy)(CO)_2]_n \quad (16)$$

Mixed systems containing **16** as a photosensitizer, $[Ru(bpy)_2(CO)X]^+$ (**21**: X = Cl^-, **22**: X = H^-) as a catalyst, and TEOA as a sacrificial donor can also produce HCOOH with similar efficiencies [38]. The TN_{HCOOH} values using **21** and **22** are 163 and 161, respectively.

The mixed system of **16**, $[Ni(cyclam)]^{2+}$ (**23**, cyclam = 1,4,8,11-tetraazacyclotetradecane), and ascorbic acid (H_2A) was irradiated under a CO_2 atmosphere using 340–600-nm light. This mostly evolved H_2 along with a small amount of CO. The TN and quantum yield for CO production were $TN_{CO} < 1$ and $\Phi_{CO} = 0.0006$ [39, 40]. Control experiments carried out in the dark or without **16**, **23**, H_2A or CO_2 produce no CO [39]. A labeling experiment using $^{14}CO_2$ revealed that the CO is produced from CO_2 [40]. This photocatalytic reaction cycle is also initiated by reductive quenching of the ^{3}MLCT excited state of **16** by HA^-.

As an improvement to the **16** + **23** system, **23** was replaced by **24**, which has a pyridinium cation as an electron acceptor covalently linked to the cyclam [41]. The photocatalytic performance of a mixed system of **16**, **24** and H_2A was better than that of the **16** + **23** system; TN_{H2} and TN_{CO} were 22 and 2, respectively. Because the reduction potential of the pyridinium cation unit is more positive than that of [Ni (cyclam)]$^{2+}$ unit, the pyridinium unit is supposed to function as the initial electron acceptor (17).

$$\xrightarrow{[(bpy)_2Ru^{II}(bpy^{\cdot-})]^+} \quad (17)$$

24
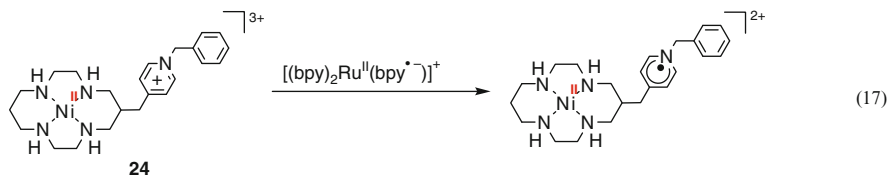
Willner and co-workers reported interesting applications of enzymes to the reductive fixation of CO_2 into organic substrates. In these experiments, **16** was employed as the photosensitizer, thiols (RSH) as an electron donors, methylviologen (MV^{2+}) as an electron carrier, an NADP/enzyme combination as $1e^-/2e^-$ relay,

1 : ferredoxin-NADP-reductase (FDR), 2 : malic enzyme
3 : isocitrate dehydrogenase (ICDH), 4 : formate dehydrogenase (FDH)
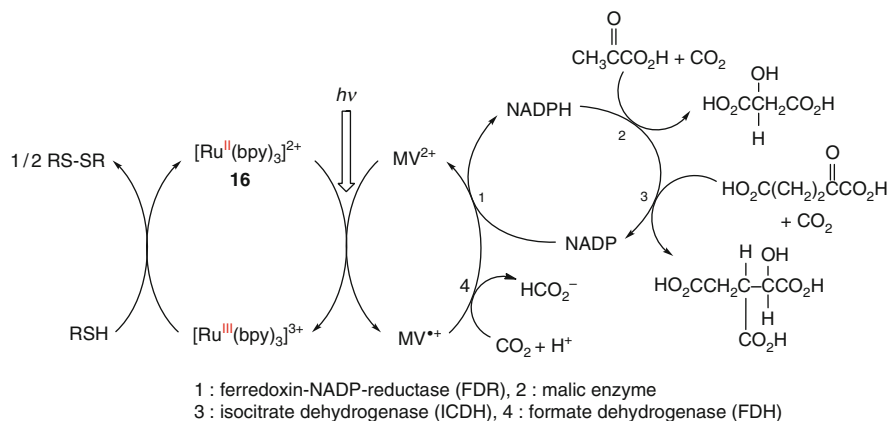
Scheme 5 Photocatalytic CO_2 fixation by **16** + enzymes system

Table 3 Turnover numbers of the components in photocatalytic CO_2 fixation experiments in the presence of **16**, RSH, MV^{2+}, NADP, and enzymes

Product	16	MV^{2+}	NADP	FDR	FDH	Malic enzyme	ICDH
Malic acid	1074	117	62.2	2.3×10^4	–	7.4×10^5	–
Aspartic acid	174	25	6.3	1.6×10^3	–	6.3×10^4	–
Isocitric acid	272	23	1.4	2.5×10^3	–	–	5.5×10^4
Formic acid	67	2	–	–	2×10^3	–	–

and other enzyme(s) as a catalyst, as shown in Scheme 5 [50, 51]. Table 3 summarizes the results.

2.2.2 Rhenium(I) Diimine Photosensitizer

As described above, the OER species of rhenium complexes have two roles in the photocatalytic CO_2 reduction reaction. (1) They are one-electron reductants, and (2) they produce 17-electron species by dissociation of a ligand, which subsequently react with CO_2 to produce the CO_2 adduct. There is a dilemma in optimizing the OER species to fulfill these two roles. The OER species should be stable for role (1) and unstable for role (2). On the basis of this consideration, a mixed system composed of two rhenium(I) complexes optimized to each role was developed. A 24:1 mixed system of **2b** as a photosensitizer and fac-[Re(bpy)(CO)$_3$(CH$_3$CN)]$^+$ (**25**) as a catalyst with TEOA was irradiated under a CO_2 atmosphere using 365-nm light. This produced CO with highest efficiency of known homogeneous photo-catalytic systems ($\Phi_{CO} = 0.59$) [8]. The photosensitizer **2b** can be efficiently converted to the corresponding OER species ($\Phi = 1.6$), which has a strong reducing power ($E_{1/2}^{red} = -1.67$ V vs Ag/AgNO$_3$). The CH$_3$CN ligand of the OER species of **25** rapidly dissociates to allow the complex to react with CO_2.

2.2.3 Organic Photosensitizers

Irradiation of the mixed system containing **15** as a photosensitizer and [Co(cya-clam)]$^{3+}$ (**26**) as a catalyst with TEA as a sacrificial donor using > 290-nm light gave mainly CO [42, 43]. As described in Sect. 2.1.3, **15** itself can function as a photocatalyst for CO$_2$ reduction [17]. However, the addition of **26** improved the stability of **15** and the photocatalytic performance of the system considerably. This is because the TP$^{\cdot-}$ produced by photochemical electron transfer donates an extra electron to **26** quickly ($k = 1.1 \times 10^{10}$ M^{-1}s^{-1}). Using TEOA instead of TEA also improved the photocatalytic process ($\Phi_{CO} = 0.15$, $\Phi_{HCOOH} = 0.10$).

A mixed system using [Co(HMD)]$^{2+}$ (**27**, HMD = 5,7,7,12,14,14-hexamethyl-1,4,8,11-tetraazacyclotetradeca-4,11-diene) as a catalyst instead of **26** also photocatalyzes CO$_2$ reduction. The reaction mechanism of this system has been investigated in detail by Fujita et al. [44]. One-electron reduction of **27** by TP$^{\cdot-}$ produces [Co^I(HMD)]$^+$. An adduct between [Co^I(HMD)]$^+$ and CO$_2$ produces CO, while a H$^+$ adduct gives HCOOH and H$_2$ (Scheme 6).

A photocatalytic system using phenazine (Phen, **28**) as a photosensitizer instead of **15** has been reported. A solution containing **28**, **26**, and TEA was irradiated using > 290-nm light under a CO$_2$ atmosphere to produce HCOOH selectively ($\Phi_{HCOOH} = 0.07$) [45]. Since the oxidation potential of Phen$^{\cdot-}$ produced by photochemical electron transfer is -1.18 V vs SCE, Phen$^{\cdot-}$ can reduce Co^{III} to Co^{II} (E_p (Co$^{III/II}$) = -0.69 V) but cannot reduce Co^{II} to Co^I (E_p (Co$^{II/I}$) = -1.9 V). Time-resolved spectroscopy and pulse radiolysis studies showed that Phen$^{\cdot-}$ was
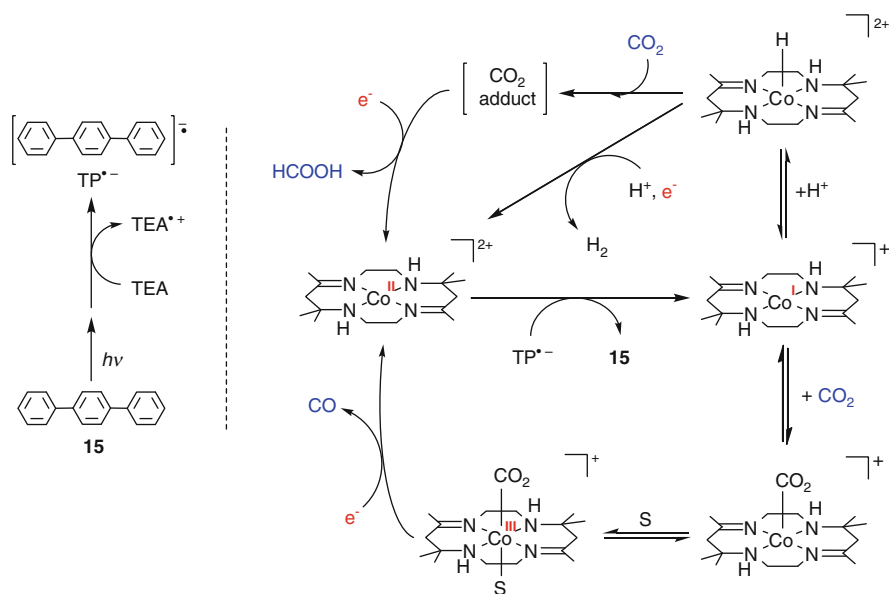
Scheme 6 Catalytic cycle for the reduction of CO$_2$ by the mixed system of **15** and **27** [32, 44]
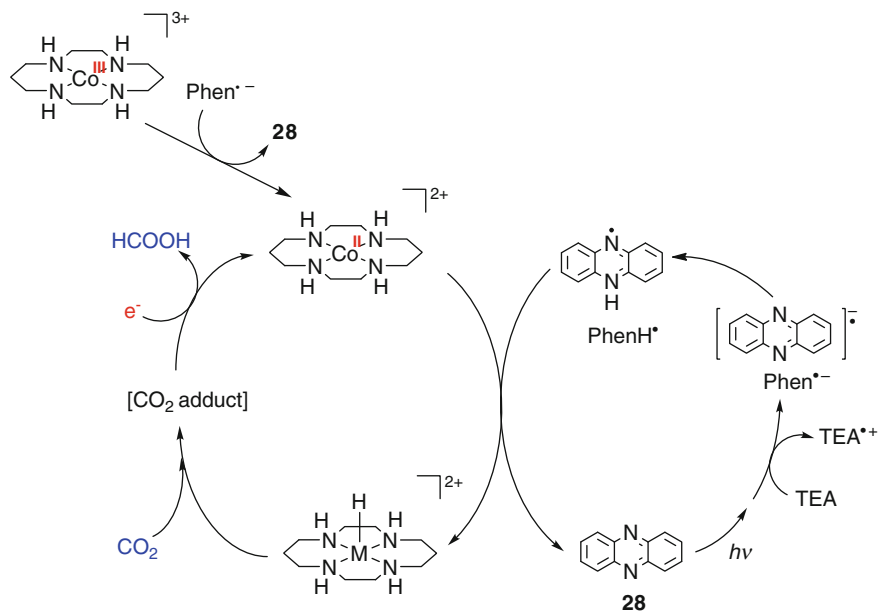
Scheme 7 Photocatalytic reaction mechanism using the **28** + **26** mixed system [45]

protonated giving PhenH·, which is supposed to donate hydrogen to $[Co^{II}(cyclam)]^{2+}$ giving $[Co(cyclam)-H]^{2+}$. $[Co(cyclam)-H]^{2+}$ reacts with CO_2 to produce HCOOH (Scheme 7).

2.3 Supramolecular Photocatalysts

Structures and abbreviations of the supramolecular photocatalysts are shown in Scheme 8, and data relating to their photocatalytic performance are summarized in Table 4.

2.3.1 Ru(II)–Ni(I)

The first supramolecular system for photochemical reduction of CO_2 was reported by Kimura et al. in 1992 [52, 57]. The supramolecular complex **30**, composed of $[Ru(phen)_3]^{2+}$ (**29**, phen = 1,10-phenanthroline) derivative as a photosensitizer unit and **23** as a catalyst unit, was irradiated in the presence of H_2A using > 350-nm light to reduce CO_2 to CO [52]. Although **30** produced CO less efficiently than a mixed system of the corresponding mononuclear complexes (**29** + **23**) in the initial stages of the reaction, **30** eventually produced more CO than the mixed system. The selectivity of CO formation over H_2 formation using **30** (CO/H_2 = 2.5)
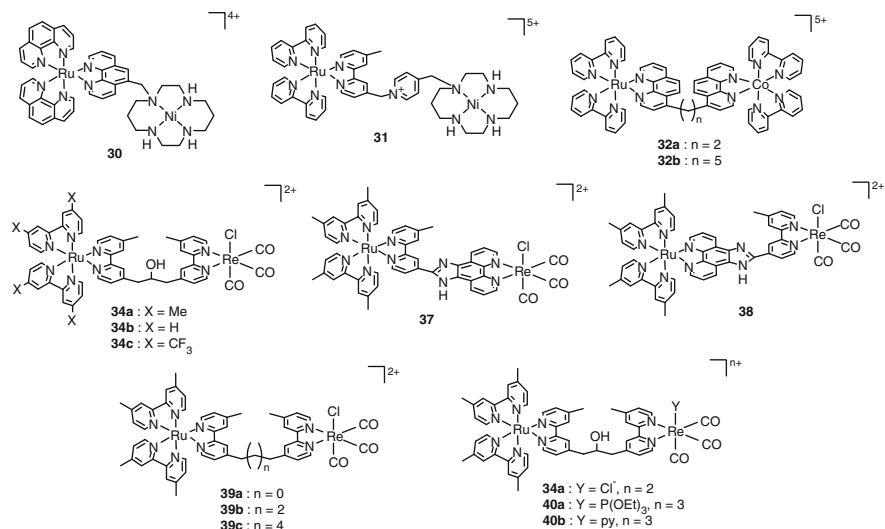
Scheme 8 Structures and abbreviations of supramolecular complexes

Table 4 Photocatalytic activities of supramolecular complexes for CO$_2$ reduction

Photosensitizer	Catalyst	Donor	Product(s)	Φ	TN	TF/h^{-1}	Ref.
29	**23**	H$_2$A	H$_2$, CO	–	< 1	–	[52]
30		H$_2$A	CO, H$_2$	–	< 1	–	[52]
16	**24**	H$_2$A	H$_2$, CO	0.005	2	–	[41]
31		H$_2$A	H$_2$, CO	–	< 1	–	[41]
16	**33**	TEOA	H$_2$, CO	–	25	–	[53]
32a		TEOA	CO, H$_2$	–	4	–	[53]
32b		TEOA	CO, H$_2$	–	6	–	[53]
35	**36**	BNAH	CO	0.06	101	9.7	[54]
34a		BNAH	CO	0.12	170	20	[54]
34b		BNAH	CO	–	50	–	[54]
34c		BNAH	CO	–	3	–	[54]
37		BNAH	CO	–	28	–	[54]
38		BNAH	CO	–	14	–	[54]
39a		BNAH	CO	0.13	180	66	[55]
39b,c		BNAH	CO	0.11	120	48	[55]
40a		BNAH	CO	0.21	232	56	[56]
40b		BNAH	CO	–	97	19	[56]

H$_2$A ascorbic acid, *TEOA* triethanolamine, *BNAH* 1-benzyl-1,4-dihydronicotinamide

was higher than that using the mixed system (CO/H$_2$ = 0.6). However, the
TN for CO formation using **30** was less than 1, indicating **30** does not work as
a photocatalyst.

The attachment of a pyridinium cation as an electron acceptor unit between
the photosensitizer and catalyst units (**31**) did not induce catalysis (TN$_{CO}$ < 1),
and the TN remained lower than that of the mixed system of the corresponding
model complexes, **16** and **24** (TN$_{CO}$ = 2) [41].

2.3.2   Ru(II)–Co(III)

The supramolecular complexes **32**, constructed with Ru(II) and Co(III) metal centers, was irradiated in the presence of TEOA under a CO_2 atmosphere using 400–750-nm light to give CO and H_2. The photocatalytic performances of the supramolecules (**32a**: $TN_{CO} = 3$, $TN_{H2} = 1$, **32b**: $TN_{CO} = 5$, $TN_{H2} = 1$), however, is not as good as system comprising the isolated components **16** and $[Co(bpy)_3]^{2+}$ (**33**) ($TN_{CO} = 9$, $TN_{H2} = 16$) [53].

2.3.3   Ru(II)–Re(I)

As described in Sect. 2.1.1, rhenium(I) diimine carbonyl complexes exhibit high photocatalytic abilities for CO_2 reduction. However, rhenium complexes have some disadvantages such as (1) low absorbance in visible region and (2) low TN. To overcome these problems, various supramolecular complexes (**34**, **37**–**40**) wherein the Re(I) catalyst unit(s) is/are linked with the Ru(II) photosensitizer unit(s) have been developed [54–56, 58–60]. The Ru(II) units can strongly absorb visible light, and some of the Ru(II)–Re(I) supramolecules can photocatalyze CO_2 reduction to CO with high product selectivity, high quantum yield, and high durability.

The supramolecular complex (**34a**) bridged by a $-CH_2CH(OH)CH_2-$ chain with two dmb units as a peripheral ligands on the Ru center exhibited a high photocatalytic ability for CO_2 reduction to CO ($\Phi_{CO} = 0.12$, $TN_{CO} = 170$). This supramolecule was a much better photocatalyst than the 1:1 mixed system of mononuclear model complexes $[Ru(dmb)_3]^{2+}$ (**35**) and *fac*-Re(dmb)(CO)$_3$Cl (**36**) ($\Phi_{CO} = 0.062$, $TN_{CO} = 101$). Supramolecule **34a** was the first example of a supramolecular photocatalyst exhibiting a high catalytic activity for this reaction [54].

On the other hand, supramolecules wherein two diimines are conjugated in the bridging ligands (**37**, **38**) showed lower photocatalytic abilities than that of the corresponding mixed system (**35** + **36**) [54]. This is because the extended conjugation of bridging ligand lowers the π^* orbital energy of the diimine ligand coordinating to the rhenium unit, which is reflected in the first reduction potential of the Re(I) unit [$E_{1/2}^{red} = -1.10$ V vs Ag/AgNO$_3$ (**37**) and -1.33 V vs Ag/AgNO$_3$ (**38**)]. This decreases the reducing power of the OER species of the Re(I) unit. As described in Sect. 2.1.1, only the rhenium complexes with $E_{1/2}^{red} < -1.4$ V vs Ag/AgNO$_3$ have high activities for CO_2 reduction.

The propensity of the peripheral ligands coordinating to the ruthenium ion to accept electrons also affects photocatalytic abilities of the supramolecules [54]. As described above, the supramolecular complex with two dmb peripheral ligands (**34a**) had a high photocatalytic ability, while the complexes with bpy (**34b**, $TN_{CO} = 50$) and 4,4′-bis(trifluoromethyl)-2,2′-bipyridine (**34c**, $TN_{CO} = 3$) were not as catalytically active as **34a**. This indicates that the unpaired electron in the OER species of the Ru(II) unit produced by photochemical electron transfer is mainly localized on the bridging ligand. In the case that the electron is located on the peripheral

ligands of the Ru(II), electron transfer from the reduced Ru(II) unit to the Re(I) unit probably does not occur or is not fast enough for efficient CO_2 reduction.

The peripheral ligand of the Re(I) unit also affects the photocatalytic reaction [56]. Introduction of triethylphosphite as a peripheral ligand (**40a**) instead of Cl^- improved the photocatalytic ability ($\Phi_{CO} = 0.21$, $TN_{CO} = 232$), while introduction of a pyridine ligand (**40b**) lowered the photocatalytic performance ($TN_{CO} = 97$).

Among supramolecules linked with an alkyl chain, **39a**, which has an ethylene chain, exhibits the higher catalytic activity ($\Phi_{CO} = 0.13$, $TN_{CO} = 180$). Other supramolecule systems with 3-, or 4-, or 6-carbon alkyl chains were less effective and similar to one another [55].

3 Photocatalytic Systems with Inorganic Semiconductor

Fujishima et al. reported pioneering studies on photocatalytic CO_2 reduction using various inorganic semiconductor photocatalysts in 1979 [61]. Since that time, various other photocatalytic systems that employ semiconductors have been studied [62–71]. Although there remain many problems, such as low selectivity of the products and low quantum yield, further development of semiconductor photocatalysts is a useful goal due to the durability of inorganic semiconductors, typically metal oxides, and their light harvesting properties. In this section, we review reported photocatalytic systems that utilize inorganic semiconductors for CO_2 reduction. Important data are summarized in Table 5.

3.1 Operating Principles

The operating principle of semiconductor photocatalysts is illustrated in Fig. 1. Absorption of light by a semiconductor electrode or particles causes the transition of an electron from the valence band (VB) to the conduction band (CB). Both an excited electron (e^-) and a hole (h^+) are generated concurrently in the CB and VB, respectively [66, 134–137]. The photo-generated excited e^- can potential be used for CO_2 reduction. Because protons can also accept the excited electron, hydrogen evolution often competes with CO_2 reduction, and this remains as one of the most serious problems to be solved in the field. On the other hand, the photo-generated h^+ is quenched by electron injection from a reductant such as organic molecules or water. For the use of water as a reductant, the potential of the VB must be more positive than the oxidation potential of water. Considerable amounts of various organic molecules, such as acetic acid, can be adsorbed on the surface of semiconductors that have not undergone any pre-treatment. Because such organic adsorbates can work as reductants and/or carbon sources for the products, removal of the organic contamination is essential prior to photocatalytic CO_2 reduction experiment.

Table 5 Representative semiconductor-based photocatalytic CO_2 reduction systems

System	Light source	Reductant and reaction condition	Major product(s)	Reactivity	Isotope experiment	Ref.
Ru complex/TiO$_2$/enzyme CODH I	> 420 nm	MES buffer aq. sol.	CO	TF = 250 μmol of CO (g of Cat.)$^{-1}$ h^{-1}	–	[72]
TiO$_2$ nanotube	365 nm	H$_2$O gas phase	CH$_4$	TF ~ 0.5 μmol (g of Cat.)$^{-1}$ h^{-1}	–	[73]
TiO$_2$ nanotube	380 or 400 nm	H$_2$O gas phase	CH$_4$	TF ~ 0.8 μmol h^{-1}	–	[74]
ATaO$_3$ (A = Li, Na, K)	200 W Hg–Xe lamp	H$_2$ Gas phase	CO	TF = 0.0175 μmol (g of Cat.)$^{-1}$ h^{-1}	–	[75]
Ga$_2$O$_3$, MgO, CaO, ZrO$_2$, and Al$_2$O$_3$	200 W Hg–Xe lamp	H$_2$ Gas phase	CO	TF ~ 0.7 μmol (g of Cat.)$^{-1}$ h^{-1}	–	[76]
[Ru(H$_2$O)SiW$_{11}$O$_{39}$]$^{5-}$	Xe arc lump	TEA	CO	Φ = 0.02	–	[77]
CdSe/Pt/TiO$_2$	> 420 nm	H$_2$O	CH$_4$, CH$_3$OH	TF = 48 ppm	–	[78]
TiO$_2$ or CuTiO$_2$ in SBA15	365 nm	H$_2$O	CH$_3$OH	TF = 627 μmol (g of Cat.)$^{-1}$ h^{-1}	–	[79]
Pt–TiO$_2$	365 nm	H$_2$O	CH$_4$	TF = 4.8 μmol (g of Cat.)$^{-1}$ h^{-1}	–	[80]
Ag–TiO$_2$	320–500 nm	H$_2$O	CH$_3$OH	TF = 4.12 μmol (g of Cat.)$^{-1}$ h^{-1}	–	[81]
TiO$_2$	254 nm	H$_2$O	CH$_4$, CH$_3$OH	TF = 0.38 μmol (g of Cat.)$^{-1}$ h^{-1}	–	[82]
p-InP electrode and Cu particle	< 300 nm	0.1 M NaOH in CH$_3$OH	CH$_4$, C$_2$H$_6$, CO, HCOO$^-$	Current eff. = 1.21%	–	[83]
BiVO$_4$	300 W Xe arc	H$_2$O at 0 °C	C$_2$H$_5$OH	TF ~ 1.500 μmol (g of Cat.)$^{-1}$ h^{-1}	–	[84]
Ag–TiO$_2$	320–500 nm	H$_2$O	CH$_3$OH	TF = 4.12 μmol (g of Cat.)$^{-1}$ h^{-1}	–	[85]
p-GaP	365 or 465 nm		CH$_3$OH	Φ = 0.44	–	[86]
N3 dye/Cu–Fe/TiO$_2$	150 W Hg or concentrated natural sunlight	H$_2$O	C$_2$H$_6$, CH$_4$	Φ ~ 0.0045	–	[87]
NiO-InTaO$_4$	Pyrex filter	H$_2$O	CH$_3$OH	Φ = 0.0245	–	[88]

Catalyst	Light source	Reductant	Products	Rate	Isotope	Ref.
Ru complex or perylene diimine/TiO_2 film/Pt	75 W day light lump	H_2O	CH_4	TF < 0.3 μmol (g of Cat.)$^{-1}$ h^{-1}	—	[89]
TiO_2 film on Cu substrate	350 nm	H_2O	CO, CH_4	TF ~ 0.2 μmol h^{-1}	—	[90]
Pd-TiO_2 film on cu substrate	350 nm	H_2O	CO, CH_4	TF ~ 40 ppm h^{-1}	—	[91]
TiO_2 or ZrO_2	365 or 254 nm	H_2O and H_2	CH_4	TF $= 4.1$ μmol (g of Cat.)$^{-1}$ h^{-1}	—	[92]
TiO_2/SO_4^{2-}	365 nm	H_2O and H_2	CO, CH_4	TF ~ 4.5 μmol (g of Cat.)$^{-1}$ h^{-1}	—	[93]
TiO_2	350 nm	H_2O 2-propanol	CO, CH_4, H_2	TF < 3 μ L h^{-1}	—	[94]
Co phthalocyanine/TiO_2	500 W tungsten halogen lamp	H_2O	HCOOH, CO, CH_4	TF $= 34$ μmol (g of Cat.)$^{-1}$ h^{-1}	—	[95]
ZrCu(I) in MCM-41	355 nm	H_2O	CO		$^{13}CO_2$, $C^{18}O_2$	[96]
p-GaAs and p-InP electrode	> 300 nm	CH_3OH	CO, HCOOH.	Current efficiency for CO ($rf = 41.5\%$)	—	[97]
Metal modified p-InP	> 300 nm	CH_3OH	CO, HCOOH	Current efficiency for CO ($rf = 80.4\%$)	—	[98]
ZrCu(I) in MCM-41	355 nm	H_2O	CO	$\Phi = 0.1923$	$^{13}CO_2$, $C^{18}O_2$	[99]
CuO/TiO_2	Black light UV lamps	H_2O	CH_3OH		—	[100]
TiO_2 nano particle in Nafion film	990 W Xe arc	Liquid CO_2	HCOOH, CH_3OH, CH_3CO_2H	TF > 100 μmol (g of Cat.)$^{-1}$ h^{-1}	—	[101]
Ti in MCM-41		H_2O vapor	CO, O_2		$^{13}CO_2$, $C^{18}O_2$	[102]
MgO	500 W high pressure Hg lamp	H_2 or CH_4	CO	TF ~ 0.46 μmol h^{-1}	$^{13}CO_2$	[103]
Ti-containing mesoporous silica	100 W high pressure Hg lamp	H_2O	CH_4, CH_3OH	TF ~ 10 μmol (g of Cat.)$^{-1}$ h^{-1}	—	[104]
Pt loaded $K_2Ti_6O_{13}$	300 W Xe or 150 W Hg	H_2O	HCHO, HCOOH	TF ~ 6 μmol h^{-1}	—	[105]
Ti-containing mesoporous silica	100 W high pressure Hg lamp	H_2O	CH_4, CH_3OH	TF ~ 10 μmol (g of Cat.)$^{-1}$ h^{-1}	—	[106]
Ti-containing mesoporous silica	> 250 nm	H_2O	CH_4, CH_3OH	$\Phi = 0.0028$	—	[107]
MgO	A 500 W ultrahigh pressure mercury lamp	CO_2 and H_2 gas phase	CO	TF < 1 μmol (g of Cat.)$^{-1}$ h^{-1}	—	[108]
Ti in beta zeolites	> 250 nm	H_2O	CH_4, CH_3OH		—	[109]

(continued)

**Table 5** (continued)

System	Light source	Reductant and reaction condition	Major product(s)	Reactivity	Isotope experiment	Ref.
ZrO_2	500 W ultra high pressure Hg lamp	CO_2 and H_2 gas phase	CO	TF $<$ 30 mol (g of Cat.)$^{-1}$ h^{-1}	$^{13}CO_2$	[110]
ZrO_2	500 W ultra high pressure Hg lamp	Gas phase at 673 K	CO	TF $<$ 0.6 μmol (g of Cat.)$^{-1}$ h^{-1}	$^{13}CO_2$	[111]
ZrO_2	500 W ultra high pressure Hg lamp	Gas phase	CO	TF $\sim$ 17 μmol h^{-1}	$^{13}CO_2$, D_2	[112]
Li–TiO_2 Cu–Zn, TiO_2/Pd	Mercury arc lamp source (250 mW)	H_2O	CH_3COCH_3, CH_3OH C_2H_5OH	TF $\sim$ 15 μmol h^{-1}	–	[113]
Rh–TiO_2	500 W ultra high pressure Hg lamp	Gas phase	CO, CH_4	TF $<$ 1 μmol h^{-1}	–	[114]
TiO_2	990 W Xe lamp	Super critical fluid CO_2	HCOOH	TF $\sim$ 1.8 μmol (g of Cat.)$^{-1}$ h^{-1}	–	[115]
Ti-oxide/FSM-16	$>$ 280 nm	H_2O	CH_4, CH_3OH	TF $\sim$ 90 μmol (g of Cat.)$^{-1}$ h^{-1}	–	[116]
TiO_2 zeolite in mesoporous silica	$>$ 280 nm	H_2O gas phase	CH_4, CH_3OH	TF $\sim$ 13 μmol (g of Cat.)$^{-1}$ h^{-1}	–	[117]
TiO_2 in SiO_2 matrix	$>$ 300 nm	2-propanol	HCOOH, CO, urea	TF $\sim$ 2 μmol h^{-1}	–	[118]
CdS	$>$ 300 nm	2-propanol	HCOOH, CO	TF $<$ 0.2 μmol h^{-1}	–	[119]
ZrO_2	500 W ultra high pressure Hg lamp	Gas phase	CO	TF $<$ 0.6 μmol h^{-1}	$^{13}CO_2$	[120]
TiO_2	Xe lamp	2-propanol solution under 2.8 Mpa	CH_4	TF $=$ 0.43 μmol (g of Cat.)$^{-1}$ h^{-1}	–	[121]
p-InP, p-GaAs, p-Si photoelectrode	$>$ 370 nm	Methanol 40-atom of CO_2	CO, $HCOOCH_3$	Current efficiencies over 90%	$^{13}CO_2$	[122]

Catalyst	Light source	Medium	Products	Quantum yield / TF	Labeled CO_2	Ref.
Ti in MCM-41 and MCM48	> 280 nm	H_2O gas phase	CH_4, CH_3OH	TF > 10 μmol (g of Cat.)$^{-1}$ h^{-1}	–	[123]
CdS	> 400 nm	TEA	CO	TF ∼ 30 μmol h^{-1}	–	[124]
CdS	405 nm	TEA	CO	Φ = 0.098	$^{13}CO_2$	[125]
ZrO_2	500 W ultra high pressure Hg lamp	CO_2 and H_2 gas phase	CO	TF < 0.1 μmol h^{-1}	$^{13}CO_2$	[126]
ZnS nano crystal	> 290 nm	TEA	HCOOH, CO, H_2	TF = 21 μmol h^{-1}	–	[127]
ZnS–CdS mixture	280 nm	H_2O	HCOOH, CH_3COCH_3	Φ = 0.325 for HCOOH, 0.42 for CH_3COCH_3	–	[128]
Metal deposited ZrO_2	400 W high pressure Hg lamp	H_2O	H_2, O_2, CO	TF = 2.5 μmol h^{-1} for CO	–	[129]
Metal deposited TiO_2	> 300 nm	H_2O	CH_4, C_2H_6	TF > 30 μmol (g of Cat.)$^{-1}$ h^{-1}	$^{13}CO_2$	[130]
ZnS	313 nm	H_2O, NaH_2PO_2	HCOOH, CO	Φ = 0.24 for HCOO–	–	[131]
Cu–TiO_2	500 W Xe, Pyrex	H_2O, Cu	CH_3OH	TF < 1 μmol h^{-1}	–	[132]
$K_7[PTi_2W_{10}O_{40}]$ 6H_2O and $K_5[BW_{12}O_{40}]$ 15H_2O	500 W high pressure Hg lamp	CH_3OH	HCHO	TF ∼ 4 μmol h^{-1}	–	[133]
TiO_2, ZnO, CdS, GaP, SiC, WO_3	500 W Xe, Hg lamp	H_2O	HCHO, CH_3OH	Φ ∼ 5 × 10^{-4}	–	[61]

Fig. 1 Reaction mechanism
of inorganic semiconductor
photocatalysts
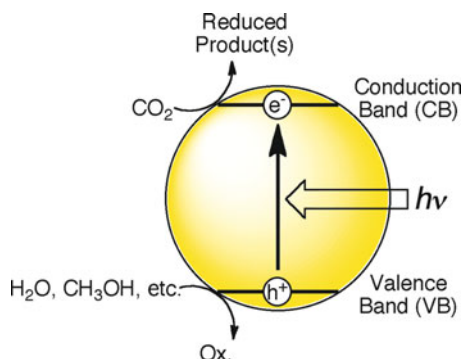
3.2 TiO$_2$ and Related Materials

Photocatalytic reduction of CO_2 in aqueous solutions using various semiconductors, i.e., TiO_2, ZnO, CdS, GaP, SiC, and WO_3, was reported for the first time in 1979 [61]. Figure 2 shows the correlation between the yield of methanol as a major product and the CB potential of the semiconductor catalyst. A larger amount of CH_3OH was obtained from semiconductors with more negative CB potentials, while CH_3OH was not generated from semiconductors with more positive CB potentials than the redox potential of CH_3OH/H_2CO_3. It was suggested that water works as reductant because no reducing regent was added to the reaction solution [(18) and (19)]. The authors proposed that the reduction proceeds in a stepwise manner, and two-, four-, six-, and eight-electron reduction products, i.e., formic acid, formaldehyde, CH_3OH, and methane are produced according to (20)–(23). The reported quantum yields of production were 5×10^{-4} and 1.9×10^{-4} for HCHO and CH_3OH, respectively.

$$\text{Cat.} + h\nu \rightarrow e^- + h^+ \tag{18}$$

$$H_2O + 2h^+ \rightarrow 1/2O_2 + 2H^+ \tag{19}$$

$$CO_2(aq) + 2H^+ + 2e^- \rightarrow HCOOH \tag{20}$$

$$HCOOH + 2H^+ + 2e^- \rightarrow HCHO + H_2O \tag{21}$$

$$HCHO + 2H^+ + 2e^- \rightarrow CH_3OH \tag{22}$$

$$CH_3OH + 2H^+ + 2e^- \rightarrow CH_4 + H_2O \tag{23}$$
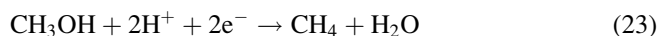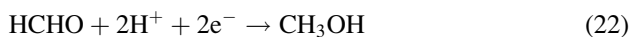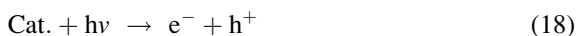
In 1983, Halmann et al. evaluated the CO_2 reduction ability of prototype solar collector systems by using the photocatalytic properties of TiO_2, $SrTiO_3$, and
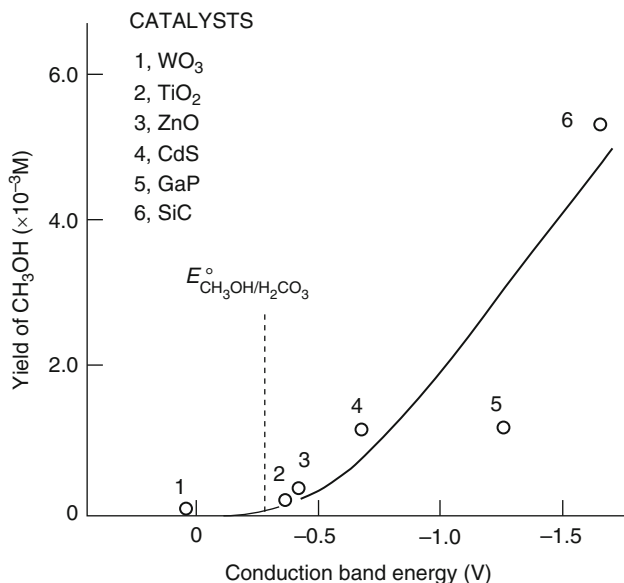
Fig. 2 Correlation between the yield of methanol and the conduction bands of semiconductor catalysts. The *dashed line* denotes the standard redox potential of the CH$_3$OH/H$_2$CO$_3$ couple vs NHE. (Reprinted from [61] with permission by the Nature Publishing Group)

CaTiO$_3$ semiconductors (Fig. 3) [138]. The light energy conversion efficiencies were estimated to be 0.001–0.016% in these systems.

Because one possible rate determining step is the water oxidation process, the photocatalytic reduction of CO$_2$ has been tried in the presence of sacrificial electron donors, such as alcohols [94, 118, 121, 133, 139]. It has been reported that photocatalytic CO$_2$ reduction by TiO$_2$ in the presence of 2-propanol selectively gives CH$_4$ [121]. Acetone was also detected as an oxidation product of 2-propanol. However, only a slight increase in the reaction efficiency was observed following the addition of 2-propanol. The reported TN and TF of CH$_4$ production are TN = 1.3 μmol (g cat.)$^{-1}$ and TF = 0.43 μmol (g cat.)$^{-1}$ h^{-1} [121].

A photocatalytic CO$_2$ reduction system with TiO$_2$ and Cu powders was found to produce CH$_3$OH, HCHO, CH$_4$, and CO [132]. Because no reduced products of CO$_2$ were observed in the absence of Cu, Cu is thought to function as a reductant and co-catalyst for the photocatalytic reaction.

The photocatalytic reduction of CO$_2$ by Cu-, Cu$_2$O-, and CuO-doped TiO$_2$ were compared in aqueous dispersions in the absence of a sacrificial electron donor [100]. In all cases, CH$_3$OH was the only reaction product, and the best result was obtained using 3.0 wt% CuO doped TiO$_2$ (3%CuO/TiO$_2$). The reactivity of bare TiO$_2$ was determined to be TF = 809 μmol (g cat.)$^{-1}$ 6 h^{-1} and Φ = 0.586, while 3%CuO/TiO$_2$ exhibited TF = 2,655 μmol (g cat.)$^{-1}$ 6 h^{-1}, Φ = 0.19, which is about three times higher than that using bare TiO$_2$.
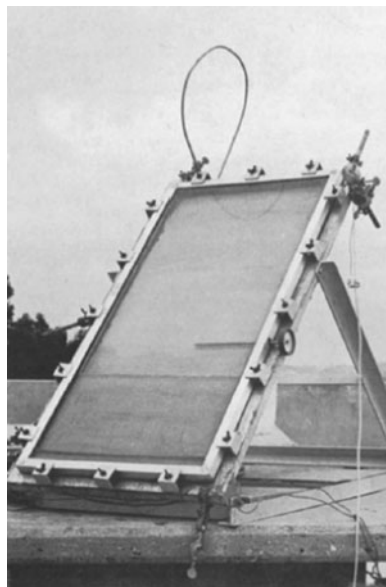
The UV-light induced photocatalytic reduction of CO_2 to CH_4 using various metal-deposited (Pd, Rh, Pt, Au, Cu, and Ru) TiO_2 particles in aqueous dispersion has been investigated [130]. The Pd-deposited TiO_2 (Pd-TiO_2) was the most efficient photocatalyst in such systems (Table 6). Organic contaminants on the photocatalyst were thoroughly removed before the photocatalytic reactions. Photochemical reactions carried out under $^{13}CO_2$ using Pd-TiO_2 gave $^{13}CH_4$ as a product. Therefore it was concluded that CO_2 is the carbon source. TiO_2 without any added metal could not produce CH_4, and therefore Pd is thought to act as a co-catalyst for the multi-electron reduction of CO_2. Water is probably the reducing regent in this system (Fig. 4), because after photocatalytic reactions of 4 h duration, oxidized products of Pd were not detected.

Photocatalytic CO_2 reduction using Ti^{4+}-doped zeolites or mesoporous silica has been reported [70, 104, 106, 107, 109, 116, 117, 123, 140–147]. In these systems, some of the Si^{4+} centers were isomorphously substituted with Ti^{4+}. The doped Ti^{4+} was tetrahedrally coordinated and was highly isolated within the SiO_2 framework. The doped Ti^{4+} species do not exhibit semiconductor properties, and can emit from the $O^{2-} \rightarrow Ti^{4+}$ charge-transfer (CT) excited state (Fig. 5) [70]. The emission was quenched in the presence of CO_2. By using this system, CO_2 was photocatalytically reduced to CH_3OH and CH_4. The selectivity was strongly affected by the hydrophobicity of the surface of the supports, for example, a higher hydrophobicity led to greater selectivity in the formation of CH_3OH. With a Ti^{4+}-doped mesoporous silica thin film made by sol–gel techniques, which had good transparency, the total quantum yield of CH_4 and CH_3OH formation was 0.3 [104].

Photocatalytic CO_2 reduction using TiO_2 or Cu/TiO_2 deposited in mesoporous silica (SBA-15) cavities was found to produce CH_3OH [79]. A photocatalytic

Table 6 The photocatalytic reduction of CO$_2$ using metal-deposited TiO$_2$[a] (reprinted from [130] with permission by Elsevier)

M–TiO$_2$	Amount of the following products (10^{-8} mol)				
	CH$_4$	C$_2$H$_6$	CH$_3$OH	HCO$_2$H	CH$_3$CO$_2$H
TiO$_2$	0.7	0.1	<1	<0.5	<1
Pd–TiO$_2$	24.7	1.4	<1	<0.5	<1
Rh–TiO$_2$	10.0	0.9	<1	<0.5	5.0
Pt–TiO$_2$	5.0	<0.1	<1	<0.5	<1
Au–TiO$_2$	3.3	0.6	<1	<0.5	<2.8
Cu–TiO$_2$	1.9	0.2	<1	0.6	4.1
Ru–TiO$_2$	0.6	<0.1	<1	<0.5	2.0

[a]A suspension of metal-deposited TiO$_2$ (150 mg) in water (1.5 mL) was irradiated at $>$ 300 nm for 5 h under a CO$_2$ atmosphere

Fig. 4 Photocatalytic CO$_2$ reduction mechanism using Pd–TiO$_2$
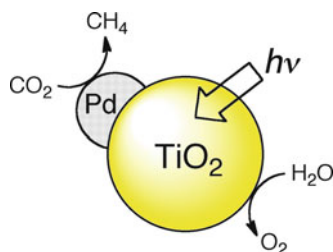
Fig. 5 Photoluminescence spectra of Ti^{4+} in Y-zeolite catalyst; (*curve a*) under degassed condition and (*curve b*) in the presence of CO$_2$ at 77 K. The corresponding excitation spectrum is indicated with *Ex*. (Reprinted from [70] with permission by the Elsevier)
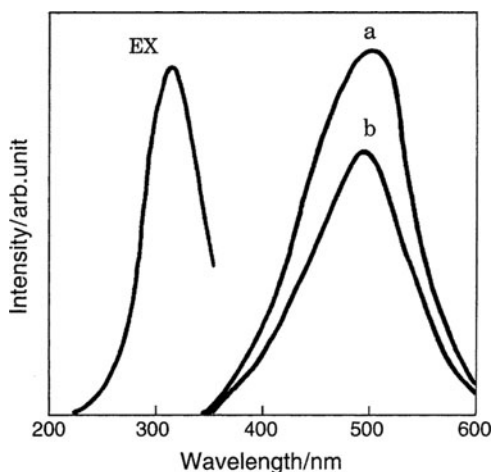
system using (2 wt% Cu/TiO$_2$)/SBA-15 showed the most efficient photocatalytic activity in this series, and the TF for CH$_3$OH formation reached 627 µmol (g cat.)$^{-1}$ h^{-1}. The authors supposed that the origins of such high catalytic activity are the high dispersion of the anatase type TiO$_2$ nano-crystals in the SBA-15 cavities, and the Cu that works as an efficient electron capture catalyst.

3.3 Other Semiconductors

Photocatalysis employing various metal oxide semiconductors [71] such as Ga_2O_3 [76, 148], GaP [86], InTaO$_4$ [88], MgO [76, 103, 108], ZrO_2 [76, 92, 110–112, 120, 126, 129], BiVO$_4$ [84], and ATaO$_3$ [75] (A = Li, Na, K) have been reported.

Monoclinic crystals of BiVO$_4$ photocatalyzed CO_2 reduction to C_2H_5OH in aqueous solution without a sacrificial electron donor [84]. BiVO$_4$ can act as visible-light responsive photocatalyst, and photocatalytic activity improved under intense light irradiation. The maximum TF reached ca. 1.5 mmol (g cat.)$^{-1}$ h^{-1}. The authors presumed that the intense irradiation enhances the production of reaction intermediates.

Irradiation of a photoelectrochemical cell constructed with a p-GaP electrode [149] selectively produced CH_3OH from CO_2 in aqueous solution (pH = 5.2) containing pyridine (10 mM) [86]. Both the yield of CH_3OH formation and the faradaic efficiency were strongly dependent on the bias potential (E) vs SCE. Quantitative faradaic efficiency could be obtained at $E = -0.2$ V, and the maximum quantum yield was 0.44 at $E = -0.5$ V (Table 7). The authors have proposed the reaction mechanism shown in Scheme 9 [150]. A photoelectrochemically-generated pyridinium radical initially reacts with CO_2 to give a CO_2 adduct. Further multistep reduction of the CO_2 adduct by pyridinium radicals produces formic acid, formaldehyde, and CH_3OH.

Metal sulfides such as ZnS, CdS, and $Cd_xZn_{1+x}S$ can work as CO_2 photoreduction catalysts in the presence of a sacrificial electron donor [119, 124, 125, 127, 128, 151]. Although the reaction products of CO_2 are formic acid and CO in dry conditions, H_2 is also generated in the presence of H_2O. The quantum yields of CO_2

Table 7 Photoelectrochemical conversion of CO_2 to methanol using p-GaP with pyridine (reprinted from [86] with permission by the American Chemical Society)

E (V)[a]	Under potential[a] (mV)	J (mA/cm^2)	Faradaic eff. CH$_3$OH ξ (%)	Quantum yield Φ_{e^-} (%)	Quantum eff. CH$_3$OH[b] Φ_{MeOH} (%)	OCE[c] η (%)
465 nm						
−0.70		1.1	56	(8.3)[d]	(4.6)[d]	(1.3)[d]
−0.60		1.0	51	(5.1)[d]	(2.6)[d]	(1.3)[d]
−0.50	20	0.46	78	3.4	2.6$_5$	1.0$_5$
−0.40	120	0.33	83	2.3	1.9	1.0$_3$
−0.30	220	0.27	90	1.6	1.3$_5$	0.84
365 nm						
−0.50	20	0.92	62	71	44	10.9
−0.40	120	0.48	89	38	34	8.9
−0.30	220	0.28	92	16	15	5.8
−0.25	270	0.21	96	12	11.$_5$	4.6$_5$
−0.20	320	0.21	96	13	12.$_5$	4.8

[a]All potentials references vs SCE. Underpotentials stated are vs the standard potential of −0.52 V for the reduction of CO_2 to methanol at pH 5.2
[b]As defined by (1) to be (mol methanol × 6)/mol photons
[c]As defined by (4) to be (chemical power out − electrical power in)/light power in
[d]These values were obtained at an overpotential, and thus external electrical power was also used
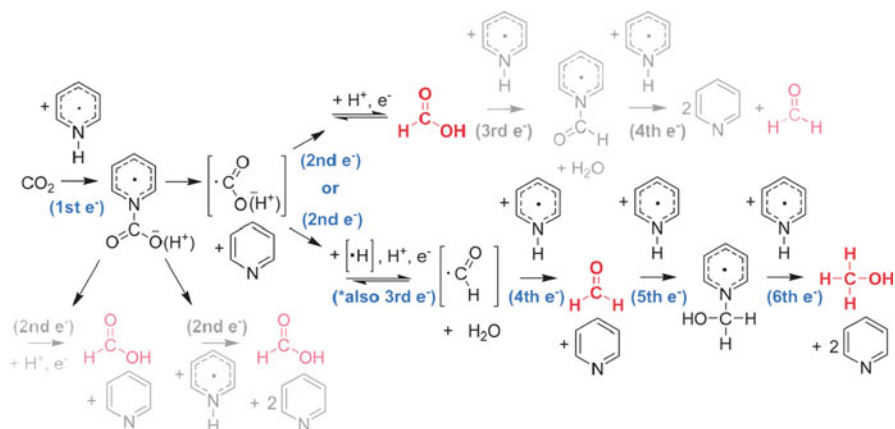
Scheme 9 Proposed reaction mechanism of the pyridinium-catalyzed reduction of CO$_2$. (Reprinted from [150] with permission by the American Chemical Society)
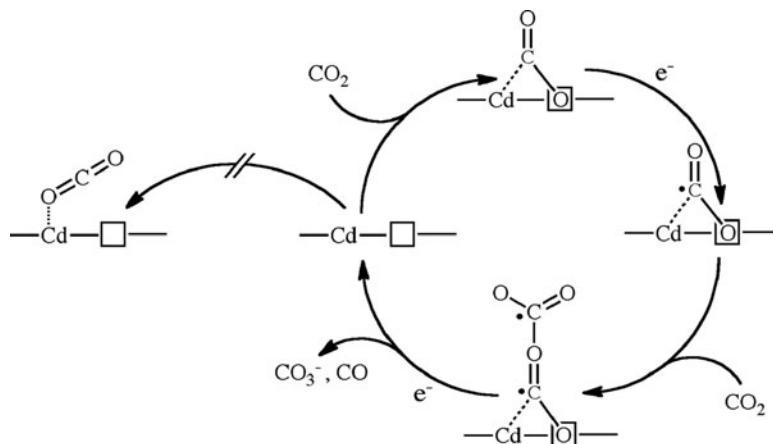
Scheme 10 Proposed mechanism for the photocatalytic reduction of CO$_2$ to CO on CdS with sulfur vacancies

reduction range from 0.1 to 0.4. Because CdS can absorb < 480-nm light, it can be used as visible light-driven photocatalyst for CO$_2$ reduction to CO in the presence of TEA as reductant. Sulfur vacancies on the surface of the CdS particles were revealed by EXAFS and emission measurements [124]. The proposed reaction mechanism is shown in Scheme 10. The vacant site and the neighboring Cd atom strongly interact with CO$_2$ molecules and its reduction gives a CO$_2$ anion radical in the adsorption site. The CO$_2$ anion radical accepts a further electron and oxygen is captured by another CO$_2$ to give CO and CO$_3^{2-}$. ZnS can also work as a photocatalyst of CO$_2$ reduction to formic acid using TEA as a reductant [127, 128]. The addition of Cd^{2+} enhanced the photocatalytic ability of ZnS, and the quantum yield of formic acid production is 0.375.

3.4 Polyoxometalates

Various polyoxometalate (POM) oxygen bridged clusters with metals such as W, Ti, and Ru have been reported, and some of them can function as photocatalysts under UV-light irradiation. Photocatalytic CO_2 reduction to CH_4 was achieved using $K_7[PTi_2W_{10}O_{40}]$ $6H_2O$ or $K_5[BW_{12}O_{40}]$ $15H_2O$ as photocatalyst in the presence of CH_3OH as a sacrificial donor [133]. Another POM [$Ru^{III}(H_2O)$ $SiW_{11}O_{39}$] [$(C_6H_{13})_4N^+$]$_5$ photocatalyzes CO_2 reduction to CO in toluene containing various amines [77]. Isotope labeling experiments using $^{13}CO_2$ revealed that after [$Ru^{III}(H_2O)SiW_{11}O_{39}$] eliminates the water ligand in dry toluene, CO_2 can interact with [$Ru^{III}SiW_{11}O_{39}$] to give ([$Ru^{III}(CO_2)SiW_{11}O_{39}$]). The authors proposed that a 1:1 adduct of [$Ru^{III}(CO_2)SiW_{11}O_{39}$] and the amine is formed in the solution, and the CO_2 ligand is reduced to CO by irradiation to the adduct (Scheme 11). The efficiency of the reduction of CO_2 was found to depend strongly on the added amines, and the highest yield of CO was obtained using TEA as reductant ($TN_{CO} = 3$, $\Phi_{CO} = 0.02$).

3.5 Hybrid Systems

In recent years, novel photocatalytic CO_2 reduction systems, which combine semiconductor photocatalysts and other functional units, have been reported. Visible light driven photocatalysis of CO_2 was achieved using CdSe quantum dots as a photosensitizer and Pt/TiO_2 as the catalyst unit [78]. Electron injection from bulk CdSe to TiO_2 does not proceed because bulk CdSe has a more positive CB energy than TiO_2. However, because the CdSe quantum dots exhibit a negative shift of the CB energy, electron injection to the TiO_2 can proceed. Visible light irradiation of the $CdSe/Pt/TiO_2$ hybrid catalyst in an aqueous solution gave CH_4 and CH_3OH with
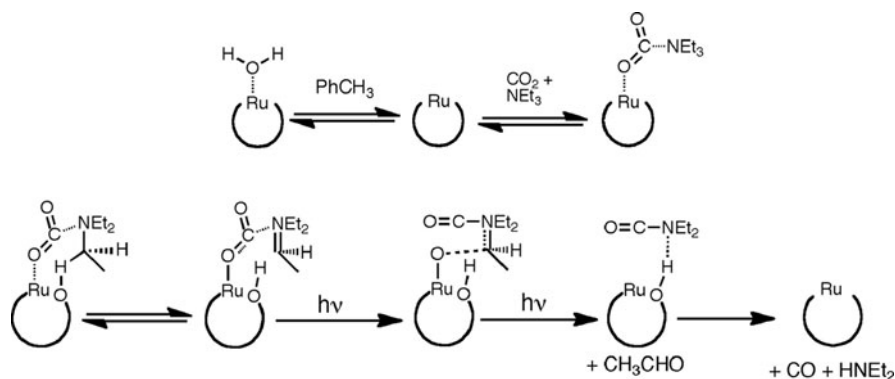

Scheme 11 Proposed mechanism for the photocatalytic reduction of CO_2 by [$Ru^{III}(H_2O)$ $SiW_{11}O_{39}$]

TF $=$ 48 and 3.3 ppm (g cat.)$^{-1}$ h^{-1}, respectively, without formation of CO or H$_2$. Interestingly, when Fe was used instead of Pt as co-catalyst, only H$_2$ evolution was observed upon irradiation ($>$ 55 ppm (g cat.)$^{-1}$ h^{-1}).

Combined photocatalytic systems of TiO$_2$ with metal complexes have been reported [95]. Visible light irradiation of Cu–Fe/TiO$_2$ chemically combined with Ru(4,4'-(COOH)$_2$-bpy)$_2$(NCS)$_2$ (N3 dye: bpy $=$ 2,2'-bipyridine) under a CO$_2$ atmosphere in the presence of water as a reductant gave C$_2$H$_6$ and CH$_4$ [87]. A mixed photocatalytic system with Pt deposited on a TiO$_2$ catalyst and [Ru(bpy)$_3$]$^{2+}$ (**16**) have also been reported. There CH$_4$ was detected and the reductant was supposed to be water [89]. A three-component system with [Ru(bpy)$_2$(4,4'-(PO$_3$H$_2$)$_2$-bpy)]$^{2+}$, TiO$_2$ nanoparticles, and an enzyme (CODH I) from *Carboxydothermus hydrogenoformans* (Ch) has been recently reported (Fig. 6) [72]. CODH I has an [Ni4Fe-4S] active site for CO$_2$ reduction. Selective CO production was observed upon visible light irradiation in a buffer aqueous solution containing 2-(*N*-morpholino)ethanesulfonic acid (MES) as reductant. At pH 6 and 20 °C the visible light sensitized system produces $\sim$ 5 µmol CO during a 4 h period of irradiation. The TF of CO formation was 250 µmol (g of TiO$_2$)$^{-1}$ h^{-1} on the basis of TiO$_2$, and 530 (mol^{-1} of CODH I) h^{-1} on the basis of CODH I, which changed dramatically with the temperature. The TF at 50 °C was 2 $\sim$ 3 times higher than that at 20 °C.

A newly-designed photoelectrocatalytic (PEC) reactor for CO$_2$ reduction, which combines photocatalysis by TiO$_2$ and electrocatalysis by carbon nanotubes (CNT), has recently been proposed (Fig. 7) [152]. A proton-conductive Nafion® membrane connects the TiO$_2$ and CNT. Irradiation of the combined system of nano-structured TiO$_2$ deposited on a metal Ti electrode with Pt modified CNT deposited on carbon sheet caused water splitting to H$_2$ and O$_2$. A half-cell for the cathodic electrode, i.e., Pt or Fe modified CNT electrode, produces various organic molecules such as 2-propanol due to electrocatalytic reduction of CO$_2$ on the electrode. The proposed PEC reactor is incomplete in its present state. However, these systems are expected to couple water splitting and CO$_2$ reduction, and thus it may establish a new artificial photosynthetic system.
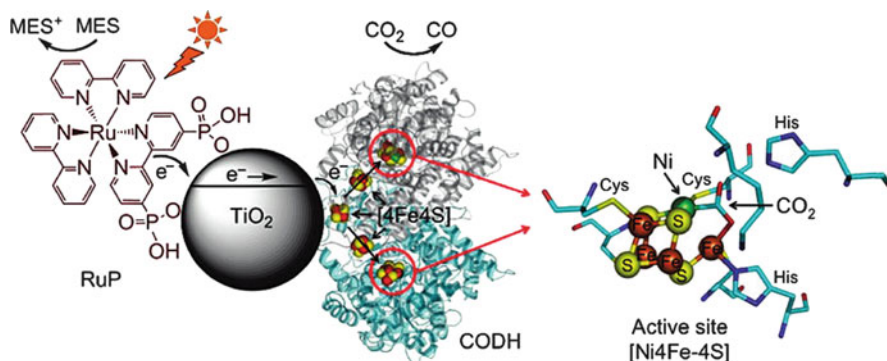
Fig. 6 A photocatalytic system for CO$_2$ reduction using TiO$_2$ nanoparticles with CODH I and a Ru(II) complex. (Reprinted from [72] with permission by the American Chemical Society)
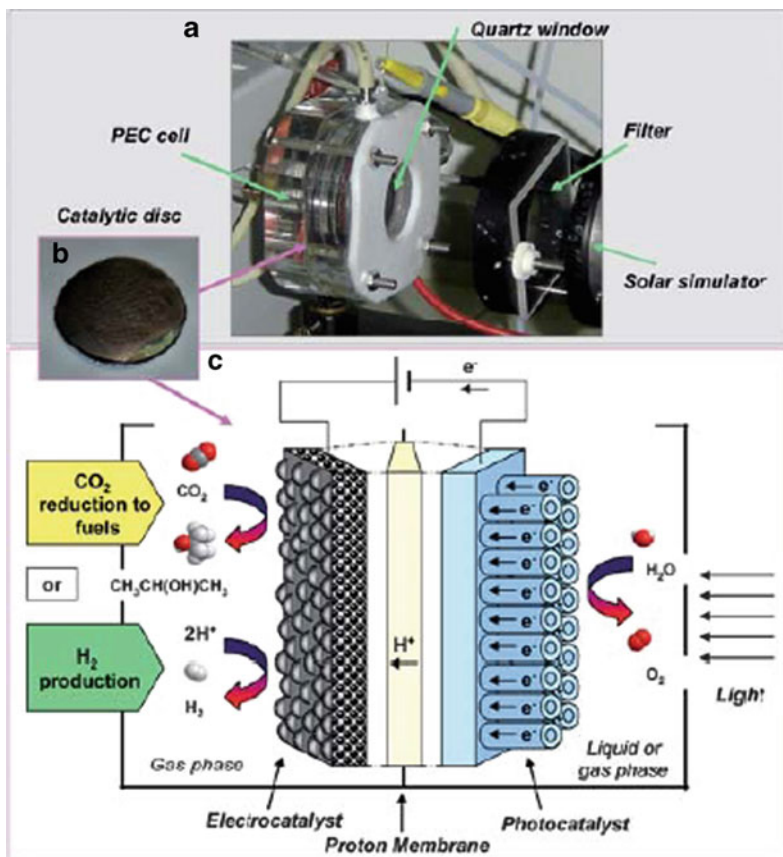
Fig. 7 (**a**) View and cell structure of the PEC device. (**b**) Photo/electro-catalytic disc. (**c**) Scheme of PEC device. (Reprinted from [152] with permission by the Royal Society of Chemistry)

4 Summary

Photocatalysis using both homogeneous and heterogeneous systems for CO_2 reduction have been reviewed.

In homogeneous systems, some photocatalysts using transition metal complexes show outstanding performance, such as high absorbance in the visible region, high quantum yields, and high product selectivities. However, no metal complex which can use water as the reductant for CO_2 reduction has been reported so far.

Recently, the number of reports about CO_2 reduction using semiconductor photocatalysts has been increasing rapidly. Some metal oxide semiconductors, typically TiO_2, have advantages over molecular catalysts, in that they can use water as a reductant. However, the efficiencies of many of the semiconductor photocatalysts for CO_2 reduction remain quite low, mainly because of competition

with hydrogen evolution from water. It should be noted that, in many cases, the carbon source of the photoproducts has not been identified. Recently, it has been pointed out that the organic contaminants become both carbon sources and reductants of the reaction products for photocatalytic reduction of CO$_2$ using TiO$_2$ [153]. Careful experiments should always be undertaken to clarify this point, such as isotope-labeling experiments using ^{13}CO$_2$ (Table 5).

References

1. Bard AJ (1976) Encyclopedia of electrochemistry of the elements. Dekker, New York
2. Lehn JM, Ziessel R (1982) Proc Natl Acad Sci USA Phys Sci 79:701
3. Fujita E (1999) Coord Chem Rev 185–186:373
4. Hawecker J, Lehn J-M, Ziessel R (1983) J Chem Soc Chem Commun 536
5. Hawecker J, Lehn J-M, Ziessel R (1986) Helv Chim Acta 69:1990
6. Hori H, Johnson FPA, Koike K, Ishitani O, Ibusuki T (1996) J Photochem Photobiol A 96:171
7. Hori H, Koike K, Ishizuka M, Takeuchi K, Ibusuki T, Ishitani O (1997) J Organomet Chem 530:169
8. Takeda H, Koike K, Inoue H, Ishitani O (2008) J Am Chem Soc 130:2023
9. Koike K, Hori H, Ishizuka M, Westwell JR, Takeuchi K, Ibusuki T, Enjouji K, Konno H, Sakamoto K, Ishitani O (1997) Organometallics 16:5724
10. Hori H, Johnson FPA, Koike K, Takeuchi K, Ibusuki T, Ishitani O (1997) J Chem Soc Dalton Trans 1019
11. Hori H, Ishihara J, Koike K, Takeuchi K, Ibusuki T, Ishitani O (1999) J Photochem Photobiol A 120:119
12. Tsubaki H, Sekine A, Ohashi Y, Koike K, Takeda H, Ishitani O (2005) J Am Chem Soc 127:15544
13. Tsubaki H, Sugawara A, Takeda H, Gholamkhass B, Koike K, Ishitani O (2007) Res Chem Intermed 33:37
14. Ishitani O, George MW, Ibusuki T, Johnson FPA, Koike K, Nozaki K, Pac C, Turner JJ, Westwell JR (1994) Inorg Chem 33:4712
15. Grodkowski J, Behar D, Neta P, Hambright P (1997) J Phys Chem A 101:248
16. Behar D, Dhanasekaran T, Neta P, Hosten CM, Ejeh D, Hambright P, Fujita E (1998) J Phys Chem A 102:2870
17. Matsuoka S, Kohzuki T, Pac C, Ishida A, Takamuku S, Kusaba M, Nakashima N, Yanagida S (1992) J Phys Chem 96:4437
18. Koike K, Okoshi N, Hori H, Takeuchi K, Ishitani O, Tsubaki H, Clark IP, George MW, Johnson FPA, Turner JJ (2002) J Am Chem Soc 124:11448
19. Kurz P, Probst B, Spingler B, Alberto R (2006) Eur J Inorg Chem 2006:2966
20. Kutal C, Weber MA, Ferraudi G, Geiger D (1985) Organometallics 4:2161
21. Kalyanasundaram K (1986) J Chem Soc Faraday Trans II 82:2401
22. Kutal C, Corbin AJ, Ferraudi G (1987) Organometallics 6:553
23. Stor GJ, Hartl F, van Outersterp JWM, Stufkens DJ (1995) Organometallics 14:1115
24. Hayashi Y, Kita S, Brunschwig BS, Fujita E (2003) J Am Chem Soc 125:11976
25. Fujita E, Muckerman JT (2004) Inorg Chem 43:7636
26. Gibson DH, Yin X, He H, Mashuta MS (2003) Organometallics 22:337

27. Dhanasekaran T, Grodkowski J, Neta P, Hambright P, Fujita E (1999) J Phys Chem A 103:7742
28. Grodkowski J, Dhanasekaran T, Neta P, Hambright P, Brunschwig BS, Shinozaki K, Fujita E (2000) J Phys Chem A 104:11332
29. Grodkowski J, Neta P (2000) J Phys Chem A 104:1848
30. Grodkowski J, Neta P (2000) J Phys Chem A 104:4475
31. Grodkowski J, Neta P, Fujita E, Mahammed A, Simkhovich L, Gross Z (2002) J Phys Chem A 106:4722
32. Morris AJ, Meyer GJ, Fujita E (2009) Acc Chem Res 42:1983
33. Willner I, Maidan R, Mandler D, Durr H, Dorr G, Zengerle K (1987) J Am Chem Soc 109:6080
34. Maidan R, Willner I (1986) J Am Chem Soc 108:8101
35. Ishida H, Tanaka K, Tanaka T (1987) Chem Lett 1035
36. Ishida H, Terada T, Tanaka K, Tanaka T (1990) Inorg Chem 29:905
37. Ishida H, Tanaka K, Tanaka T (1988) Chem Lett 339
38. Lehn J-M, Ziessel R (1990) J Organomet Chem 382:157
39. Grant JL, Goswami K, Spreer LO, Otvos JW, Calvin M (1987) J Chem Soc Dalton Trans 2105
40. Craig CA, Spreer LO, Otvos JW, Calvin M (1990) J Phys Chem 94:7957
41. Kimura E, Wada S, Shionoya M, Okazaki Y (1994) Inorg Chem 33:770
42. Matsuoka S, Yamamoto K, Pac C, Yanagida S (1991) Chem Lett 2099
43. Matsuoka S, Yamamoto K, Ogata T, Kusaba M, Nakashima N, Fujita E, Yanagida S (1993) J Am Chem Soc 115:601
44. Ogata T, Yanagida S, Brunschwig BS, Fujita E (1995) J Am Chem Soc 117:6708
45. Ogata T, Yamamoto Y, Wada Y, Murakoshi K, Kusaba M, Nakashima N, Ishida A, Takamuku S, Yanagida S (1995) J Phys Chem 99:11916
46. Ishida H, Tanaka K, Tanaka T (1985) Chem Lett 405
47. Ishida H, Tanaka K, Morimoto M, Tanaka T (1986) Organometallics 5:724
48. Ishida H, Tanaka K, Tanaka T (1987) Organometallics 6:181
49. Chardon-Noblat S, Collomb-Dunand-Sauthier M-N, Deronzier A, Ziessel R, Zsoldos D (1994) Inorg Chem 33:4410
50. Willner I, Mandler D, Riklin A (1986) J Chem Soc Chem Commun 1022
51. Mandler D, Willner I (1988) J Chem Soc Perkin Trans 2:997
52. Kimura E, Bu X, Shionoya M, Wada S, Maruyama S (1992) Inorg Chem 31:4542
53. Komatsuzaki N, Himeda Y, Hirose T, Sugihara H, Kasuga K (1999) Bull Chem Soc Jpn 72:725
54. Gholamkhass B, Mametsuka H, Koike K, Tanabe T, Furue M, Ishitani O (2005) Inorg Chem 44:2326
55. Koike K, Naito S, Sato S, Tamaki Y, Ishitani O (2009) J Photochem Photobiol A 207:109
56. Sato S, Koike K, Inoue H, Ishitani O (2007) Photochem Photobiol Sci 6:454
57. Kimura E, Wada S, Shionoya M, Takahashi T, Litaka Y (1990) J Chem Soc Chem Commun 397
58. Bian Z-Y, Sumi K, Furue M, Sato S, Koike K, Ishitani O (2008) Inorg Chem 47:10801
59. Bian Z-Y, Sumi K, Furue M, Sato S, Koike K, Ishitani O (2009) Dalton Trans 983
60. Bian Z-Y, Chi S-M, Li L, Fu W (2010) Dalton Trans 39:7884
61. Inoue T, Fujishima A, Konishi S, Honda K (1979) Nature 277:637
62. Roy SC, Varghese OK, Paulose M, Grimes CA (2010) ACS Nano 4:1259
63. Mikkelsen M, Jorgensen M, Krebs FC (2010) Energy Environ Sci 3:43
64. Varghese OK, Paulose M, LaTempa TJ, Grimes CA (2009) Nano Lett 9:731
65. Indrakanti VP, Kubicki JD, Schobert HH (2009) Energy Environ Sci 2:745
66. Shiraishi Y, Hirai T (2008) J Photochem Photobiol C 9:157
67. Kočí K, Obalová L, Lacný Z (2008) Chem Pap 62:1
68. Dey GR (2007) J Nat Gas Chem 16:217

69. Usubharatana P, McMartin D, Veawab A, Tontiwachwuthikul P (2006) Ind Eng Chem Res 45:2558
70. Matsuoka M, Anpo M (2003) J Photochem Photobiol C 3:225
71. Yoneyama H (1997) Catal Today 39:169
72. Woolerton TW, Sheard S, Reisner E, Pierce E, Ragsdale SW, Armstrong FA (2010) J Am Chem Soc 132:2132
73. Vijayan B, Dimitrijevic NM, Rajh T, Gray K (2010) J Phys Chem C 114:12994
74. Schulte KL, DeSario PA, Gray KA (2010) Appl Catal B 97:354
75. Teramura K, Okuoka S, Tsuneoka H, Shishido T, Tanaka T (2010) Appl Catal B 96:565
76. Tsuneoka H, Teramura K, Shishido T, Tanaka T (2010) J Phys Chem C 114:8892
77. Khenkin AM, Efremenko I, Weiner L, Martin JML, Neumann R (2010) Chem Eur J 16:1356
78. Wang C, Thompson RL, Baltrus J, Matranga C (2010) J Phys Chem Lett 1:48
79. Yang H-C, Lin H-Y, Chien Y-S, Wu J, Wu H-H (2009) Catal Lett 131:381
80. Zhang Q-H, Han W-D, Hong Y-J, Yu J-G (2009) Catal Today 148:335
81. Wu JCS (2009) Catal Surv Asia 13:30
82. Koci K, Obalova L, Matejova L, Placha D, Lacny Z, Jirkovsky J, Solcova O (2009) Appl Catal B 89:494
83. Kaneco S, Ueno Y, Katsumata H, Suzuki KT, Ohta K (2009) Chem Eng J 148:57
84. Liu Y, Huang B, Dai Y, Zhang X, Qin X, Jiang M, Whangbo M-H (2009) Catal Commun 11:210
85. Wu JCS, Wu TH, Chu TC, Huang HJ, Tsai DP (2008) Top Catal 47:131
86. Barton EE, Rampulla DM, Bocarsly AB (2008) J Am Chem Soc 130:6342
87. Nguyen T-V, Wu JCS, Chiou C-H (2008) Catal Commun 9:2073
88. Pan P-W, Chen Y-W (2007) Catal Commun 8:1546
89. Ozcan O, Yukruk F, Akkaya E, Uner D (2007) Top Catal 44:523
90. Nishimura A, Sugiura N, Fujita M, Kato S (2007) Kagaku Kogaku Ronbunshu 33:146
91. Nishimura A, Fujita M, Kato S (2007) Kagaku Kogaku Ronbunshu 33:432
92. Lo C-C, Hung C-H, Yuan C-S, Wu J-F (2007) Sol Energy Mater Sol Cells 91:1765
93. Lo C-C, Hung C-H, Yuan C-S, Hung Y-L (2007) Chin J Catal 28:528
94. Dey GR, Pushpa KK (2007) Res Chem Intermed 33:631
95. Liu S, Zhao Z, Wang Z (2007) Photochem Photobiol Sci 6:695
96. Lin W, Frei H (2006) CR Chim 9:207
97. Kaneco S, Katsumata H, Suzuki T, Ohta K (2006) Chem Eng J 116:227
98. Kaneco S, Katsumata H, Suzuki T, Ohta K (2006) Appl Catal B 64:139
99. Lin W, Frei H (2005) J Am Chem Soc 127:1610
100. Slamet, Nasution HW, Purnama E, Kosela S, Gunlazuardi J (2005) Catal Commun 6:313
101. Pathak P, Meziani MJ, Li Y, Cureton LT, Sun Y-P (2004) Chem Commun 1234
102. Lin W, Han H, Frei H (2004) J Phys Chem B 108:18269
103. Teramura K, Tanaka T, Ishikawa H, Kohno Y, Funabiki T (2003) J Phys Chem B 108:346
104. Shioya Y, Ikeue K, Ogawa M, Anpo M (2003) Appl Catal A 254:251
105. Guan G, Kida T, Yoshida A (2003) Appl Catal B 41:387
106. Ikeue K, Nozaki S, Ogawa M, Anpo M (2002) Catal Today 74:241
107. Ikeue K, Nozaki S, Ogawa M, Anpo M (2002) Catal Lett 80:111
108. Kohno Y, Ishikawa H, Tanaka T, Funabiki T, Yoshida S (2001) Phys Chem Chem Phys 3:1108
109. Ikeue K, Yamashita H, Anpo M, Takewaki T (2001) J Phys Chem B 105:8350
110. Tanaka T, Kohno Y, Yoshida S (2000) Res Chem Intermed 26:93
111. Kohno Y, Tanaka T, Funabiki T, Yoshida S (2000) Phys Chem Chem Phys 2:5302
112. Kohno Y, Tanaka T, Funabiki T, Yoshida S (2000) Phys Chem Chem Phys 2:2635
113. Subrahmanyam M, Kaneco S, Alonso-Vante N (1999) Appl Catal B 23:169
114. Kohno Y, Hayashi H, Takenaka S, Tanaka T, Funabiki T, Yoshida S (1999) J Photochem Photobiol A 126:117
115. Kaneco S, Kurimoto H, Shimizu Y, Ohta K, Mizuno T (1999) Energy 24:21

116. Ikeue K, Yamashita H, Anpo M (1999) Chem Lett 1135
117. Yamashita H, Fujii Y, Ichihashi Y, Zhang SG, Ikeue K, Park DR, Koyano K, Tatsumi T, Anpo M (1998) Catal Today 45:221
118. Liu B-J, Torimoto T, Yoneyama H (1998) J Photochem Photobiol A 115:227
119. Liu B-J, Torimoto T, Yoneyama H (1998) J Photochem Photobiol A 113:93
120. Kohno Y, Tanaka T, Funabiki T, Yoshida S (1998) J Chem Soc Faraday Trans 94:1875
121. Kaneco S, Shimizu Y, Ohta K, Mizuno T (1998) J Photochem Photobiol A 115:223
122. Hirota K, Tryk DA, Yamamoto T, Hashimoto K, Okawa M, Fujishima A (1998) J Phys Chem B 102:9834
123. Anpo M, Yamashita H, Ikeue K, Fujii Y, Zhang SG, Ichihashi Y, Park DR, Suzuki Y, Koyano K, Tatsumi T (1998) Catal Today 44:327
124. Fujiwara H, Hosokawa H, Murakoshi K, Wada Y, Yanagida S, Okada T, Kobayashi H (1997) J Phys Chem B 101:8270
125. Yanagida S, Kanemoto M, Ishihara KI, Wada Y, Sakata T, Mori H (1997) Bull Chem Soc Jpn 70:2063
126. Kohno Y, Tanaka T, Funabiki T, Yoshida S (1997) Chem Commun 841
127. Kanemoto M, Hosokawa H, Wada Y, Murakoshi K, Yanagida S, Sakata T, Mori H, Ishikawa M, Kobayashi H (1996) J Chem Soc Faraday Trans 92:2401
128. Inoue H, Moriwaki H, Maeda K, Yoneyama H (1995) J Photochem Photobiol A 86:191
129. Sayama K, Arakawa H (1993) J Phys Chem 97:531
130. Ishitani O, Inoue C, Suzuki Y, Ibusuki T (1993) J Photochem Photobiol A 72:269
131. Kanemoto M, Shiragami T, Pac CJ, Yanagida S (1992) J Phys Chem 96:3521
132. Hirano K, Inoue K, Yatsu T (1992) J Photochem Photobiol A 64:255
133. Yamase T, Sugeta M (1990) Inorg Chim Acta 172:131
134. Fujishima A, Rao TN, Tryk DA (2000) J Photochem Photobiol C 1:1
135. Fujishima A, Honda K (1972) Nature 238:37
136. Yui T, Tsuchino T, Mino H, Kajino T, Itoh S, Fukushima Y, Takagi K (2009) Bull Chem Soc Jpn 82:914
137. Yui T, Tsuchino T, Akatsuka K, Yamauchi A, Kobayashi Y, Hattori T, Haga MA, Takagi K (2006) Bull Chem Soc Jpn 79:386
138. Halmann M, Ulman M, Aurian-Blajeni B (1983) Sol Energy 31:429
139. Dey GR, Belapurkar AD, Kishore K (2004) J Photochem Photobiol A 163:503
140. Yamashita H, Okazaki M, Ikeue K, Anpo M (2004) In: Sang-Eon Park J-SC, Kyu-Wan L (eds) Studies in surface science and catalysis, vol 153. Elsevier, p 289
141. Hwang JS, Chang JS, Park SE, Ikeue K, Anpo M (2004) In: Sang-Eon Park J-SC, Kyu-Wan L (eds) Studies in surface science and catalysis, vol 153. Elsevier, p 299
142. Ikeue K, Yamashita H, Anpo M (2002) Electrochemistry 70:402
143. Park D-R, Zhang J, Ikeue K, Yamashita H, Anpo M (1999) J Catal 185:114
144. Zhang SG, Fujii Y, Yamashita H, Koyano K, Tatsumi T, Anpo M (1997) Chem Lett 26:659
145. Zhang SG, Fujii Y, Yamashita H, Koyano K, Tatsumi T, Anpo M (1997) Chem Lett 659
146. Anpo M, Yamashita H, Ichihashi Y, Fujii Y, Honda M (1997) J Phys Chem B 101:2632
147. Yamashita H, Ichihashi Y, Anpo M, Hashimoto M, Louis C, Che M (1996) J Phys Chem 100:16041
148. Teramura K, Tsuneoka H, Shishido T, Tanaka T (2008) Chem Phys Lett 467:191
149. Flaisher H, Tenne R, Halmann M (1996) J Electroanal Chem 402:97
150. Barton CE, Lakkaraju PS, Rampulla DM, Morris AJ, Abelev E, Bocarsly AB (2010) J Am Chem Soc 132:11539
151. Johne P, Kisch H (1997) J Photochem Photobiol A 111:223
152. Ampelli C, Centi G, Passalacqua R, Perathoner S (2010) Energy Environ Sci 3:292
153. Yang C-C, Yu Y-H, van der Linden B, Wu JCS, Mul G (2010) J Am Chem Soc 132:8398

Design of Heterogeneous Photocatalysts Based on Metal Oxides to Control the Selectivity of Chemical Reactions

Andrea Maldotti and Alessandra Molinari

Abstract Photocatalysis is particularly relevant in order to realize chemical transformations of interest in synthesis and, at the same time, to move towards a "sustainable chemistry" with a minimal environmental impact. Heterogeneous systems with well-defined textural characteristics represent a suitable means to tailor the selectivity of photocatalytic processes. Here, we summarize and classify the significant features of photocatalysts consisting of photoactive metal oxides dispersed on high-surface-area solid supports, or constrained inside their porous network. These systems are based on the use of titanium dioxide, highly dispersed oxides of titanium, chromium, vanadium, and polyoxotungstates. They share similar primary photoprocesses: light absorption induces a charge separation process with formation of positive holes able to oxidize organic substrates. A great number of the papers discussed here concern oxidation reactions carried out in the presence of O_2 for inducing partial oxidation of alcohols and monooxygenation of hydrocarbons. We also devote some attention to photocatalysis in the absence of O_2. In these conditions, the photogenerated charge separation offers the possibility to induce the formation of C–C and C–N bonds. We emphasize that the optimal tailoring of photoactive materials for synthetic purposes can be achieved by combining recent advances in the preparation of nanostructured materials with mechanistic knowledge derived from surface science and molecular level investigations.

A. Maldotti (✉) and A. Molinari
Dipartimento di Chimica, Università di Ferrara, Via Luigi Borsari 46, 44121 Ferrara, Italy
e-mail: mla@unife.it

Contents

1 Introduction

The term photocatalysis is often used to refer to processes carried out in the presence of semiconductor materials and aimed at wastewater decontamination or water splitting for the generation of hydrogen as a fuel. However, the idea that photocatalysis can provide an alternative to more conventional synthetic pathways has been gradually emerging [1–12]. In its broadest sense, photocatalysis for synthetic purposes concerns the use of light to induce chemical transformations of organic or inorganic substrates that are transparent in the wavelength range employed. The radiation is absorbed by a photocatalyst, whose electronically excited states are able to trigger the chemical reactions of interest. The overall process can be considered photocatalytic when (1) the photoactive species is regenerated in its initial state at the end of a reaction cycle, just as happens in thermal catalysis and (2) the photocatalyst is consumed less than in stoichiometric amounts, while light is a stoichiometric reagent. Photocatalysis is particularly relevant in order to realize chemical transformations of interest in synthesis and, at the same time, to move towards a "sustainable chemistry" with a minimal environmental impact. In fact, photochemical reactions require milder conditions than thermal processes, may allow the conception of short and efficient reaction sequences, minimizing side processes, and may employ sunlight as a completely renewable source of energy leaving no residue.

Selectivity is a key issue in photocatalytic processes aimed at the production of functionalized intermediates of interest in fine chemistry. In order to pursue this objective, all steps of the catalytic process must be optimized. Heterogeneous systems represent a suitable means to tailor efficiency and selectivity of photocatalytic processes through the control of the microscopic environment surrounding the photoactive center, which is located on the catalyst surface, inside pores, or in a

thin liquid film at the surface. In particular, type and textural characteristics of the material employed may affect important physical and chemical properties of the photocatalytic system that act as rate determining steps: absorption of light, adsorption–desorption equilibria of reaction intermediates, and control of the diffusion of reactants and products in or out of catalytic sites located inside of a porous network. It is in this context that recent developments in the discovery of new synthetic routes for the preparation of materials with well-defined structures at the nanometer scale may afford better design of active sites for selective catalytic processes, including photocatalytic processes [13]. Of course, another main role of a solid support is that the photocatalysts become more easily handled and recycled.

Herein we summarize and classify the significant features of photocatalytic systems based on the use of titanium dioxide, highly dispersed oxides of titanium, chromium, vanadium, and polyoxotungstates. They share similar primary photoprocesses: light absorption induces a charge separation process with formation of positive holes that are able to oxidize organic substrates. A great number of the works discussed here concern oxidation reactions carried out in the presence of O_2, whose role is not only that of scavenging the photogenerated electrons but also that of producing active oxygen species. Among oxidation reactions, most of the photocatalytic processes concern the conversion of alcohols to carbonylic compounds and the monooxygenation of hydrocarbons. In this connection, it is to underline that the search of new catalysts able to induce the oxidation of organic substrates with an environmentally friendly and cheap molecule like O_2 represents a major target from the synthetic and industrial points of view [14–16]. We also devote some attention to photocatalysis under anaerobic conditions since, in the absence of O_2, the photogenerated charge separation offers the possibility to induce redox-combined processes leading to the formation of C–C and C–N bonds. We emphasize that the optimal tailoring of the photoactive materials for synthetic purposes can be achieved by combining recent advances in the preparation of nanostructured materials with mechanistic knowledge derived from surface science and molecular level investigations.

2   Titanium Dioxide

Titanium dioxide is certainly the most investigated semiconductor in photocatalysis since it combines unique and attractive characteristics, such as high photocatalytic activity, stability, and environmental tolerance. There is an ever increasing attention to tailoring the reactivity of TiO_2-based photocatalysts to drive reactions of interest from the synthetic point of view [1–11]. It is generally accepted [1–11, 17–21] that excitation of TiO_2 with supra bandgap photons causes a charge separation in the semiconductor solid according to Fig. 1: electrons are promoted to the conduction band (e^-) and holes are left in the valence band (h^+). Subsequent interfacial electron transfer processes may then occur with adsorbed substrates. In

$$TiO_2 \xrightarrow{h\nu} (e^-/h^+)$$

$$(OH^-)_{surf} + h^+ \longrightarrow (OH^\bullet)_{surf}$$

$$O_2 + e^- (+H^+) \longrightarrow O_2^{\bullet-} (HO_2^\bullet)$$

$$Ox + e^- \longrightarrow Red$$
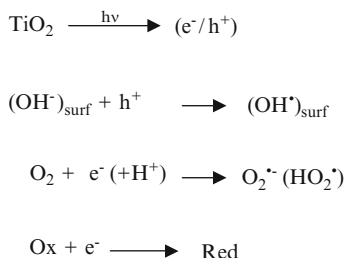
particular, oxidation of an organic substrate (RH) to radical species can take place through either direct electron transfer to the photogenerated positive holes or hydrogen atom abstraction by $OH^\bullet$ radicals, which are formed as a consequence of hole capture by adsorbed OH^- groups. Because of its considerable oxidizing capability, TiO_2 is able to photooxidize further partially oxygenated products up to full mineralization of the starting organic substrate. This over-oxidation process, which has contributed to the development of many studies focusing on environmental cleanup, may be a problem when photoexcited TiO_2 must be employed for synthetic purposes.

Due to its unlimited availability, O_2 is usually employed as scavenger of the photogenerated electrons, undergoing reductive activation to $O_2^{-\bullet}$ or $HO_2^\bullet$. These, in turn, may yield other reactive oxygen species that contribute to the final product distribution. Under anaerobic conditions, the conduction band electrons can be transferred to various organic or inorganic substrates (Ox in Fig. 1), whose reduction intermediates may take part effectively in the formation of useful products. While in an n-type photoelectrode electrons can be conveyed through an external circuit, in a suspension of the same semiconductor both charges have to be transferred through the interface to independent (acceptor and donor) species. This means that, for charge transfer to compete with recombination, capture of at least one of the photogenerated charges by species in solution must be a fast process.

There are now a number of studies indicating that it is possible to control activity and selectivity of photoexcited TiO_2 in order to accumulate partially oxidized products with only negligible over-oxidation and mineralization of the substrate. In particular, it is becoming evident that the photocatalytic activity of TiO_2-based photocatalysts is governed by several important parameters including (1) crystallographic and morphological characteristics, (2) adsorption phenomena, (3) surface modification, and (4) composition of the reaction medium.

2.1 Oxidations

2.1.1 Alkanes

Catalytic oxidation of alkanes represents a fundamental process for the production of fine chemicals [22–24]. Unfortunately, many of these processes are characterized

by several drawbacks, such as low selectivity, poor catalyst stability, and the employment of large amounts of pollutant chemical oxidants. Therefore, there is a strong demand for the development of robust heterogeneous catalysts that can promote selective oxygenation of C–H bonds by O_2 under mild temperature and pressure conditions. In this context, the liquid-phase oxygenation of cyclohexane by photoexcited semiconductors such as TiO_2 continues to be the object of intense research for two main reasons. On the one hand, the study of this representative key reaction can provide insights on the oxygenation mechanism of non-activated C–H bonds; on the other hand, the conversion of cyclohexane to cyclohexanone is important since this ketone is a precursor in the synthesis of adipic acid and caprolactam, which are ultimately used in the production of monomer for nylon 66 and nylon 6.

A number of articles indicate that the photocatalytic oxidation of cyclohexane at room temperature and atmospheric pressure yields cyclohexanone as the main product (selectivity higher than 80%) and minor amounts of cyclohexanol and carbon dioxide [25–37]. Figure 2 summarizes the main steps of the reaction mechanism. The photogenerated cyclohexyl radicals are able to react with O_2 under a diffusion-controlled rate to give peroxy radicals. Since hydrogen atom abstraction by cyclohexyl-peroxy radicals is energetically unfavorable due to the high C–H bond dissociation energy in cyclohexane, the fate of these radicals is strongly determined by the competition between their reaction with the photogenerated electrons and their bimolecular radical disproportionation. This competition affects the final yields to cyclohexanone and cyclohexanol [29, 31, 32, 35]. Cyclohexanol may also be formed on the surface of the semiconductor as a consequence of the reaction between cyclohexyl radical and OH$^\bullet$ radicals. Consecutive photocatalytic oxidation of adsorbed cyclohexanol is a likely additional source of cyclohexanone [26]. Further over-oxidation processes may yield strongly adsorbed carboxylates and carbonates that, likely, are a main cause of TiO_2 deactivation [30, 38] and that, finally, lead to the formation of carbon dioxide.
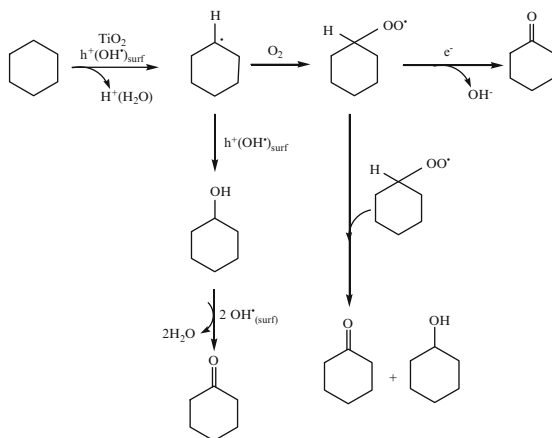
Fig. 2 Photocatalytic oxidation of cyclohexane

Several investigations report that adsorption equilibria of cyclohexanol and cyclohexanone strongly affect the final product distribution of the photocatalytic process [25–27, 30, 35, 39]. More specifically, it has been demonstrated [27, 30] that cyclohexanol is preferentially adsorbed onto the hydrophilic surface of TiO_2 with respect to both cyclohexane and cyclohexanone and, therefore, it undergoes facile over-oxidation ultimately to CO_2. On the other hand, cyclohexanone is less adsorbed than cyclohexanol, thus explaining, at least in part, its accumulation in the solution bulk. The competitive interaction of the oxygenated intermediates on the semiconductor is also affected by the nature of the dispersing medium. Research in our laboratories [26] shows that the presence of CH_2Cl_2 as co-solvent inhibits cyclohexanol interaction with TiO_2, so improving the final yield to this photoproduct. Other authors provide evidence that the effect of CH_2Cl_2 may also be ascribed to its direct participation in the photocatalytic redox process [27, 39]. The influence of other dispersing media on the photocatalytic oxidation of cyclohexane by TiO_2 has been investigated [27]. It has been found that isopropanol and chloroform are preferentially adsorbed in comparison to cyclohexane and that they form radicals that react with other solvent molecules more readily than with cyclohexane.

In addition to adsorption phenomena, the photoreactivity of TiO_2 towards cyclohexane can be controlled by textural effects. We have recently reported that a TiO_2-based mesoporous material, prepared by templating preformed TiO_2 nanoparticles, is a robust photocatalyst for inducing cyclohexane photooxidation to cyclohexanone with only traces of cyclohexanol [32]. This high selectivity has been ascribed to a different reactivity of O_2 and $C_6H_{11}OO^{\bullet}$ towards trapped and free conduction band electrons of the semiconductor: the structure of this material, constituted exclusively of arrays of sintered TiO_2 particles, favors an inter-particle electron connection which would entail a better utilization of electron traps. According to a previous investigation [29], once trapped, electrons are removed by $C_6H_{11}OO^{\bullet}$ radicals to yield cyclohexanone (Fig. 2) rather than being scavenged by O_2. This statement is confirmed by the observation that the selectivity to cyclohexanone decreases significantly when the mesoporous material contains silica domains able to inhibit the inter-particle electron mobility.

Very recently, novel insights into the effect of crystallinity, availability of holes and electrons, and the amount of surface OH-groups of anatase TiO_2 in the presence of cyclohexane have been reported [33, 35]. In those works, it has been shown that, upon increasing the crystallite size, productivity decreases, due to the smaller OH-group concentration and the cyclohexanol/cyclohexanone ratio increases. The influence of particle size and crystallinity on this ratio is explained in terms of lifetime of the photogenerated conduction band electrons. In particular, relatively large TiO_2 crystals (10–25 nm) are characterized by high effective hole concentration and, consequently, by accumulation of cyclohexyl peroxy radicals, which, in turn, undergo disproportionation to both cyclohexanone and cyclohexanol. The presence of Au on the TiO_2 surface gives similar effects [34]: the enhanced lifetime of the photogenerated electrons stabilized by Au particles allows a higher effective hole concentration and, consequently, a higher cyclohexanol formation rate as compared to unmodified TiO_2.
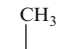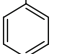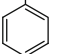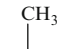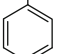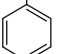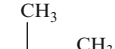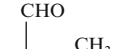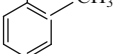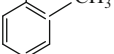
2.1.2 Aromatics

The search for new reaction pathways for the selective oxidation of aromatics continues to be of great interest in applied synthesis, since the main followed routes present several drawbacks in terms of cost and environmental impact. The ability of photoexcited TiO_2 to induce oxidation of aromatic substrates has been well recognized [40–44]. Alkylaromatics mainly undergo oxidation of their alkyl chain according to the mechanism reported in Fig. 2 for cyclohexane. Direct hydroxylation of the aromatic ring via electrophilic addition of the photogenerated OH· is possible when the substrate is benzene. This process occurs with a relatively low selectivity (about 15%) since phenol is easily decomposed through its subsequent reaction with $OH^\bullet$ radicals. Hydroxylation of mono-substituted benzene derivatives by photoexcited TiO_2 depends on the electron withdrawing properties of the substituents [45, 46]. In particular, photoexcitation of TiO_2 suspended in water containing benzene derivatives with an electron donating group leads to the formation of *ortho* and *para* hydroxylated isomers, in agreement with the directing properties of the substituent. In contrast, with substrates containing an electron withdrawing group, the OH· radical attack is non selective. Other investigations show that photocatalysis with TiO_2 can be employed for inducing the oxidation of naphthalene [47, 48]. Irradiation of TiO_2 suspended in water containing O_2 and 1% acetonitrile leads to the conversion of naphthalene to the corresponding 2-formyl-cinnamaldehyde and 1,4-naphthoquinone with 16% yield and about 50% naphthalene conversion. TiO_2 has also been employed for the photooxidation of phenanthrene [49]. A coumarin derivative is obtained as the main product when the dispersing medium is an acetonitrile solution containing 8% of water. The production of a coumarin derivative is attractive since its formation from phenanthrene opens new synthetic routes by a one-pot process.

There are many recent examples of how yield and selectivity of photocatalytic oxygenation of aromatics can be improved by designing TiO_2-based materials with specific morphology and surface properties [50–53]. A mesoporous photocatalytic system showing high conversion of benzene to phenol has been prepared by conventional particle aggregation or surfactant-templating methods [50]. The observed selectivity is ascribed to the fact that the sequential hydroxylation of phenol by $OH^\bullet$ radicals is suppressed due to competitive adsorption phenomena. Other works give evidence that the hydrophobic nature of the photoactive surface is beneficial for the selective oxidation of aromatic compounds. It has been shown that the high affinity of benzene for the surface of TiO_2-loaded ZSM-5 zeolites [51], for TiO_2-pillared clays [52], and for mesoporous silica containing TiO_2 nanoparticles [54] contributes to increasing its conversion rate to phenol when the photocatalytic experiment is carried out in aqueous solution.

A TiO_2 pillared montmorillonite clay (Ti-PILC) has recently been investigated as photocatalyst for the selective oxygenation of several alkylaromatics [53]. As shown in Table 1, accumulation of valuable carbonylic derivatives is possible since their over-oxidation to CO_2 is negligible. In particular, proper reaction conditions are found for obtaining carbonylic compounds with about 90% selectivity, a value

Table 1 Photocatalytic oxidation of alkylaromatics by Ti-PILC and TiO_2-P25

Photocatalyst	Substrate	μ moles of product/gram of TiO_2		μ moles of CO_2/gram of TiO_2
Ti-PILC	CH₃–(benzene)	CHO–(benzene)	2.7	<0.4
TiO₂-P25			*3.6*	*4.5*
Ti-PILC	CH₃–(benzene)–CH₃ (para)	CHO–(benzene)–CH₃ (para)	6.4	<0.4
TiO₂-P25			*1.8*	*1.3*
Ti-PILC	CH₃,CH₃–(benzene) (ortho)	CHO,CH₃–(benzene) (ortho)	2.2	<0.4
TiO₂-P25			*2.3*	*2.5*

significantly higher than that obtained with commercial TiO_2 Degussa P25. The physical chemical characterization of the photoactive material indicates that its large and hydrophobic surface is beneficial for the alkylaromatics to reach the photoexcited TiO_2 inside the micropores of the sheet. The same surface characteristics inhibit the adsorption of the more polar carbonylic photoproducts, which, therefore, are free to diffuse in the solution bulk, so preventing their further over-oxidation to CO_2. A series of Y, beta, mordenite and ZSM-5 zeolites containing nanosized TiO_2 clusters has been prepared by ionic exchange between Na^+ with titanyl cations ($Ti=O^{2+}$) followed by condensation [55]. The maximum loading of TiO_2 is determined by the cavity size and by the number of exchangeable cations. TiO_2/Y and TiO_2/mordenite show higher photoactivity than commercial anatase for the photooxygenation of thianthrene to thianthrene oxide ($\lambda = 254$ nm).

2.1.3 Alcohols

The partial oxidation of alcohols to carbonylic derivatives is another demanding chemical transformation for the production of fine and specialty chemicals. In this context, a vast number of studies have been devoted to the selective oxidation of alcohols catalyzed by photoexcited TiO_2 [56–73]. It is generally accepted that direct adsorption of the alcohol onto the semiconductor surface is a compulsory requirement for its oxidation; in particular, it is proposed by many authors to be a dissociative adsorption of the alcohol as an alkoxide intermediate [60, 72–74]. Two different oxidation pathways have been proposed: oxidation of the adsorbed alkoxide by direct electron transfer to the positive holes [60, 73] or oxidation of the adsorbed alkoxide mediated by OH• radicals formed by the reaction between holes

and superficial OH^- [75]. Subsequent coupling reactions may lead to the formation of partial oxidation products or to total combustion. Through current efficiency measurements, obtained from the photoelectrochemical oxidation at TiO_2/Ti anodes, it has been established that, in deaerated medium, two electrons are captured by the semiconductor from the alcohols under consideration. In contrast, in aerated conditions the number of TiO_2-captured electrons can be reduced to one because the alcoholic radical can be competitively captured by oxygen [63].

It has been demonstrated that oxidation mechanism, efficiency, and selectivity of the photocatalytic oxidation of alcohols by TiO_2 Degussa P25 strongly depend on the nature of the dispersing medium. Indeed, as evidenced by ESR-spin trapping investigation, addition of small amounts of water to CH_3CN strongly inhibits alcohol adsorption and its subsequent oxidation [60]. The reactivity of alcohols on the surface of photoexcited TiO_2 is also affected by the nature of their hydrophobic aliphatic chain [60]: geraniol and citronellol are more susceptible to the water content than their short analogues *trans*-2-penten-1-ol and 1-pentanol. Proper reaction conditions have been found for the photocatalytic oxidation of geraniol, citronellol, *trans*-2-penten-1-ol, and 1-pentanol to the corresponding aldehydes with good selectivity (>70%). These results are important in applied synthesis considering that citral, obtained through the partial oxidation of geraniol, is widely used in perfumes and flavorings.

In another study, it has been reported that the polar surface of TiO_2 favors the preferential adsorption of the primary OH group of diols such as 1,2 propanediol, 1,3 butanediol, and 1,4 pentanediol, thus favoring the subsequent oxidation of this alcoholic functionality [61]. In particular, it has been found that more than 75% of 4-hydroxypentanal from 1,4 pentanediol can be obtained with very low mineralization to CO_2 also under high conversion conditions. The regioselective oxidation of diols can also be achieved in water by photoexcitation of a composite system in which the natural enzyme glucose oxidase is adsorbed on the surface of TiO_2 Degussa P25 [62, 76]. Electrochemical measurements show that the enzyme is adsorbed on TiO_2 without changing the flat band potential [62]. The main role of glucose oxidase is to mediate the electron transfer process from photoexcited TiO_2 to O_2, leading to the formation of H_2O_2 [76]. ESR spin trapping investigations indicate that the enzyme favors the formation of $OH^{\bullet}$ radicals due to inhibition of electron-hole recombination and H_2O_2 reduction by conduction band electrons. The photooxidation of 1,2-propandiol with this photocatalytic system is regioselective, in that partial oxidation to hydroxyacetone is observed and no mineralization to CO_2 occurs [62].

Anatase, rutile, and brookite TiO_2 can be prepared with a simple sol–gel procedure that allows one to avoid any calcination treatment. These materials have been extensively studied in the partial oxidation of aromatic alcohols in aqueous medium [65–70]. Their electronic properties have been investigated by diffuse reflectance spectroscopy and quasi-Fermi level measurements [70]: the values of band gap, valence band, and conduction band edges are almost identical for all the samples in which anatase phase is predominant, whereas appreciable differences can be noticed in the presence of high amounts of rutile. ATR-FTIR

results indicate that these TiO_2-based materials show a very dissimilar hydrophilicity and different ability for adsorbing reaction intermediates in comparison to commercial TiO_2 Degussa P25 [70]. The anatase samples are significantly more selective than commercial TiO_2 in the oxidation of 4-methoxybenzyl alcohol to the corresponding aldehyde [68], which is a fragrance and an intermediate in many industrial processes. CO_2 is the other main oxidation product together with traces of 4-methoxybenzoic acid and open ring compounds. Subsequent investigations give evidence that the rutile samples are also able to photocatalyze the partial oxidation of benzylic alcohols [67, 69]. More specifically, with this material, the selectivity of the conversion of benzyl and 4-methoxybenzyl alcohols to the corresponding aldehydes maintains a value not less than 40% even when the conversion reaches 50%, with a carbon balance higher than 95% [69]. The physical chemical characterization of rutile samples points to a primary influence of crystallinity on selectivity. The photocatalytic properties of anatase, rutile, and brookite TiO_2 have been compared in the oxidation of 4-methoxybenzyl alcohol in water [59]. Rutile exhibits the highest yield to aldehyde at a rate of the same order of magnitude of that shown by the other materials. In another study, the photocatalytic oxidation of benzyl, 4-methylbenzyl, and 4-nitrobenzyl alcohols has been carried out in order to investigate the influence of $-OCH_3$ and $-NO_2$ substituents on oxidation rate and selectivity [65].

Visible light illumination of nitrogen-doped TiO_2 prepared by a sol–gel method brings about the selective oxidation of benzyl and cinnamyl alcohols to the corresponding aldehyde [59]. The reaction takes place in oxygenated dry nitrile solvents and is totally inhibited in the presence of water. The alcohols are shown to be weakly adsorbed and interaction of acetonitrile with the surface is demonstrated by its quenching of luminescence from band gap energy levels introduced by nitrogen. It is proposed that the formation of active oxygen species is a key channel leading to aldehyde formation.

2.2   Reductions

Photocatalysis by TiO_2 has attracted the attention of several researchers interested in developing new photocatalytic processes which can compete with conventional chemical reductions. The conduction-band-assisted reduction of nitro-aromatics to the corresponding aniline products by photoexcited TiO_2 is usually carried out in the presence of suitable electron donors such as alcohols [77–81]. The final product distribution is affected by several parameters: (1) the polarity of the reaction medium, which likely controls the stability of the charged intermediates [79], (2) adsorption phenomena involving reaction intermediates [80], and (3) steric effects and acid sites on the semiconductor [81]. The photocatalytic reduction of nitroaromatics by TiO_2 is usually carried out after removal of the competitive electron scavenger O_2. However, it has been recently reported that small amounts of O_2 can favor the conversion of nitrobenzene to aniline when TiO_2 is irradiated in aqueous solutions containing oxalic acid as hole scavenger [82]. More specifically,

30 min irradiation in the presence of 5% O_2 leads to the formation of aniline with 95% yield.

Loading with silver is a suitable means for enhancing the reactivity of TiO_2 towards nitroaromatics. A photocatalytic system formed of Ag clusters deposited on TiO_2 particles converts nitrobenzene to aniline with good selectivity in the presence of methanol [83]. The Ag clusters favor both the charge separation inside the semiconductor and the interaction of nitrobenzene with the photogenerated reducing centers. A turnover number of 1,230 molecules per second has been found, assuming that the reduction sites are the Ag atoms of the clusters. Nitro-aromatics can be chemoselectively reduced to the corresponding amines by using N-doped TiO_2 and KI as photocatalysts in the presence of methanol and upon solar-light photoexcitation [84]. This process is very efficient with short reaction time (<20 min) and excellent yields (>90%).

In recent years, much attention has been devoted to chemical reactions in microreactors characterized by short molecular diffusion distance, fast mixing, laminar flow, and large surface-to-volume ratio. Moreover, microreactors are expected to exhibit very important properties in photocatalysis: higher spatial illumination homogeneity and better light penetration through the entire reactor in comparison to large-scale systems [85]. The possible advantages of this kind of reactors in applied synthesis have been investigated. In particular, TiO_2 layers have been deposited on the bottom and side walls of microchannels of 500 μm width, 10–500 μm depth, and 50 mm length. It has been found that, in this microreactor, the photoreduction rate of *p*-nitroacetophenone to *p*-aminoacetophenone in the presence of ethanol increases with increasing the residence time up to 45% yield of amine with a residence time of 60 s [85].

2.3 Coupling Reactions

The charge separation occurring on the photoexcited surface of TiO_2 offers the possibility to induce redox-combined processes in which intermediates generated by one redox center become the substrates for another. In this context, the ability of TiO_2 to generate alkyl radicals as a consequence of organic substrate oxidation is of great interest for the formation of C–C bonds via conjugate alkylation [7]. Benzylation of conjugated acids, esters, and carbonyls has been carried out employing TiO_2 as photocatalyst [86–88]. Benzyl radicals are generated using precursors such as benzyl-trimethylsilanes or phenylacetic acids, since these species are characterized by the presence of a good "electrofugal group," which is easily able to leave the initially formed radical cation. Maleic and fumaric acids, as well as the corresponding anhy-dride and nitriles, are monobenzylated in 40–80% yield. Figure 3 reports the mecha-nism for the functionalization of tetracyanoethylene to the corresponding benzylethane upon TiO_2 photocatalysis in the presence of a benzyltrimethylsilane [86].

Photoexcited TiO_2 can work as a catalyst for radical addition of tertiary amines to electron deficient alkenes. In particular, *N*-methylpyrrolidine containing α,
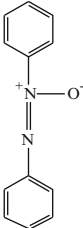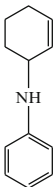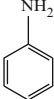
Fig. 3 Photocatalytic functionalization of tetracyanoethylene

Ar = 4-MeO-C_6H_4-
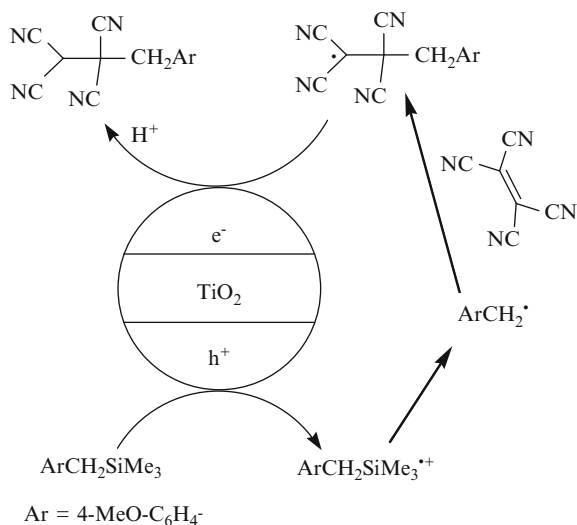
β-unsaturated lactones can be converted to the corresponding C–C coupling products with good yields [89, 90]. Photoexcitation of TiO_2 in aqueous solutions containing heterocyclic bases and an amide gives the corresponding amide-functionalized heterocycles [91]. It is proposed that photoexcitation yields an amide radical which attacks the heterocyclic base to yield the C–C coupling products. The presence of H_2SO_4 and H_2O_2 favors the radical formation. An analogous photocatalytic experiment carried out in the presence of ethers produced various heterocycle-ether conjugates [92]. C–N coupling reactions may occur between nitroaromatics and alcohols [93, 94]. 2-Methylimidazole is obtained from o-dinitrobenzene by photoexcitation of TiO_2 in deaerated solutions of ethanol [93]. Moreover, ethanol solutions containing m-nitrotoluene produce a tetrahydroquinoline derivative in high yield [94].

The reactive species generated by both the conduction band electrons and the valence-band positive holes may be precursors of stable final products [95, 96]. Photoexcited TiO_2 can be successfully employed to convert p-nitrotoluene to the corresponding carbamate with a selectivity higher than 80%, using ethanol as carbonylating species and without the employment of harmful reagents such as phosgene and CO. It is proposed that the process originates from cross reactions among transient species formed from both the conduction-band-assisted reduction of p-nitrotoluene and the simultaneous hole-assisted oxidation of ethanol [95]. The photochemical and photocatalytic reduction of nitrobenzene in the presence of cyclohexene has been investigated [96]. Table 2 shows the results obtained during irradiation of cyclohexene/nitrobenzene solutions with or without TiO_2. It is seen that the presence of the semiconductor yields mainly the azo-derivative. This product is likely formed via coupling reactions among reduction products of nitrobenzene and cyclohexenyl radicals, which have been evidenced by ESR spectroscopy.

**Table 2** Results of photocatalytic reaction of nitrobenzene in the presence of cyclohexene with or without TiO_2

Catalyst	Product distribution (%)			
	(azoxybenzene structure)	(azobenzene structure)	(N-cyclohexenylaniline structure)	(NH_2, aniline structure)
Without TiO_2	32	21	32	15
With TiO_2	11	47	23	19

The combination of TiO_2 and p-sulfonic acid as co-catalyst has been successfully applied for the reduction of nitrobenzene derivatives in O_2-free ethanol solutions to substituted quinolines and tetrahydroquinolines [97]. The ratio of the cyclization products depends on the position or the type of the substituents present on the nitrobenzene employed. A reaction mechanism is proposed comprising the photocatalytic formation of methylanilines and acetaldehyde and their subsequent reaction to quinolines and tetrahydroquinolines via a Schiff base as an intermediate.

A number of articles show that the photocatalytic activity of TiO_2 in C–C and C–N coupling processes can be improved using organized multicomponent systems. TiO_2-loaded Hβ zeolite ($SiO_2/Al_2O_3 = 20$) dispersed in oxygenated CH_3CN solutions is able to catalyze several kinds of C–N coupling reactions [98–100]. The proposed mechanism is summarized in Fig. 4 for the reaction between ethylenediamine and propylene glycol to give dihydropyrazine [98]. Propylene glycol is oxidized to the corresponding dicarbonylic derivative, which, in turn, couples with ethylenediamine to form dihydromethylpyrazine. This species supplies an electron to the photogenerated hole forming a radical cation stabilized by zeolite. Then, subsequent reaction with O_2^- leads to demethylation and yields dihydropyrazine. A similar photocatalyst, which is based on the use of a mixture of TiO_2 and K10 montmorillonite, converts 1,2-phenylenediamine and propylene glycol to 2-methylbenzimidazole and benzimidazole with good selectivity [101].

Irradiation of aqueous solution containing powdered mixtures of TiO_2 and Pt black induces the conversion of primary amines to secondary amines through C–N coupling [102]. Electron transfer from the amine to positive holes leads to a radical cation that is able to react with another amine molecule to form an imine whose subsequent hydrogenation on the photocatalyst leads to the formation of the final product. This process has been employed for the one-pot synthesis of L-pipecolinic acid from L-lysine [103, 104]. A TiO_2-based microreactor has been fabricated to implement the photocatalytic synthesis of L-pipecolinic acid from L-lysine [105]. The conversion rate in this microreactor is 70 times higher than that in a cuvette using nanometer-sized TiO_2 particles with almost the same selectivity and enantiomeric excess. It has also been found that irradiation of TiO_2/Pt mixtures dispersed

**Fig. 4** C–N coupling between ethylenediamine and propylene glycol by photoexcited TiO_2-loaded Hβ zeolite
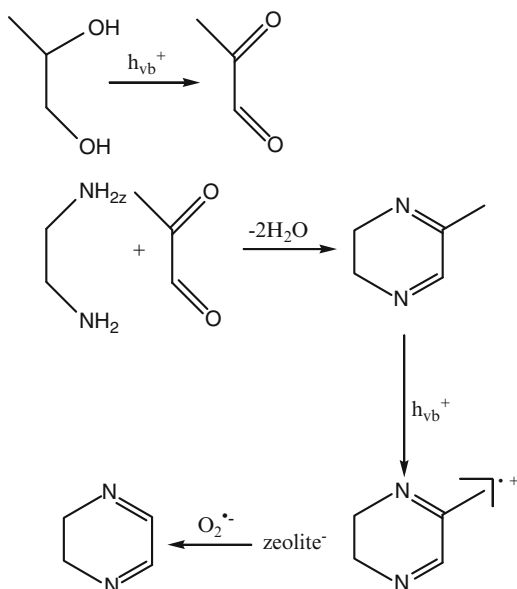
in alcohol solutions containing primary or secondary amines forms the corresponding secondary or tertiary amines [106, 107]. The formation of benzyl radicals is more efficient when TiO_2 is loaded with platinum or silver salts [87, 88, 108, 109] which enhance the photocatalytic efficiency, working as traps of electrons and inhibiting the charge recombination inside the semiconductor. In this way it has been possible to photocatalyze the synthesis of diarylethanes from alkylbenzenes, aryl-2-propanols, or benzyltrimethylsilanes [108, 109]. A new strategy based on the combination of photocatalytic and catalytic reactions has recently been developed for the one-pot synthesis of benzimidazoles [110]. This process employs nanoparticles of TiO_2 loaded with platinum, which are able to promote the conversion of alcohols to aldehydes through a Pt-assisted photocatalytic oxidation and the catalytic dehydrogenation of the benzimidazoline intermediates. The conduction band electrons are captured by H^+ to give H_2.

3 Highly Dispersed Oxides

3.1 Titanium

Highly dispersed oxides loaded on inorganic supports exhibit interesting photocatalytic activities for synthetic purposes. In particular, these "single-site" photocatalysts can often promote more selective transformations with respect to bulk semiconductor oxides [5]. Upon photoexcitation of isolated Ti-oxide species, a localized excited state is produced [Fig. 5 (**I**)]. Yoshida and co-workers report that silica containing isolated Ti-oxide species is able to perform the photocatalytic epoxidation of light
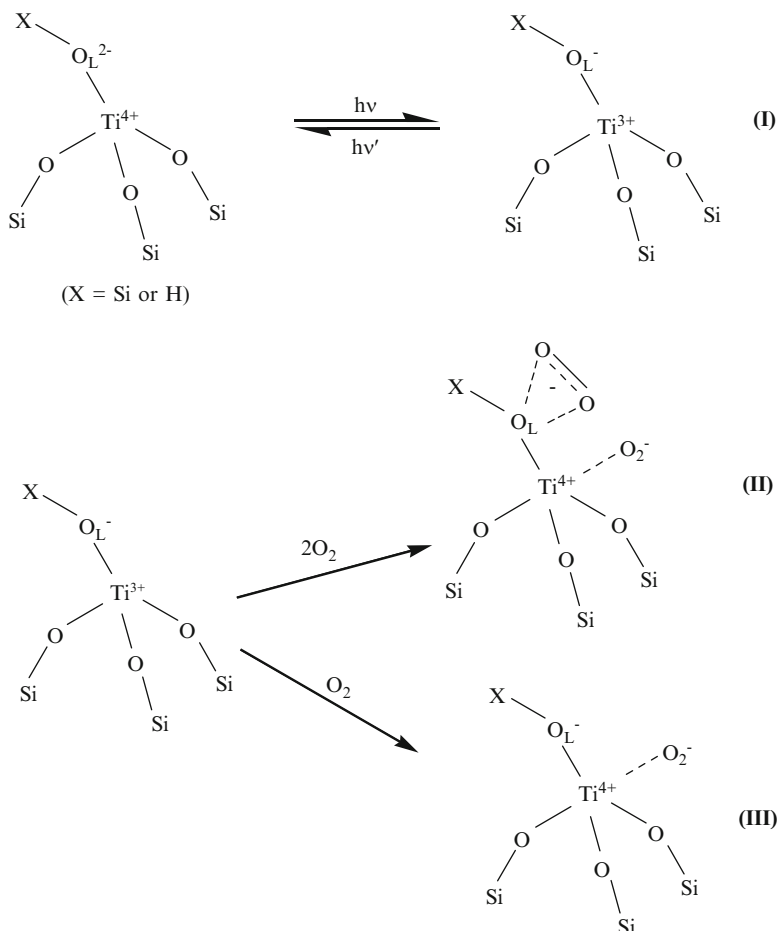
Fig. 5 Photoinduced redox processes on isolated Ti-oxide species and subsequent reaction with O_2

alkenes [111–113]. Irradiation of the catalyst T–S(0.34), with Ti/(Ti + Si) = 0.34 mol% in the presence of propene and O_2, leads to the corresponding epoxide with 57.5% selectivity, CO_2 6.6%, and other products such as acrolein and acetaldehyde. It should be noted that the use of bulk TiO_2 does not produce epoxide and the main product is CO_2 with 96.2% yield. Another catalyst containing isolated Ti-oxide species has been employed for gas phase photocatalytic epoxidation of styrene with O_2 [114]. The products obtained are styrene oxide (62%), benzaldehyde (23%), and CO_2 (15%), with 18% styrene conversion. In contrast, when TiO_2 Degussa P-25 is used, no styrene oxide is accumulated, benzaldehyde selectivity is only 2%, and the main product is carbon dioxide.

Extensive studies concerning the mechanism of the above photocatalytic processes have been reported [112, 113]. T–S(0.34) and T–S(0.1) show a narrow absorption band centered at 210 nm that is assigned to a ligand-to-metal charge

transfer of highly dispersed tetrahedral titanium species. So, when isolated $[Ti^{4+}–O_L^{2-}]$ absorbs UV light ($\lambda < 250$ nm), a charge transfer from O^{2-} to Ti^{4+} occurs and the excited state $[Ti^{3+}–O_L^-]^*$ is formed [Fig. 5 (**I**)]. Then both O_L^- and Ti^{3+} react with O_2 to produce O_3^- and O_2^- respectively [Fig. 5 (**II**) and (**III**)]. O_3^- has an electrophilic nature and is responsible for the attack on the electron rich C=C bond of alkenes to produce epoxides, while O_2^- attracts the electron on Ti^{3+}, so preventing the otherwise very fast charge recombination with the hole on the lattice oxygen and stabilizing O_3^-. Increasing the Ti content causes important variations in the UV spectra of the samples obtained: in addition to the absorption band below 250 nm, new bands above 250 nm are present, likely due to aggregated titanium dioxide species. As a consequence, (1) conversion of propene increases, (2) yield to propene oxide decreases, and (3) side reactions for production of other products and CO_2 are favored. Shiraishi and co-workers report that addition of CH_3CN to a Ti-containing mesoporous silica, forming a conventional liquid-solid system, markedly improves epoxide selectivity (>98%) upon irradiation [115, 116]. Authors conclude that acetonitrile, a weak base, stabilizes the alkene by solvation, inhibiting the proton transfer from olefin to O_L^- [Fig. 5 (**III**)] and preventing the formation of radical species that afford undesirable allylic oxidation products. Moreover, highly stereo-retentive (>99%) epoxidation is achieved in these conditions: reaction of *cis*- and *trans*-2-hexene affords the corresponding epoxides retaining the C=C moiety of the olefin in the resulting epoxide. In order to improve the conversion yields, Ti-containing mesoporous organosilicas, synthesized by a surfactant-templating method using an organosilane precursor, have also been prepared [116]. The hydrophobicity of these materials enhances the access of hydrophobic alkenes to the photoexcited Ti-oxide species, as expected, but a destabilization of the active oxidant $O_3^{-\bullet}$ for olefin epoxidation is observed. This destabilization counteracts the enhanced olefin access to the excited species, resulting in almost no improvement in olefin conversion.

An interesting example of "size screening" photocatalytic activity has been reported by Shiraishi et al. [117]. The photocatalysts consist of titanosilicate molecular sieve zeolites containing isolated Ti-oxide species, such as titanium silicalites TS-1 and TS-2. They promote the selective conversion of "appropriate" size molecules, i.e., with a size close to the pore of the catalyst. A slim molecule diffuses smoothly inside the pore and is scarcely trapped by $[Ti^{3+}–O_L^-]^*$. A fat molecule cannot enter the pore, thus showing zero conversion. In contrast, diffusion of a molecule with size close to the pore is restricted by the pore wall, trapped by $[Ti^{3+}–O_L^-]^*$ and converted. Authors highlight a successful application of this activity to a selective transformation of molecules that is associated with a size reduction, the so-labeled "molecular shave" transformation. Photoirradiation of TS-1 or TS-2 in chlorohydroquinone containing water gives rise to the corresponding 1,2,4-trihydroxybenzene derivative with high selectivity at about 70% substrate conversion (Table 3). This reaction is particularly interesting since the product is non-toxic and valuable. The size of chlorohydroquinone is similar to the catalyst pore, thus allowing effective conversion. In contrast, the size of 1,2,4-trihydroxybenzene is smaller than the pore, leading to smooth diffusion inside the

Table 3 Photocatalytic properties of TS-1, TS-2 and of bulk TiO_2 in the transformation of chlorohydroquinone to 1,2,4-trihydroxybenzene

System	Substrate conversion (%)	Product selectivity (%)
TS-1	67	85
TS-2	74	99
TiO_2	99	1

pores and avoiding subsequent reactions of this molecule. When bulk TiO_2 is used, 1,2,4-trihydroxybenzene is initially formed but it is subsequently completely decomposed (Table 3).

A microporous titanosilicate ETS-10 has recently been used for selective organic transformations [118]. This photocatalyst has Ti–OH groups at the defect sites exposed on the external surface, whereas these groups are scarcely present on the channel walls. When the material is illuminated, $OH^\bullet$ radicals, formed at the titanol groups on the external surface, behave as active species. As a consequence, small substrates that can diffuse inside the pore system are protected from the photocatalytic reaction and, in contrast, large substrates that cannot enter the pores react efficiently at the defect site on the external surface. Moreover, since the inner pore environment is highly polarized, the material is able to discriminate among small molecules on the basis of their polarity. This peculiar ability of ETS-10 to control photocatalytic activity by size and polarity of substrates is employed for the hydroxylation of benzene to phenol. The reactant is a non-polar molecule that can react efficiently with $OH^\bullet$ radicals on the external surface to give phenol, which is, in contrast, a polar product. This can enter into the pores of ETS-10 where it is protected from reaction with $OH^\bullet$. The sequential oxidation of phenol is therefore suppressed and it can be accumulated with a high selectivity (65%) when the benzene conversion is 40%.

Design of visible light-responsive Ti/SiO_2 has been accomplished by applying an advanced metal ion implantation method [119–122]. Introduction of Cu(I) or Sn(II) centers in Ti-MCM-41 leads to metal to metal charge transfer moieties (Ti^{IV}–O–Cu^{I} and Ti^{IV}–O–Sn^{II}) that absorb in the visible region (around 620 nm) [119]. Irradiation at these wavelengths allows the formation of Ti(III), showing that the assembly of MMCT sites inside mesoporous silicas, with each metal in a preselected oxidation state, opens the possibility of initiating photocatalytic processes by visible light. More recently, Ti^{IV}–O–Ce^{III} bimetallic assembly on mesoporous silica is employed for the photooxidation of 2-propanol to acetone by O_2 under $\lambda = 460$ nm [121] and V-containing Ti-MCM-41 shows an enhanced photoactivity in the conversion of propane to acetone with respect to Ti-MCM-41 [120].

3.2 Chromium

Different types of Cr–Si binary oxides are able to induce the partial photooxidation of cyclohexane and of aliphatic and aromatic olefins by O_2 under visible light

($\lambda > 400$ nm) [123–126]. Highly dispersed Cr-oxide species show three absorption bands centered at 245, 330, and 460 nm, which are assigned to the LMCT (from O^{2-} to Cr^{6+}) transitions of chromate species. A series of photocatalysts, with the same Cr content, but prepared by different procedures, has been studied: (1) sol–gel method (Cr–SiO_2), (2) impregnation method on amorphous silica (Cr/SiO_2), and (3) templating method (Cr/MCM-41). All the catalysts are active in the partial photo-oxidation of the investigated hydrocarbons by visible light, and, in contrast to TiO_2, they do not produce significant amounts of CO_2. Among them, Cr–SiO_2 shows the highest activity. ESR analysis reveals that photoirradiation of the chromate species with tetrahedral coordination on Cr/SiO_2 and Cr/MCM-41 leads to the formation of an excited state (Cr^{5+*}) that is different from that produced in the case of Cr–SiO_2 (Cr^{4+*}). The oxygen (O^-) adjacent to the highly reduced Cr^{4+} has greater electro-philicity than the O^- close to Cr^{5+}. This fact produces an enhanced interaction with the hydrocarbon, resulting in higher oxidation activity. The rate of cyclohexane oxidation by Cr/MCM-41 photocatalyst is improved by introducing, during the synthesis of the material, 10% of 1,2-bis(triethoxysilyl)ethane (BTESE), whose role is that of making the surface of the mesoporous silica more hydrophobic thanks to the presence of organic fragments [124]. Access of cyclohexane to the photo-active chromate species is favored, leading to improved yields. The selectivity to cyclohexanol and cyclohexanone with respect to CO_2 is maintained around 90%.

3.3 Vanadium

Vanadium-containing mesoporous silica with highly dispersed and tetrahedrally coordinated V-oxide species (V^VO_4) has been prepared by a modified surfactant templating method [127]. This catalyst shows high photocatalytic activity ($\lambda > 300$ nm) even in water, while other V-containing silica catalysts, prepared by impregnation or conventional templating methods, have no activity in the presence of water due to hydrolysis of the V^VO_4 species. Retention of activity in water is due to the fact that V^VO_4 species are confined within the silica layer and not exposed on the surface. Despite its confined structure, this photocatalyst is able to oxidize cyclohexane mainly to its alcohol and ketone with only traces of CO_2.

Rubidium-ion-modified V_2O_5/SiO_2 is a good catalyst for the selective photooxi-dation of propane to acetone [128]. The presence of the alkali ion leads to an improvement of the photocatalytic activity. The rate determining step is the reaction of propane on the lattice oxygen of the photoexcited VO_4Rb species to yield the vanadium isopropoxide species. Vanadium supported on mesoporous silica SBA-15 is used for the selective oxidation of methane to formaldehyde under UV irradiation [129]. Selectivity in formaldehyde is very high (about 90%) whereas methanol is formed in very small amounts. Moreover, a strong dependence of the selectivity to formaldehyde on the vanadium content is clearly observed. Selectivity is high (>90%) when V loading is below 2.65 wt% and decreases for higher vanadium loadings in favor of carbon oxides formed by overoxidation of the

aldehyde. Photoexcited V-MCM-41 is able to catalyze the selective photooxidation of methane by nitric oxide ($\lambda < 300$ nm) [130]. Methanol (80% selectivity) and N_2 are the main products, while small amounts of CO_2, CO, C_2H_4, and N_2O are observed. Interestingly, when O_2 is employed in place of NO, the complete oxidation of methane to CO_2 and H_2O is obtained. Charge transfer excited triplet state of the tetrahedrally coordinated V-oxide species is the active site.

4 Polyoxotungstates

Polyoxotungstates, tungsten–oxygen anionic clusters, can be considered soluble models of semiconductor metal oxide surfaces. These oxides have been intensively studied over the past 20 years because they exhibit interesting properties as catalysts and photocatalysts [6, 8, 131–133]. In particular, the ability to undergo photoinduced multielectron transfers, without any change in structure, makes polyoxotungstates a very attractive class of photocatalysts. Among them, the polyoxotungstate $W_{10}O_{32}^{4-}$ presents an absorption spectrum that partially overlaps the UV solar emission spectrum, opening the possibility to carry out benign solar-photoassisted applications [134, 135]. The cascade of events that follow light absorption by $W_{10}O_{32}^{4-}$ has been deeply investigated and is described in the following (Fig. 6) [136–139]. Excitation of $W_{10}O_{32}^{4-}$ ($\lambda = 323$ nm) leads to an oxygen to metal $[O^{2-} - W^{6+}]$ charge transfer excited state $[W_{10}O_{32}^{4-*}$, Fig. 6 (a)], in analogy to the photoinduced charge separation processes that occur in TiO_2 and highly dispersed oxides [8, 140, 141]. Then $W_{10}O_{32}^{4-*}$ decays in less than 30 ps to a very reactive non-emissive transient, indicated as wO [Fig. 6 (b)]. This species has an oxyradical-like character due to the presence of an electron deficient oxygen center and has a lifetime of 65 ± 5 ns and a quantum yield of formation of 0.57. wO
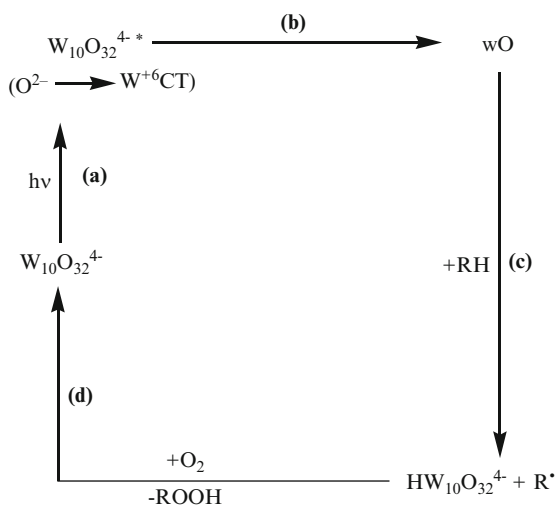
Fig. 6 Reaction mechanism of photoexcited $W_{10}O_{32}^{4-}$

possesses a very high reactivity towards any organic substrate RH: quenching of wO may occur either by hydrogen-atom abstraction or electron transfer mechanism, depending on the chemical nature of RH. In any case, both mechanisms lead to the one electron reduced form of decatungstate ($HW_{10}O_{32}^{4-}$) and to the substrate derived radical ($R^{\bullet}$) [Fig. 6 (**c**)]. At this stage, O_2 can regenerate the starting $W_{10}O_{32}^{4-}$ with parallel formation of peroxy compounds [Fig. 6 (**d**)].

4.1 Heterogenization by Impregnation

The first attempts to prepare heterogeneous photocatalysts through impregnation of polyoxotungstates (POT), such as (n-Bu$_4$N)$_4$W$_{10}$O$_{32}$ and $H_3PW_{12}O_{40}$, on amorphous silica go back to about 10 years ago [142–146]. The main features of these photoactive materials are that they are easily handled and recyclable and that they can be employed in reaction media where the polyoxotungstates are insoluble. It has been reported that photoexcitation of heterogenized (n-Bu$_4$N)$_4$W$_{10}$O$_{32}$ and $H_3PW_{12}O_{40}$ dispersed in neat cyclohexane leads to the formation of cyclohexanol and cyclohexanone [142]. The heterogeneous photocatalysts can be recycled without leaching and any loss in photoactivity. Moreover, in contrast to what was obtained with photoexcited TiO_2, they do not cause any mineralization of cyclohexane to CO_2, indicating that they are very promising photocatalysts for applied synthetic purposes. Further research developments have been devoted to improve the selective conversion yield of cyclohexane to cyclohexanone. It has been found that, depending on the nature of the cation, the heterogenous photocatalysts show different and tunable photoreactivities (Table 4) [143]: n-Bu$_4$N$^+$ cations enhance the efficiency of cyclohexane photooxidation, likely because they create a hydrophobic environment around the photoactive species, favoring the approach and the subsequent oxidation of the cycloalkane. NH_4^+ and Na^+ cations improve the chemoselectivity, since the concentration ratios cyclohexanone/cyclohexanol are 1.8 and 2.3 respectively. Likely, cyclohexanol, remaining close to the polar surface of these materials, is easily oxidized to cyclohexanone. In 2002 we reported on the immobilization of (n-Bu$_4$N)$_4$W$_{10}$O$_{32}$ on the mesoporous silica MCM-41, (mesopores ranging from 20 to 100 Å and surface area of ~1,000 m^2/g) [144]. Thanks to the large surface area of MCM-41, decatungstate is well dispersed, providing a great number of photocatalytic sites that lead to an

Table 4 Surface areas, polarity measurements[a] and photocatalytic properties of (n-Bu$_4$N)$_4$ W$_{10}$O$_{32}$/SiO$_2$, (NH$_4$)$_4$W$_{10}$O$_{32}$ and of Na$_4$W$_{10}$O$_{32}$

Material	Surface area (m^2/g)	E_T^{Na}	Cyclohexanol + cyclohexanone (M)	Cyclohexanone/ cyclohexanol
SiO$_2$	95 ± 2	0.93	–	–
Na$_4$W$_{10}$O$_{32}$/SiO$_2$	83 ± 2	0.83	0.3×10^{-3}	2.3
(NH$_4$)$_4$W$_{10}$O$_{32}$/SiO$_2$	83 ± 2	0.80	0.6×10^{-3}	1.8
(n-Bu$_4$N)$_4$W$_{10}$O$_{32}$/SiO$_2$	54 ± 2	0.51	1.7×10^{-3}	1.0

[a]Polarity measurements are carried out following a reported procedure using Reichardt's dye. E_T^N values ranges from 0 to 1 with surface polarity increase

enhancement of photochemical efficiency. Concerning the chemoselectivity in the photocatalytic oxidation of cyclohexane, the maximum value of ketone/alcohol ratio is 2.6. Authors report that the polar surface of MCM-41 favors the accumulation of cyclohexanol formed at the interfaces and, consequently, its subsequent oxidation to ketone by the photoexcited decatungstate.

The photocatalytic properties of $(n\text{-}Bu_4N)_4W_{10}O_{32}$ impregnated on amorphous silica have also been investigated in the oxidation of cycloalkenes, (cyclohexene and cyclooctene). This study has been carried out in the presence of Fe^{III}[*meso*-tetrakis(2,6-dichlorophenyl)porphyrin] chloride (Fe(TDCPP)Cl) as a co-catalyst [145]. Cycloalkenes are mainly oxidized to the corresponding hydroperoxides by the photoexcited decatungstate according to Fig. 6. The iron porphyrin reacts with the allylic hydroperoxides to give the corresponding alcohols as main products.

Photooxidation of benzyl alcohols by $W_{10}O_{32}{}^{4-}$ impregnated on silica and on γ-alumina has been studied by Orfanopoulos and co-workers [147]. These photocatalysts have been investigated in the oxidation of a series of *p*-alkyl-substituted benzyl alcohols, **1–7** (Fig. 7). These substrates bear two distinguishable benzylic hydrogen atoms, one on the alcohol carbon and one on the *p*-alkyl substituent, both of which can potentially be cleaved under photooxidation conditions to give aryl ketones **1a–7a** or dioxygenated products **1b–7b** respectively. A strong preference for the hydrogen atom abstraction from the alcohol carbon is observed: selectivity for **1a–7a** compounds is, in most cases, higher than 80%. This can be ascribed to the surface polarity of the supports that probably favors accumulation of the polar alcohol moiety. Shen and co-workers report that $H_3PW_{12}O_{40}$ impregnated on MCM-41 is able to photooxidize several alcohols to the corresponding carbonylic derivatives in the presence of O_2 [148]. In particular, an enhancement in activity is
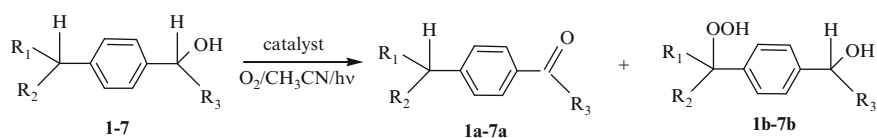
R_1	R_2	R_3	
H	H	CH_3	**1**
CH_3	H	CH_3	**2**
CH_3	CH_3	CH_3	**3**
Ph	H	CH_3	**4**
Ph	Ph	CH_3	**5**
CH_3	H	Ph	**6**
CH_3	CH_3	Ph	**7**

Fig. 7 Photocatalytic oxidation of *p*-substituted secondary benzyl alcohols by decatungstate supported on silica and γ-alumina

observed if an ionic liquid is used as dispersing medium instead of CH_3CN. Although this work has some interest from the synthetic point of view, a deeper investigation is needed in order to establish which is the photoactive species and the role of the ionic liquid in the reaction mechanism. Zeolite Y (in the Na^+ form) has been used as a solid support for $H_2NaPW_{12}O_{40}$, $H_4SiW_{12}O_{40}$, and $H_3PMo_{12}O_{40}$ [149]. The photocatalytic activities of these systems have been investigated choosing 1,2-dichlorobenzene as oxidizable probe. The constrained environment is responsible for a rate enhancement of the reaction, since it increases the encounter probability between photoexcited polyoxometalate and 1,2-dichlorobenzene, suppressing back electron transfer reaction.

4.2 Heterogenization by Sol Gel Procedure

Some years ago Hu et al. set a new heterogenization procedure, where a POT, such as $H_3PW_{12}O_{40}$, $H_4SiW_{12}O_{40}$, $(n\text{-}Bu_4N)_4W_{10}O_{32}$, or $Na_4W_{10}O_{32}$, is encapsulated inside a silica network via a sol gel technique [150, 151]: CH_3CN/H_2O solution of the chosen POT, adjusted to pH 2, is added dropwise to a solution of tetraethylortho silane (TEOS) and 1-butanol. After some hours of stirring and gentle warming, the hydrogel is dried and calcined to fasten the formation of the silica network. Structural integrity of $W_{10}O_{32}^{4-}$ is preserved and protonated silanol groups act as counter-ions for the polyoxoanion. Following this procedure, Farhadi and Afshari have entrapped $(n\text{-}Bu_4N)_4W_{10}O_{32}$ and $H_3PW_{12}O_{40}$ in a silica matrix and have used these photocatalysts in the oxidation of benzylic alcohols in the presence of O_2 [152, 153]. They performed a screening study choosing a variety of ring-substituted primary and secondary benzylic alcohols. These substrates are efficiently oxidized to the corresponding carbonylic compounds, without overoxidation of benzaldehydes to carboxylic acids. This result is in contrast to what was reported by Orfanopoulos with decatungstate immobilized on silica by impregnation [147], thus indicating that different preparation methods lead to a completely dissimilar morphology of the photocatalyst and, consequently, to a different photoreactivity.

In 2010 we reported about the photochemical characterization of two heterogeneous photocatalysts prepared by entrapment of $(n\text{-}Bu_4N)_4W_{10}O_{32}$ in a silica matrix through sol gel procedure: $SiO_2/W30\%$, with 30 wt% of decatungstate, and $SiO_2/W10\%$, obtained after the removal of the decatungstate not firmly incorporated inside the silica network and weakly adsorbed on the external surface [154]. These two heterogeneous photocatalysts are characterized by the presence of both micropores (7 and 15 Å) and mesopores (25 Å), but, due to different preparation procedures, $SiO_2/W10\%$ presents a more remarkable porous network than $SiO_2/W30\%$. Moreover, morphological features of $SiO_2/W30\%$ and $SiO_2/W10\%$ differ from those of their parent material $SiO_2/W0\%$, indicating that incorporation of decatungstate induces a significant modification of the porous texture of the siliceous material. Both photocatalysts are robust and able to induce the O_2-assisted

oxidation of 1-pentanol and 3-pentanol to pentanal and 3-pentanone, respectively. A very strong effect of the solid support on the relative reactivity of the two alcoholic substrates is observed. In fact, oxidation of 1-pentanol with SiO_2/W10% is about four times faster than in homogeneous solution. Preferential adsorption effects are of great importance in controlling the nature of the products and conversion yields of the photocatalytic process. It has also been observed that other textural parameters, related to the microporous structure of the heterogeneous photocatalysts, differentiate the relative reactivity of the two alcohols investigated, favoring the approach to the surface of the less hindered primary OH group of 1-pentanol. These findings are of particular importance since the selective oxidation of aliphatic primary alcohols at the aldehyde stage without further oxidation still remains a challenging transformation.

Zirconia-supported $Na_4W_{10}O_{32}$ and $H_3PW_{12}O_{40}$ have been prepared via sol–gel procedure by the Farhadi's group [155, 156]. $Na_4W_{10}O_{32}$/ZrO_2 is more active than the homogeneous $Na_4W_{10}O_{32}$ in the photooxidation of primary and secondary benzylic alcohols. This fact is tentatively attributed to a synergistic effect between the polyoxoanion and the support that is a semiconductor. Interestingly, in the $H_3PW_{12}O_{40}$/ZrO_2 system, the absorption band typical of $H_3PW_{12}O_{40}$ at 270 nm is not present and a new broad band, shifted to the visible region, is observable. Authors attribute the photocatalytic activity of the nanocomposite system to the existence of this broad band. $Na_4W_{10}O_{32}$/ZrO_2 has also been employed for the reductive cleavage of a series of substituted azobenzenes into their corresponding amines using 2-propanol as hydrogen source under a nitrogen atmosphere [157]. Amines are obtained in high to excellent yields (76–94%) and with short reaction times. Efficiency of the photocatalytic process is influenced by steric factors: substituents in *ortho-* or *meta-* positions to the N=N functional group decrease the reaction rate. Interestingly, no other reducible substituents, such as –NO_2, are affected by the photocatalyst.

Colloidal $Cs_3PW_{12}O_{40}$, synthesized by metathesis of $H_3PW_{12}O_{40}$ and CsCl in water, has been supported on silica via sol gel procedure using tetraethoxy orthosilane (TEOS) [158]. The material obtained is extremely porous (pore size centered at 23 Å) and with a very large surface area. It is effective in the photooxidation of aqueous solutions of 2-propanol to acetone and it does not undergo any leaching of polyoxometalate. A deep investigation of the factors influencing the efficiency of this heterogeneous photocatalyst, such as events that follow the absorption of light and substrate adsorption, has been published by the same authors in 2000 [159].

4.3 Heterogenization by Ionic Exchange

As an alternative to the conventional impregnation or sol–gel entrapment procedures, it has been reported that $W_{10}O_{32}^{4-}$ can be supported on a silica matrix previously functionalized with different ammonium cations, covalently bound on the solid

Fig. 8 Structures of the photocatalysts obtained upon heterogenization of $W_{10}O_{32}^{4-}$ on silica previously functionalized with different ammonium cations
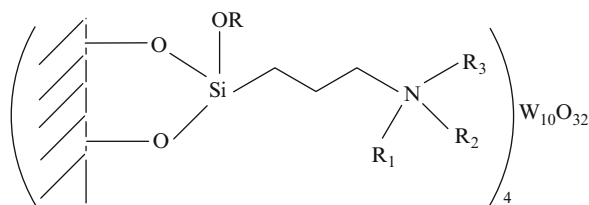
R_1, R_2, R_3 = H, H, H   Si-alkylNH$_3$W
R_1, R_2, R_3 = Et, Et, H   Si-(alkyl)$_3$NHW
R_1, R_2, R_3 = Et, Et, Et   Si-(alkyl)$_4$NW

support [160]. The polyoxoanion is firmly held on the support by ionic bond with tetraalkylammonium cations in Si-(alkyl)$_4$NW, with trialkylammonium cations in Si-(alkyl)$_3$NHW and with monoalkylammonium cations in Si-alkylNH$_3$W (Fig. 8). These materials have been employed as photocatalysts for the O_2-assisted oxidation of 1,3-butanediol and 1,4-pentanediol. For both the investigated diols, the only products obtained are the hydroxy-aldehyde and the hydroxy-ketone. The ratio between aldehyde and ketone depends on the nature of the alkyl-ammonium cations; in particular, it increases markedly (from 0.06 to 0.63 for 1,3-butanediol and from 3.0 to 7.5 for 1,4-pentanediol) as the alkyl chains are substituted by hydrogen atoms. This substitution enhances the polarity of the environment surrounding $W_{10}O_{32}^{4-}$, favoring the preferential adsorption of primary OH group of the more hydrophilic head of diol molecule with respect to the secondary OH group placed in the more hydrophobic tail. Concerning the stability, these photocatalysts are robust and reusable at least five times without leaching of polyoxotungstate anion. The decatungstate $W_{10}O_{32}^{4-}$ has been immobilized on a hydrophobically organomodified mesoporous silica SBA-15 by the Cao's group [161]. Introduction of a hydrophobic organic fragment onto the silica surface, which is intrinsically hydrophilic, produces a photocatalyst where the active sites are more easily accessible to hydrocarbon molecules. The organo-modified SBA-15 is prepared by initial insertion of alkyl groups of chosen length using C_n-Si(OEt)$_3$ (n = 2, 4, 8, 16), followed by grafting of 3-aminopropyl groups. The resultant material is acidified and then ion exchange by decatungstate is carried out. 3-Ammoniumpropyl groups ($-(CH_2)_3NH_3^+$) immobilize $W_{10}O_{32}^{4-}$ on the pore walls, while the alkyl chains form hydrophobic regions around decatungstate. These novel photocatalysts have been investigated in the oxidation of some aryl alkanes to the corresponding phenones by O_2. Length of alkyl chains affects the photocatalytic efficiency, with the octyl-grafted (n = 8) showing the best performance. Interestingly, this photocatalyst is also able to convert cyclohexane to cyclohexanone with very high yield, complete selectivity, and high stability.

A simple ion-exchange procedure allowed Fornal and Giannotti to immobilize $W_{10}O_{32}^{4-}$ on poly(4-vinylpyridine), cross-linked methyl chloride quaternary salt [162]. The ionic interaction is strong enough to prevent the release of the polyoxoanion into the solution. This material has been investigated in the photooxidation of

Table 5 Photocatalytic properties of Amb/$W_{10}O_{32}^{4-}$ and of $W_{10}O_{32}^{4-}$ in the bromide-assisted functionalization of alkenes

Alkene	System	Alkene products distribution (%)		
		EP + BrOH[a]	BrBr[a]	OMP[a]
Cyclohexene	Amb/$W_{10}O_{32}^{4-}$	36	42	22
	$W_{10}O_{32}^{4-}$	24	7	69
1-Methyl-1-cyclohexene	Amb/$W_{10}O_{32}^{4-}$	69	5	26
	$W_{10}O_{32}^{4-}$	38	4	58
Styrene	Amb/$W_{10}O_{32}^{4-}$	44	2	50
	$W_{10}O_{32}^{4-}$	22	0	70

[a]*EP* epoxide, *BrOH* bromohydrin, *BrBr* dibromoalkane, *OMP* other monooxygenated products, such as allylic alcohols and ketones

cyclohexane in the presence of O_2. Cyclohexyl hydroperoxide is the main product but cyclohexanol and cyclohexanone are also formed. The selectivity depends on the decatungstate loading: cyclohexanone production is promoted by lower loadings, whereas cyclohexyl hydroperoxide formation is favored by higher loadings. Amberlite IRA-900 in the chloride form has been employed as support for $(n\text{-}Bu_4N)_4W_{10}O_{32}$ by our research group [163]. The ion exchange of Cl^- with $W_{10}O_{32}^{4-}$ is favored by the soft character of $-N(CH_3)_3^+$ cations. This photocatalytic system promotes the conversion of olefins to the corresponding bromohydrins and dibromoalkanes in the presence of NaBr. By simply adjusting the pH value, bromohydrins can be quantitatively transformed into epoxides, which are important intermediates in organic synthesis. Photoexcited $(n\text{-}Bu_4N)_4W_{10}O_{32}$ causes the reductive activation of O_2 to alkyl hydroperoxides (Fig. 6). These, in turn, reacting with bromide ions, give a brominating species that attacks the C=C double bond of olefins. A nucleophile such as H_2O or Br^- leads to bromohydrin and dibromoderivative respectively. Under analogous experimental conditions, phenol and anisole are converted to their monobrominated derivatives, a transformation of particular interest if one considers the otherwise difficult monobromination of activated arenes. As shown in Table 5, the polymeric matrix increases the yields to epoxides and bromohydrins and inhibits undesirable autooxidation processes leading to monooxygenated products. It is evident that the crucial role of the resin is fostering the enrichment of Br^- ions close to the surface, promoting their reaction with photogenerated alkyl hydroperoxides before their diffusion in the solution bulk.

4.4 Heterogenization with Membranes

Among the different techniques for the immobilization of decatungstate, the occlusion in polymeric membranes offers new developments in aqueous photocatalysis. In fact, in water, the choice of an appropriate hydrophobic support may be the key to discriminate among reactants. In this context, Bonchio and co-workers have embedded $W_{10}O_{32}^{4-}$ in several polymeric membranes, using a phase inversion technique or a hydrosilylation reaction [164, 165]. Polyvinylidene fluoride (PVDF)

and polydimethylsiloxane (PDMS) are the most resistant membranes in terms of self-induced degradation upon irradiation in water. These systems have been studied in the photooxidation of several water soluble alcohols (*n*-pentanol, cyclo-hexanol, cyclopentanol). Carbonyl products accumulate in solution up to a substrate conversion in the range 10–30% and then they undergo consecutive oxidation. In comparison with homogeneous $Na_4W_{10}O_{32}$, the heterogeneous photooxidation is slower but proceeds to completion in a few hours. Interestingly, heterogeneous matrix exerts a specific substrate recognition, a key factor to achieve selective processes: the preferential interaction with the polymeric membrane promotes the oxidation, favoring adsorption equilibrium and leading to a substrate enrich-ment on the surface close to the photoactive sites. Concerning the stability, the PDMS-$W_{10}O_{32}{}^{4-}$ photocatalyst is the most stable and effective in multiple runs, probably thanks to an optimal surface dispersion of decatungstate and to a better substrate supply. The same group of researchers has prepared a new hybrid photo-catalyst by embedding the fluorous-tagged decatungstate $(R_fN)_4W_{10}O_{32}$ $(R_fN=$ $[CF_3(CF_2)_7(CH_2)_3]_3CH_3N^+)$ within fluoropolymeric films, like Hyflon® [165, 166]. The perfluoropolymer has thermal and oxidative resistance and high perme-ability of O_2. The resulting hybrid materials exhibit remarkable activity in the solvent-free oxygenation of benzylic hydrocarbons. As an example, with tetraline and indane high turnover numbers (>6,000) are obtained.

A very new generation of catalytically active membranes has been developed by using a low-temperature-plasma surface modification technique, which allows one to modify or functionalize by grafting, in a controlled way, only the topmost few layers of membranes while retaining their mechanical, physical, and bulk proper-ties. Poly(vinylidene fluoride) (PVDF) membrane is modified by plasma treatment to graft amino groups at its surface, which, in turn, are used as anchor groups for the immobilization of decatungstate and of phosphotungstic acid ($H_3PW_{12}O_{40}$) in a highly precise way [167, 168]. These novel heterogeneous systems, used for the complete aerobic degradation of phenol, exhibit improved photocatalytic perfor-mances with respect to the corresponding homogeneous systems. Although no applications for synthetic purposes are present in the literature to date, we consider these results as a first successful example of plasma treatments applied for the heterogenization of polyoxotungstates on polymeric membranes.

4.5 Heterogenization with Photoactive Semiconductors

Addition of $PW_{12}O_{40}{}^{3-}$ to a TiO_2 suspension greatly enhances the hydroxylation reaction of benzene to phenol [169]. This effect is attributed to the dual role of the polyoxometalate, which can act as a photocatalyst itself and as an electron shuttle, scavenging electrons of the conduction band of photoexcited TiO_2 and inhibiting the charges recombination reaction. $H_3PW_{12}O_{40}$ has been incorporated into a titanium exchanged zeolite and into TiO_2 colloids [170, 171]. These two systems have been studied in the photoreduction of methyl orange. Photoreduction of

$PW_{12}O_{40}{}^{3-}$ is synergistically enhanced by the coupling with TiO_2, which transfers electrons directly to the polyoxoanion. This, in turn, as a heteropoly blue, absorbs visible light and is able to catalyze the reduction of methyl orange.

5   Conclusions

In this chapter we have provided evidence that heterogeneous photocatalysis is emerging as an innovative and green method for achieving chemical transformations of interest in synthesis. An important advantage in the use of solid photocatalysts is that they can be easily removed from the reaction vessel by simple filtration and, in a large number of cases, they can be reused without significant loss of activity. However, our main objective in this contribution has been to demonstrate that the use of heterogeneous systems with well-defined textural characteristics and adsorption properties represents a suitable means to tailor the selectivity of photocatalytic processes. Examples are reported of organized assemblies on matrix surfaces, of adsorption-controlled reactions, of grafting on modified surfaces, and of nanostructured photoactive materials with well defined sizes and shapes. We have illustrated both the basic principles that govern the primary photochemical steps of these systems and the textural effects on the overall photocatalytic process.

In this framework photoactive metal oxides are of great interest. The necessity to optimize the performance of TiO_2 has stimulated researchers on its modification. In particular, control of its crystallographic and morphological characteristics, use of constrained systems, surface modification, and loading with inorganic elements are successful strategies to obtain TiO_2-based photocatalysts with predictable properties. The photochemical reactivity of metal oxides is influenced by their degree of dispersion on inorganic supports. Highly isolated metal oxides loaded on silica, mixed oxides, and zeolites induce the occurrence of organic transformations that are not observed with the bulk metal oxides. Photocatalytic efficiencies that are comparable to that of TiO_2 and good selectivity are achieved with polyoxotungstates heterogenized with polymeric membranes or micro- and mesoporous inorganic materials. These systems do not cause mineralization of the substrate to carbon dioxide.

The organic substrates considered here are important starting materials for producing a variety of chemicals. In particular, the selective oxidation of alcohols and the monooxygenation of C–H bonds with molecular oxygen at room temperature and atmospheric pressure represent attractive synthetic routes. The possibility to photocatalyze the formation of C–C and C–N bonds in mild conditions is another important contribution of photocatalysis in organic synthesis. As a concluding remark, we believe that further efforts in both fundamental photochemical studies and new synthetic methodology is needed to optimize the photocatalytic properties of metal oxides in order to achieve levels of efficiency and selectivity suitable for high scale applications.

References

1. Fox MA (2001) Synthetic applications of photocatalytic oxidation and reduction reactions of organic reactants on irradiated semiconductors surfaces. In: Balzani V (ed) Electron transfer in chemistry, vol I. Wiley-VCH, Weinheim, p 271
2. Li Y, Wang L (1997) Stud Surf Sci Catal 103:391
3. Ohtani B (1994) Trends Photochem Photobiol 3:531
4. Fujishima A, Rao TN, Tryk DA (2000) J Photochem Photobiol C Photochem Rev 1:1
5. Shiraishi Y, Hirai T (2008) J Photochem Photobiol C Photochem Rev 9:157
6. Palmisano G, Augugliaro V, Pagliaro M, Palmisano L (2007) Chem Commun 3425
7. Fagnoni M, Dondi D, Ravelli D, Albini A (2007) Chem Rev 107:2725
8. Maldotti A, Molinari A, Amadelli R (2002) Chem Rev 102:3811
9. Tzirakis MD, Lykakis IN, Orfanopoulos M (2009) Chem Soc Rev 38:2609
10. Kisch H (2001) Adv Photochem 62:93
11. Griesbeck AG, Mattay J (2005) Synthetic organic photochemistry. Dekker, New York
12. Gambarotti C, Punta C, Recupero F, Caronna T, Palmisano L (2010) Curr Org Chem 14:1153
13. Zaera FJ (2010) Phys Chem Lett 1:621
14. Sheldon RA, Kochi JK (1981) Metal-catalyzed oxidation of organic compounds. Academic, New York
15. Foote CS (1995) Active oxygen in chemistry. Chapman and Hall, New York
16. Bielanski A, Haber J (1991) Oxygen in catalysis. Dekker, New York
17. Hoffmann ML, Martin ST, Choi W, Bahnemann DW (1995) Chem Rev 95:69
18. Linsebigler AL, Lu G, Yates JT Jr (1995) Chem Rev 95:735
19. Herrmann JM (1999) Catal Today 53:115
20. Fox MA, Dulay MT (1993) Chem Rev 93:341
21. Augugliaro V, Loddo V, Marcì G, Palmisano L, Lopez-Munoz MJ (1997) J Catal 166:172
22. Albonetti S, Cavani F, Trifirò F (1996) Catal Rev Sci Eng 38:413
23. Arends IWCE, Sheldon RA, Wallau M, Schuchardt U (1997) Angew Chem Int Ed Engl 36:144
24. Tryk DA, Fujishima A, Honda K (2000) Electrochim Acta 45:2363
25. Lu G, Gao H, Suo J, Li S (1994) J Chem Soc Chem Commun 2423
26. Boarini P, Carassiti V, Maldotti A, Amadelli R (1998) Langmuir 14:2080
27. Almquist CB, Biswas P (2001) Appl Catal A 214:259
28. Li X, Quan X, Kutal C (2004) Struct Mater 50:499
29. Brusa MA, Grela MA (2005) J Phys Chem B109:1914
30. Du P, Moulijn JA, Mul G (2006) J Catal 238:342
31. Goldstein S, Meyrestein D (1999) Acc Chem Res 32:547
32. Maldotti A, Molinari A, Amadelli R, Carbonell E, Garcia HP (2008) Photochem Photobiol Sci 7:819
33. Carneiro JT, Savenije TJ, Moulijn JA, Mul G (2010) J Phys Chem 114:327
34. Carneiro JT, Yang CC, Moma JA, Moulijn JA, Mul G (2009) Catal Lett 129:12
35. Carneiro JT, Almeida AR, Moulijn JA, Mul G (2010) Phys Chem Chem Phys 12:2744
36. Herrman JM, Pichat P, Mu W (1989) Catal Lett 3:73
37. Gonzales MA, Howell SG, Sikdar SK (1999) J Catal 183:159
38. Almeida AR, Moulijn JA, Mul G (2008) J Phys Chem C 112:1552
39. Brusa MA, Di Iorio Y, Churio MS, Grela MA (2007) J Mol Catal A Chem 268:29
40. Navio JA, Garcia Gomez M, Pradera Adrian MA, Fuentes Mota J (1996) J Mol Catal A Chem 104:329
41. Augugliaro V, Coluccia S, Loddo V (1999) Appl Catal B Environ 20:15
42. Cao L, Gao Z, Suib SL, Obee TN, Hay SO, Freihaut JD (2000) J Catal 196:253
43. Fujihira M, Satoh Y, Osa T (1981) Nature 293:206

44. Shimizu K-I, Kaneko T, Fujishima T, Kodama T, Yoshida H, Kitayama Y (2004) Appl Catal A Gen 269:75
45. Palmisano G, Addamo M, Augugliaro V, Caronna T, Di Paola A, Garcia-Lopez E, Loddo V, Palmisano L (2006) Chem Commun 1012
46. Palmisano G, Addamo M, Augugliaro V, Caronna T, Di Paola A, Garcia-Lopez E, Loddo V, Marci G, Palmisano L, Schiavello M (2007) Catal Today 122:118
47. Soana F, Sturini M, Cermenati L, Albini A (2000) J Chem Soc Perkin Trans 2:699
48. Cermenati L, Dondi D, Fagnoni M, Albini A (2003) Tetrahedron 59:6409
49. Higashida S, Harada A, Kawakatsu R, Fujiwara N, Matsumura M (2006) Chem Commun 2804
50. Shiraishi Y, Saito N, Hirai T (2005) J Am Chem Soc 127:12820
51. Chen J, Eberlein L, Langford CH (2002) J Photochem Photobiol A Chem 148:183
52. Shimizu K-I, Kaneko T, Fujishima T, Kodama T, Yoshida H, Kitayama Y (2002) Appl Catal A Gen 225:185
53. Rezala H, Khalaf H, Valverde JL, Romero A, Molinari A, Maldotti A (2009) Appl Catal A Gen 352:234
54. Shiraishi Y, Sugano Y, Inoue D, Hirai T (2009) J Catal 264:175
55. Cosa G, Galletero MS, Fernandez L, Marquez F, Garcia H, Scaiano JC (2002) New J Chem 26:1448
56. Pichat P, Mozzanega M, Courbon H (1987) J Chem Soc Faraday Trans 1(83):697
57. Muggli DS, Falconer JL (1998) J Catal 175:213
58. Pillai UR, Sahle-Demessie E (2002) J Catal 211:434
59. Samiolo L, Valigi M, Gazzoli D, Amadelli R (2010) Electrochim Acta 55:7788
60. Molinari A, Montoncello M, Houria R, Maldotti A (2009) Photochem Photobiol Sci 8:613
61. Molinari A, Bruni M, Maldotti A (2008) J Adv Oxid Technol 11:143
62. Amadelli R, Molinari A, Vitali I, Samiolo L, Mura GM, Maldotti A (2005) Catal Today 101:397
63. Bettoni M, Rol C, Sebastiani GV (2008) J Phys Org Chem 21:219
64. Augugliaro V, Loddo V, Lopez-Munoz MJ, Marquez-Alvarez C, Palmisano G, Palmisano L, Yurdakal S (2009) Photochem Photobiol Sci 8:663
65. Yurdakal S, Palmisano G, Loddo V, Alagoez O, Augugliaro V, Palmisano L (2009) Green Chem 11:510
66. Addamo M, Augugliaro V, Bellardita M, Di Paola A, Loddo V, Palmisano G, Palmisano L, Yurdakal S (2008) Catal Lett 126:58
67. Augugliaro V, Caronna T, Loddo V, Marcì G, Palmisano G, Palmisano L, Yurkadal S (2008) Chem Eur J 14:4640
68. Palmisano G, Yurkadal S, Augugliaro V, Loddo V, Palmisano L (2007) Adv Synth Catal 349:964
69. Yurdakal S, Palmisano G, Loddo V, Augugliaro V, Palmisano L (2008) J Am Chem Soc 130:1568
70. Augugliaro V, Kisch H, Loddo V, Lopez-Munoz MJ, Marquez-Alvarez C, Palmisano L, Palmisano L, Parrino F, Yurdakal S (2008) Appl Catal A 349:182
71. Blake NR, Griffin GL (1988) J Phys Chem 92:5697
72. Mohamed OS, Gaber AM, Abdel-Wahab AA (2002) J Photochem Photobiol A Chem 148:205
73. Chen J, Ollis DF, Rulkens WH, Bruning H (1999) Water Res 33:669
74. Zhang Z, Bondarchuk O, White JM, Kay BD, Dohnalek Z (2006) J Am Chem Soc 128:4198
75. Mandelbaum PA, Regazzoni AE, Blesa MA, Bilmes SA (1999) J Phys Chem B 103:5505
76. Ganadu ML, Andreotti L, Vitali I, Maldotti A, Molinari A, Mura GM (2002) Photochem Photobiol Sci 1:951
77. Ferry JL, Glaze WH (1998) Langmuir 14:3551
78. Ferry JL, Glaze WH (1998) J Phys Chem 102:2239
79. Brezova V, Blazkova A, Surina I, Halinova B (1997) J Photochem Photobiol A 107:233

80. Flores SO, Rios-Berny O, Valenzuela MA, Cordova I, Gomez R, Gutierrez R (2007) Top Catal 44:507
81. Rios-Berny O, Flores SO, Cordova I, Valenzuela MA (2010) Tetrahedron Lett 51:2730
82. Kominami H, Iwaasaki S, Maeda T, Imamura K, Hashimoto K, Kera Y, Ohtani B (2009) Chem Lett 38:410
83. Tada H, Ishida T, Takao A, Ito S (2004) Langmuir 20:7898
84. Wang H, Yan J, Chang W, Zhang Z (2009) Catal Commun 10:989
85. Matsushita Y, Ohba N, Kumada S, Sakeda K, Suzuki T, Ichimura T (2008) Chem Eng J 135:303
86. Cermenati L, Mella M, Albini A (1998) Tetrahedron 54:2575
87. Cermenati L, Albini A (2002) J Adv Oxid Technol 5:58
88. Cermenati L, Fagnoni M, Albini A (2003) Can J Chem 81:560
89. Marinkovic S, Hoffmann N (2001) Chem Commun 1576
90. Marinkovic S, Hoffmann N (2004) Eur J Org Chem 3102
91. Caronna T, Gambarotti C, Palmisano L, Punta C, Recupero F (2003) Chem Commun 2350
92. Caronna T, Gambarotti C, Palmisano L, Punta C, Recupero F (2005) J Photochem Photobiol A Chem 171:237
93. Wang H, Partch RE, Li Y (1997) J Org Chem 62:5222
94. Park KH, Joo HS, Ahn KI, Jun K (1995) Tetrahedron Lett 36:5943
95. Maldotti A, Amadelli R, Samiolo L, Molinari A, Penoni A, Tollari S, Cenini S (2005) Chem Commun 1749
96. Maldotti A, Andreotti L, Molinari A, Tollari S, Penoni A, Cenini S (2000) J Photochem Photobiol A 133:129
97. Hakki A, Dillert R, Bahnemann D (2009) Catal Today 144:154
98. Subba Rao KV, Srinivas B, Prasad AR, Subrahmanyam M (2000) Chem Commun 1533
99. Subba Rao KV, Subrahmanyam M (2002) Photochem Photobiol Sci 1:597
100. Subba Rao KV, Srinivas B, Prasad AR, Subrahmanyam M (2002) Chem Lett 236
101. Selvam K, Swaminathan M (2007) Chem Lett 36:1060
102. Nishimoto S-i, Ohtani B, Yoshikawa T, Kaguya T (1983) J Am Chem Soc 105:7180
103. Ohtani B, Iwai K, Kominami H, Matsuura T, Kera Y, Nishimoto S-i (1995) Chem Phys Lett 242:315
104. Ohtani B, Kawaguchi J, Kozawa M, Nakaoka Y, Nosaka Y, Nishimoto S (1995) J Photochem Photobiol A Chem 90:75
105. Takei G, Kitamori T, Kim HB (2005) Catal Commun 6:357
106. Ohtani B, Osaki H, Nishimoto S-i, Kagiya T (1986) J Am Chem Soc 108:308
107. Ohtani B, Goto Y, Nishimoto S-I, Inui T (1996) J Chem Soc Faraday Trans 92:4291
108. Baciocchi E, Rol C, Rosato G, Sebastiani GV (1992) J Chem Soc Chem Commun 59
109. Baciocchi E, Rol C, Sebastiani GV, Taglieri L (1994) J Org Chem 59:5972
110. Shiraishi Y, Sugano Y, Tanaka S, Hirai T (2010) Angew Chem Int Ed 49:1656
111. Yoshida H, Murata C, Hattori T (1999) Chem Commun 1551
112. Murata C, Yoshida H, Kumagai J, Hattori T (2003) J Phys Chem B 107:4364
113. Murata C, Hattori T, Yoshida H (2005) J Catal 231:292
114. Li X, Kutal C (2002) J Mater Sci Lett 21:1525
115. Shiraishi Y, Morishita M, Hirai T (2005) Chem Commun 5977
116. Morishita M, Shiraishi Y, Hirai T (2006) J Phys Chem B 110:17898
117. Shiraishi Y, Saito N, Hirai T (2005) J Am Chem Soc 127:8304
118. Shiraishi Y, Tsukamoto D, Hirai T (2008) Langmuir 24:12658
119. Lin W, Frei H (2005) J Phys Chem B 109:4929
120. Hu Y, Wada N, Tsujimaru K, Anpo M (2007) Catal Today 120:139
121. Nakamura R, Okamoto A, Osawa H, Irie H, Hashimoto K (2007) J Am Chem Soc 129:9596
122. Anpo M, Kim T, Matsuoka M (2009) Catal Today 142:114
123. Shiraishi Y, Teshima Y, Hirai T (2005) Chem Commun 4569
124. Shiraishi Y, Ohara H, Hirai T (2008) J Catal 254:365

125. Murata C, Yoshida H, Hattori T (2001) Chem Commun 2412
126. Shiraishi Y, Teshima Y, Hirai T (2006) J Phys Chem B 110:6257
127. Shiraishi Y, Morishita M, Teshima Y, Hirai T (2006) J Phys Chem B 110:6587
128. Amano F, Ito T, Takenaka S, Tanaka T (2005) J Phys Chem B 109:10973
129. Lopez HH, Martinez A (2002) Catal Lett 83:37
130. Hu Y, Higashimoto S, Takahashi S, Nagai Y, Anpo M (2005) Catal Lett 100:35
131. Hill CL, Prosser-McCartha CM (1995) Coord Chem Rev 143:407
132. Mizuno N, Misono M (1998) Chem Rev 98:199
133. Khenkin AM, Ben-Daniel R, Rosenberger A, Vigdergauz I, Neumann R (2001) In: Pope MT, Muller A (eds) Polyoxometalate chemistry from topology via self-assembly to applications. Kluwer, Dordrecht, p 347
134. Tzirakis MD, Likakis IN, Orfanopoulos M (2009) Chem Soc Rev 38:2609
135. Maldotti A, Molinari A (2008) In: Marmaduke DL (ed) Progress in heterogeneous catalysis. Nova, New York, p 1
136. Duncan DC, Netzel TL, Hill CL (1995) Inorg Chem 34:4640
137. Tanielian C, Duffy K, Jones A (1997) J Phys Chem B 101:4276
138. Duncan DC, Fox MA (1998) J Phys Chem A 102:4559
139. Tanielian C (1998) Coord Chem Rev 178–180:1165
140. Maldotti A, Amadelli R, Varani G, Tollari S, Porta F (1994) Inorg Chem 33:2968
141. Hiskia A, Mylonas A, Papaconstantinou E (2001) Chem Soc Rev 30:62
142. Molinari A, Amadelli R, Andreotti L, Maldotti A (1999) Dalton Commun 1203
143. Molinari A, Amadelli R, Mazzacani A, Sartori G, Maldotti A (2002) Langmuir 18:5400
144. Maldotti A, Molinari A, Varani G, Lenarda M, Storaro L, Bigi F, Maggi R, Mazzacani A, Sartori G (2002) J Catal 209:210
145. Molinari A, Amadelli R, Carassiti V, Maldotti A (2000) Eur J Inorg Chem 91
146. Maldotti A, Amadelli R, Vitali I, Borgatti L, Molinari A (2003) J Mol Catal A Chem 204–205:703
147. Tzirakis MD, Lykakis IN, Panagiotou GD, Bourikas K, Lycourghiotis A, Kordulis C, Orfanopoulos M (2007) J Catal 252:178
148. Shen HY, Mao HL, Ying LY, Xia QH (2007) J Mol Catal A Chem 276:73
149. Ozer RR, Ferry JL (2002) J Phys Chem B 106:4336
150. Guo Y, Hu C, Wang X, Wang Y, Wang E, Zou Y, Ding H, Feng S (2001) Chem Mater 13:4058
151. Guo Y, Hu C, Jiang S, Guo C, Yang Y, Wang E (2002) Appl Catal B Environ 36:9
152. Farhadi S, Afshari M (2006) J Chem Res 188
153. Farhadi S, Afshari M, Malesi M, Babazadeh Z (2005) Tetrahedron Lett 46:8483
154. Molinari A, Bratovcic A, Magnacca G, Maldotti A (2010) Dalton Trans 39:7826
155. Farhadi S, Momeni Z (2007) J Mol Catal A Chem 277:47
156. Farhadi S, Zaidi M (2009) J Catal 354:119
157. Farhadi S, Sepahvand S (2010) J Mol Catal A Chem 318:75
158. Friesen DA, Gibson DB, Langford CH (1998) Chem Commun 543
159. Friesen DA, Morello L, Headley JV, Langford CH (2000) J Photochem Photobiol A Chem 133:213
160. Maldotti A, Molinari A, Bigi F (2008) J Catal 253:312
161. Ni L, Ni J, Lv Y, Yang P, Cao Y (2009) Chem Commun 2171
162. Fornal E, Giannotti C (2007) J Photochem Photobiol A Chem 188:279
163. Molinari A, Varani G, Polo E, Vaccari S, Maldotti A (2007) J Mol Catal A Chem 262:156
164. Bonchio M, Carraro M, Scorrano G, Fontananova E, Drioli E (2003) Adv Synth Catal 345:1119
165. Bonchio M, Carraro M, Gardan M, Scorrano G, Drioli E, Fontananova E (2006) Top Catal 40:133
166. Carraro M, Gardan M, Scorrano G, Drioli E, Fontananova E, Bonchio M (2006) Chem Commun 4533

167. Lopez LC, Buonomenna MG, Fontananova E, Iacoviello G, Drioli E, d'Agostino R, Favia P (2006) Adv Funct Mater 16:1417
168. Fontananova E, Donato L, Drioli E, Lopez LC, Favia P, d'Agostino R (2006) Chem Mater 18:1561
169. Park H, Choi W (2005) Catal Today 101:291
170. Anandan S, Ryu SY, Cho W, Yoon M (2003) J Mol Catal A Chem 195:201
171. Yoon M, Chang JA, Kim Y, Choi JR, Kim K, Lee SJ (2001) J Phys Chem B 105:2539

Index